



저작자표시 2.0 대한민국

이용자는 아래의 조건을 따르는 경우에 한하여 자유롭게

- 이 저작물을 복제, 배포, 전송, 전시, 공연 및 방송할 수 있습니다.
- 이차적 저작물을 작성할 수 있습니다.
- 이 저작물을 영리 목적으로 이용할 수 있습니다.

다음과 같은 조건을 따라야 합니다:



저작자표시. 귀하는 원저작자를 표시하여야 합니다.

- 귀하는, 이 저작물의 재이용이나 배포의 경우, 이 저작물에 적용된 이용허락조건을 명확하게 나타내어야 합니다.
- 저작권자로부터 별도의 허가를 받으면 이러한 조건들은 적용되지 않습니다.

저작권법에 따른 이용자의 권리는 위의 내용에 의하여 영향을 받지 않습니다.

이것은 [이용허락규약\(Legal Code\)](#)을 이해하기 쉽게 요약한 것입니다.

[Disclaimer](#) 

공학박사 학위논문

**Heteroepitaxial Growth of
Nanobranches on SnO₂ Nanobelt for
Electrochemical Devices**

전기화학 장치용 산화주석 나노벨트 위에 형성된
나노브랜치의 이중적층 성장

AUGUST 2014

By

Sangbaek Park

DEPARTMENT OF
MATERIALS SCIENCE AND ENGINEERING
COLLEGE OF ENGINEERING
SEOUL NATIONAL UNIVERSITY

Abstract

Heteroepitaxial Growth of Nanobranches on SnO₂ Nanobelt for Electrochemical Devices

Sangbaek Park

Department of Materials Science & Engineering

College of Engineering

Seoul National University

Three dimensional (3-D) heteroepitaxial nanoarchitectures composed of transparent conducting oxide (TCO) backbone and metal oxide branch were designed and synthesized to enhance the electrochemical properties in energy conversion and storage devices. The synthesized heteroepitaxially nanostructured electrodes were practically applied to electrochemical devices. Additionally, the correlations between structural factors of 3-D electrode and device performance were explored. In particular, photoelectrochemical (PEC) cells and Li-ion batteries, which are accepted as representative electrochemical conversion and storage devices in the hydrogen energy system by renewable solar energy conversion, were studied. These PEC cells and Li-ion batteries currently face significant challenges in low efficiency and long-term stability, respectively. Since metal oxide electrode materials are essential in charge transfer and transport of the PEC cell and Li ion battery, efficient structure control and design provide high efficiency and long-term stability. Nanostructures, especially 3-D nanoarchitectures, are efficient at charge transfer and transport. However, novel approaches are needed to further improve charge transfer and transport, since metal oxide nanoarchitecturing almost reached the limit in both fabrication method and structure modification. Therefore, this thesis suggests two strategies for the charge transfer and transport in PEC cells and Li-ion batteries. The

first employs the 1-D TCO backbone for effective charge extraction and transport from metal oxide branches. The second fabricates the 3-D heteroepitaxial nanostructures that can lead to defect-free interface and self-assembled array, which enhance the electrochemical device performance.

In order to systematically study the epitaxial growth in 3-D nanoarchitecturing, a rutile based heteroepitaxial structure was selected and explored. Thermally and chemically stable rutile SnO_2 was developed for 1-D TCO backbones through Sb doping. Sb:SnO_2 (ATO) nanobelts were found to grow vertically on both FTO glass and Ti substrate with metallic conductivity attributed to the unique Sb doping behavior. To understand the fundamental aspects of heteroepitaxial growth on nanobranching, various metal oxides – TiO_2 , Fe_2O_3 , and VO_2 – were synthesized on ATO nanobelts by the facile solution process. TiO_2 and Fe_2O_3 nanorods were grown on all four ATO nanobelt sides like wheel spokes while VO_2 nanorods were linearly grown on only two ATO nanobelt sides. The structural analysis showed that both the dendritic and linear growth modes are attributed to interfacial lattice mismatch. For TiO_2 and Fe_2O_3 , the lattice mismatch between backbone and branch was minimized through tilted nanobranches that induce dendritic growth. For VO_2 , the lattice mismatch was minimized through strained nanobranches that induce linear growth. Furthermore, the epitaxial strain of nanorods reduced the VO_2 metal-insulator transition (MIT) temperature, which is due to compressive strain along the c-axis ($\sim 0.2\%$).

In addition, this thesis examined the heteroepitaxial nanoarchitecturing on the charge transfer and transport properties of metal oxide electrodes for PEC cells and Li-ion batteries. A comparison of the TiO_2 -ATO core-shell and heteroepitaxially branched structures found that the branched structure had better charge transfer properties due to the well-aligned nanorods that result in a branched structure twice as effective than core-shell structures. The CdS-TiO_2 -ATO multi-junction nanostructures were developed to realize the structural-factor-optimizable nanostructure and achieved a saturated photocurrent density of 7.75 mA/cm^2 at 0.4 V/RHE under AM 1.5 solar illumination. To control both the morphology and electronic properties of Fe_2O_3 nanorods simultaneously, Fe_2O_3 -ATO was further post-annealed. The Fe_2O_3 nanorod

flat band potential and carrier density was effectively improved by diffusing Sn^{4+} from SnO_2 nanobelts into $\alpha\text{-Fe}_2\text{O}_3$ nanorods, which provided enhanced charge transfer properties.

Finally, $\text{TiO}_2\text{-ATO}$ and $\text{VO}_2\text{-ATO}$ heteroepitaxial structures were proposed to improve the long-term stability of Li-ion batteries. A combination of ATO nanobelts and decorated TiO_2 branches produced great synergistic effects that enhanced cycle retention and rate capabilities in anodes due to the advantageous geometrical and structural features. Interestingly, the specific capacities originating from only TiO_2 nanorods were almost near the theoretical value of rutile TiO_2 and were maintained even after 150 cycles. In the same manner, outstanding rate capabilities and cycling stability were evaluated in the cathode $\text{VO}_2\text{-ATO}$. These excellent $\text{TiO}_2\text{-ATO}$ and $\text{VO}_2\text{-ATO}$ electrochemical properties are attributed to superior charge collection properties due to conductive 1-D backbone and effective Li transport from 1-D diffusion along the [001] direction.

This thesis focused on synthesis and control of heteroepitaxially branched metal oxide based on the 1-D TCO backbone to improve charge transfer and transport in PEC cells and Li-ion batteries. It also tried to suggest a possibility to resolve problems and create breakthroughs in energy conversion and storage devices.

Keywords: Nanostructure, heterostructure, epitaxial, three-dimensional, vapor-liquid-solid mechanism, chemical bath deposition, SnO_2 , transparent conducting oxide, TiO_2 , Fe_2O_3 , VO_2 , photoelectrochemical, Li ion battery, cycle performance

Student Number: 2007-22950

Table of Contents

Abstract	i
Table of Contents	v
List of Tables	viii
List of Figures	ix
Chapter 1 Introduction	1
1.1 Energy conversion and storage devices for sustainable development.....	1
1.2 Nanoarchitecturing for electrochemical devices.....	6
1.2.1 Nanoarchitecturing for efficient electrodes.....	6
1.2.2 Metal oxide-based 3-D nanostructures	10
1.2.3 1-D conductive backbone	12
1.2.4 3-D heteroepitaxial branch.....	14
1.3 Aim and approach	15
Chapter 2 Background and literature review	19
2.1 Heteroepitaxial growth.....	19
2.1.1 Heteroepitaxy	19
2.1.2 Applications of heteroepitaxy	28
2.1.3 Heteroepitaxy for 3-D nanoarchitecturing	30
2.2 Preparation of 3-D heteroepitaxial nanostructures	44
2.2.1 Subsequent solution growth.....	44
2.2.2 Subsequent vapor growth.....	46

2.2.3	Vapor-solution combination growth.....	47
2.2.4	Summary	47
2.3	Materials	51
2.3.1	Rutile.....	51
2.3.2	SnO ₂	54
2.3.3	TiO ₂	60
2.3.4	VO ₂	68
Chapter 3 Experiments		74
3.1	Synthesis of 1-D nanostructure	74
3.2	Synthesis of 3-D nanostructure	76
3.3	Fabrication of PEC cell and Li ion battery	80
3.4	Characterization	81
Chapter 4 1-D nanoarrays		85
4.1	Sb:SnO ₂ (ATO) nanobelt array	85
4.1.1	Growth of ATO nanobelts on substrates.....	85
Chapter 5 3-D nanobranches		98
5.1	Dendritic growth I: TiO ₂ –ATO	98
5.1.1	Morphology and structure.....	98
5.1.2	Formation mechanism.....	106
5.1.3	Epitaxial relationship	137
5.2	Dendritic growth II: Fe ₂ O ₃ –ATO	143
5.2.1	Morphology and structure.....	143
5.2.2	Epitaxial relationship	148

5.3	Linear growth: VO ₂ -ATO	152
5.3.1	Morphology and structure	152
5.3.2	Epitaxial relationship	161
5.3.3	Epitaxial strain effect	169
Chapter 6 Electrochemical applications		177
6.1	Photoelectrochemical cell	177
6.1.1	TiO ₂ -ATO photoanode for water splitting	177
6.1.2	Quantum-dot-sensitized TiO ₂ -ATO	182
6.1.3	Fe ₂ O ₃ -ATO photoanode for solar water oxidation	201
6.2	Li ion battery	219
6.2.1	TiO ₂ -ATO anode for Li ion battery	219
6.2.2	VO ₂ -ATO cathode for Li ion battery	233
Chapter 7 Conclusion.....		244
Bibliography		252
Abstract in Korean.....		277
Research Achievements.....		280
Acknowledgement		288

List of Tables

Table 2.1	3-D heteroepitaxial nanostructures sort by growth methods and their compounds, morphology and applications.	49
Table 2.2	Structural data for representative rutile materials	52
Table 4.1.1	EPMA analysis of the ATO nanobelts.....	89
Table 5.3.1	Lattice planes (<i>hkl</i>) and their <i>d</i> -spacings of tetragonal rutile VO ₂ (R) and monoclinic VO ₂ (M).	164
Table 5.3.2	Lattice parameter and strain of VO ₂ nanorods epitaxially grown on ATO nanobelt by hydrothermal reaction for 3, 6 h and 12 h. Lattice parameters (<i>a</i> , <i>b</i> and <i>c</i>) were calculate from Rietveld refinement of XRD pattern. Strain at each axis was evaluated by difference of lattice parameters between unstrained VO ₂ (M) phase and strained VO ₂ nanorods.	172
Table 5.3.3	Lattice plane (<i>hkl</i>), <i>d</i> -spacings, lattice mismatch and strain of VO ₂ nanorods epitaxially grown on ATO nanobelt by hydrothermal reaction for 3 h, 6 h and 12 h. <i>d</i> -spacings of nanorods were calculate from Rietveld refinement of XRD pattern. Lattice mismatch at each plane was derived by difference of <i>d</i> -spacing between SnO ₂ backbone and VO ₂ nanorods.	173
Table 6.1.1	The electrical properties of Fe ₂ O ₃ -FTO at 4 h before and after post annealing at 650 °C and Fe ₂ O ₃ -ATO for 4 h before and after post annealing at 650 °C. (ϵ : dielectric permittivity, E_{fb} : flat band potential, N_D : carrier concentration)	211
Table 6.2.1	Comparison of the electrochemical performance with various reported VO ₂ -based cathode materials for Li-ion batteries	236

List of Figures

Figure 1.1	Environmental and energy problem induced by use of fossil fuels	4
Figure 1.2	Schematic representation for hydrogen energy cycle based on hydrogen fuel cell vehicle.	5
Figure 1.3	Structure of a typical PEC cell with photoanode (n-type semiconducting materials), cathode (Pt), an aqueous electrolyte and a separator.	8
Figure 1.4	Scheme of a typical Li-ion battery with negative electrode (graphite on copper current collector), positive electrode (LiCoO ₂ on aluminum current collector), a nonaqueous liquid electrolyte (LiPF ₆ , EC:DMC) and a separator.	9
Figure 2.1	Scheme of the geometrical configuration for the epitaxial growth in different stages; (a) before growth, (b) in the nucleation stage related to the first monolayer growth, (c) at the early stage of growth, and (d) in the stage for regular epitaxial growth proceeds	21
Figure 2.2	Schematic illustrations of interfacial atomic registry in the epilayer and substrate with different crystallographic symmetry. Black dots: the substrate atoms, Empty circles: epilayer atoms	25
Figure 2.3	Schemes of (a) strained and (b) relaxed epitaxial layers.	26
Figure 2.4	Effect of strain on the valence bands and the lowest conduction band.	27
Figure 2.5	Electronic DOS in semiconductors with different dimensionalities: 3-D bulk, 2-D quantum well, 1-D quantum wire and 0-D quantum dot.	29
Figure 2.6	Schematic of the three epitaxial growth modes. (a) 2-D layer-by-layer (FM-mode), (b) 3-D island (VW-mode) and (c) layer-by-	

	layer growth followed by islanding (SK-mode)	35
Figure 2.7	Free energy (ΔG) of (a) 3D epitaxial formation and (b) 2D epitaxial formation as a function of the number of the particles (n) at the supersaturation $\Delta\mu$	39
Figure 2.8	Schematic illustration of elastic strain relaxation in 3D self-ordered arrays	41
Figure 2.9	Faceting of a (001) surface to a surface with {011} facets.	43
Figure 2.10	Total energy gain from island formation in which $\rho=10^{10}$ cm ⁻² and $\theta_0 = 1.8$ monolayers. Arrows indicate the minimum of the total energy curves.....	43
Figure 2.11	The rutile structure viewed along the [001] direction, where the metal atoms and oxygen atoms are located at the center and edge of octahedra.	53
Figure 2.12	Energy band diagram of Sb-doped SnO ₂	56
Figure 2.13	(a) curved and (b) zig-zag shaped Sb:SnO ₂ nanobelt arrays by vapor-liquid-solution mechanism.	59
Figure 2.14	Molecular-orbital bonding structure for TiO ₂ : (a) atomic levels; (b) crystal-field split levels; (c) final interaction (DOS) states..	62
Figure 2.15	Schematic illustration of the energy levels diagram of the lowest unoccupied molecular orbitals of a [TiO ₆] ⁸⁻ cluster and rutile with O _h and D _{2h} symmetry, respectively.	64
Figure 2.16	Phonon eigenvectors of the lowest frequency mode at rutile VO ₂ unit cell.	69
Figure 2.17	Crystal structures of (a) V ₂ O ₅ projected along the b-axis, (b) VO ₂ (B) projected along the b-axis and (c) VO ₂ (A) projected along the c-axis, which shows the layered structure. (d) Crystal structure of VO ₂ (B) along c-axis, which also shows the tunnel for Li ⁺ diffusion pathway.	73
Figure 3.1	Schematic view of the thermal evaporation system.....	75

Figure 3.2	Schematic view of chemical bath deposition method.....	79
Figure 4.1.1	(a) Low and (b) high magnification of cross-sectional SEM images of the ATO nanobelts on FTO substrate.	90
Figure 4.1.2	(a) Plane and (b) cross-sectional SEM images of the ATO nanobelts on Ti substrate, and (c) high-magnification SEM image of the middle region of the ATO nanobelts.....	90
Figure 4.1.3	XRD graphs of the FTO substrate, Sb:SnO ₂ nanobelts, and undoped-SnO ₂ nanowires	91
Figure 4.1.4	(a, b) TEM images of an ATO nanobelt, (c) high-resolution TEM image and (d) the corresponding SAED pattern in marked region of (b).	92
Figure 4.1.5	EDS mapping of an ATO nanobelt showing Sn, Sb, Au, and O atomic profiles.	93
Figure 4.1.6	Schematic representations of growth mechanism: an ATO nanobelt.	94
Figure 4.1.7	XPS of ATO nanobelt arrays.....	95
Figure 4.1.8	Raman spectra of ATO nanobelt arrays	96
Figure 4.1.9	(a) A plane SEM image of a device fabricated for electrical transport of an ATO nanobelt and (b) typical I _{ds} -V _{ds} curve of an ATO nanobelt.....	97
Figure 5.1.1	(a) A tilted SEM image of TiO ₂ -ATO arrays. High magnification SEM images of (b) the top regions and (c) the middle regions of the TiO ₂ -ATO arrays.	100
Figure 5.1.2	SEM images of TiO ₂ nanorods in CBD (a) with and (b) without the ATO nanobelts substrates.....	101
Figure 5.1.3	A XRD graph of the TiO ₂ -ATO arrays.....	102
Figure 5.1.4	XPS of TiO ₂ -ATO arrays.....	103
Figure 5.1.5	(a) A TEM image of a TiO ₂ -ATO and (b) the HRTEM image of the small marked region in (a), inset shows reduced FFT for	

selected area of the TiO ₂ nanorod.	104
Figure 5.1.6 EDS analysis of a TiO ₂ -ATO: (a) line-scan and (b) elemental mapping.	105
Figure 5.1.7 As a function of reaction time, equilibrium pH of (a) the TiCl ₄ exchanged every 8 hours (●) and (b) the TiCl ₄ maintained during reaction (■). (c) Schematic diagrams and TEM image of the ATO nanowire covered with TiO ₂ nano shell-like structure through (a) process. (d) Schematic diagrams and FESEM image of the ATO nanowire covered with TiO ₂ nano needle leaf-like structure through (b) process.	110
Figure 5.1.8 TEM images ATO nanowire covered with TiO ₂ nano shell-like structure by TiCl ₄ treatment in (a) 24 hours, (b) 48 hours, (c) 72 hours, (d) 96 hours and (e) 144 hours. Each inset shows the SAED pattern and low magnification of nano shell.	111
Figure 5.1.9 SEM images ATO nanobelt covered with TiO ₂ nano needle leaf-like structure by TiCl ₄ treatment in (a) 24 hours, (b) 48 hours, (c) 72 hours, (d) 96 hours and (e) 144 hours.	112
Figure 5.1.10 XRD graphs of (a) AS144 and (b) RR144 before and after annealing at 450 °C for 1h.	113
Figure 5.1.11 HRTEM images of (a) AS48-450 and (b) RR48-450. Each Inset shows low-magnification of the HR image.	113
Figure 5.1.12 Schematic representation of TiO ₂ anatase and rutile growth mechanism on the ATO nanobelt by CBD method.	114
Figure 5.1.13 SEM images of nanobranches synthesized with the addition of different acids: (a) HNO ₃ , (b) HCl, (c) H ₂ SO ₄ , and (d) HCOOH. Scale bar, 300 nm.	118
Figure 5.1.14 TEM images of TiO ₂ nanobranches synthesized by CBD with the addition of (a) HNO ₃ and (b) HCl.	118

Figure 5.1.15 Raman spectra of nanobranched synthesized with the addition of different acids: (a) HNO ₃ , (b) HCl, (c) H ₂ SO ₄ , and (d) HCOOH.	119
Figure 5.1.16 SEM images of nanobranched synthesized in the presence of HNO ₃ at different concentrations: (a) 0.02 M, (b) 0.06 M, (c) 0.1 M, (d) 0.2 M, (e) 0.3 M, and (f) 0.6 M. Scale bar, 300 nm.....	121
Figure 5.1.17 XRD graphs of nanobranched synthesized in the presence of HNO ₃ at different concentrations: (a) 0.02 M, (b) 0.06 M, (c) 0.1 M, (d) 0.2 M, (e) 0.3 M, and (f) 0.6 M..	122
Figure 5.1.18 FESEM images of an ATO nanobelt covered with TiO ₂ nanorod by TiCl ₄ treatment for (a) 0.5 h, (b) 1 h, (c) 1.5 h, (d) 2 h, (e) 2.5 h, and (f) 3 h.	125
Figure 5.1.19 XRD graphs of nanobranched synthesized in the presence of 0.2 M HNO ₃ along the reaction time: (a) 0.5 h, (b) 1 h, (c) 1.5 h, (d) 2 h, (e) 2.5 h, and (f) 3 h.	126
Figure 5.1.20 SEM images of nanobranched synthesized in the presence of HNO ₃ with different concentrations and reaction time. Scale bar, 500 nm.	129
Figure 5.1.21 The dependence of average length of TiO ₂ nanorods on (a) HNO ₃ concentration and (b, c) reaction time.....	135
Figure 5.1.22 Schematic representations of the growth mechanism of TiO ₂ nanorods on an ATO nanobelt at different HNO ₃ concentrations	136
Figure 5.1.23 (a) A cross-sectional TEM image of a TiO ₂ -ATO. SAED patterns of (b) the ATO nanobelt region and (c) the TiO ₂ nanorods region. (d-f) HRTEM images of interface between an ATO nanobelt and TiO ₂ nanorods.....	141
Figure 5.1.24 Schematic representations of crystallography of an ATO	

	nanobelt, (b) TiO ₂ nanorods on ATO { $\bar{1}01$ } planes, and (c) TiO ₂ nanorods on an ATO (010) plane.	142
Figure 5.2.1	XRD patterns of (a-c) Fe ₂ O ₃ -ATO arrays synthesized by chemical bath deposition at different times: (a) 2 h, (b) 4 h, and (c) 12 h. The vertical lines denote the reference XRD patterns of the rutile SnO ₂ (JCPDF #1-1445) and rhombohedral α -Fe ₂ O ₃ (JCPDF #33-0664).....	145
Figure 5.2.2	Low and high magnification FESEM images of Fe ₂ O ₃ -ATO arrays synthesized by chemical bath deposition at different times: (a-b) 2 h, (c-d) 4 h, and (e-f) 12 h.....	146
Figure 5.2.3	(a) TEM image of a Fe ₂ O ₃ -ATO for 12 h, (b) the SAED pattern of the marked region in (a), (c) magnification of (a), and (d) the HRTEM image of the marked region in (c).	147
Figure 5.2.4	(a) A cross-sectional TEM image of a FeOOH-ATO; (b) HRTEM image of the marked region in (a); (c) Schematic of the interface of the (101) _{SnO₂} plane of a ATO nanobelt and the (420) _{FeOOH} plane of FeOOH nanorods, revealing the lower interfacial lattice mismatch of inclined growth compared to that of perpendicular growth.	150
Figure 5.2.5	(a) A cross-sectional TEM image of a Fe ₂ O ₃ -ATO; (b) HRTEM image of the marked region in (a); (c) Schematic of the interface of the (020) _{SnO₂} plane of a ATO nanobelt and the (121) _{Fe₂O₃} plane of Fe ₂ O ₃ nanorods, revealing the lower interfacial lattice mismatch of inclined growth compared to that of perpendicular growth.	151
Figure 5.3.1	(a) A typical SEM image of VO ₂ -ATO arrays, in which VO ₂ nanobranches were synthesized for 3 h by hydrothermal method, and (b) a magnification image of (a).....	155

Figure 5.3.2	TEM analysis of a VO ₂ -ATO heterostructure: (a) a low-mag TEM image, (b) a magnification image of (a), (c) a SAED pattern observed from region 1 of (a) and (d) a SAED pattern observed from region 2. SAED analysis indicates that VO ₂ nanorods grew epitaxially on ATO nanobelt and their growth direction was [002].	156
Figure 5.3.3	EDS elemental mapping of a VO ₂ -ATO heterostructure.	157
Figure 5.3.4	The illustrations of atomic arrangements at the interface between (a) SnO ₂ and VO ₂ (R) and (b) SnO ₂ and VO ₂ (M), which are projected along [010] direction of SnO ₂ .	158
Figure 5.3.5	SEM images of the VO ₂ -ATO heterostructure at various reaction stages by setting the reaction time: (a) 2 h, (b) 2.5 h, (c) 3 h, (d) 6 h and (e) 12 h.	159
Figure 5.3.6	XRD graphs of VO ₂ -ATO heterostructure at various reaction stages by setting the reaction time.	159
Figure 5.3.7	(a) XRD graphs and (b-c) SEM images of VO ₂ (B) particles precipitated by hydrothermal method without insertion of ATO nanobelt substrate.	160
Figure 5.3.8	(a) A TEM image of cross-section of a VO ₂ -ATO fabricated by focused ion beam method. (b) HRTEM images obtained from marked regions in (a), (c) SAED pattern of (a) and (d) the fast-Fourier transformation (FFT) patterns of the backbone and branch of (b-3).	165
Figure 5.3.9	EDS elemental mapping of cross-section of a VO ₂ -ATO showing V, Sn, O and Au atomic profiles.	166
Figure 5.3.10	Schematic description of lattice deformation from (a) tetragonal rutile VO ₂ (R) to (b) monoclinic VO ₂ (M) with a small distortion along the tetragonal c-axis ($\beta=122.6^\circ$).	167
Figure 5.3.11	The descriptions of atomic arrangements at the interface	

between (a) SnO₂ and VO₂ (R) and (b) SnO₂ and VO₂ (M), which are projected along $[\bar{1}01]$ direction of SnO₂. The b-axis length of VO₂ bulk (4.554 Å) is shorter than that of SnO₂ (4.738 Å) with the lattice mismatch of 4%, resulting in a tensile strain along the b axis for VO₂ nanorods..... 168

Figure 5.3.12 XRD graphs measured at a scan rate of 0.3 degrees per min (2θ) for VO₂-ATO heterostructure samples in which VO₂ nanobranches were synthesized for 3 h, 6 h and 12 h by hydrothermal method. Each 2θ region is related to (a) rutile (101), (b) rutile (020) and (111), and (c) rutile (121). Bold lines indicate XRD pattern measured from VO₂-ATO heterostructure. Sharp pink and green lines are simulated XRD patterns from crystallographic information file (CIF) of VO₂ (M) and SnO₂, respectively. 174

Figure 5.3.13 Temperature dependence of XRD data of VO₂-ATO arrays synthesized for 12 h, indicating the phase transition of VO₂ from monoclinic rutile (M) to tetragonal rutile (R) at about 55 ~ 60 °C... .. 175

Figure 5.3.14 Temperature dependence of Raman spectra of individual VO₂-ATO heterostructure synthesized for 12 h, presenting the phase transition from insulating VO₂ (M) to metallic VO₂ (R) at about 55 ~ 60 °C during the temperature cycling.. 176

Figure 6.1.1 J-V curves of (a) anatase sphere TiO₂-ATO and (b) rutile rod TiO₂-ATO with ATO length of 10 μm and TiO₂ thickness of 130 nm. 179

Figure 6.1.2 Amperometric *J*-*t* curves of (a) anatase sphere TiO₂-ATO and (b) rutile rod TiO₂-ATO at an applied potential of 1.0 V vs. RHE. 180

Figure 6.1.3 Photoconversion efficiency of (a) anatase sphere TiO₂-ATO and

	(b) rutile rod TiO ₂ -ATO calculated from <i>J-V</i> data.....	180
Figure 6.1.4	Nyquist plots of (a) anatase sphere TiO ₂ -ATO and (b) rutile rod TiO ₂ -ATO.....	181
Figure 6.1.5	(a) Schematic description of the fabrication procedure : i) ATO nanobelt, ii) TiO ₂ -ATO nanostructure and iii) CdS sensitized TiO ₂ -ATO heterostructure; (b) TEM images at each fabrication procedure stage; (c) SAED and HRTEM images at each stage were also measured.....	192
Figure 6.1.6	(a-c) Cross-sectional SEM images and (d-f) TEM images of TiO ₂ -ATO heterostructures: (a, d) dot TiO ₂ -ATO, (b, e) rod TiO ₂ -ATO and (c, f) lamella TiO ₂ -ATO.....	193
Figure 6.1.7	EDS mapping of the CdS-sensitized TiO ₂ -ATO heterostructure with (a) dot, (b) rod and (c) lamella shaped TiO ₂ . The Ti/Cd ratio was obtained by means of a quantitative analysis of the marked region.....	194
Figure 6.1.8	Optical characterization of CdS sensitized TiO ₂ -ATO heterostructures: (a) transmittance, (b) reflectance and (c) absorption plus scattering ($A + S = 100 - R - T$) properties.....	195
Figure 6.1.9	Chopped <i>J-V</i> curves under illumination by a solar simulation (AM 1.5G, 1SUN) (scan rate of 20 mV/s): (a) CdS sensitized dot, rod and lamella shaped TiO ₂ -ATO heterostructures and (b) bare dot, rod and lamella shaped TiO ₂ -ATO.....	196
Figure 6.1.10	Measurements of the incident photon-to-electron conversion efficiency (IPCE) under 1 V vs. RHE for CdS sensitized dot, rod and lamella shaped TiO ₂ -ATO heterostructures.....	197
Figure 6.1.11	Nyquist plots for CdS sensitized dot, rod and lamella shaped TiO ₂ -ATO heterostructures measured at 0 V vs. RHE (1 V vs. Ag/AgCl) under illumination. The inset of d shows an analogous equivalent circuit for the PEC device.....	197

Figure 6.1.12	(a) Open circuit voltage decay spectra of the CdS sensitized TiO ₂ -ATO heterostructure with dot, rod and lamella shaped TiO ₂ and (b) electron lifetime as a function of open circuit voltage (V_{oc}) derived from the V_{oc} decay rates.....	198
Figure 6.1.13	Diagram of relative energy levels of QD, TiO ₂ and ATO at pH 0 and possible charge carrier pathway	199
Figure 6.1.14	(a) TEM images of CdS sensitized-rod TiO ₂ -ATO fabricated by SILAR method (Inset shows magnification of a) and (b) Chopped J - V curves under Solar simulator illumination. (scan rate of 20 mV/s).....	200
Figure 6.1.15	Time course of H ₂ evolution for photoelectrochemical device equipped with CdS sensitized rod TiO ₂ -ATO electrode as working electrode. The applied potential was fixed to 0.6 V vs. RHE. The gas phase was evacuated at every 1 h after startup..	200
Figure 6.1.16	EDS elemental Mapping of a Fe ₂ O ₃ -ATO at 12 h (a) before and (b) after post annealing at 650 °C during the 24 h. Scale bar : 200 nm	212
Figure 6.1.17	(a) A dark field STEM image of Fe ₂ O ₃ -ATO for 12 h, (b) the EDS line-scan across the Fe ₂ O ₃ branch revealing the concentration and distribution of Fe, Sn, and O, and (c) magnified EDS line-scan indicating the Sn distribution in the Fe ₂ O ₃ nanorod.....	213
Figure 6.1.18	(a) Mott-Schottky analysis of Fe ₂ O ₃ -FTO at 4 h (a) before and (b) after post annealing at 650 °C and Fe ₂ O ₃ -ATO for 4 h (c) before and (d) after post annealing at 650 °C under frequency of 500 Hz.....	214
Figure 6.1.19	Optical characterization of a Fe ₂ O ₃ -FTO and Fe ₂ O ₃ -ATO at 4 h after post annealing at 650 °C during the 24 h : (a) Transmittance (T), (b) reflectance (R) and (c) absorbance plus scattering (A + S	

	= 100 – R – T) properties. A vertical line presents the 620 nm wavelength conforming to the bandgap of α -Fe ₂ O ₃	215
Figure 6.1.20	(a) J-V curves collected for Fe ₂ O ₃ –ATO photoanodes prepared for a different reaction time before and after post annealing (650 °C and 24 h), with a scan rate of 10 mV/s, 1 M NaOH electrolyte (pH 13.6) and AM 1.5G simulated solar light at 72 mW/cm ² . (b) J-V curves of α -Fe ₂ O ₃ nanorods on the FTO substrate at different times before and after post annealing (650 °C and 24 h) under same conditions.	216
Figure 6.1.21	(a) J-V curves collected for Fe ₂ O ₃ –ATO photoanodes prepared at 100 °C for 4 h, with a scan rate of 10 mV/s, 1 M NaOH electrolyte (pH 13.6) and AM 1.5G simulated solar light at 72 mW/cm ² . Each sample was post-annealed at 650 °C for different reaction time (6 h, 12 h and 24 h). (b) J-V curves of Fe ₂ O ₃ –ATO photoanodes prepared at 100 °C for 4 h. Each sample was post-annealed for 24 h at different temperature (550 °C, 600 °C, 650 °C and 700 °C)..	217
Figure 6.1.22	Nyquist plots of a Fe ₂ O ₃ –FTO at 4 h (a) before and (b) after post annealing at 650 °C and a Fe ₂ O ₃ –ATO at 4 h (c) before and (d) after post annealing at 650 °C under 1.23 V/RHE..	218
Figure 6.2.1	Cyclic voltammograms of the (a) pure ATO nanobelt and (b) TiO ₂ –ATO nanostructured electrodes at scanning rate of 0.3 mV s ⁻¹ in the first ten cycles..	225
Figure 6.2.2	Charging-discharging curves of the (a) pure ATO nanobelt and (b) TiO ₂ –ATO nanostructured electrodes at a rate of C/5..	226
Figure 6.2.3	Variation of the discharge-charge specific capacity versus the cycle number at a rate of C/5 for the pure ATO nanobelt and TiO ₂ –ATO nanostructured electrodes. Inset shows cycling performance of the TiO ₂ –ATO nanostructured electrode	

	measured by considering area of the electrode at a current density of 135 mA cm ⁻²	227
Figure 6.2.4	Specific capacity versus cycle number of the TiO ₂ -ATO nanostructured electrode cycled ten times at every C-rate (0.1 C, 0.2 C, 0.5 C, 1 C, and 3 C) and its corresponding Coulombic efficiency.....	228
Figure 6.2.5	Specific capacity versus cycle number of ATO nanobelts and TiO ₂ -ATO electrodes cycled ten times at every C-rate (0.1 C, 0.2 C, 0.5 C, 1 C, and 3 C).....	228
Figure 6.2.6	Charging-discharging curves of the TiO ₂ -ATO at various C-rate (0.1 C, 0.2 C, 0.5 C, 1 C, and 2 C).....	231
Figure 6.2.7	Charging-discharging curves of the ATO nanobelts electrode over 1.0 – 2.5 V.....	231
Figure 6.2.8	Specific capacity versus cycle number of the TiO ₂ -ATO electrode cycled ten times at every C-rate (0.1 C, 0.2 C, 0.5 C, 1 C, and 2 C).....	232
Figure 6.2.9	Specific capacity versus cycle number of the TiO ₂ -ATO electrode cycled ten times at every C-rate (0.1 C, 0.2 C, 0.5 C, 1 C, 2 C, 3 C, 6 C, and 10 C) over 1.0–2.5 V.....	232
Figure 6.2.10	The discharge-charge specific capacity versus the cycle number for VO ₂ -ATO heterostructure and VO ₂ (M) bulk powder, which was operated at a rate of 100 mA g ⁻¹ over a voltage window between 3.5 and 1.5 V. VO ₂ -ATO heterostructure prepared for 3 h was used as cathode.	238
Figure 6.2.11	Specific capacity versus the cycle number for VO ₂ -ATO cathode cycled 10 times at different current density (50, 100, 200, 500, 1000 and 2000 mA g ⁻¹) over a voltage window between 3.5 and 1.5 V.	239
Figure 6.2.12	Cyclic voltammograms of electrodes for (a) VO ₂ -ATO and (b)	

	VO ₂ (M) bulk powder at a scanning rate of 0.3 mV s ⁻¹ in the first 6 cycles.	240
Figure 6.2.13	(a) Typical TEM image of the discharged VO ₂ -ATO heterostructured electrodes after 55 cycles. (b) Magnified HRTEM image of a VO ₂ -ATO at the discharged state (extraction of Li ⁺) after 55 cycles.	241
Figure 6.2.14	Charging-discharging curves of electrodes for (a) VO ₂ -ATO and (b) VO ₂ (M) bulk powder at a rate of 100 mA g ⁻¹ . (c) Illustration of Li ion diffusion and electron transport in VO ₂ -ATO heterostructures based on rutile crystal structure. Crystallography of rutile type VO ₂ projected along c-axis was also presented, in which the tunnel can function as pathway for the diffusion of Li ⁺ ions during Li insertion/extraction.	242

Chapter 1. Introduction

1.1 Energy conversion and storage devices for sustainable development

The development of economic and environment-friendly energy resources is essential and urgent for sustainable growth. The world currently uses energy at a rate of 4.1×10^{20} J per year (13 terawatts). Due to population increases, fast technology development, and rapid global economic growth, the energy demand will double to 30 TW by 2040 and triple to 46 TW by the end of the century [1]. Unfortunately, 80% of the energy now depends on fossil fuels, which leads to inevitable environment problems such as CO₂, as shown in Figure 1.1. Over the last 150 years, CO₂ concentrations in the atmosphere have already risen from 280 to 380 ppm, leading to serious global warming and climate change [2]. Thus, one of society's major challenges for the future is in finding sufficient clean energy supplies.

Over the past few decades, hydrogen has received a great deal of attention as an ideal and clean fuel. Hydrogen is the most-abundant gas and the simplest element in the universe. It can easily be used for fuel cell electricity generation without any CO₂ emission. The amount of energy produced from

hydrogen gas is 122 kJ g^{-1} , which is 2.75 times higher than that from hydrocarbon fuels, and 5 times greater than that from methanol and ethanol [3]. Therefore, hydrogen is an alternative fossil fuel as a promising energy carrier for the future. Hydrogen fuel can be generated from renewable and clean energy sources like solar energy, indicating that its life cycle can be the same [4]. Hydrogen can be produced from solar energy by various processes: thermolysis by solar heat, electrolysis by wind or solar cell electricity, thermochemical & biological conversion by biomass, and photolysis by solar-light [5]. If part (1.5%) of the Pacific Ocean sunlight can be used with 5 % efficient solar water splitting and 50 % fuel cell conversion, 30 TW of energy can be produced and stored [6]. Hence, hydrogen energy system development by renewable solar energy conversion is an important challenge that has been of great interest to both scientists and engineers. Figure 1.2 is a simple schematic of the hydrogen energy cycle using a hydrogen fuel cell vehicle divided into four categories: (i) photon to hydrogen conversion, (ii) hydrogen storage, (iii) hydrogen to electricity conversion, and (iv) electricity storage and usage. Most of the steps (first, third and fourth) are electrochemical reactions, so efficient and stable electrochemical conversion and storage devices are required for an effective hydrogen energy cycle. The photoelectrochemical (PEC) cell and Li-ion battery have been accepted as

representative electrochemical conversion and storage devices, respectively. They have been widely studied since the 1970s, but the PEC cell and Li-ion battery still face significant technical hurdles regarding the low efficiency and long-term stability, respectively, in the hydrogen energy industry. Therefore, a novel and effective approach to the electrochemical conversion and storage device is needed for sustainable development.

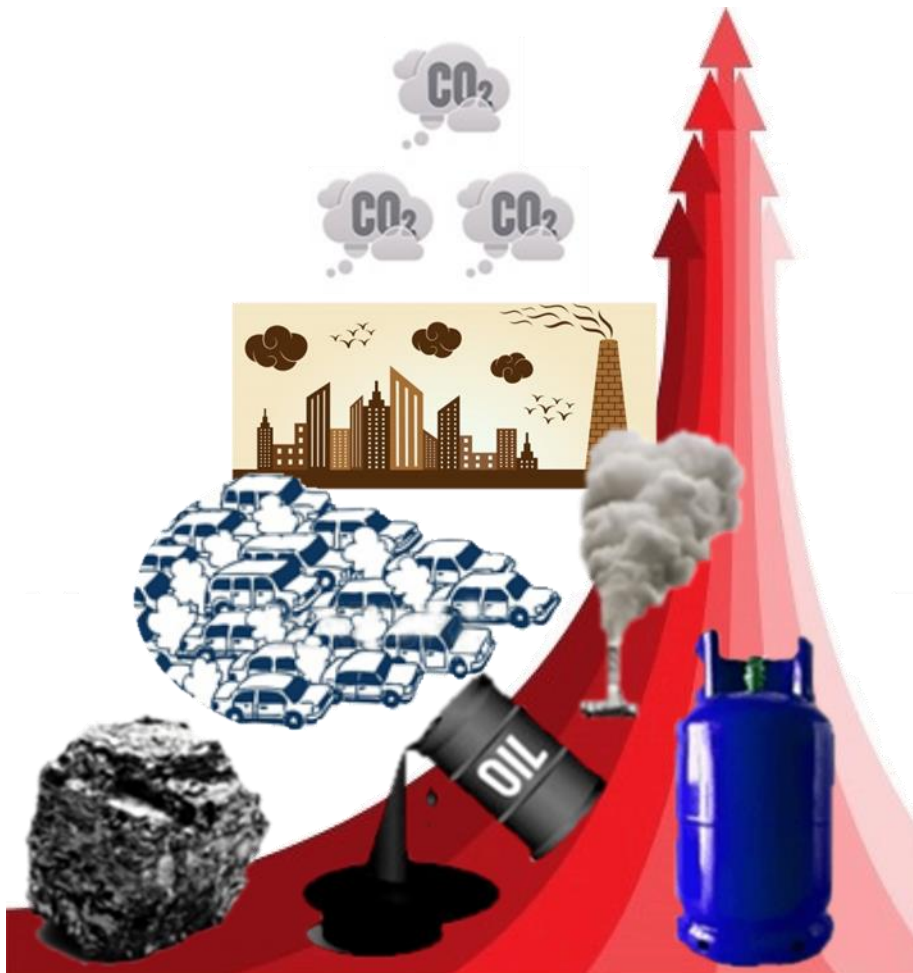


Figure 1.1. Environmental and energy problem induced by use of fossil fuels.

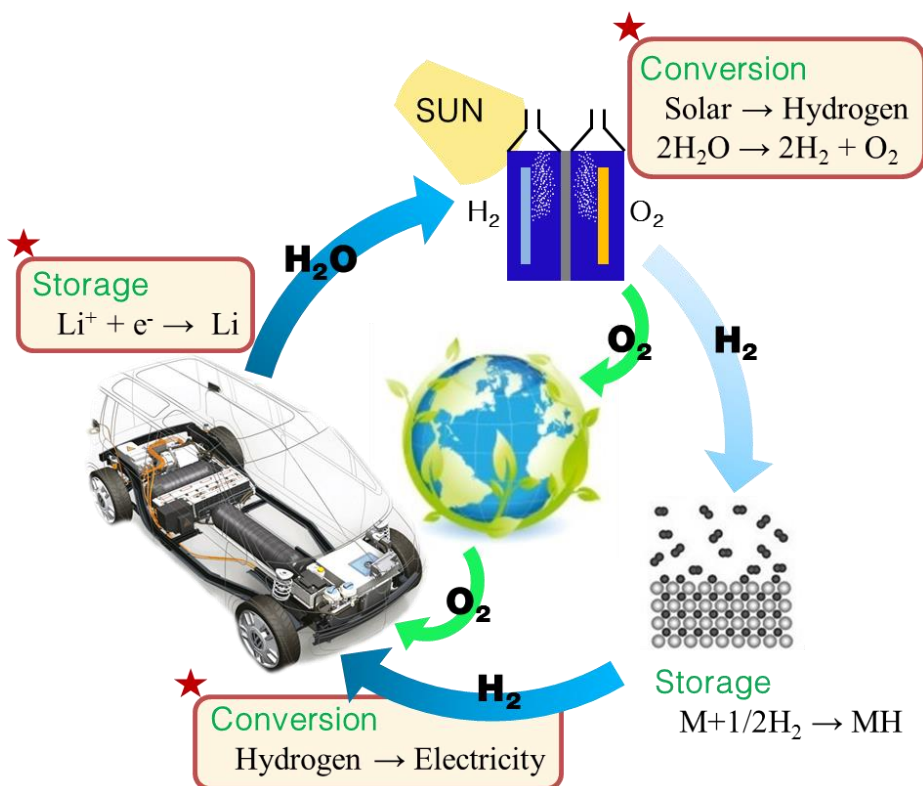


Figure 1.2. Schematic representation for hydrogen energy cycle based on hydrogen fuel cell vehicle.

1.2 Nanoarchitecturing for electrochemical devices

1.2.1 Nanoarchitecturing for efficient electrodes

Charge transfer and transport in electrochemical devices are critical for determining energy conversion and storage efficiency. Typically, the principle of PEC water splitting is based on solar energy conversion into electricity within a cell containing two electrodes immersed in an aqueous electrolyte. At least one of the two electrodes is made of a semiconductor to absorb light. For a PEC cell with photoanode (Figure 1.3), solar light induces n-type semiconductor ionization over the band gap that generates electron-hole pairs. The photo-generated holes result in water molecule oxidation into oxygen gas and hydrogen ions. Because this reaction occurs at the photoanode/electrolyte interface, the charge transfer property at the anode interface is important for conversion efficiency. Simultaneously, photo-generated electrons are transported over the external circuit to the counter electrode (typically Pt) to reduce hydrogen ions into hydrogen gas. Thus, charge transport property from anode surface to cathode is also important, so numerous researchers have made efforts to improve the photon to hydrogen conversion in terms of charge transfer and transport [7-12]. This trend is also confirmed in a Li-ion battery (Figure 1.4) where the negative electrode (anode) is typically composed of

graphitic carbon with theoretical capacities of 372 mAh g^{-1} . The positive electrode (cathode) is typically made of a layered oxide (e.g. LiCoO_2) with theoretical capacities of 274 mAh g^{-1} . During battery cycling (charge/discharge reaction), lithium ions move back and forth through the electrolyte between the anode and cathode. This is accompanied by electron transfer and transport through the electrode/electrolyte interface and circuits, respectively. Many efforts have been made to improve the electrochemical performance of Li-ion batteries by controlling charge transfer and transport [13-17]. Recently, nanomaterials and novel designs based on nano-architecturing have demonstrated very promising energy conversion and storage results by enhancing the charge transfer and transport property in electrodes [18-21]. The oriented and controlled nanostructured electrodes are strongly expected to promote charge generation, transfer, and transport in PEC cells and Li-ion batteries to overcome their low efficiency and stability.

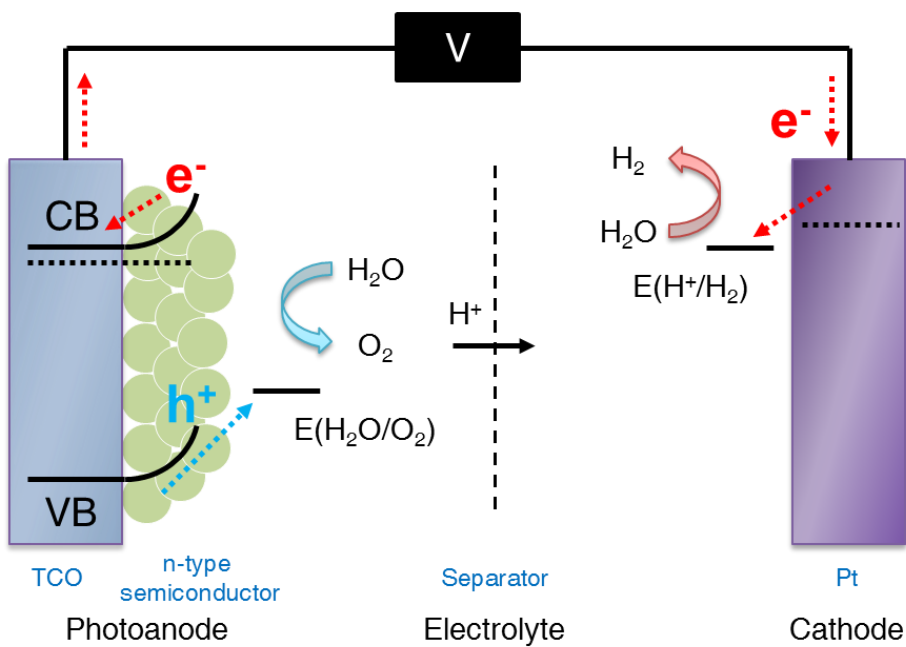


Figure 1.3. Structure of a typical PEC cell with photoanode (n-type semiconducting materials), cathode (Pt), an aqueous electrolyte and a separator.

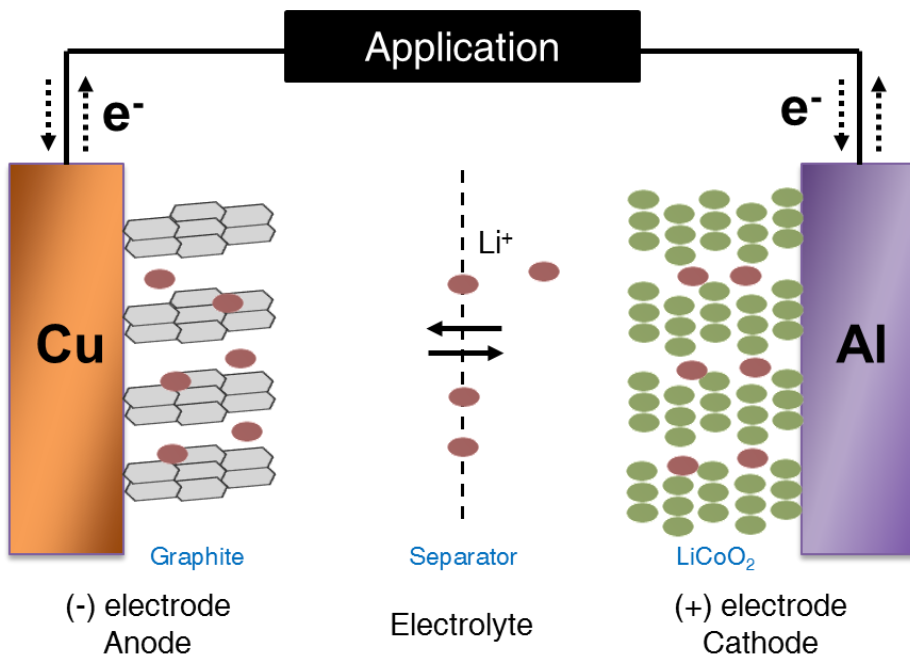


Figure 1.4. Scheme of a typical Li-ion battery with negative electrode (graphite on copper current collector), positive electrode (LiCoO₂ on aluminum current collector), a nonaqueous liquid electrolyte (LiPF₆, EC:DMC) and a separator.

1.2.2 Metal oxide-based 3-D nanostructures

Along with the rapid nanotechnology development, a variety of nanomaterials and nanostructures have proved promising in diverse electronic and optoelectronic applications due to their unique size and physicochemical properties [22]. Recently, there has been growing interest in the development of three-dimensional (3D) nanostructures in an effort to utilize the remarkable properties of one-dimensional (1D) objects in a 3D space. For instance, 3D integrated circuits fabricated by sequential metal-oxide nanowire-contact printing steps represent the important advantages of the integration density, power consumption, and operation speed compared to their two-dimensional counterpart circuits [23-25]. In recent energy technologies involving photovoltaic devices and Li-ion batteries, better light absorption and charge collection properties have been reported through the use of 3D architecture [26-30]. Therefore, 3D nanoarchitecturing is a worthwhile and fascinating approach to enhance the nanoscale devices performance. Among the 3D nanostructures, branched 1D structures have been widely studied because these structures can be easily fabricated by modification of previously developed 1D structures. They apply to a wide range of compounds such as $\text{SnO}_2\text{-Fe}_2\text{O}_3$, In-ZnS , $\text{TiO}_2\text{-ZnO}$, $\text{TiO}_2\text{-NiO}$, and $\text{SnO}_2\text{-TiO}_2$ [31-42].

In particular, extensive studies have been performed to increase solar water

splitting performance in PEC cells [12,34,40,43-45]. Solar-to-hydrogen (STH) efficiency can be divided into four steps: absorption, exciton diffusion, charge transport, and charge collection/reaction [12]. Modifying charge transport and collection properties with three-dimensional (3D) nanoarchitecturing have shown the potential for enhancing STH efficiency [34,40,43-45]. 3D nanowire networks are expected to effectively translate the remarkable properties of one-dimensional (1D) objects into a 3D space [33]. For instance, 3D integrated circuits fabricated by sequential steps of metal oxide nanowire contact printing are advantageous in integration density, power consumption, and operating speed when compared to two-dimensional (2D) circuits [23-25]. Photoconversion devices equipped with 3D architecture have led to better light absorption and charge collection properties [29,30,34,44,45].

In the past decade, nanomaterials have been extensively studied to satisfy the next generation device condition of Li ion battery electrodes for high energy density at high rate capabilities [46-48]. Their small sizes provide high reactive surface-to-volume ratio. The short path lengths of Li ion and buffer space release the stress related to volume change during the charge/discharge process, all of which benefit the Li ion battery [46-48]. However, single-phased nanomaterials limit the demands of future device conditions since their intrinsic characteristics (e.g. slow kinetics, low conductivities, and weak

mechanical stabilities) and extrinsic characteristics (e.g. side reaction increase with electrolyte and agglomeration due to high surface energy and surface area) lead to a poor cycle life [49]. In order to overcome the limitations, heterogeneous nanostructures have been introduced to show the synergic performance by combining the merits of each component [46-49]. In this respect, 3-dimensional (3-D) branched nanostructures are promising for PEC cell and Li ion battery.

1.2.3 1-D conductive backbone

Various 3D nanostructure fabrication methods have been reported, such as growing branches on a nanowire backbone by depositing seed particles [33,39], using thermal evaporation to synthesize a hyper-branch structure [32,38], forming a nanowire network using a templated electrodeposition technique [50], and integrating heterogeneous nanowires using a shear printing process [23-25]. These approaches indicate that most researchers have focused on 3D nanostructure fabrication using 1-D backbones. Although the 1-D transparent conductive oxide (TCO) nanowire is also promising for electronic and photonic applications [51-55], less attention has been paid to developing 1D TCO nanowire-based 3D nanostructures. The reasons are: 1) 1D TCO nanowire deposited on Si or oriented substrates (e.g. sapphire and

yttrium-stabilized zirconia (YSZ)) that problematically block the light and are impractical for photonic application [51-53]; and 2) vertically aligned 1D TCO nanowires, which transmit light better, have only been studied under oriented substrates [51,52]. As a preliminary, the ITO(Sn:In₂O₃)/TiO₂ core/shell structure was fabricated and revealed that 1-D ITO could enhance the charge collection property in electrodes. This implies that 1-D TCO is effective as a backbone in the photo-conversion devices [27,56]. However, ITO has very low stability in acidic condition, which is not suitable for branching synthesis in the wet-chemical route. An alternative TCO material is required for 3-D nanoarchitecturing based on 1-D TCO. The first aim of this thesis is to propose a method to fabricate the hybrid 3-D nanostructures using a combination of 1-D TCO backbone and nanobranches. In this study, the Sb-doped SnO₂ (ATO) nanobelt was selected as the 3-D architecture backbone since SnO₂-based TCO materials are cheap [53] and chemically stable [57], which allow them to withstand various chemical conditions during reaction.

1.2.4 3-D heteroepitaxial branch

The syntheses and characterizations of heterostructures such as core-shell, coaxial nanowire/nanocable, and one- and two-dimensional (1D and 2D) heterojunction structures have attracted great attention due to the improved

properties and/or synergistic effects [28,58-61]. Among these structures, 1D nanostructure-branched heteronanostructures based on epitaxial growth can enhance electronic device performance through facial electron transport from defect-free interface between different materials. In the past few years, the various 1D nanostructure-branched heteronanostructures such as SnO₂-Fe₂O₃, In-ZnS, TiO₂-ZnO, TiO₂-NiO, and SnO₂-TiO₂ have been investigated for wider applications [31,35,37,42]. However, reliable and systematic investigations on the epitaxial growth of such heteronanostructures have been limited to few materials due to difficulty of synthesis and analysis for heteronanostructures [31,62,63]. For example, although several reports have been published on SnO₂-TiO₂ heteronanostructures acting as anodes for Li ion battery [64-67], the reversible capacities of the heteronanostructured electrodes exhibited very low values ($< 200 \mu\text{A h cm}^{-2}$) in most situations since TiO₂ was more dominant in the electrode capacity contribution. Therefore, new metal oxide nanoarchitecturing that improve electrochemical performance are required. On the basis of the foregoing, it is expected that the electrochemical performance of heteronanostructures composed of different metal oxides can be enhanced by epitaxial growth between materials. This thesis mainly focuses on the synthesis and control of heteroepitaxially branched metal oxides on the 1-D TCO backbone to improve charge transfer

and transport in the nanoarchitected electrodes of electrochemical devices, especially PEC cells and Li-ion batteries.

1.3 Aim and approach

3-D nanoarchitected electrodes can enhance efficiency and improve long-term stability in electrochemical conversion and storage devices in PEC cells and Li-ion batteries. In particular, charge transfer and transport abilities through nanostructured electrodes are important for efficient and stable PEC cells and Li-ion batteries. The aim of this thesis is to develop and design 3-D heteroepitaxially branched electrodes with high efficient charge transfer and transport properties. Furthermore, the goal is to provide background on the epitaxial growth mechanism of nanobranches on the 1-D backbone in order to control and optimize the shape and morphology for high efficiency and long-term stability.

This thesis suggests two strategies for efficient charge transfer and transport in PEC cells and Li-ion batteries. The first is fabricating 1-D TCO backbones with high conductivity and good thermal and chemical stability. Typically, planar metallic substrates (including TCOs) have been used for charge collection and transport, but their role is restricted to the charge transport to the external circuit. In this study, this role is expanded (i.e., charge extraction

and transport of 1-D TCO backbone or participation in an electrochemical reaction as the 1-D conductive metal oxide). The second is a heteroepitaxial growth of 3-D branched metal oxides on the 1-D backbone. Epitaxial growth leads to a defect-free interface between different materials, which enhance the electrochemical device performance. Moreover, metal oxide branches can be self-assembled during growth by an epitaxial relationship between branch and backbone that lead to optimized structure. In order to achieve these two strategies, rutile materials were selected as branch and backbone compounds since they are the most stable transition metal oxides.

In chapter 2, heteroepitaxy and 3-D branching methods are reviewed in order to design and develop heteroepitaxially branched nanoarchitectures for efficient electrodes of PEC cells and Li-ion batteries. In addition, rutile materials in the PEC cells and Li-ion batteries are reviewed in terms of high efficiency and long-term stability.

Chapter 3 describes the synthetic procedures for 3-D nanoarchitecturing, PEC cell and Li-ion battery electrode fabrication, and characteristics analysis methods.

In chapter 4, vertical Sb:SnO₂ (ATO) nanobelt array with high conductivity on arbitrary substrates (FTO glass substrate and Ti foil) is fabricated by the vapor transport method. The vertical growth behavior and conductivity by

doping in defect-free single crystalline ATO nanobelts are also discussed.

Chapter 5 expands upon various metal oxides – TiO_2 , Fe_2O_3 and VO_2 – as they grow on ATO nanobelts by wet-chemical routes in an epitaxial relationship between branch and backbone. TiO_2 and Fe_2O_3 nanobranches are synthesized on ATO nanobelts with dendritic growth behavior due to lattice mismatch minimization. A TiO_2 branching mechanism is described in detail as a representative structure. Interestingly, VO_2 nanobranches are synthesized on ATO nanobelts with linear growth behavior, which is interpreted as an epitaxial strain effect. The detailed strain behavior of the preferred-oriented VO_2 nanobranches is described by crystal structure and metal-insulator transition (MIT) temperature.

In chapter 6, electrochemical performances of heteroepitaxial 3-D nanostructures (TiO_2 -ATO, Fe_2O_3 -ATO and VO_2 -ATO) for PEC cells and Li-ion batteries are evaluated. ATO core- TiO_2 branch 3-D structures applied-PEC cells show high charge transfer properties compared to ATO core- TiO_2 shell 1-D structures applied-PEC cells. To absorb visible light, quantum dot sensitized TiO_2 -ATO are fabricated and the PEC cells are characterized in terms of light harvesting as well as charge transfer and transport. In order to improve charge transfer property, a Sn self-doped 3-D Fe_2O_3 -ATO is proposed by using a SnO_2 nanobelt array as a dopant source. TiO_2 -ATO is

also fabricated as a Li-ion battery anode and the cycle performance is examined for long-term stability. Finally, VO₂-ATO as a Li-ion battery cathode exhibits high capacity and cycle stability compared to conventional VO₂ nanoparticle applied-cathodes, which is described in terms of charge & ion transport along the open-channel structure.

Chapter 2. Background and literature review

2.1 Heteroepitaxial growth

2.1.1 Heteroepitaxy

Definition

Epitaxy is defined as the growth of one crystal on the surface of another crystal, where there is a fixed orientation relationship between the lattices of two crystals [68]. In fact, as to all forms of crystal growth, epitaxy is a well-controlled phase transition leading to a single crystalline solid [69]. The term *epitaxy* has origins in Greek roots with *epi* meaning ‘on’ and *taxis* meaning ‘arrangement’ [70]. When a crystal is grown on another crystal of the same material, then the epitaxial growth process is usually referred to as homoepitaxy. On the other hand, when the two-phase system is heterochemical in composition, the epitaxial growth process is termed heteroepitaxy.

Principle

Heteroepitaxial is accomplished by nucleation and growth relationship between substrate and epilayer, which enable the epilayer to be grown in a structure-dependent manner on a substrate of given structure [71]. In general,

a chemically and structurally inhomogeneous interface is developed. A two-phase system exists at the end of epitaxial growth, which consists of two adjacent heterochemical parts (epilayer and substrate) [72]. When a system has zero or small misfit in which all atom positions are in exact register, the interface is referred as coherent [68]. As strain energy increases, coherence breaks down and the interface accommodates the lattice-mismatch with an array of dislocations, which is described as semi-coherent. When two crystals have different lattice fringes meet with no apparent coincidence at an interface, both crystals retain their bulk lattice and atomic arrangement becomes a linear function of position, which is termed incoherent. From the experimental data, Royer suggested the rule of epitaxy: epitaxial growth occurs only when the misfit, defined as $\delta = (l_e - l_s)/l_s$, where l_s and l_e are the in-plane lattice constants of the substrate and epilayer, respectively, is no greater than about 15% [70]. This geometrical approach has remained prominent to the current.

Epitaxial growth is based on several key processes. Figure 2.1 indicates the key processes related to heteroepitaxy as a schematic illustration of the epitaxial growth system [71]. First is the phase transition between the epilayer and the metastable phase, which is related to mass transport of the components from the metastable bulk to the growth front. Second is the

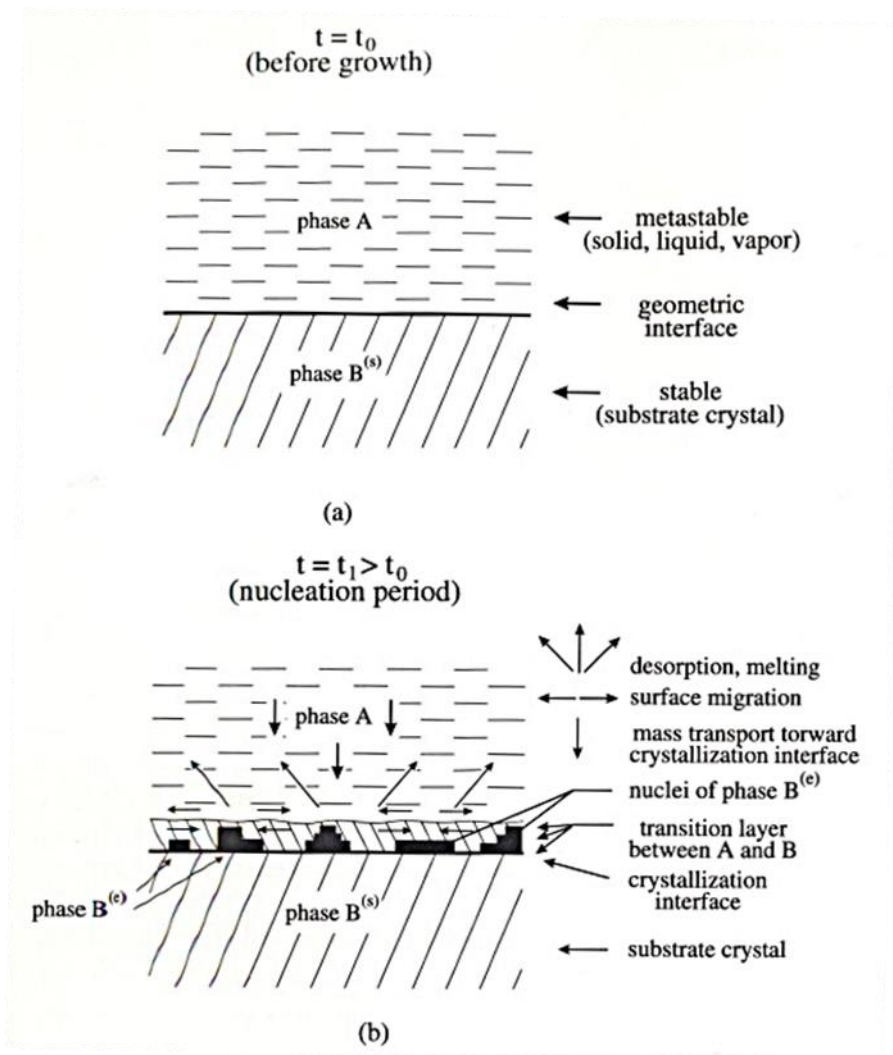


Figure 2.1. Scheme of the geometrical configuration for the epitaxial growth in different stages; (a) before growth, (b) in the nucleation stage related to the first monolayer growth, (c) at the early stage of growth, and (d) in the stage for regular epitaxial growth proceeds [71]. (Figure continued next page)

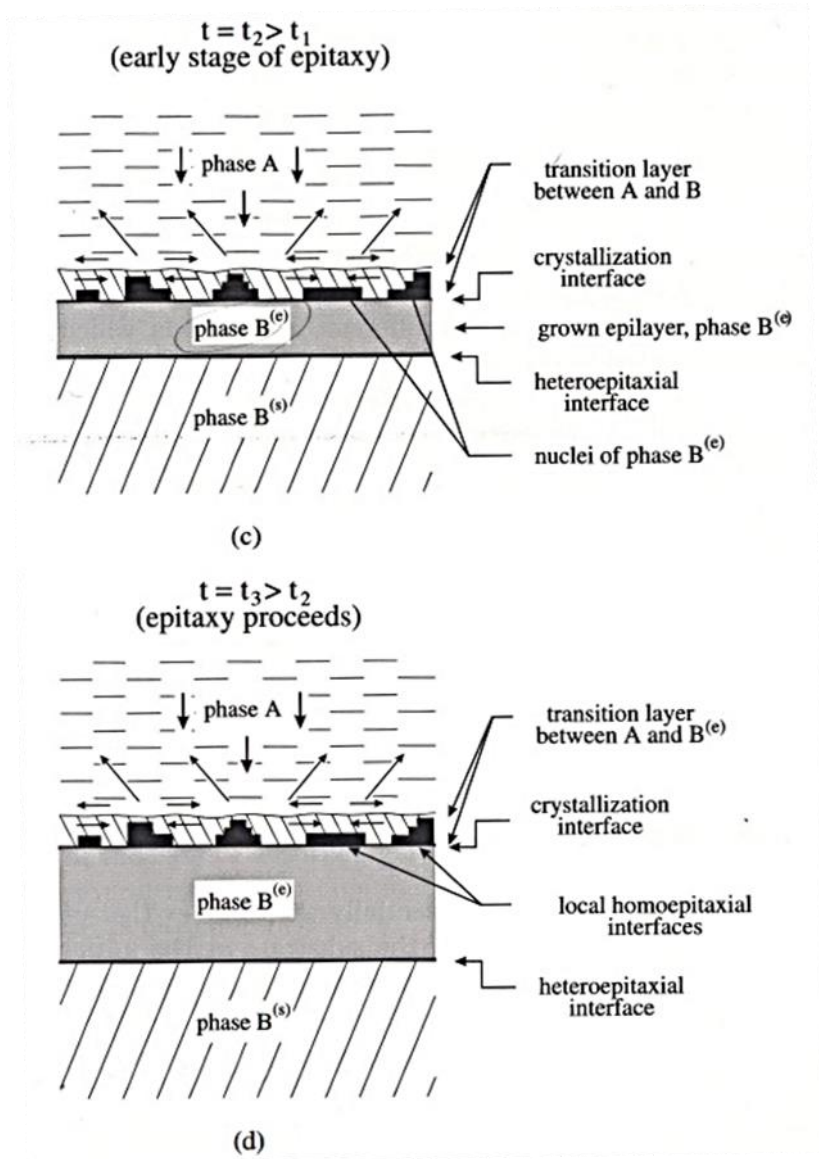


Figure 2.1. (continued)

driving force of crystallization which keeps the process running, such as the supersaturation of the metastable phase. Atomic ordering, a surface kinetic process dependent on the chemical and the structure activity of the substrate surface, is also an important factor in the growth process in epitaxy. It leads to formation of the first molecular monolayer of the growing epilayer.

Phenomena in heteroepitaxy

The important phenomena of heteroepitaxy are related to lattice mismatch. Misfit refers to the disregistry of the interfacial atomic arrays of the substrate and epilayer [73]. It is attributed to differences in d-spacing of lattice symmetries as shown in Figure 2.2 [71]. In the simple case, the misfit δ may be defined as

$$\delta = (l_e - l_s)/l_s$$

where the l_e and l_s are the lattice constants normal to the growth direction in the epilayer and substrate, respectively. When the misfit between a substrate and an epilayer is sufficiently small, the first monolayers will be strained to fit with the substrate [74]. However, as the thickness of epilayer increases, the strain energy increases, inducing the misfit dislocations to release the strain energy (Figure 2.3) [71]. Thus, overall strain decreases but the dislocation energy increases at the same time.

Strain plays a significant role in determining various physical properties of epilayer. For examples, it is well known that the energy of the electronic bands could be modulated by the strain [75]. Splittings of the valence band (or conduction band) depend on the strain direction and magnitude. The shifts of the heavy hole (hh), the light hole (lh), and the split-off (so) band for strain along the [001] direction are as follow [76].

$$E_{v,hh} = \frac{\Delta_0}{3} - \frac{1}{2}\delta E_{001}$$

$$E_{v,lh} = -\frac{\Delta_0}{6} + \frac{1}{4}\delta E_{001} + \frac{1}{2}\sqrt{\Delta_0^2 + \Delta_0 \times \delta E_{001} + \frac{9}{4}\delta E_{001}^2}$$

$$E_{v,so} = -\frac{\Delta_0}{6} + \frac{1}{4}\delta E_{001} - \frac{1}{2}\sqrt{\Delta_0^2 + \Delta_0 \times \delta E_{001} + \frac{9}{4}\delta E_{001}^2}$$

where E_v is the valence band energy and Δ_0 is the spin-orbit splitting. Also,

$$\delta E_{001} = 2b(\varepsilon_{zz} - \varepsilon_{xx})$$

with the b is the shear deformation potential for biaxial strain, and ε_{xx} and ε_{zz} are the in-plane strains. The effect of strain along the [001] direction is shown in Figure 2.4 [77]. In general, the bandgap energy increases by compressive strain.

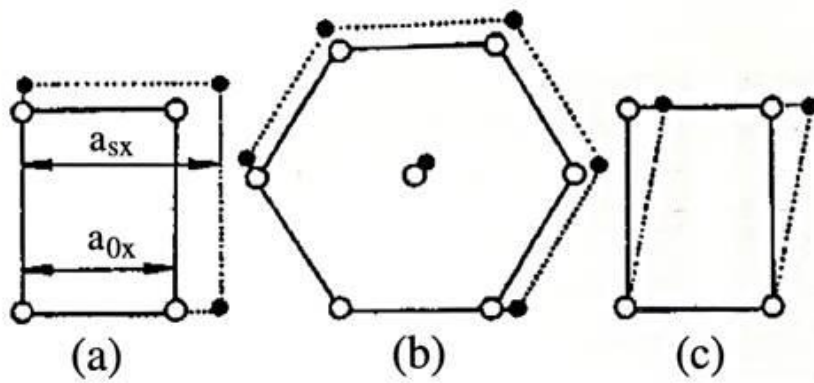
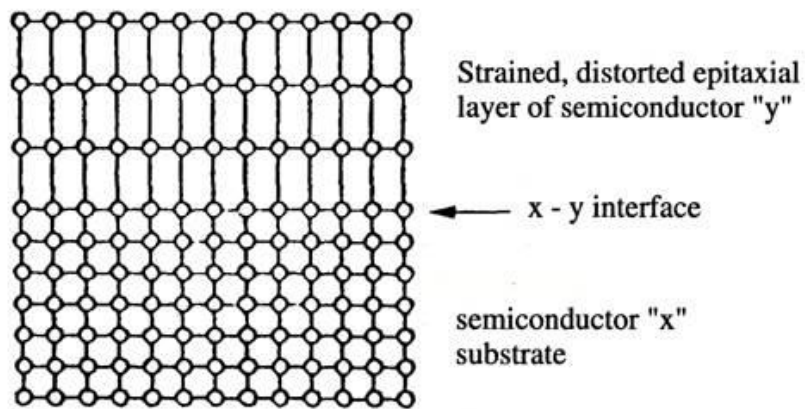
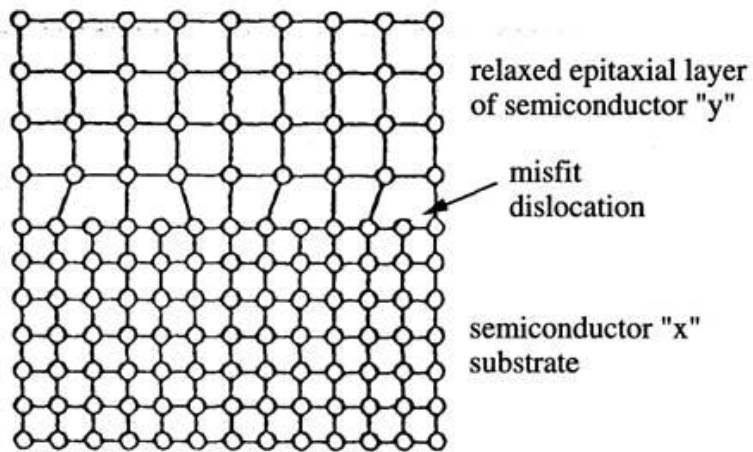


Figure 2.2. Schematic illustrations of interfacial atomic registry in the epilayer and substrate with different crystallographic symmetry [71]. Black dots: the substrate atoms, Empty circles: epilayer atoms



(a)



(b)

Figure 2.3. Schemes of (a) strained and (b) relaxed epitaxial layers [71].

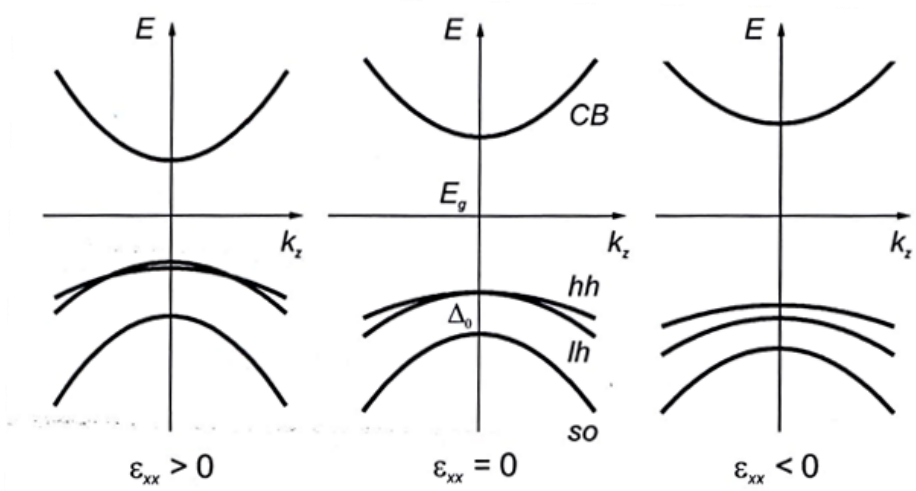


Figure 2.4. Effect of strain on the valence bands and the lowest conduction band [77].

2.1.2 Applications of heteroepitaxy

Heteroepitaxial growth can be widely used for crystallization of overlayer structures of different material systems. Above all, epitaxially grown layers show high perfection, satisfying the device-quality demands [71]. Therefore, they have been applied in various high technology parts, especially electronics, optoelectronics, and photonics [78].

Low-dimensional heterostructures

Size quantization in low-dimensional heteroepitaxial structures belongs to the most fascinating issues, such as quantum dots, quantum wells, and quantum wires [79]. They show distinctive physical properties originating from the modification of the electronic density-of-states (DOS) generated by the confinement of charge carriers. Figure 2.5 illustrates the low-dimensional heterostructures and their DOS of electrons as the quantization dimension increases [77]. The quantum well structures have been already well-studied from high electron mobility transistors to quantum well lasers and photodetectors [80]. Also, quantum wire and quantum dot structures have been reported for efficient optoelectronic devices [81].

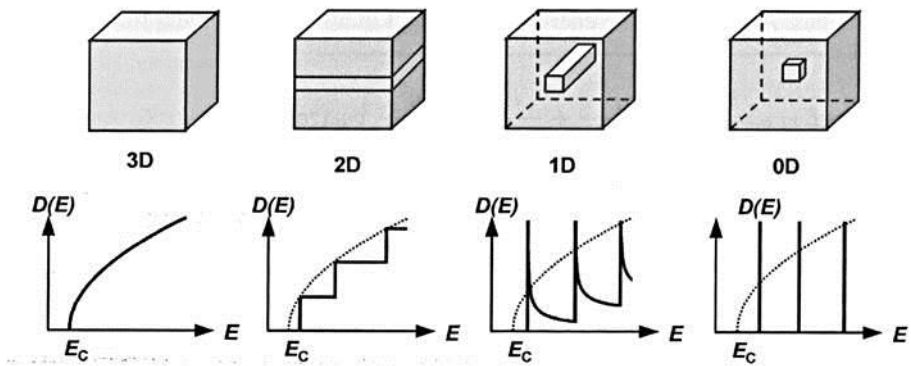


Figure 2.5. Electronic DOS in semiconductors with different dimensionalities: 3-D bulk, 2-D quantum well, 1-D quantum wire and 0-D quantum dot.

Epitaxial layers for device structures

Manufacturing single crystalline layered structures is an important issue for device applications. Up to this day, almost all kinds of optoelectronic and electronic devices have been developed in single crystalline layered form by epitaxial growth [82]. Performance of device is crucially dependent on the morphological and electrical quality of epilayer and interfaces [71]. For instance, heterojunction lasers, photodiodes or high electron mobility transistor require pure materials, smooth and defect-free interfaces. In early 1960s, GaAs devices of high complexity were developed by heteroepitaxially grown structures. In the half of the 1990s, as semiconductor based industry was booming, heteroepitaxial growth started to be used in all of semiconducting devices, such as semiconductor chips, light-emitting diodes, III-V compound lasers and III-V solar cells, for efficient and stable performance.

2.1.3 Heteroepitaxy for 3-D nanoarchitecturing

Recently, growth of heteroepitaxial structures including combinations of metals, semiconductors and insulators also have been demonstrated as an effective approach to 3-D device integration [68]. In this chapter, scientific backgrounds and engineering issues for introduction of heteroepitaxy to 3-D nanoarchitecturing were investigated.

Merits of heteroepitaxy for nanotechnology

The heteroepitaxial growth for nanotechnology has several advantages [83]:

- (1) The great variety of combinations is possible [84].
- (2) A better match of lattices ensures a lower stress and a greater stability at the interface, which are desirable for reliable and stable Ohmic and Schottky contacts [85].
- (3) A low density of defects would improve the conductivity of epilayer and charge transfer at interface [83]. Heteroepitaxy is known as the only way for formation of defect-free structures.
- (4) Grain boundary effects are greatly relieved, which makes it possible for nanostructures that have a single grain boundary in them. Also, the degradation of contacts induced by inter-diffusion can be reduced [83].
- (5) Self-organized formation of nanostructures could be induced during heteroepitaxial growth. The driving force for the self-organization is the misfit between the lattice of the epilayer and that of the substrate [86]. In semiconductor heteroepitaxy, the epilayer frequently undergoes a series of strain relief processes including surface reconstruction, faceting, and formation of misfit dislocations [87]. These mechanisms and their interplay could lead to self-organized nanostructure arrays with a high uniformity under certain conditions.

(6) Various physical properties, such as optical, electrical and magnetic characteristics, of epilayer can be modulated by epitaxial strain effect with change of lattice parameter and crystallographic symmetry. It was reported that dielectric and ferroelectric properties are changed by very thin strain layers [88]. The magnetic anisotropy of thinfilms is largely controlled by epitaxial strains [89]. Epitaxial thin films of VO₂ on TiO₂ substrate suppresses the metal-to-insulator transition and sustains the metallic phase at room-temperature [90].

Among advantages, (1) ~ (4) have been well known and studied for high performance of electronic and optoelectronics. Thus, this thesis focused on merits of (5) and (6), self-organization and epitaxial strain effect, in order to obtain a 3-D nanoarchitecture with a high degree of uniformity and superior performance.

Liquid phase epitaxy

Liquid phase epitaxy (LPE) is the deposition method by using a liquid phase [91]. In LPE, an epilayer usually grows from a supersaturated liquid solution onto a substrate. LPE has a many advantages as comparison with other growth techniques [71]:

(1) LPE allows for heteroepitaxy at relatively low temperature.

- (2) It enables growth of epilayers with an extraordinary high structural perfection.
- (3) It leads to crystallization of epilayers with lower densities of defects.
- (4) High growth rates can be applied.

Because LPE operates near thermodynamic equilibrium, atoms can efficiently migrate to the interface and find optimum positions. It means that mass transport and diffusion effects are more important than surface reaction and incorporation phenomena in LPE process. On the other hands, there are some shortcomings [77]:

- (1) The interface quality depends on lattice misfit very strongly.
- (2) Rough interfaces are obtained frequently due to back-dissolution.
- (3) Miscible materials at growth temperature are limited.

Generally, in LPE method, the substrate is immersed into the supersaturated solution due to growth from a solution on the substrate. An LPE procedure is consists of four steps as follow [71].

- (1) Fabrication of supersaturated solution
- (2) Introduction of the substrate to the solution
- (3) Control of the morphology, perfection and uniformity of the epilayer
- (4) Removal of the solution from the substrate.

Growth modes

Epitaxy is sometimes considered as a post-nucleation phenomenon in which the rearrangement of stable clusters occurs by migration and rotation [92]. Thus, whether crystal growth is 2-D or 3-D is one of important factors for heteroepitaxial nanoarchitecturing. Three possible modes of epitaxial growth may be distinguished in heteroepitaxial systems; 2-D layer-by-layer growth identified by Frank and van der Merwe (FM) [93], 3-D island growth revealed by Volmer and Weber (VW) [94], and a combination of FM and VW mechanisms described by Stranski and Krastanow (SK) in which layer-by-layer growth initially occurs followed by islanding [95]. Three growth modes are illustrated schematically in Figure 2.6 [68]. The equilibrium growth mode is determined by the balance between the relative free energies of the substrate surface (γ_s), the epilayer surface (γ_e) and the interface (γ_i) [96]. According to Young's relation for the absolute tension values in balance,

$$\gamma_s = \gamma_e + \gamma_i \cos\theta$$

For $0 < \theta < \pi$, island growth is driven by a low substrate surface energy and a high interface energy. In other words, it is more favorable for atoms to stick together than wet the substrate. Thus, non-wetting results in 3-D drops. For $\theta = 0$, layer-by-layer growth is driven due to the droplet wetting the surface. The deposited atoms are more attached to the substrate rather

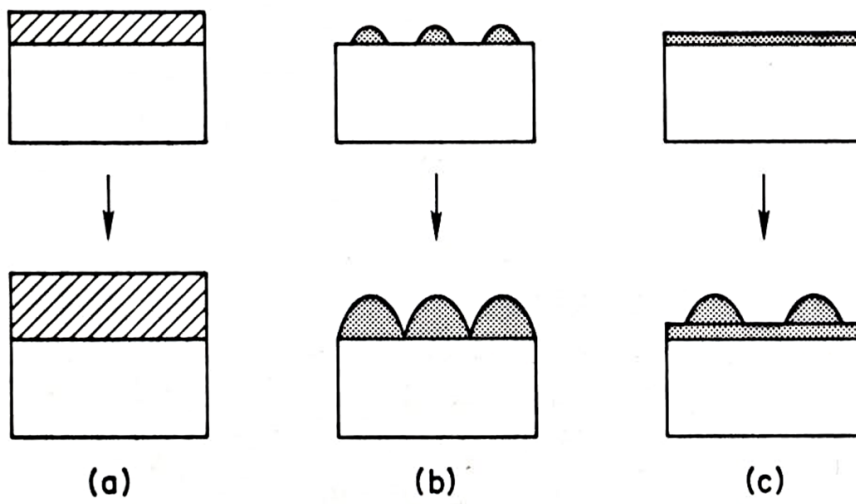


Figure 2.6. Schematic of the three epitaxial growth modes. (a) 2-D layer-by-layer (FM-mode), (b) 3-D island (VW-mode) and (c) layer-by-layer growth followed by islanding (SK-mode) [68].

than to themselves. For $\theta \geq 0$, SK growth occurs. In SK mode, the growth changes from FM mode to the VW mode at some critical coverage thickness, which is caused by the gradual strain accumulation in the epilayer.

Thermodynamics and kinetics in formation

Interface formation [71]

Solid surfaces can vary their energy in two approaches. One way is increasing the physical area of the surface, such as cleaving a surface or attaching atoms to the surface. This case includes simply creating more or less surface area, which is independent of the surface nature. Other way is changing the position of atoms through elastic deformation at the surface, such as surface relaxation or reconstruction. This case includes the detailed arrays of atoms on a surface, which may involve the straining.

Let us consider a crystalline body with a surface S_i , specific surface free energy σ_i and the central distances h_i to the different faces. According to Wulff theorem,

$$\frac{\sigma_i}{h_i} = \frac{\sigma_j}{h_j} = \dots = \frac{\Delta\mu}{2V_1}$$

When the crystal A and B are contacted with each other in epitaxial orientation, the gained work is equal to $-\beta$. Thus, specific interfacial free energy σ^* is defined as Dupre's relation,

$$\sigma^* = \sigma_A + \sigma_B - \beta$$

where the separation work refers to the specific adhesion free energy. When a crystal A grows on B, the formation balance can be written as follow.

$$\Delta G_{3D}(n) = -n\Delta\mu + \sum_1^i \sigma_i dS_i + (\sigma^* - \sigma_B)S_{AB}$$

Also, the variation of volume can be written as follow.

$$dV = \frac{1}{2} \left(\sum_1^i h_i dS_i + h_{AB} dS_{AB} \right)$$

in which h_{AB} is the distance from center to the interface. Therefore,

$$d\Delta G_{3D}(n) = -\left(\frac{\Delta\mu}{2V_1}\right) \left(\sum_1^i h_i dS_i + h_{AB} dS_{AB} \right) + \sum_1^i \sigma_i dS_i + (\sigma^* - \sigma_B) dS_{AB}$$

Thus, equilibriums of the interface and the free face of A are evaluated as follow.

$$\left(\frac{\partial\Delta G}{\partial S_{AB}}\right)_{S,T,\Delta\mu} = 0, \quad \left(\frac{\partial\Delta G}{\partial S_i}\right)_{S,T,\Delta\mu} = 0$$

From these conditions, generalized Wulff theorem is derived:

$$\frac{\Delta\mu}{2V_1} = \frac{\sigma_i}{h_i} = \frac{\sigma_j}{h_j} = \dots = \frac{(\sigma^* - \sigma_B)}{h_{AB}} = \frac{(\sigma_A - \beta)}{h_{AB}}$$

When $\beta = 0$, homogeneous case is yielded. It means that both surfaces are just in contact ($h_{AB} = h_A$) and they have no affinity with each other ($\sigma^* = \sigma_A + \sigma_B$). When the adhesion energy (β) has same value of σ_A ($\sigma^* = \sigma_B$),

$h_{AB} = 0$, indicating that the polyhedron is reduced by a half in comparison with the homogeneous case. In the case of $\sigma_A < \beta < 2\sigma_A$ ($h_{AB} < 0$), the polyhedron grows flat. When $\beta = 2\sigma_A$ ($\sigma^* = \sigma_B - \sigma_A$), $h_{AB} = -h_A$ is derived, which means that the lateral faces are evanescent. In this point, 3D phase of A is suppressed and 2D phase begins to fall on the substrate B.

According to thermodynamic consideration, two important conclusions can be derived:

- (1) Epitaxial 3D nucleation can occur on a substrate only when $\Delta\mu > 0$, indicating that the phase has to be supersaturated.
- (2) Epitaxial 2D nucleation can take place on a substrate only when $\Delta\mu \leq 0$ (undersaturation condition of the phase).

Also, epitaxial growth modes (3D or 2D) can be defined as the characteristic surface quantities:

- (1) In the case of $\beta < 2\sigma_A$ ($\sigma^* > \sigma_B - \sigma_A$), 3D growth mode occurs.
- (2) In the case of $\beta > 2\sigma_A$ ($\sigma^* < \sigma_B - \sigma_A$), 2D growth mode occurs.

These conclusions are summarized in Figure 2.7 [71].

Effect of strain on heterogeneous nucleation [77]

In epitaxial nucleation stage, the strained nucleus accumulates strain energy. Thus, the volume term ΔG_V is diminished by increase of chemical potential

in the nucleus which originates from the strained atomic bonds. On the other hand, the surface term ΔG_s is increased due to the effect of elastically relaxed facets (as shown in Figure 2.8 [77]) and the anisotropic nature of the strain. Therefore, the heterogeneous nucleation energy ΔG_N^* for formation of a nucleus of critical size is increased by the presence of strain as follow [97].

$$\Delta G_{N,strained}^* = \Delta G_{N,unstrained}^* \left(1 - \frac{\varepsilon}{E_1}\right)^2 \left(1 - \frac{2\varepsilon}{\Delta\mu}\right)^{-2}$$

where E_1 is the first neighbor bond interaction between two adjacent atoms, ε is strain, and $\Delta\mu$ is the supersaturation.

Strain-induced self-ordering [77]

According to Stranski-Krastanow growth mode, the transition of 2D to 3D growth is induced by strain originated from different lateral lattice constant between 2D layer and substrate. As thickness of epilayer increases, strain accumulates and may be relaxed elastically below critical thickness in which misfit dislocations occurs by reorganization of flat surface, e.g. the formation of 3D surface structures (Figure 2.8) [77], in order to minimize the strain and surface energy [98]. Elastic strain relaxation induces to an energy diminish of the structure. Let us consider epilayers composed of (001) surface and {011} facets (Figure 2.9) [77]. When the surface energy γ_{011} satisfy the condition of $\sqrt{2}\gamma_{001} < \gamma_{011}$, (001) surface will obtain energy upon a faceting

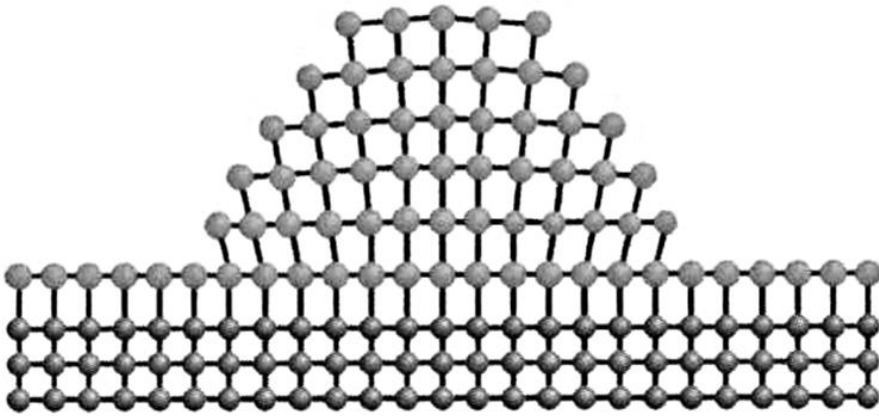


Figure 2.8. Schematic illustration of elastic strain relaxation in 3D self-ordered arrays [77].

with $\{011\}$ facets. More generally, when a 2D epilayer with thickness θ_0 reorganizes to a faceted 3D island on a layer with thickness θ , the gain energy per unit volume can be derived as [99]

$$\frac{E_{total}}{V} = \varepsilon_{island}^{elast} - \varepsilon_{layer}^{elast} + \frac{A\gamma_{facet} - L^2\gamma_{WL}(\theta_0)}{V} + \left(\frac{1}{\rho} - L^2\right) \frac{\gamma_{WL}(\theta) - \gamma_{WL}(\theta_0)}{V}$$

where an island is given by the pyramid shape with length L , ε_{layer} and ε_{island} are the elastic energy densities of the uniformly strained layer and the island, respectively, γ_{WL} is the surface energy of wetting layer, γ_{facet} is the surface energy of the facets of island and A is their area. Here, V is expressed as

$$V = \frac{1}{\rho} (\theta_0 - \theta) d_{ML} = \frac{1}{6} L^3 \tan \alpha$$

Where ρ is the areal density of the islands, d_{ML} is the thickness of a monolayer and α is the tilt angle of the facets. The energy gains per unit volume by island formation are calculated as shown in Figure 2.10 [77]. It indicates that the major contributions may originate from the elastic energy relief. Also, as shown in Figure 2.10, the total energy density has a minimum energy which determines a particular island size. Such minimum is important for achieving a narrow size distribution for arrays of islands.

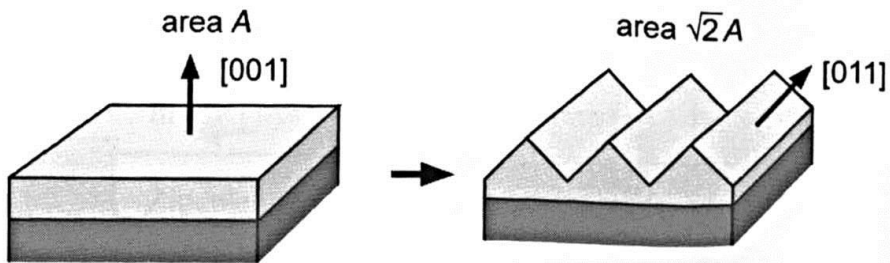


Figure 2.9. Faceting of a (001) surface to a surface with {011} facets [77].

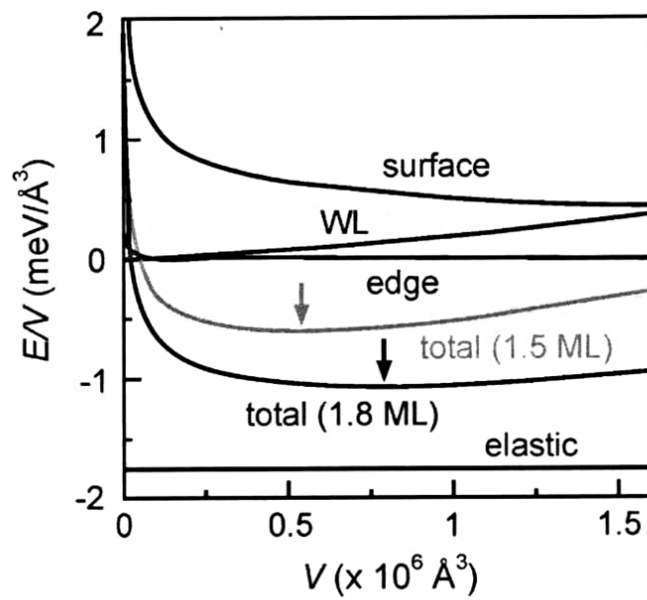


Figure 2.10. Total energy gain from island formation in which $\rho=10^{10} \text{ cm}^{-2}$ and $\theta_0 = 1.8$ monolayers. Arrows indicate the minimum of the total energy curves [77].

2.2 Preparation of 3-D heteroepitaxial nanostructures

Various methods have been attempted for the realization of 3-D heteroepitaxial nanoarchitecturing. Different fabrication strategies for 3-D heteroepitaxial nanostructures are summarized in Table 2.1. As shown in Table 2.1, representative methods are subsequent solution growth, subsequent vapor growth, Vapor-solution combination growth and one-step self-catalytic growth.

2.2.1 Subsequent solution growth

Solution methods, such as hydrothermal, suspension, electrodeposition and chemical bath deposition, have been widely employed for epitaxial growth of nanobranched (nanodots, rods, wires or plates) on 0-D, 1-D, 2-D or 3-D nanostructures. Solution methods have several advantages for epitaxial growth of nanobranched as follows.

- (1) High yield and large-scale homogeneity at low temperature.
- (2) Facile control of the length and density of nanobranched, which is particularly beneficial to the study for growth mechanisms and kinetics.
- (3) Growth of epilayers with an extraordinary high structural perfection.

As shown in Table 2.1, numerous heteroepitaxial structures have been synthesized by subsequent solution growth due to several advantages. Thus, growth of epilayer by solution technique may be feasible and inevitable approach. Chemical bath deposition (CBD) is a low-temperature (30 to 100 °C) and surfactant-free technique in which semiconductor nanoparticles are deposited on substrates immersed in solutions [100,101]. This method has been used for preparing additional thin layers or attaching minute particles of several nanometers to a substrate surface [100-103]. For example, in the case of dye-sensitized solar cells (DSSCs), a TiO₂ electrode was frequently surface-treated in a diluted TiCl₄ solution by CBD to improve the efficiency of the electrode [102,103]. Other articles have reported that TiO₂ and ZnO nanorods can be grown on substrates by CBD at ~ 100 °C with a surfactant or a nucleation seed needs [104-106]. Meanwhile, it was reported that in the presence of HCl, rutile TiO₂ nanorods can be precipitated by the thermal hydrolysis of TiCl₄ at a relative low temperature (~ 40 °C) [107]. On the basis of this information, it is expected that metal oxide nanorods can be grown on 1-D backbones at a low temperature with the acidic medium and without seeds or surfactants. However, up to now, there is no report on the synthetic procedure by CBD method for 3-D heteroepitaxial nanoarchitecturing. In this thesis, CBD method was adopted for deposition

of various binary compounds on 1-D Sb:SnO₂ nanobelt arrays.

2.2.2 Subsequent vapor growth

There are diverse methods for deposition of heteroepitaxial layer on nanostructure, such as atomic layer deposition, molecular-beam epitaxy and vapor-liquid-solid. Among them, vapor-liquid-solid (VLS) process is well-known approach for facile synthesis of 1-D nanowires, nanobelts or nanorods. According to this mechanism, the anisotropic growth is promoted at the liquid alloy/solid interface. In order to induce the liquid alloy/solid interface, metal nanoparticles are generally required for catalysts in VLS. For example, under Si-Au binary phase diagram, the eutectic point composed of Si and Au alloys exists, which leads to Si-Au liquid alloy that is a preferred deposition site for incoming Si vapor. After the liquid alloy becomes supersaturated with Si, Si nanowire grows by precipitation at the solid-liquid interface [108]. Thus, 3-D nanoarchitecturing can be realized by the growth of secondary nanowire branches onto the primary nanowire surfaces via two-step VLS growth. However, compared with the homobranching nanostructures, heteroepitaxial growth of branches by sequential catalyst-assisted VLS are much less reported due to limits of combination of materials [109]. Also, as shown in Table 2.1, there are little

reports on the synthetic procedure by only using vapor growth for 3-D heteroepitaxial nanoarchitecturing. Thus, this method may be not proper to synthesis of 3D heteroepitaxial architecturing.

2.2.3 Vapor-Solution Combination Growth [109]

Recently, various types of 3D branched metal oxide heterostructures have been fabricated by a combination of VLS growth for the backbones and the subsequent solution growth of the branches. VLS-grown SnO₂ nanowires are very stable and are an ideal candidate for this approach. Some 3-D heterostructures have been achieved, such as ZnO-SnO₂, Fe₂O₃-SnO₂, MnO₂-SnO₂ and TiO₂-SnO₂. Interestingly, non-perpendicular orientation was induced by the lattice mismatch minimization at heterojunction interfaces at Fe₂O₃-SnO₂. In this case, 6-fold-symmetry FeOOH branches were first formed on surfaces of rutile SnO₂ nanowires. A subsequent thermal treatment transformed the FeOOH into Fe₂O₃ nanorods without destroying the overall morphology.

2.2.4 Summary

Overall, solution-phase and vapor-phase are competitive methods in terms of advantages and drawbacks. The vapor-phase method provides fine tuning

of the branches but requires high temperatures and complicated growth facilities. The obtained 3-D heteroepitaxial structures by vapor-phase method are useful in electronic and optoelectronic applications, for which a well-defined interface and a high crystalline quality is required. The solution-phase method can carry out at low temperatures with low cost and high yield. It enables the production of 3-D branched nanostructures with a variety of morphologies by controlling the precursor conditions. However, in most cases of the 3-D nanostructures fabricated by solution method, branches tend to be grown with random orientation, which means that epitaxial growth doesn't occur. Therefore, in order to obtain heteroepitaxially nanobrached structures, merits of vapor and solution-phase methods have to be properly combined. Thus, in this thesis, VLS and chemical bath deposition methods are selected for high crystal quality of backbone and slow growth rate of epilayer, respectively.

Table 2.1 3-D heteroepitaxial nanostructures sort by growth methods and their compounds, morphology and applications.

Growth Method	Materials		Morphology		Deposition Method of Epilayer	Application	Ref
	Backbone	Epilayer	Backbone	Epilayer			
Subsequent Solution Growth	TiO ₂	ZnO	Rod	Rod	Hydrothermal	-	[110]
	CuO	ZnO	Wire	Rod	Hydrothermal	-	[111]
	MnO ₂	SnO ₂	Wire	Dot	Hydrothermal	-	[112]
	Fe ₂ O ₃	SnO ₂	Tube, Rod	Rod	Hydrothermal	Photocatalyst	[113]
	CuO	ZnO	Wire	Rod	Hydrothermal	PEC cells	[114]
	CdS	CdS	Rod	Rod	Hydrothermal	PEC cells	[115]
	TiO ₂	TiO ₂	Wire	Rod	Hydrothermal	DSSCs	[116]
	MnO ₂	Fe ₂ O ₃	Rod	Rod	Hydrothermal	LIBs	[117]
	Co ₃ O ₄	Fe ₂ O ₃	Wire	Rod	Hydrothermal	LIBs	[118]
	SnO ₂	Fe ₂ O ₃	Sheet	Rod	Hydrothermal	Gas sensors	[119]
	SnO ₂	Fe ₂ O ₃	Hollow Fiber	Rod	Hydrothermal	Gas sensors	[120]
	CdSe	CdS	Plate	Plate	Suspension	-	[121]

	SiO ₂	SiO ₂	Particle	Branch	Suspension	-	[122]
	ZnO	ZnS·(HDA) _{0.5}	Rod	Plate	Suspension	-	[123]
	CuGaO ₂	ZnO	Plate	Wire	Suspension with heat	Diodes	[124]
	TiO ₂	ZnO	Belt	Rod	Suspension with heat	PEC cells	[125]
	CdSe	ZnSe	Wire	Rod	Solution-liquid-solid	-	[126]
	Si	Au	Wire	Dot	Galvanic displacement	-	[127]
	Si	ZnO	Wire	Rod	Atomic layer deposition	-	[128]
	Si	GaAs	Wire	Rod	Molecular-beam epitaxy	-	[129]
Subsequent Vapor growth	W	WO _{2.72}	Wire	Rod	Self-catalyst vapor-solid	Field emission	[130]
	ZnO	ZnO	Rod	Rod	Vapor-liquid-solid	-	[131]
	GeS	GeS	Wire	Sheet	Self-catalyst vapor-liquid-solid	-	[132]
Vapor-Solution Combination Growth	SnO ₂	TiO ₂	Wire	Rod	Hydrothermal	PEC cells	[41]
	SnO ₂	Fe ₂ O ₃	Wire	Rod	Hydrothermal	LIBs	[31]
One step self-Catalyzed Growth	GaSb	GaSb	Wire	Nanorod	Chemical beam epitaxy	-	[133]

2.3 Materials

2.3.1 Rutile

The rutile structure is one of most common and the simplest structural types among metal dioxides [134]. At least ten metal dioxides have a rutile phase at room temperature. In some cases the rutile structure is the most stable oxide (TiO_2 , RuO_2 , IrO_2 , SnO_2 , PbO_2), whereas for others the rutile is a metastable form produced under high temperature and pressure conditions (RhO_2 , SiO_2 , GeO_2) [135]. The rutile has edge-shared octahedral (MO_6) which form chains along the c-axis. Each chain is connected to four adjacent chains and cross-linked by corners sharing as shown in Figure 2.11. The MO_6 octahedra are tetragonally distorted, which includes different M–O bond lengths. Also, O–O bonds in MO_6 are not equal (the shared edge is shorter than the edge parallel to the [001] direction). The crystal structure information, such as lattice parameters and bond distances, for representative rutile materials are summarized in Table 2.2 [134]. Although metal oxides with rutile-structure have very similar lattice parameters, they show pronounced differences in their physical properties [136]. For example, SnO_2 and GeO_2 are insulators, which have no dielectric singularity whereas TiO_2 is an incipient ferroelectric. Such diverse physical properties and similar and

Table 2.2 Structural data for representative rutile materials [134].

		TiO ₂	VO ₂	CrO ₂	MnO ₂	NbO ₂	
Metal ionic radii (Å)		0.68	0.63	0.62	0.60	0.74	
Lattice parameters (Å)							
	<i>a</i>	4.5937 (1)	4.5546 (3)	4.4219 (3)	4.3980 (1)	4.8464 (1)	
	<i>c</i>	2.9587 (1)	2.8514 (2)	2.9166 (4)	2.8726 (1)	3.0316 (1)	
<i>c/a</i> ratio		0.6441 (3)	0.6260 (1)	0.6596 (1)	0.65316 (3)	0.62554 (2)	
Oxygen position	<i>x</i>	0.30478 (6)	0.3001 (2)	0.3024 (8)	0.3046 (1)	0.2925 (2)	
Anisotropic displacement parameters (Å ² × 10 ⁻³)							
Metal	<i>U</i> ³³	4.6 (5)	9.6 (3)	1.7 (4)	2.3 (8)	33.8 (6)	
	<i>U</i> ¹¹ - <i>U</i> ¹²	7.2 (4)	12.3 (4)	4.2 (5)	3.2 (4)	22 (1)	
	<i>U</i> ¹¹ + <i>U</i> ¹²	6.4 (4)	10.0 (4)	5.0 (5)	5.6 (4)	20 (1)	
Oxygen	<i>U</i> ³³	3.5 (2)	6.2 (1)	4.4 (2)	4.2 (4)	26.9 (9)	
	<i>U</i> ¹¹ - <i>U</i> ¹²	7.2 (2)	10.4 (4)	8.1 (3)	11 (1)	41 (1)	
	<i>U</i> ¹¹ + <i>U</i> ¹²	3.2 (2)	6.7 (4)	4.1 (3)	4.1 (5)	21 (1)	
Interatomic separations (Å)							
Equatorial <i>M</i> -O		1.949 (1)	1.921 (1)	1.911 (1)	1.882 (2)	2.079 (3)	
Axial <i>M</i> -O		1.980 (1)	1.933 (1)	1.891 (1)	1.894 (1)	2.005 (1)	
O-O(O ₂)		2.536 (2)	2.575 (1)	2.471 (3)	2.431 (1)	2.844 (2)	
<i>M</i> - <i>M</i>		3.569 (1)	3.522 (1)	3.450 (1)	3.426 (9)	3.747 (8)	
O _i /O _j *		0.855	0.905	0.849	0.843	0.939	
		RuO ₂	IrO ₂	SiO ₂	GeO ₂	SnO ₂	PbO ₂
Metal ionic radii (Å)		0.67	0.68	0.42	0.53	0.71	0.84
Lattice parameters (Å)							
	<i>a</i>	4.4968 (2)	4.5051 (3)	4.1773 (3)	4.4066 (1)	4.7374 (1)	4.9577 (1)
	<i>c</i>	3.1049 (1)	3.1586 (2)	2.6655 (1)	2.8619 (1)	3.1864 (1)	3.3879 (8)
<i>c/a</i> ratio		0.6905 (1)	0.7011 (2)	0.6381 (1)	0.6494 (3)	0.6726 (1)	0.6834 (2)
Oxygen position	<i>x</i>	0.3053 (1)	0.3077 (3)	0.30608 (6)	0.30604 (6)	0.3056 (1)	0.3072 (1)
Anisotropic displacement parameters (Å ² × 10 ⁻³)							
Metal	<i>U</i> ³³	4.4 (5)	6.4 (8)	1.8 (1)	2.3 (2)	3.1 (4)	5.0 (4)
	<i>U</i> ¹¹ - <i>U</i> ¹²	4.6 (4)	11.4 (9)	2.2 (1)	3.3 (3)	4.8 (5)	9.6 (5)
	<i>U</i> ¹¹ + <i>U</i> ¹²	3.2 (4)	10.6 (9)	2.5 (1)	3.3 (3)	4.0 (5)	7.6 (5)
Oxygen	<i>U</i> ³³	7.0 (4)	7.0 (9)	2.3 (10)	3.1 (2)	5.5 (4)	7.2 (4)
	<i>U</i> ¹¹ - <i>U</i> ¹²	8.4 (5)	15.0 (10)	4.0 (1)	4.8 (7)	8.3 (4)	21.0 (5)
	<i>U</i> ¹¹ + <i>U</i> ¹²	4.1 (5)	9.2 (10)	2.1 (1)	3.0 (7)	5.0 (4)	7.0 (5)
Interatomic separations (Å)							
Equatorial <i>M</i> -O		1.985 (2)	1.998 (2)	1.757 (2)	1.874 (4)	2.058 (2)	2.167 (2)
Axial <i>M</i> -O		1.941 (1)	1.958 (1)	1.808 (4)	1.906 (7)	2.047 (1)	2.154 (1)
O-O(O ₂)		2.476 (1)	2.451 (3)	2.291 (1)	2.4170 (1)	2.605 (1)	2.704 (1)
<i>M</i> - <i>M</i>		3.538 (1)	3.553 (4)	3.241 (1)	3.429 (9)	3.709 (1)	3.893 (1)
O _i /O _j *		0.799	0.777	0.860	0.844	0.816	0.798

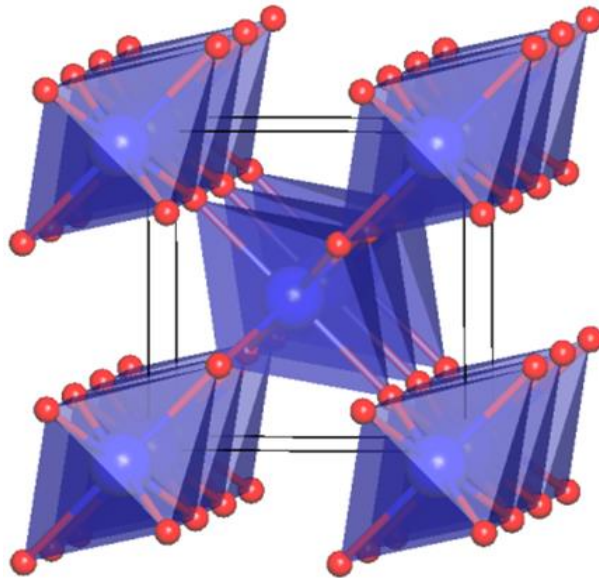


Figure 2.11. The rutile structure viewed along the $[001]$ direction, where the metal atoms and oxygen atoms are located at the center and edge of octahedra.

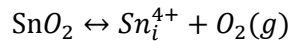
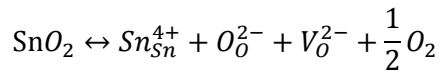
stable structures could lead to several advantages in 3-D heteroepitaxial rutile structures, i.e. wide variety of combinations, synergetic effects between two other rutile phases, easy fabrication of heteroepitaxial structures and systematical study for 3-D epitaxial growth. From these reasons, in this thesis, rutile materials are selected as candidates for epitaxial heterostructure. Most famous rutile structures – SnO₂, TiO₂ and VO₂ – are reviewed and discussed in aspects of electrochemical energy conversion and storage characteristics in following sections.

2.3.2 SnO₂

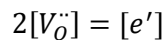
SnO₂ is an n-type wide-bandgap semiconductor with 3.6 eV. Its electrical conduction is originated from the existence of point defects which act as donors or acceptors [137]. Some unique properties of SnO₂ enable the material to be used in many applications including dye-sensitized solar cells, gas sensors, and field emission, and so on [138-141]. Also, SnO₂-based TCO materials have the advantages of being low cost [53] and thermal and chemical stable [54], allowing them to withstand various chemical conditions during reaction.

Sb doped SnO₂ (ATO)

The degenerated SnO₂ by doping the impurity, such as antimony (Sb), fluorine (F) or indium (In), have been widely used as TCO materials. A degenerate semiconductor is formed by increasing the doping concentration (> 2%), exhibiting high conductivity ($> 100 \Omega^{-1} \text{ cm}^{-1}$). Also, doped-SnO₂ thin films are transparent for visible light at low doping level (2~4%), which makes them useful for a optoelectronic device application [142]. The conduction behavior of Sb:SnO₂ can be explained by the energy band diagram as shown in Figure 2.12. Two shallow impurity states exist below the conduction band: one is an ionization energy of 0.03 eV due to oxygen vacancies, and the other is an ionization energy of 0.039 eV due to interstitial Sb [143]. Thus, the free carriers result from ionized oxygen vacancies and Sb impurities. In pure SnO₂, oxygen vacancies (V_O) and interstitial Sn atoms (Sn_i) can be generated as follow [137].



Doubly ionized oxygen vacancies in SnO₂ follows the reaction with the neutrality condition.



Also, Sn interstitials in SnO₂ follows the reaction with the neutrality

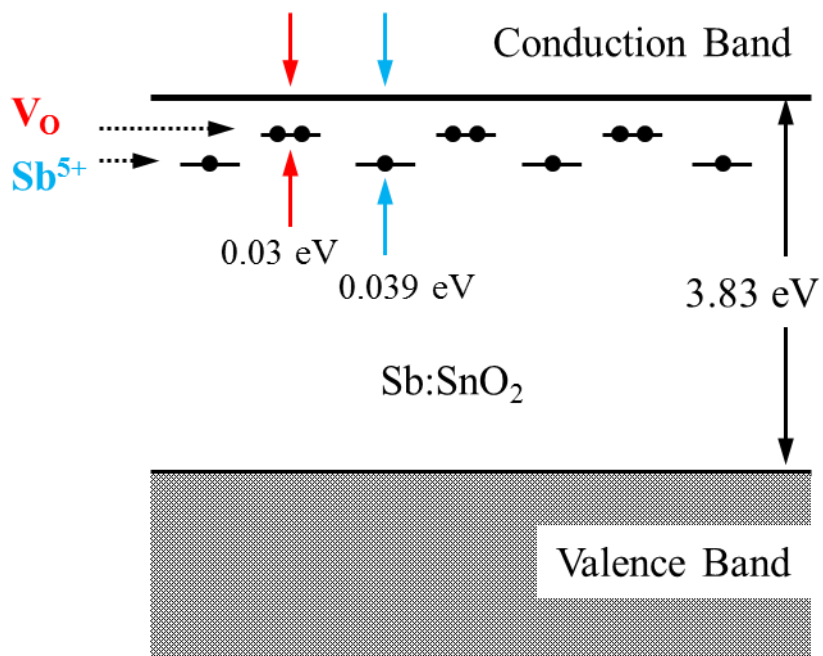
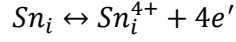


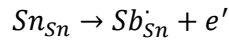
Figure 2.12. Energy band diagram of Sb-doped SnO₂.

condition.



$$4[Sn_i^{4+}] = [e']$$

When a Sb atom is implanted in SnO₂ lattice, a free electron can be generated as follow.



Therefore, oxygen vacancy and interstitial Sb in SnO₂ induce the neutrality condition as follow.

$$n + [V_{Sn}^{\cdot\cdot\cdot}] + [Sn_{Sn}^{\cdot\cdot}] = p + [Sb_{Sn}^{\cdot}] + 2[V_O^{\cdot\cdot}]$$

$$n = [Sb_{Sn}^{\cdot}] + 2[V_O^{\cdot\cdot}]$$

1-D ATO nanobelt

Some researchers synthesized the ATO nanobelts by VLS mechanism, and reported significant results, such as influence of Sb doping on the electrical properties of SnO₂ nanobelts [144], turn-on fields property of the ATO nanobelts which is lower than pure SnO₂ nanowires [145] and photoluminescence characteristics [54]. Sb doping affects significantly on the electrical properties of SnO₂ nanobelts. Undoped SnO₂ nanobelts are hardly conducting and form Schottky contacts with metal electrodes. On the other hand, an increase in the doping level induces degenerately Sb-doped SnO₂ nanobelts (2~4%) with metallic behavior [144]. Also, various

morphology and shape of ATO nanobelts were reported by altering the VLS condition, i.e. curved nanobelt [53], zig-zag nanobelt [54] and hyper branched nanowire [55] as shown in Figure 2.13. The ATO nanobelts fabricated by VLS process had low resistivity of $4.1 \times 10^{-4} \Omega \text{ cm}$ and failure-current densities of $2.1 \times 10^7 \text{ A cm}^{-2}$, which can act as metallic conductors and may provide an alternative to ITO as TCOs due to lower cost of Sn than In [53].

Application to Li-ion battery

SnO_2 -based materials have recently been considered as an alternative high-energy anode candidate to replace currently used graphite electrodes (theoretical capacity 372 mA h g^{-1}) for Li-ion rechargeable batteries because of its higher theoretical capacity (782 mA h g^{-1}). However, huge volume expansion/contraction ($\sim 300\%$) of SnO_2 -based anodes occurring during Li-alloying/de-alloying process is the most critical problem to be overcome for practical application. These volume changes lead to electrical isolation by crack and pulverization, resulting in poor cycle life of the electrode. To mitigate the pulverization problem of SnO_2 -based anodes, several strategies have been proposed, such as nanoarchitecturing of electrode and formation of SnO_2 -carbon composites [146-149]. Nanostructured materials, especially

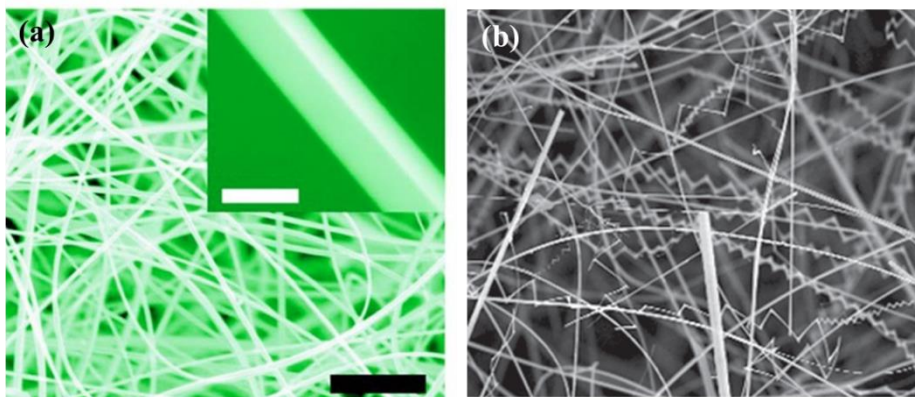


Figure 2.13. (a) curved [53] and (b) zig-zag shaped [54] Sb:SnO₂ nanobelt arrays by vapor-liquid-solution mechanism.

nanowires, can accommodate large strain without severe pulverization [147], and carbon-based materials can play a role in structural buffering as well as passage for facial electron transport [148,149]. Furthermore, wrapping the surface of Sn-based nanostructures in other anode materials showing the low volume variation during cycling could be an appropriate solution for improvement of cycle life of the electrodes. Meanwhile, Wang et al. reported that Sb-doped SnO₂ (ATO) nanoparticles have the high reversible capacity and superior cycle retention due to the presence of Sb for Sn, inducing an enhanced formation of metals from ATO [150,151]. In addition, some researchers suggested also that superior cyclability of SnO₂-based electrodes doped with various dopants was attributed to high electronic conductivity, suppression of crystallite growth, and easy dispersion of Sn atoms formed during cycling [152,153].

2.3.3 TiO₂

TiO₂ has been widely studied in various applications such as photovoltaic devices (dye-sensitized solar cell, organic photovoltaic cell and perovskite), photocatalysis, photoelectrochemical cell, photo-electrochromics and sensors [154]. Especially, in the photo-conversion applications, TiO₂ is a key material due to its good electronic properties related to photo-electron

reaction. There are three major crystalline polymorphs in TiO_2 : rutile (tetragonal), anatase (tetragonal), and brookite (orthorhombic). Among them, rutile TiO_2 is most stable phase.

Electronic properties

Rutile TiO_2 has a bandgap of 3.0 eV. The density of state (DOS) of TiO_2 consists of Ti e_g , Ti t_{2g} (d_{xy} , d_{yz} and d_{zx}), O p_π (out of the Ti_3O cluster plane) and O p_σ (in the Ti_3O cluster plane) [154]. Figure 2.14 describes the orbital bonding structures of TiO_2 at atomic levels, crystal field split level and DOS states [155]. Conduction bands are split into Ti t_{2g} (<5 eV) and e_g bands (>5 eV). The d_{xy} states dominantly existed at the edge of the conduction bands. The rest regions of the t_{2g} are related to antibonding with p states (d_{yz} and d_{zx} states). Valence bands are split into three parts. The σ bonding in the lower energy band is related to O p_σ bonding. the π bonding in the middle energy band and O p_π states in the higher energy band is mainly due to O p_π nonbonding states. Thus, the contribution of the σ bonding is much stronger than that of the π bonding. It is noted that the nonbonding states are located near the band gap: the nonbonding O p_π orbital the nonbonding d_{xy} states at the edge of the valence bands and the conduction bands, respectively. A more significant feature can be seen in anatase because anatase is less dense

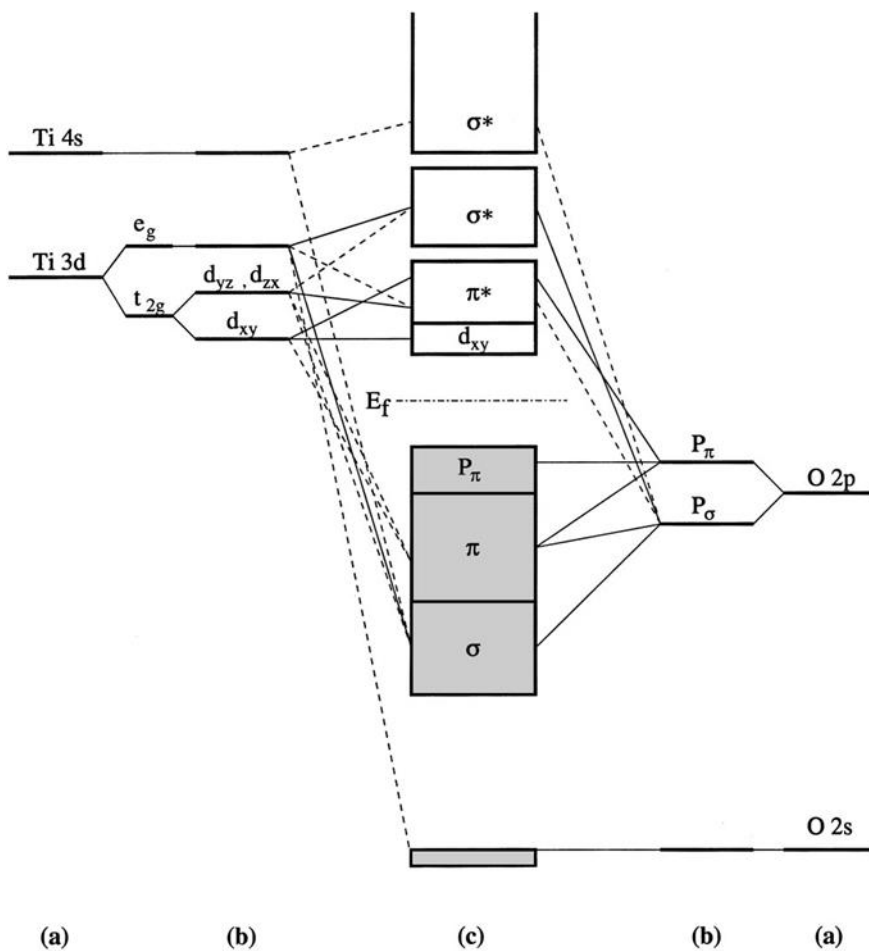
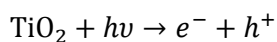


Figure 2.14. Molecular-orbital bonding structure for TiO_2 : (a) atomic levels; (b) crystal-field split levels; (c) final interaction (DOS) states [155].

than rutile (large metal-metal distance of 5.35 Å). As comparison with anatase, the Ti d_{xy} orbitals at the edge of the conduction band are less isolated due to small metal-metal distance of 2.96 Å) [156]. Figure 2.15 shows a energy level diagram of the lowest unoccupied molecular orbitals for a $[\text{TiO}_6]^{8-}$ cluster and rutile with O_h and D_{2h} symmetry, respectively [157]. The further splitting of the Ti^{3+} 3d levels is due to the asymmetric crystals of rutile which has a tetragonally distorted octahedral structure where each titanium cation is surrounded by six oxygen atoms in an elongated octahedral geometry (D_{2h}).

Photon-Induced Electron and Hole Properties

When photons with higher energy than band gap of TiO_2 (> 3.0 eV), electrons are excited from the valence band to the unoccupied conduction band, inducing the positive holes in the valence band and excited electrons in the conduction band [154]. These charge carriers can transfer into the surface of the TiO_2 and react with adsorbed acceptors or donors. But some carriers are recombined radiatively or nonradiatively during the transfer, affecting the overall efficiency of photo-conversion. The photon absorption process is as follow [158].



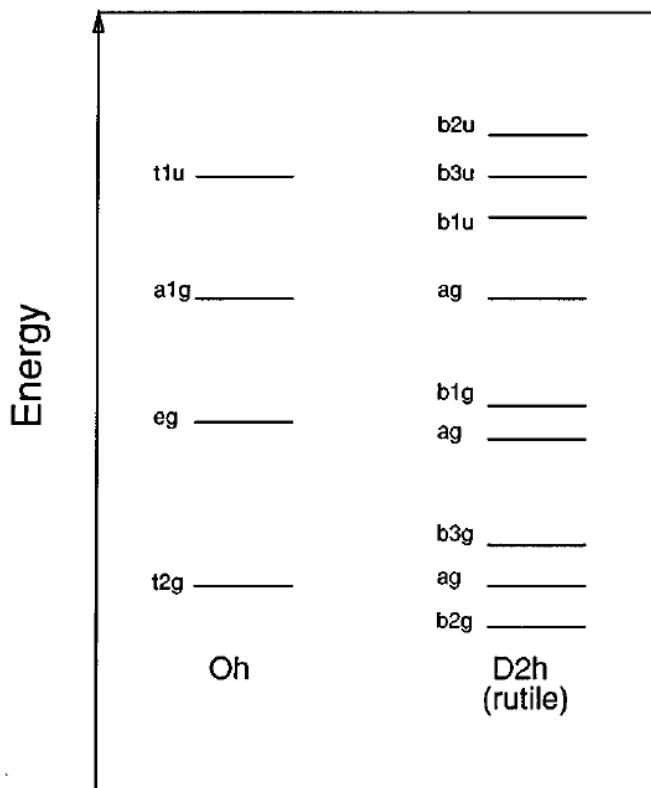
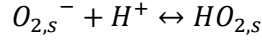
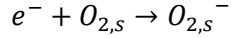
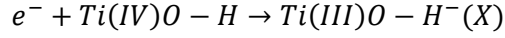
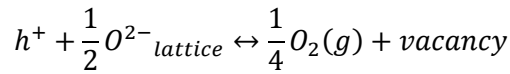
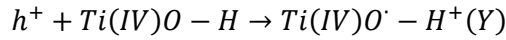


Figure 2.15. Schematic illustration of the energy levels diagram of the lowest unoccupied molecular orbitals of a $[\text{TiO}_6]^{8-}$ cluster and rutile with O_h and D_{2h} symmetry, respectively [157].

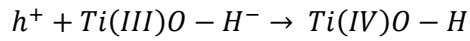
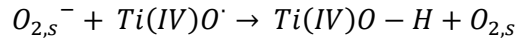
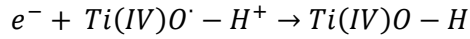
Photocatalytic redox pathways of excited electron are as follow.



In the same manner, the competition pathways for holes lead to OH radicals bound and oxygen vacancies as follow.



Also, the recombination channels are like this.



Photogenerated electrons and holes in TiO₂ are localized at various defect sites of bulk and surface. According to electron paramagnetic resonance (EPR) results, electrons were trapped into two Ti(III) centers, whereas the holes were trapped into oxygen-centered radicals which is covalently linked to surface titanium atoms [159].

Application to PEC cells

Since Fujishima and Honda found the phenomenon of PEC water splitting

on a rutile TiO₂ photoanode under ultraviolet (UV) light in 1972, enormous efforts have been devoted to the development of TiO₂ electrodes [160]. Following this initial discovery, two main approaches have been developed to enhance the efficiency of photoanode. One is increasing of the visible light absorption by doping with other elements [12], substituting TiO₂ for other metal oxide [11] or sensitizing with quantum dots (QDs) [161], the other is decreasing of the recombination loss by designing nanoarchitecture [45,162,163]. Very recently, three dimensional (3D) nanostructured-photoanode have shown promising potential for improving the hydrogen production performance, which leads to enhanced charge transportation, increased surface area and facilitated interfacial charge transfer [34,40,56]. Accordingly, almost the whole researchers in the nanotechnology and energy science field have been concerned in this regard. However, development of nanoarchitecture with optimized structural factors – extremely high conducting path way, high surface area and low interfacial resistance – was still too far. 3D hierarchical heterostructures are good candidates for optical, electro- and photoelectron-chemical applications. Shi et al have synthesized TiO₂-Si hierarchical heterostructures with 2.1 % efficiency and referred that metallic backbone could be more efficient channel than Si nanowire [34]. ITO(Sn:In₂O₃)/TiO₂ core/shell structure also shows the good PEC

performance, which revealed that transparent conducting oxide (TCO) is effective as backbone [56]. Therefore, in this thesis, TiO₂-ATO hierarchical heterostructures with TiO₂ nanobranches grown epitaxially on ATO backbone were studied for efficient 3-D PEC electrode. Furthermore, QD sensitized TiO₂-ATO heterostructures were proposed as a conceptual model of satisfying every structural factor – high conductivity by TCO backbone, high surface area by branch and low interfacial resistance by epitaxial relationship.

Application to Li-ion batteries

TiO₂ that is well-known anode material for Li-ion battery having theoretical capacity of 168 mA h g⁻¹ and showing the low volume change (<4%) during Li-insertion/extraction is very suitable as capping layer or branch. There is no clear plateau in charging-discharging curves due to a two phase intercalation process in TiO₂ [164]. Moreover, in nano-sized TiO₂, unusual high-capacity and sloped charge-discharge potential curves was reported, which is attributed to solid solution behavior of the nanosized TiO₂ particles [26,165,166] and different thermodynamics of insertion reaction from bulk TiO₂ [167,168]. Recently, several reports have been published on SnO₂-TiO₂ heteronanostructures as anode for Li ion battery [65-67]. However, in most

case, reversible capacities of the heteronanostructured electrodes exhibited very low values ($< 200 \mu\text{A h cm}^{-2}$) because TiO_2 was more dominant in the capacity contribution of the electrodes. Therefore, new nanoarchitecturing based on SnO_2 and TiO_2 for improvement of electrochemical performance are required.

2.3.4 VO_2

VO_2 has a metallic property in its rutile phase. At room temperature, VO_2 exists in monoclinic rutile form ($\text{P2}_1/\text{c}$) with insulating property, which is the most stable phase among polymorphs of VO_2 . At about 68°C , VO_2 presents a phase transition from insulator to metal with a large change in electrical resistance, optical properties, IR penetration and total reflection [169]. The oxygen polarizabilities of the metallic VO_2 is significantly larger compared with that of non-metallic SnO_2 [136]. It indicates the destabilization of the oxygen shell in the presence of d electrons. The analysis of the eigenvectors describes the displacement pattern of the vanadium atoms as shown in Figure 2.16 [136]. The vanadium ions located at center of the unit cell tend to be paired along the tetragonal c-axis while the other vanadium atoms tend to lead to a doubling of the unit cell along a-axis. This displacement pattern is consistent with the lattice distortion which occurs at the phase transition

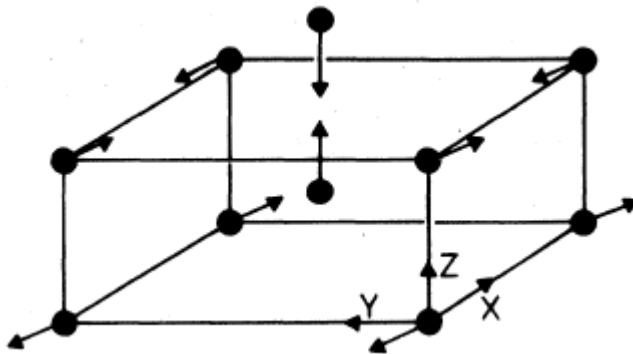


Figure 2.16. Phonon eigenvectors of the lowest frequency mode at rutile VO_2 unit cell [136].

from tetragonal rutile phase, VO₂ (R), to monoclinic rutile phase, VO₂ (M).

Metal-Insulator Transition

The metal-insulator transition (MIT) in VO₂ is characterized by a surprising change in resistivity (by a factor of 10⁴ – 10⁵) at T_C ~ 68 °C [170]. This MIT in VO₂ is known as first-order transition in which the structural transformation can proceed within picosecond or femtosecond ($t \sim 10^{-13} - 10^{-14} \text{ s}^{-1}$) [171]. The origin of the driving forces behind the MIT of VO₂ has been explained by two competitive mechanism [172]. First one is related to crystal structure change. The decrease in symmetry and the creation of a bonding-antibonding pair induce a band gap opening. Such a structural change is characteristic of a Peierls-type transition where it is totally structurally driven [172]. Secondly, in a Mott-type MIT, the band gap opening originates from strong electron-electron correlations rather than phonon or electron-phonon interaction contributions [171]. This interesting phenomena near room temperature provides the potential of using the MIT for nano-electronic applications [173]. Recently, it was found that the MIT behavior of VO₂ epilayer can be modulated by epitaxial strain introduced by misfit from the substrate [174]. Interestingly, when VO₂ layer are epitaxially grown on the TiO₂ (001) substrate with the c axis out of the plane, MIT

temperature decreases to room temperature (27 °C) by strain of -1.2% along the c axis [90].

Application to Li-ion batteries

Vanadium oxides, such as V_2O_5 and VO_2 (B) exhibit feasible layered structures that could contain a large amount of lithium, which provides high capacities over 200 mAh g^{-1} as cathodes for Li ion batteries [175,176]. However, they generally show poor cycling stability and low electronic conductivity, inducing short life time and poor rate-capabilities, respectively [177]. V_2O_5 has a poor conductivity of $10^{-4}\sim 10^{-2} \text{ S cm}^{-1}$ and a low Li diffusion coefficient of $10^{-12} \text{ cm}^2 \text{ s}^{-1}$, and VO_2 (B) also has similar values (conductivity of $10^{-2} \text{ S cm}^{-1}$ and Li diffusion coefficient of $10^{-9} \sim 10^{-10} \text{ cm}^2 \text{ s}^{-1}$) [178,179]. Thus, in order to enhance current rates and cycle performance, numerous nanoscale materials have been attempt to reduce the diffusion length of the active materials, i.e. nanoparticles [180], hollow spheres [181], nanorods [182] and nanowires [183]. Also, the route of fabrication VO_2 /carbon composite was proposed by some researchers [184]. Among polymorphs of VO_2 including R-phase ($P4_2/mnm$, 136), B-phase ($C2/m$, 12) and A-phase ($P4_2/ncm$, 138), VO_2 (B) has been widely studied for cathode because it has a layered structures similar to V_2O_5 as shown in Figure 2.17

[185]. The tunnels in VO₂ (B) play a role of diffusion pathways during Li⁺ insertion and extraction. Recently, in same manner, VO₂ (A) phase also was reported as cathode for Li-ion battery, which is attributed to the pathway tunnels in the layered structure [185]. Although VO₂ (R) also has channels for Li⁺ pathway along the c-axis similar to rutile TiO₂, there are only few reports on the electrochemical activity of VO₂ (R). Baudrin et al reported the electrochemical properties of nanosized rutile type VO₂ with a capacity of 120 mA h g⁻¹ [186]. Huang et al reported the VO₂ (M) nanobelts–carbon core–shell structures, but also recorded low capacity level (< 100 mA h g⁻¹). These trends are similar to study of rutile TiO₂; single nanostructures or carbon-composites of TiO₂ presents the low capacities, but heterostructures with high conductive path shows the high capacities almost near theoretical value. Therefore, capacity of rutile VO₂ may be increased by 3-D heteroepitaxial architecturing (heteroepitaxially branched VO₂ on metallic 1-D ATO backbone). Also, high rate capability and long-term stability are expected in this heterostructure due to short diffusion path and high conductivity.

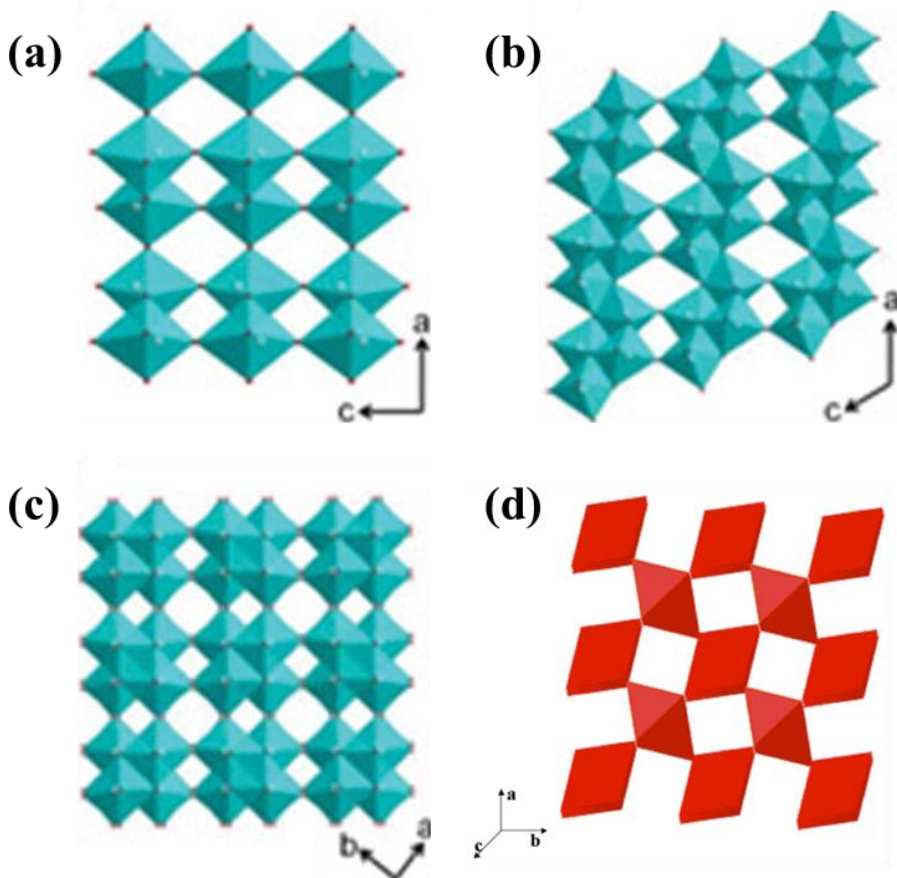


Figure 2.17. Crystal structures of (a) V_2O_5 projected along the b-axis, (b) VO_2 (B) projected along the b-axis and (c) VO_2 (A) projected along the c-axis, which shows the layered structure [185]. (d) Crystal structure of VO_2 (B) along c-axis, which also shows the tunnel for Li^+ diffusion pathway.

Chapter 3. Experiments

3.1 Synthesis of 1-D nanostructure

Thermal evaporation method

Sb:SnO₂ (ATO) nanobelt backbones were grown on various substrates, such as Ti foils (99.6%, 0.127 mm thickness, Aldrich, U.S.), F:SnO₂ (FTO) substrates (TEC-8, Pilkington, USA) and Si substrate, using a vapor–liquid–solid (VLS) growth mechanism by means of a thermal evaporation method [108]. As shown in Figure 3.1, Sn (99.5%, Samchun, Korea) and Sb powders (99.9%, high purity chemicals, Japan) were loaded into a quartz boat with a 9:1 weight ratio and inserted into a dual-zone horizontal tube furnace. The substrates were covered with 3 nm of Au film using an ion coater (IB-3, Eiko Engineering, Japan) as the catalyst, and then positioned 12 cm from the center. The furnace was heated up to 800 °C at a rate of 10 °C/min and kept at 800 °C for 30 min with vacuum condition (below 2×10^{-3} Torr) using a rotary pump. Then, oxygen gas with a flow rate of 12 sccm was introduced to the tube by mass-flow controller during the growth process. The length of ATO nanobelts could be controlled by tuning the inlet time from 1 min to 1 hour. After growth, the samples were naturally cooled in the tube.

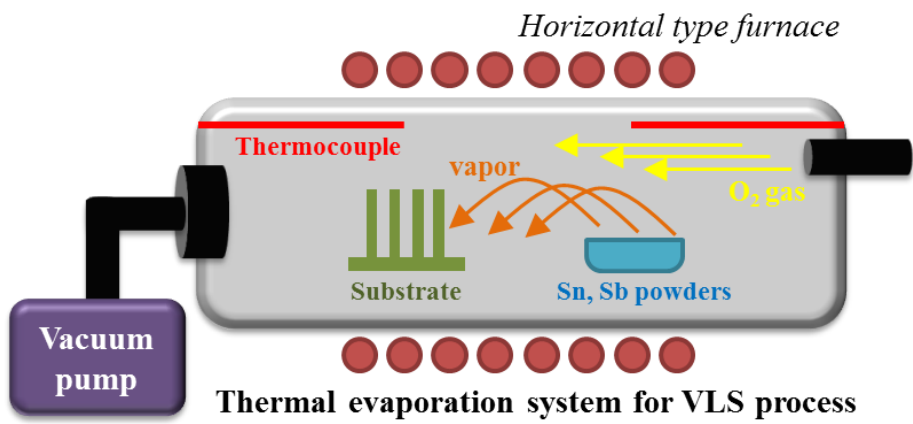


Figure 3.1. Schematic view of the thermal evaporation system

3.2 Synthesis of 3-D nanostructure

Chemical Bath Deposition

CBD method was adopted for deposition of various binary compounds on 1-D ATO nanobelt arrays as shown in Figure 3.2. By employing acids as hydrolysis control agents, improved CBD method was developed for nano-branching synthesis.

TiO₂-ATO

Rutile TiO₂ nanorods were formed on the surface of the ATO nanobelts by a CBD method. Aqueous TiCl₄ (99%, Junsei, Japan) 2 M stock solution was prepared by the conventional method [187]. The stock solution was mixed with distilled water, and the concentration of TiCl₄ was adjusted to 0.05 M. The ATO nanobelts electrodes were placed in 7 mL of 0.05 M TiCl₄ solution horizontally at 50 °C for several hours. Because rutile phase formation is favored at a high level of acidity, various acids (HCl, HNO₃, H₂SO₄, and HCOOH) were added to the solution and it was confirmed that HNO₃ is most suitable for TiO₂ nanorods formation. In addition, the HNO₃ concentrations (0.02 to 5 M) and the reaction durations (0.5 to 336 h) was changed to synthesize TiO₂ nanorods with various lengths and to study the growth mechanism. For comparison, anatase TiO₂ nanospheres were also

formed on the surface of the ATO nanobelts by a CBD method. Typically, the ATO nanobelt electrodes were placed horizontally in the 0.05 M TiCl_4 solution at room temperature ($\sim 20\text{ }^\circ\text{C}$) for 144 h. As anatase is the main phase at high pH levels [188], the TiCl_4 solution was replaced every 8 h to generate the TiO_2 anatase nanostructure. The prepared TiO_2 -ATO nanostructures were further annealed at $450 \sim 600\text{ }^\circ\text{C}$ for 1 h under air to increase crystallinity.

Fe₂O₃-ATO

Fe_2O_3 nanorods were also formed on the surface of the ATO nanobelts via CBD method. 4.5 and 30 mmol of $\text{FeCl}_3 \cdot 6\text{H}_2\text{O}$ (99%, Sigma-Aldrich, USA) and NaNO_3 (99%, Sigma-Aldrich, USA), respectively, were diluted in 30 mL of deionized water and poured into 100-mL Schott bottles. The prepared ATO nanobelts grown electrodes were placed horizontally in the aqueous solution at $100\text{ }^\circ\text{C}$ at various reaction durations (2 h, 4 h and 12 h). After the CBD method was carried out, the as-prepared samples were rinsed in water and ethanol before being dried in the oven. As-prepared samples were heat treated at $600\text{ }^\circ\text{C}$ for 2 h to convert $\beta\text{-FeOOH}$ to $\alpha\text{-Fe}_2\text{O}_3$. For comparison, $\alpha\text{-Fe}_2\text{O}_3$ NRs were also deposited on a bare-FTO glass substrate using the same procedure. To diffuse Sn from ATO nanobelts or the FTO layer to the

α -Fe₂O₃ NRs, the samples were further post-annealed at various temperatures.

Hydrothermal method

VO₂-ATO

Linear growth of VO₂ nanobranches were performed on the surface of the ATO nanobelts via facile hydrothermal method by using epitaxial relationship between rutile VO₂ and rutile SnO₂. Typically, 4 mmol of NH₄VO₃ (99%, Sigma-Aldrich, USA) and 8 mmol of C₂H₂O₄·2H₂O (99.5%, Junsei Chemical, Japan) were diluted in 100 mL of deionized and mixed until the solution becomes transparent. Then, the clear solution was poured into Teflon vessel and the fabricated ATO nanobelts electrodes were placed horizontally in the aqueous solution. And the vessel was tightly sealed and heated at 250 °C for various reaction time from 2 h to 12 h. After hydrothermal reaction was ended, the samples were rinsed in water and ethanol carefully, and dried in the oven at 50 °C for 1 h.

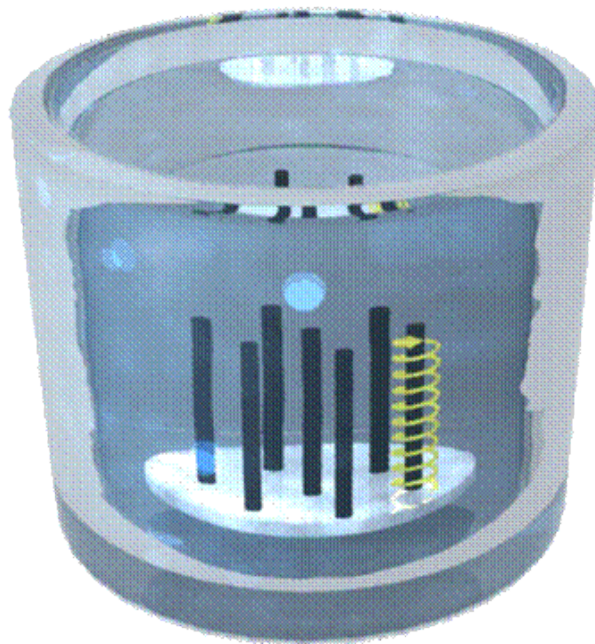


Figure 3.2. Schematic view of chemical bath deposition method

3.3 Fabrication of PEC cell and Li ion battery

Photoelectrochemical cells

The PEC performances were measured in a three-electrode setup consisting of a photoelectrode as a working electrode (sample area was fixed to be 0.28 cm² by circular mask with diameter of 6 mm), Pt wire as a counter electrode and an Ag/AgCl (saturated KCl) electrode as the reference electrode. In case of metal oxide electrodes, a 1 M NaOH (pH 13.2) solution was utilized as electrolyte. In case of quantum dot sensitized electrodes, the electrolyte was an aqueous solution of 0.25 M of Na₂S and 0.35 M of Na₂SO₃ (pH 13). The potentials versus Ag/AgCl were converted to the reversible hydrogen electrode (RHE) scale in accordance with the Nernst equation. ($E_{\text{RHE}} = E_{\text{Ag/AgCl}} + 0.0592\text{pH} + E^{\circ}_{\text{Ag/AgCl}}$) A solar simulator (HAL-320, Asahi spectra) was used to simulate the AM 1.5G spectrum and illumination intensity in a wavelength range of 350 to 1100 nm of 72 mW/cm² (1SUN) was utilized.

To prepare the quantum-dot (CdS) sensitized electrodes, constant current electrodeposition was performed. Electrolyte containing the 0.2 M of Cd(NO₃)₂ and thiourea in a dimethyl sulphoxide (DMSO) and water at a volume ratio of 1:1 was heated in 363 K water. After 8 min of electrodeposition at a constant current of 1.0 mA/cm², the electrodes were taken out and rinsed with deionized water and ethanol successively. The

conventional successive ionic layer adsorption and reaction (SILAR) process [189] was also attempted.

Li ion battery

To evaluate the electrochemical properties of nanostructured electrodes, as-prepared samples on Ti foil were directly used in a working electrode of a half-cell without conductive additives or cohesive binders. Each electrode is about 10 mm in diameter, and their active mass was measured precisely by a microbalance (0.1 μg , model UMT5, Mettler Toledo, Greifensee, Swiss). The average active masses of the ATO were evaluated to be $\sim 360 \mu\text{g}$. The electrochemical performances of the prepared electrodes were evaluated using Swagelok-type halfcells, which were assembled using the prepared electrode as the working electrode, Li metal foil as the counter electrode, a separator film (Celgard 2400(PP), Celgard, Charlotte, NC), and a liquid electrolyte (EC:DMC 1:1 by volume with 1.0 M LiPF₆, Techno Semichem Co., Ltd., Seongnam, South Korea). In this thesis, TiO₂-ATO and VO₂-ATO electrodes were used as an anode and cathode for Li-ion batteries, respectively.

3.4 Characterization

Materials characteristics

The morphology of the synthesized 3-D nanostructures was observed by a field-emission scanning electron microscope (FESEM) (JSM-6330F, JEOL, Tokyo, Japan) and high-resolution transmission electron microscopy (HRTEM) (JEM-3000F, JEOL, Tokyo, Japan). The crystalline structure and phase of 1-D and 3-D nanostructures were studied by X-ray diffraction (XRD) (D8-Advance, Bruker Miller, Karlsruhe, Germany) and with a Raman spectrometer (Raman) (inVia Raman microscope, Renishaw, Wotton-under-Edge, UK). An electron probe X-ray micro analyzer (EPMA) (JXA-8900R, JEOL, Tokyo, Japan) was used to measure the ratio between Sb and Sn in ATO nanobelts. X-ray photoelectron spectroscopy (XPS) spectra were collected using an ESCA spectrometer (Al K α X-ray source, Sigma Probe). The energy dispersion Spectroscopy (EDS) elemental mapping was used to observe the distribution of elements on the nanostructure.

The optical absorption properties were measured with an integrating sphere using a UV-vis-NIR spectrophotometer (Cary 5000). To compare the surface area of electrodes, electrodes were soaked into N719 dye aqueous solution at 50 °C. The adsorbed amounts of N719 dye were evaluated by measuring the UV-vis spectra of desorbed dye solution from samples. The pH of the solution was measured using a pH meter (Blueline 14 pH, Schott Instruments, Mainz, Germany).

To fabricate the device consisting of individual nanobelts/nanostructures, photolithography was used to define patterns of metal electrodes on an n-type silicon substrate capped with a 50 nm SiO₂ layer, followed by metal deposition of Ti/Pt/Ti (10 nm/50 nm/10 nm) by RF magnetron sputtering. ATO nanobelts/nanostructures were removed from the substrate and were deposited onto the fabricated device. The current–voltage (I – V) characteristics of an individual ATO nanobelt device were measured in two-probe configurations.

Electrochemical characteristics

Photocurrent-potential curves were measured under illumination on a potentiostat at a scan rate of 10 mV s⁻¹. For chopped J-V curves, both the darkcurrent and photocurrent were recorded using a shutter during a single scan. Photocurrent stability analysis was carried out by evaluating the photocurrent at a specific bias under chopped light irradiation. The IPCE was measured using a 1000 W Xe lamp and a monochromator (Oriel Cornerstone 130 1/8 m) at 1.0 V vs. RHE (0 V vs. Ag/AgCl). The electrochemical impedance spectroscopy (EIS) measurements were conducted in the dark to evaluate the electrical properties of the synthesized electrodes by Mott-Schottky plots. The Nyquist plots were also obtained using an electrochemical

impedance spectra analysis with a frequency range of 10^5 Hz to 10^{-1} Hz under irradiation. The AC signal was maintained at 5 mV and various applied bias were conducted. The amount of H₂ evolution in PEC device equipped with CdS sensitized TiO₂-ATO as working electrode was detected by gas chromatography (DS6200).

To measure the battery performance, the assembled cells were galvanostatically cycled over the proper voltage window using an automatic battery cycler (WBCS 3000, WonaTech, Seoul, Korea). Cyclic voltammetry measurements were taken in the same voltage range at a scanning rate of 0.3 mV s⁻¹. Various discharge–charge current densities were imposed on the electrode in order to investigate the rate capabilities.

Chapter 4. 1-D nanoarrays

4.1 Sb:SnO₂ (ATO) nanobelt array

4.1.1 Growth of ATO nanobelts on substrates

To synthesize the branched nanoarchitecture, ATO nanobelt backbones were first fabricated by a vapor–liquid–solid (VLS) growth method. Figure 4.1.1 show cross-sectional SEM images of ATO nanobelt arrays on a FTO/glass substrate, in which most of the nanobelts are vertically aligned with respect to the substrate. VLS mechanism was confirmed by the Au spot at the top of the ATO nanobelt (Figure 4.1.1b). ATO nanobelts were also grown on other substrates. Figure 4.1.2 shows plane and cross-sectional FESEM images of the ATO nanobelts grown on the Ti substrate. Considering that the Ti substrate was bent on account of its metallic nature when it was cut for the cross view measurement, the ATO nanobelts on the Ti substrate were almost vertical. Examination of individual nanobelts as shown in Figure 4.1.2c shows that each nanobelt is of rectangular shape with widths ranging from 50 to 150 nm. The width and length of the NB continued to increase steadily along the vertical direction from top to bottom.

The XRD pattern of ATO nanobelt (Figure 4.1.3) is consistent with the rutile SnO₂ structure, indicating that Sb atoms were effectively implanted

into the SnO₂ lattice and that there are no secondary phases. It is noteworthy that the relative intensity of the (101) peak of XRD in ATO nanobelt and undoped SnO₂ nanowire are stronger than that of the FTO substrate, revealing that they grew along the [101] direction. Moreover, the relative intensity of the (101) peak of XRD in ATO nanobelt is stronger than that of undoped SnO₂ nanowire. It suggests that incorporation of Sb into SnO₂ nanobelts promotes the (101) preferred orientation, inducing the vertical aligned growth of ATO nanobelts.

Examination of individual nanobelts using TEM (Figure 4.1.4) shows that each nanobelt is rectangular and has spots (~50 nm in diameter) at the tip of nanobelts, suggesting that the ATO nanobelts grew by means of the VLS mechanism. The width of the nanowire starts out at 30 nm and steadily increases along the length of the wire until it reaches 200 nm, with an average width of about 50 nm (Figure 4.1.4b). The SAED pattern, with a zone axis of [101], confirms that ATO nanobelts are single crystalline with a rutile SnO₂ structure. The high-resolution TEM image, taken from the marked region of Figure 4.1.4b, illustrates clear (101) lattice spacing of 0.26 nm and (200) lattice spacing of 0.24 nm, which are also consistent with the d-spacings of a rutile SnO₂ structure. According to the SAED pattern and the lattice fringes, the ATO nanobelts grew along the [101] direction.

The energy dispersion spectroscopy (EDS) elemental mapping at the top of an ATO nanobelt (Figure 4.1.5) revealed that the spot at the top of the ATO nanobelt is mostly composed of Au, clearly indicating that the ATO nanobelts were synthesized by VLS mechanism [108]. The ATO nanobelt is composed of Sn, Sb, and O, indicating that the Sb atoms were incorporated into the SnO₂ lattice. The atomic percentage of Sb incorporated into Sn sites is found to be about 3.3 at. %. This result corresponds to that of EPMA analysis. As a result of EPMA analysis, the atomic ratio of Sb:Sn was estimated to be about 3.2 at% (Table 4.1.1), indicating that Sb was degenerately doped in SnO₂ according to early reports [53]. Thus, Sb atoms were found to be well-doped into the SnO₂ lattice.

Figure 4.1.6 shows the ATO nanobelt growing along the [101] direction enclosed by (010), (0 $\bar{1}$ 0), ($\bar{1}$ 01), and (10 $\bar{1}$) perpendicular facets. This growth direction and the sides of ATO nanobelts correspond to that of SnO₂ nanowires reported previously [190]. However, in contrast to earlier SnO₂ nanowires reported, ATO nanobelts grew almost vertically, which is attributed to the excessive supply of Sb. XPS analysis of the ATO NBs on the Ti substrate shows that the Sb³⁺ and Sb⁵⁺ ions are present in the ATO nanobelts (Figure 4.1.7). It has been reported that Sb⁵⁺ ions were incorporated into the SnO₂ lattice for lower Sb atomic concentration, and

Sb^{3+} ions were located on the surface and in grain boundaries of SnO_2 layers for Sb atomic concentration higher than 10% [191]. Hence, under the higher Sb concentration, ATO nanobelts will grow with increasing surface and grain boundaries. This may be the reason that the narrow sides of ATO NBs have zigzag shapes. Xiang et al. reported that Sb^{3+} ions were more strongly detected than Sb^{5+} ions from ATO nanobelts with zigzag shape [54]. To locate more Sb^{3+} ions in the same width of the nanobelt, grain boundaries and zigzag frequency of the nanobelt should increase. Thus, many small zigzag shapes are formed on the narrow sides, inducing the nanobelt to grow vertically without curving. This result was also confirmed by the Raman spectrum (Figure 4.1.8). The band near 636 cm^{-1} is identified as the A_{1g} mode of the rutile SnO_2 [192], and the weak and broad bands near 452, 265, and 247 cm^{-1} appeared due to the doping of Sb or due to defects in the SnO_2 [193,194]. It indicates that synthesized ATO nanobelt has defective structure.

The electrical resistivity of ATO nanobelts was measured using the individual NB devices shown in the inset of Figure 4.1.9. It shows the typical current–voltage (I – V) curve of the ATO nanobelts at room temperature, and a linear dependence of current on voltage can be seen. The resistivity of the ATO nanobelt was about $9.7 \times 10^{-3}\ \Omega\text{ cm}$, corresponding to the metallic conductivity characteristic ranging from 10^{-2} to $10^{-4}\ \Omega\text{ cm}$ and

conforming to values previously reported for ATO nanowires ranging from 10^{-2} to $10^{-3} \Omega \text{ cm}$ [53,149].

Table 4.1.1. EPMA analysis of the ATO nanobelts

Sample	Element	Weight (%)	Atom (%)	Relative ratio of element to Sn
ATO nanobelt	Sn	71.5	30.8	1
	Sb	2.36	0.990	0.032
	O	21.4	68.2	2.22

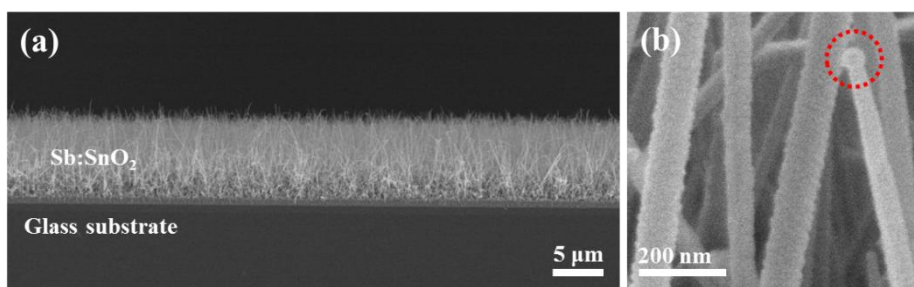


Figure 4.1.1. (a) Low and (b) high magnification of cross-sectional SEM images of the ATO nanobelts on FTO substrate

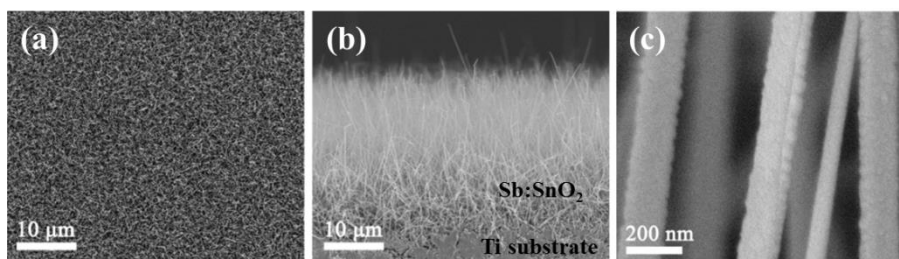


Figure 4.1.2. (a) Plane and (b) cross-sectional SEM images of the ATO nanobelts on Ti substrate, and (c) high-magnification SEM image of the middle region of the ATO nanobelts

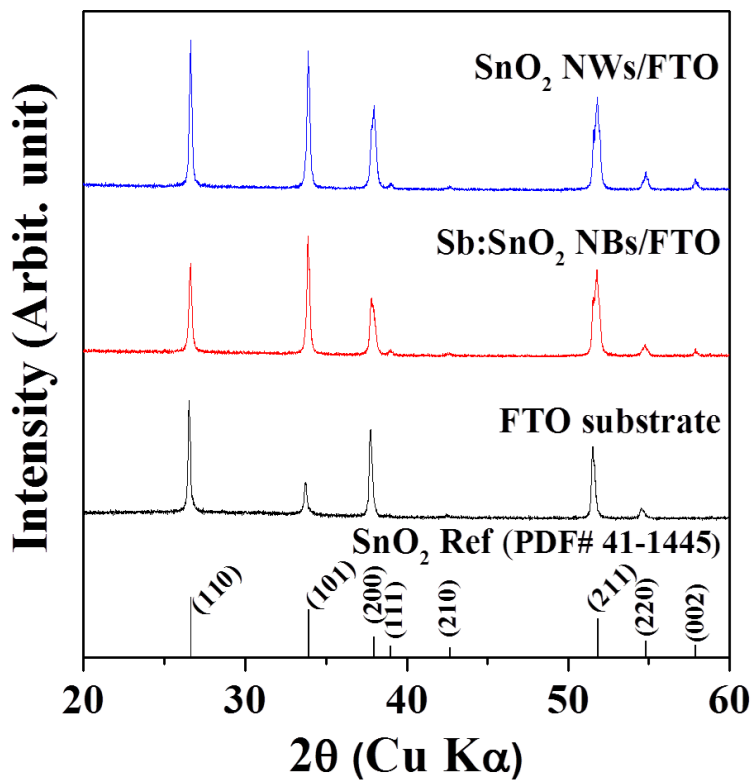


Figure 4.1.3. XRD graphs of the FTO substrate, Sb:SnO₂ nanobelts, and undoped-SnO₂ nanowires

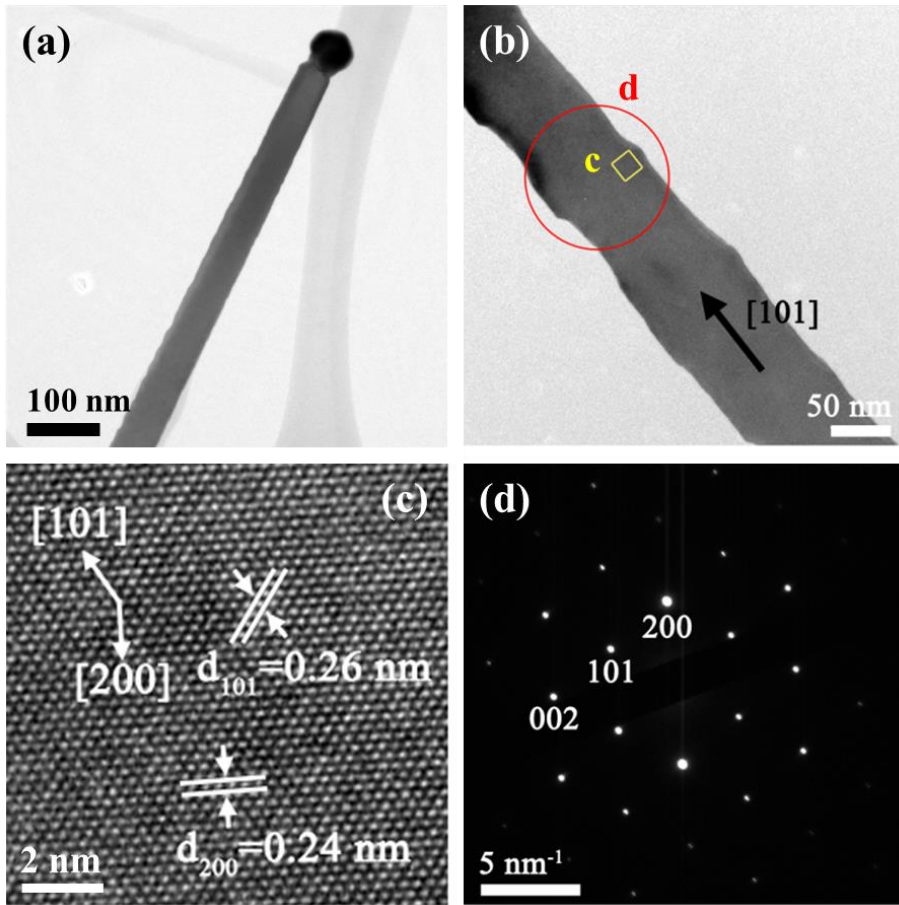


Figure 4.1.4. (a, b) TEM images of an ATO nanobelt, (c) high-resolution TEM image and (d) the corresponding SAED pattern in marked region of (b)

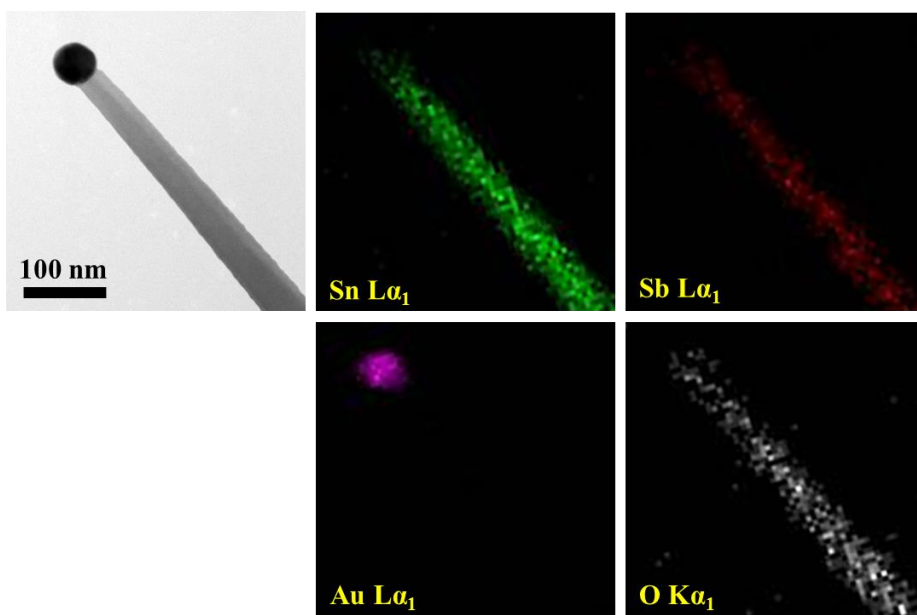


Figure 4.1.5. EDS mapping of an ATO nanobelt showing Sn, Sb, Au, and O atomic profiles

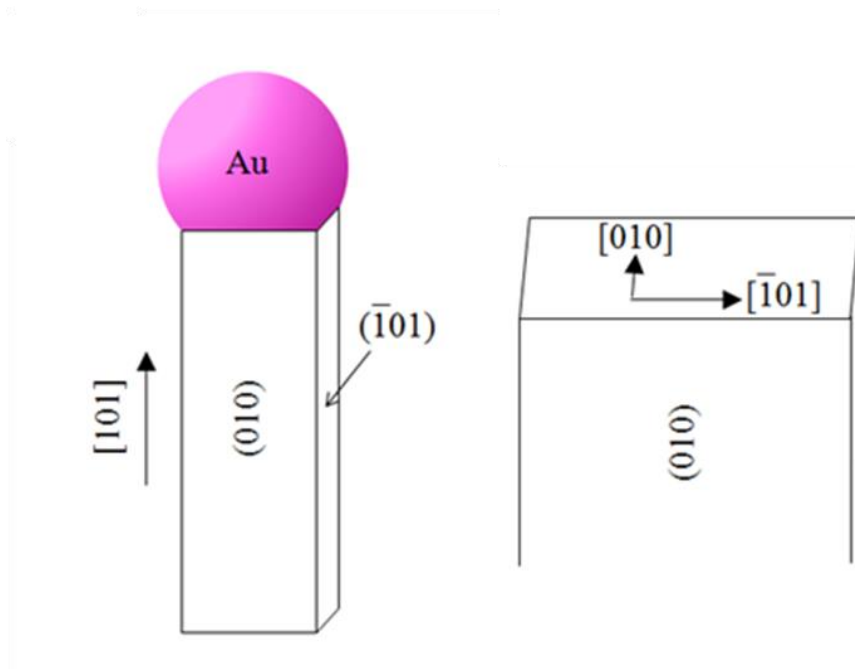


Figure 4.1.6. Schematic representations of growth mechanism: an ATO nanobelt

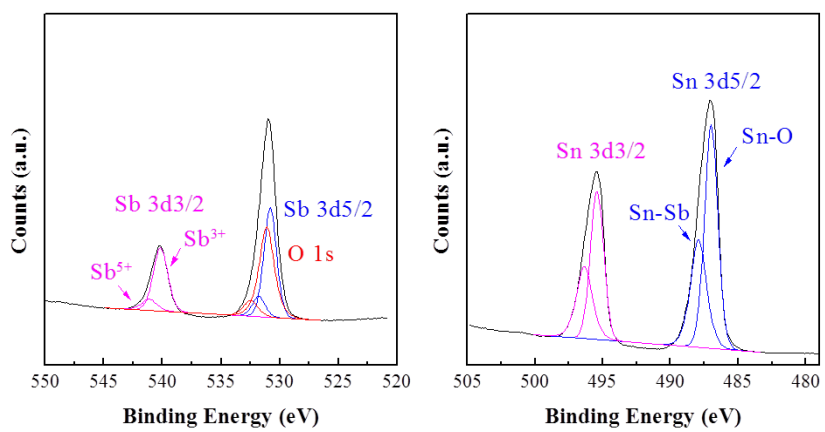


Figure 4.1.7. XPS of AT0 nanobelt arrays

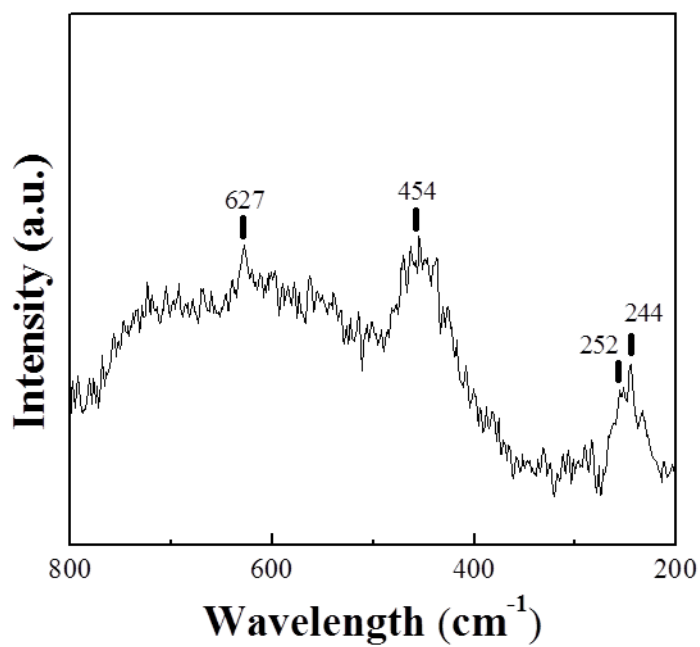


Figure 4.1.8. Raman spectra of ATO nanobelt arrays

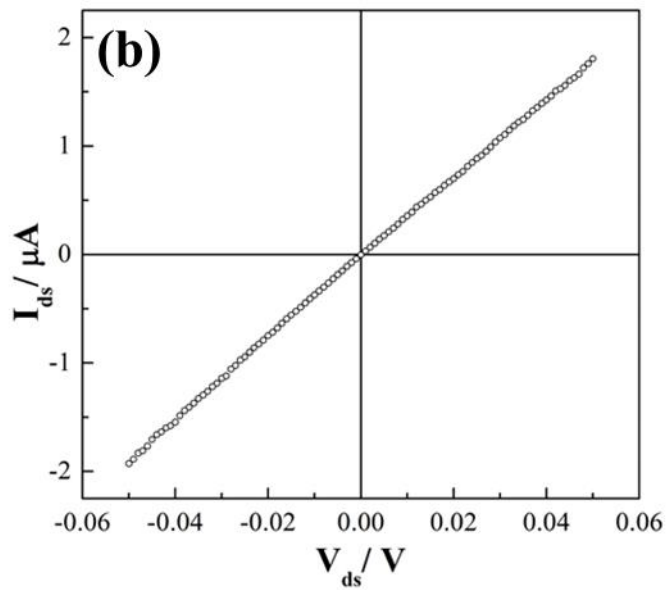
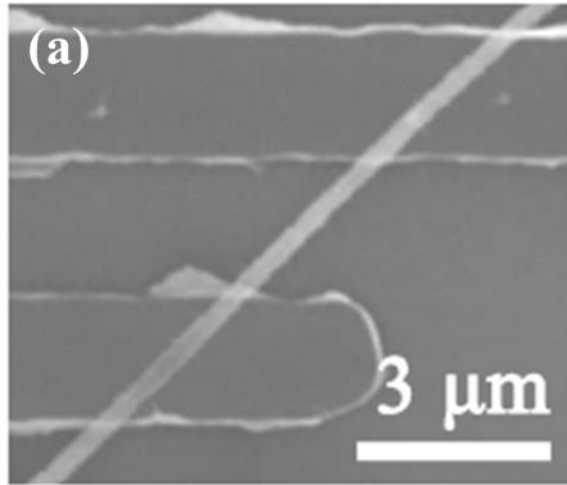


Figure 4.1.9. (a) A plane SEM image of a device fabricated for electrical transport of an ATO nanobelt and (b) typical $I_{\text{ds}}-V_{\text{ds}}$ curve of an ATO nanobelt.

Chapter 5. 3-D nanobranches

5.1 Dendritic growth I: TiO₂-ATO

5.1.1 Morphology and structure

TiO₂ nanorods were secondly synthesized on the as-prepared Sb:SnO₂ nanobelts arrays by TiCl₄ treatment. Figure 4.2.1 shows typical tilted and magnified SEM images of TiO₂-ATO nanostructures. TiO₂ nanorods with lengths of about 100 – 150 nm were uniformly grown around the ATO nanobelts in needle-leaf shapes. TiO₂ nanorods covered both the top and the middle regions of ATO nanobelts well and were more attached to the middle region because the width of the ATO nanobelts became thick toward the bottom. However, TiO₂ nanorods were rarely grown on bare Ti substrate, (Figure 4.2.2) indicating that growth of TiO₂ nanorods by chemical bath deposition is influenced by substrates.

The XRD pattern of the TiO₂-ATO nanostructures corresponded to the rutile TiO₂ and SnO₂ phase (Figure 4.2.3). Broad peaks in the XRD pattern of TiO₂-ATO nanostructures corresponded with the rutile TiO₂ phase (JCPDS no. 21-1276), and its broadness indicated that the synthetic TiO₂ was nanometer scale, coinciding with the SEM images. In the XPS analysis of TiO₂-ATO nanostructures, no signals for Sn or Sb peaks were obtained,

implying that TiO₂ nanorods thoroughly covered the ATO (Figure 4.2.4).

The morphology and crystallinity of the TiO₂-ATO nanostructures were further investigated by TEM and HRTEM images, as shown in Figure 4.2.5. ATO nanobelts were tightly enclosed by TiO₂ nanorods, which formed at an angle of 30° to the vertical direction of the ATO nanobelt sides. The length and diameter of the TiO₂ nanorods were about 130 – 160 nm and 10 – 20 nm, respectively. It was noted that TiO₂ nanorods with a uniform size could be attached to an ATO nanobelt thoroughly in spite of the simple CBD method. HRTEM lattice fringe imaging revealed TiO₂ nanorods with a d-spacing of 0.32 and 0.29 nm, corresponding to the (110) and (001) plane of rutile TiO₂, respectively, indicating that TiO₂ NRs grew along the [001] direction. These results were also verified by reduced fast Fourier transform (FFT), shown in the inset of Figure 4.2.5b. As the surface energy of the rutile TiO₂ is sequenced as $\gamma_{110} < \gamma_{100} < \gamma_{101} < \gamma_{001}$, it has frequently been reported that TiO₂ nanorods grow along the [001] direction to reduce the surface energy [188]. EDS line scan and elemental mapping (Figure 4.2.6) show that Sn and Sb atoms were located on the ATO nanobelt, and Ti atoms were located on the TiO₂ nanorods, implying that there was no diffusion of Sn or Sb atoms into the TiO₂ nanorods during synthesis. This was also supported by XPS analysis as mentioned above.

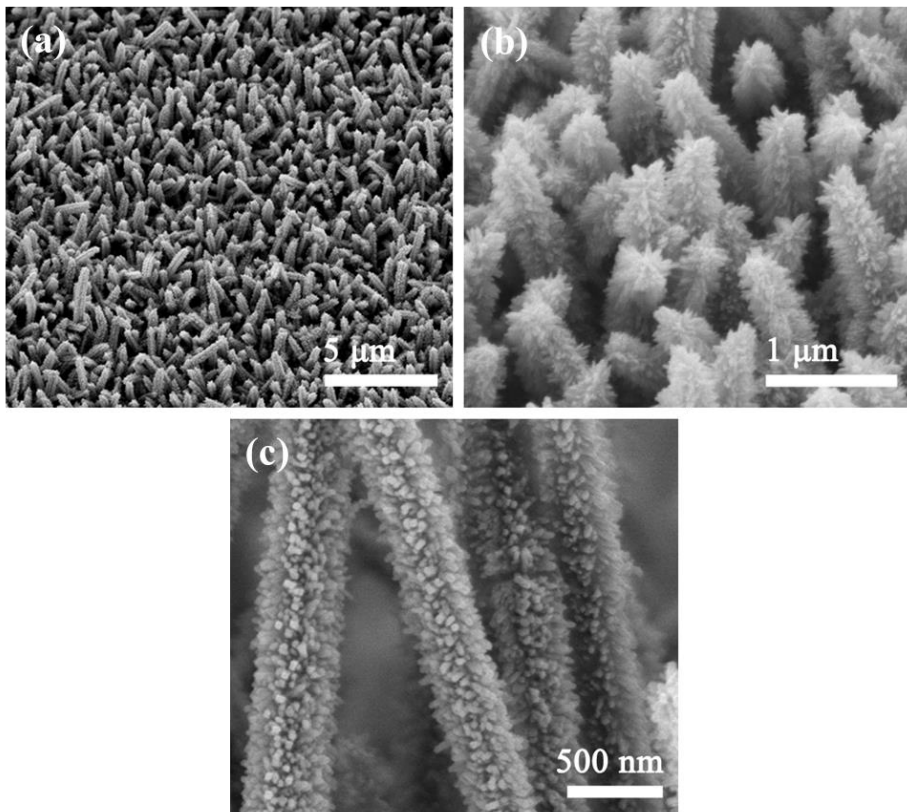


Figure 5.1.1. (a) A tilted SEM image of TiO₂-ATO arrays. High magnification SEM images of (b) the top regions and (c) the middle regions of the TiO₂-ATO arrays.

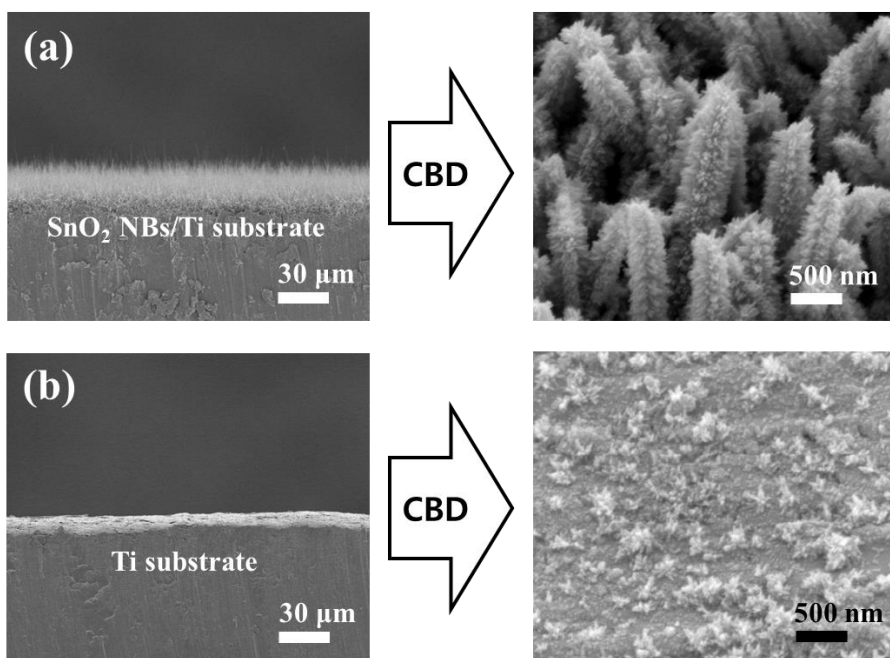


Figure 5.1.2. SEM images of TiO₂ nanorods in CBD (a) with and (b) without the ATO nanobelts substrates.

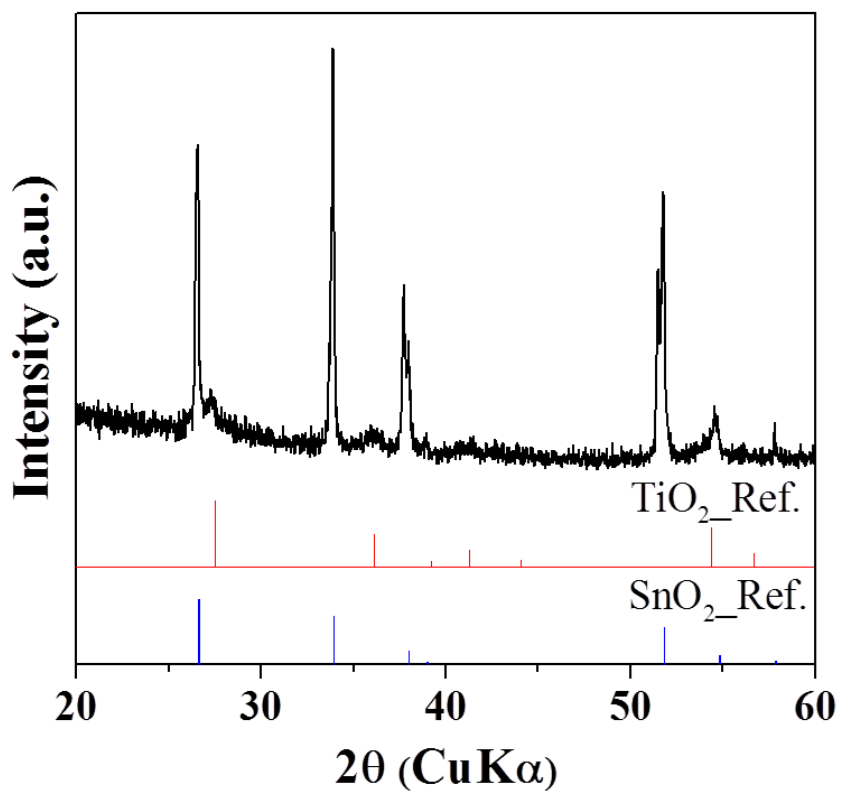


Figure 5.1.3. A XRD graph of the TiO₂-ATO arrays

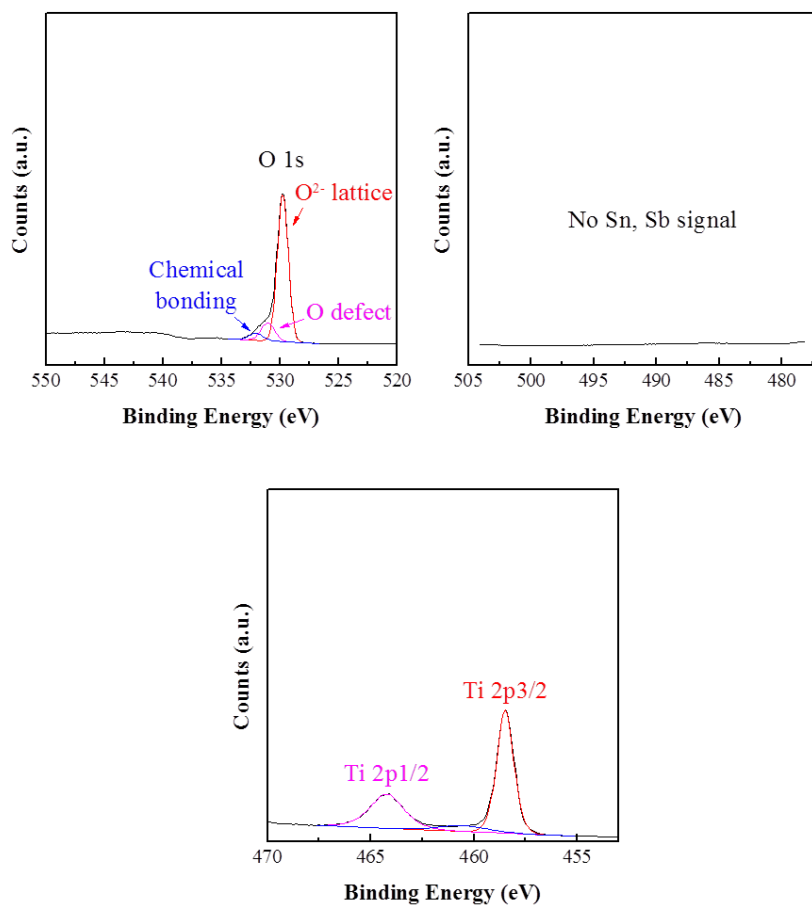


Figure 5.1.4. XPS of TiO₂-ATO arrays

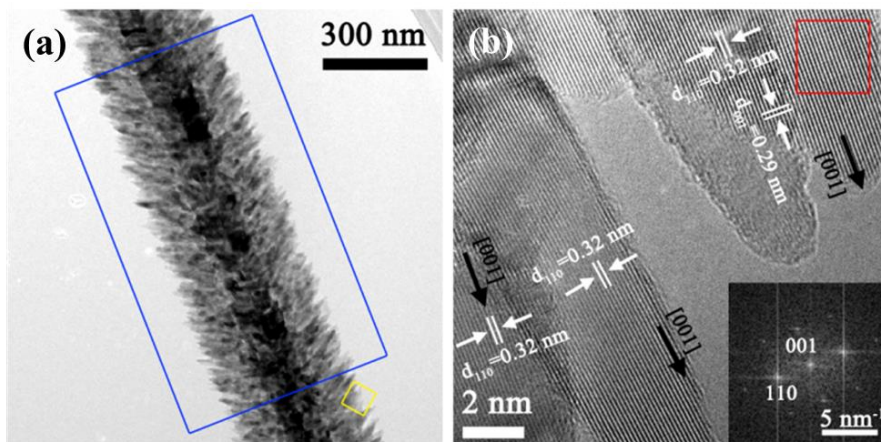


Figure 5.1.5. (a) A TEM image of a TiO₂-ATO and (b) the HRTEM image of the small marked region in (a), inset shows reduced FFT for selected area of the TiO₂ nanorod.

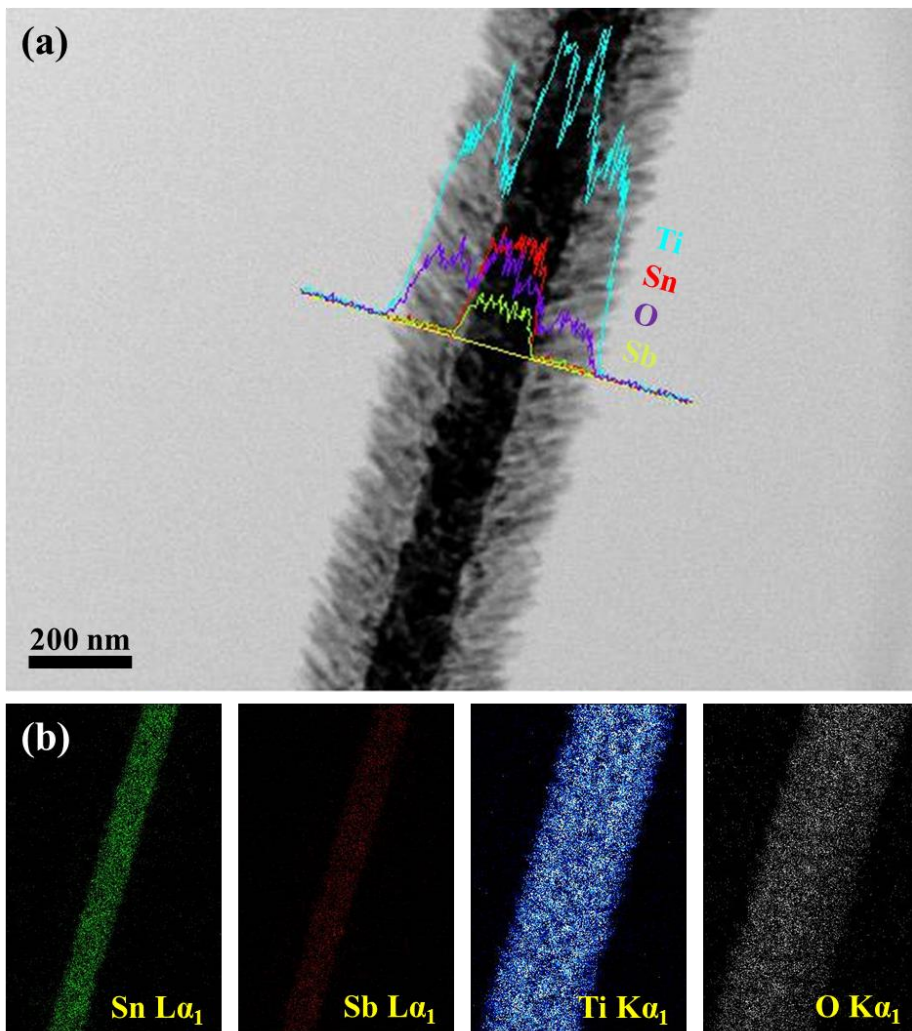


Figure 5.1.6. EDS analysis of a TiO₂-ATO: (a) line-scan and (b) elemental mapping.

5.1.2 Formation mechanism

The dependence of pH

Cheng et al reported that decreasing the pH and concentration of the TiCl_4 aqueous solution favors the formation of rutile TiO_2 while increasing the pH of the solution favors the formation of anatase TiO_2 [195]. In TiCl_4 solution, Ti(IV) complex can exist in the formula $[\text{Ti}(\text{OH})_m\text{Cl}_n]^{2-}$ ($n + m = 6$). When the pH is high, $[\text{Ti}(\text{OH})_5\text{Cl}]^{2-}$, $[\text{Ti}(\text{OH})_4\text{Cl}_2]^{2-}$, and $[\text{Ti}(\text{OH})_3\text{Cl}_3]^{2-}$ are dominant. Thus, edge-shared bonding is promoted, which could favor the formation of anatase. On the contrary, when the pH is low, TiCl_6 , $\text{Ti}(\text{OH})\text{Cl}_5$, $\text{Ti}(\text{OH})_2\text{Cl}_4$ are dominant, which could suppress edge-shared bonding and induce corner-shared bonding, which is beneficial to the formation of rutile. When the TiCl_4 solution was exchanged every 8 hours to maintain its pH at a high level (~ 1.05), anatase nanoparticles were synthesized on ATO nanobelts (Figure 4.2.7a). When the TiCl_4 solution was not renewed during the reaction, resulting in a significant pH drop as shown in Figure 4.2.7b, rutile nanorods were synthesized on ATO nanobelt. Thus, spherical TiO_2 anatase nanoparticles (hereafter, AS) which cover ATO nanobelt as a shell were formed by exchanging the TiCl_4 solution (Figure 4.2.7c), while needle-shaped TiO_2 rutile nanorods (hereafter, RR) were formed by keeping the TiCl_4 solution (Figure 4.2.7d).

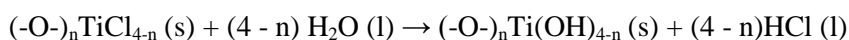
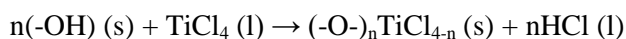
The formation of the spherical TiO₂ nanoparticles-based nanoshell on the ATO nanobelt was analyzed by TEM (Figure 4.2.8). Hereafter, AS samples reacted for X hours are denoted as ASX. The thickness of the TiO₂ shell layer increased with the reaction time, i.e. with repeating the exchange of the TiCl₄ solution. The shell layer thickness increased from 10 nm at AS24 to 70 nm at AS144. The spherical TiO₂ particles of about 3-15 nm in diameter were uniformly attached to the nanowire along its entire length. The ASs exhibited diffuse ring patterns, implying a weak crystallinity. The 1st, 2nd and 3rd ring patterns of AS144 correspond with anatase (101), (004) and (200) respectively. SEM was used to observe the formation of the TiO₂ rods on the ATO nanobelts. As shown in Figure 4.2.9, needle-shaped TiO₂ rods attached to the nanowire. Hereafter, RR samples reacted for X hours are denoted as RRX. Throughout the RR process, the density and length of the TiO₂ rods on nanowires increased steadily. The length of the TiO₂ rods increased from 35 nm at RR24 to 130 nm at RR144.

Figure 4.2.10 shows XRD patterns of the samples (AS144 and RR144) before and after the post-annealing at 450 °C. A broad amorphous-like peak near 25 degrees is observed in the as-prepared AS144. After annealing, a polycrystalline anatase phase was detected via XRD. In the as-prepared RR144, very low TiO₂ rutile peaks are observed, and after annealing, the

intensity of the rutile peak increased. Thus, the crystallinity of the ASs and RRs was enhanced by post-annealing.

The interfaces of the TiO₂-ATO nanostructure were analyzed using TEM. Figure 4.2.11 shows the interface of AS-ATO. The fringe spacing of the TiO₂ particles is estimated to be 0.353 nm, corresponding to the (101) lattice spacing of anatase TiO₂. The interface of TiO₂ rod and ATO nanobelt (RR48-450) demonstrates that the TiO₂ rod grew epitaxially on the nanobelt. The lattice spacing of 0.298 nm in the longitudinal direction corresponds to the *d*-spacing of the rutile (001) crystal planes, indicating that the rod was grown along the [001] direction. It is reported that rutile has a screw structure along the *c*-axis, which accelerates the crystal growth along that axis [196]. Epitaxial relationship between TiO₂ and ATO was discussed details in chapter 4.2.3.

The growth mechanism of the pH dependent formation of TiO₂ anatase and rutile nanostructures is briefly summarized in Figure 4.2.12. The reaction of TiCl₄ with the surface hydroxyl groups can be described as follows [197]:



where (*s*) denotes “surface”. As shown in the reaction, the pH of the solution decreases as the reaction time increases due to the formation of acid. The

crystalline structure of TiO_2 was determined from the difference between the chemical potentials of each TiO_2 phase, depending on the pH value [198]. In a TiCl_4 solution, the formation of rutile favors a lower pH, while the formation of anatase favors a higher pH [195]. Moreover, because the condensation reaction of the Ti(IV) complex occurs at room temperature, it is not enough to fully crystallize the TiO_2 nanoparticles using the CBD method. Therefore, in the AS process, weakly crystallized anatase TiO_2 is formed on the surface of the nanowire, and then the TiO_2 nanoparticles in the nanoshells aggregate each other during the post-annealing process. In the RR process, on the other hand, rutile TiO_2 is formed after 8 hours owing to the decrease of pH with the reaction time. And owing to the similar (100) lattice parameters between TiO_2 rutile and ATO, rutile TiO_2 grows along the [001] direction in the form of rods to minimize the lattice mismatch [199].

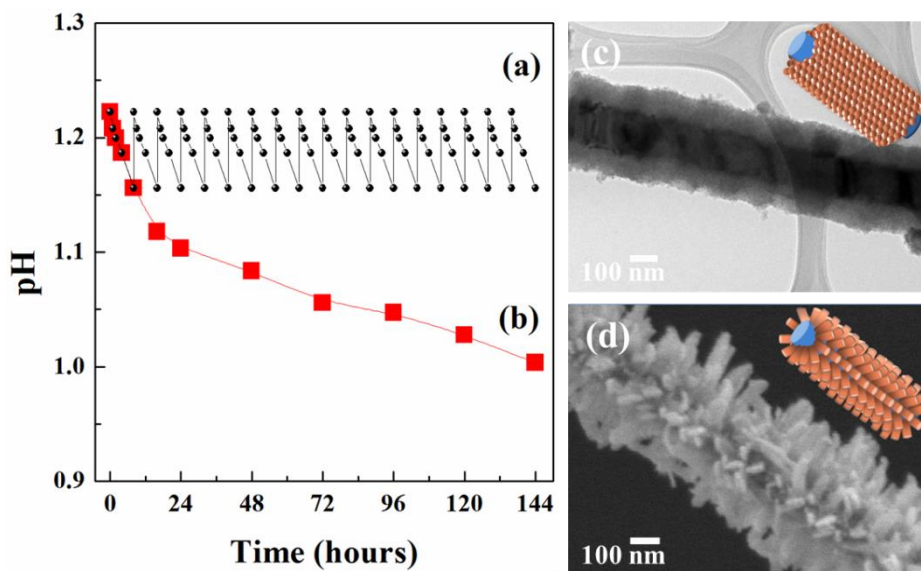


Figure 5.1.7. As a function of reaction time, equilibrium pH of (a) the TiCl₄ exchanged every 8 hours (●) and (b) the TiCl₄ maintained during reaction (■). (c) Schematic diagrams and TEM image of the ATO nanowire covered with TiO₂ nano shell-like structure through (a) process. (d) Schematic diagrams and FESEM image of the ATO nanowire covered with TiO₂ nano needle leaf-like structure through (b) process.

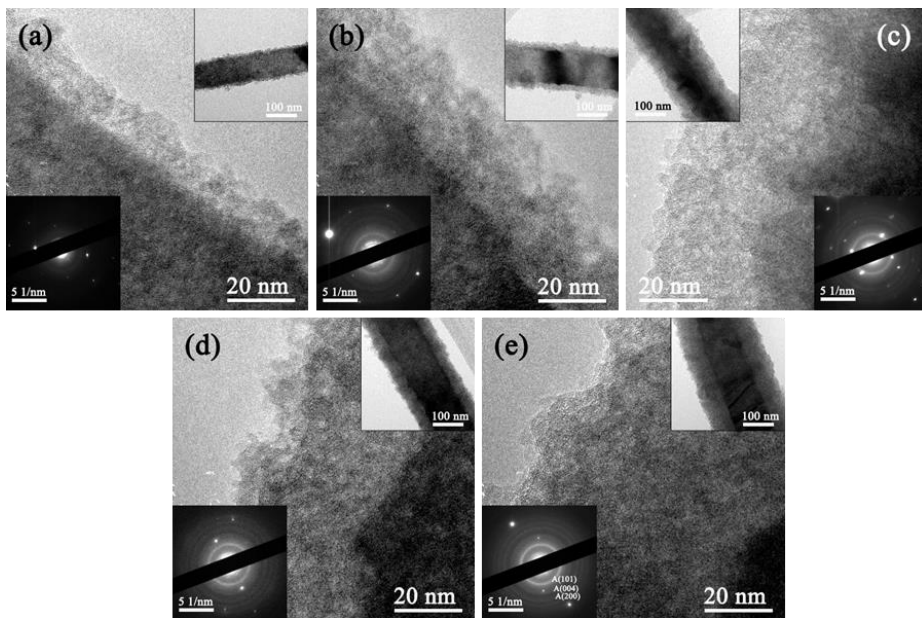


Figure 5.1.8. TEM images ATO nanowire covered with TiO_2 nano shell-like structure by TiCl_4 treatment in (a) 24 hours, (b) 48 hours, (c) 72 hours, (d) 96 hours and (e) 144 hours. Each inset shows the SAED pattern and low magnification of nano shell.

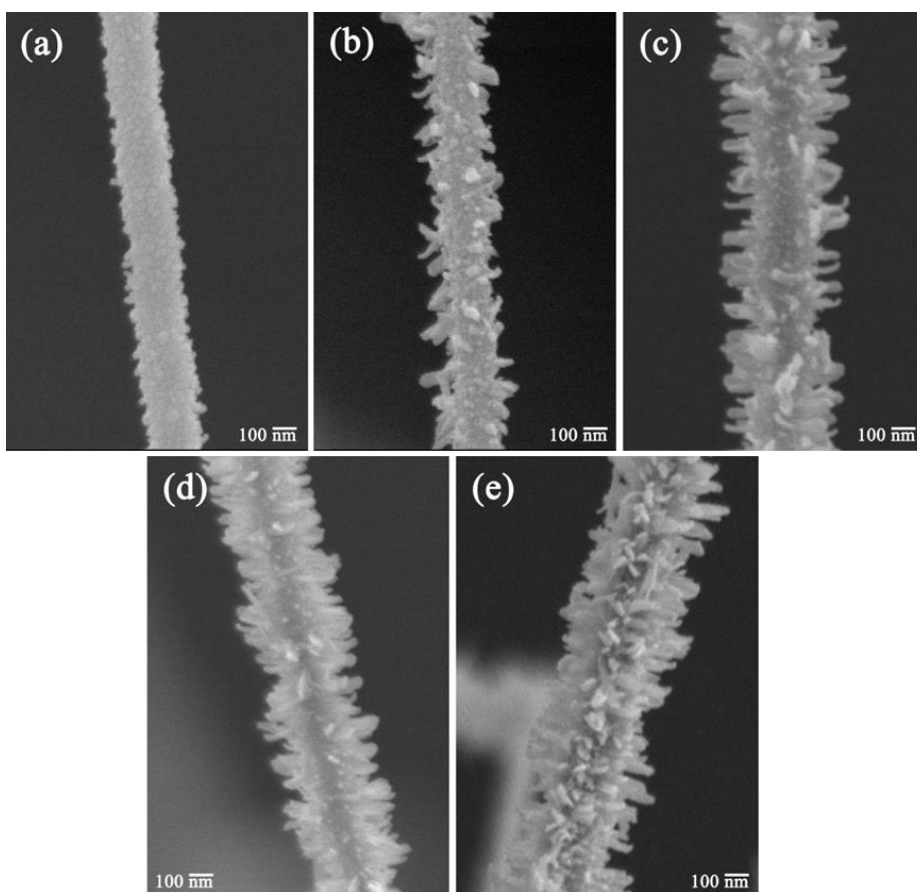


Figure 5.1.9. SEM images ATO nanobelt covered with TiO_2 nano needle leaf-like structure by TiCl_4 treatment in (a) 24 hours, (b) 48 hours, (c) 72 hours, (d) 96 hours and (e) 144 hours.

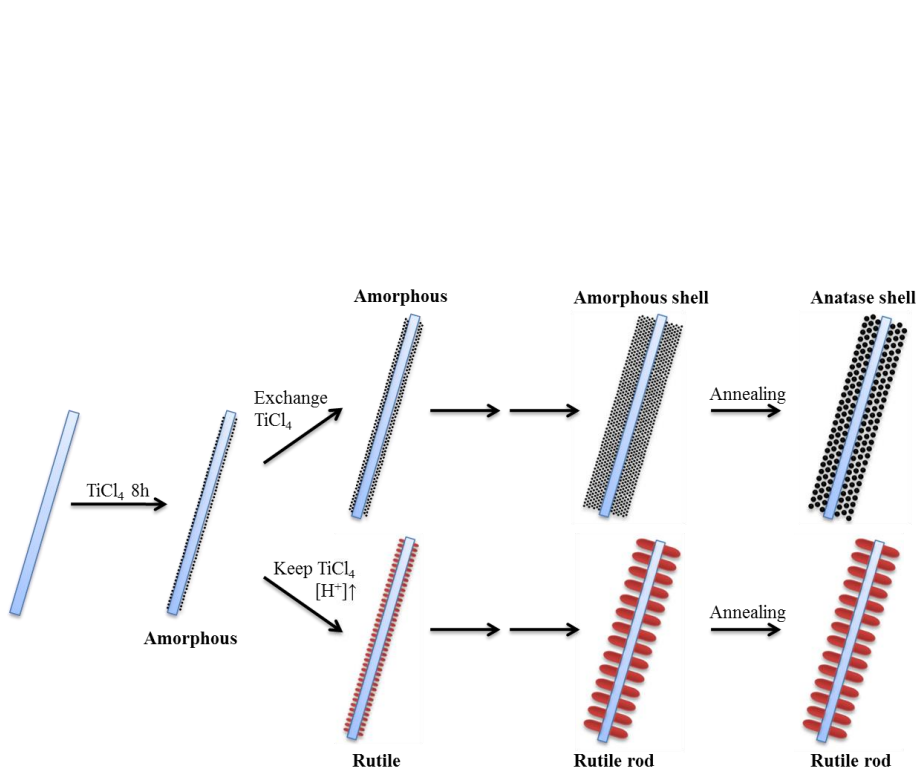


Figure 5.1.12. Schematic representation of TiO_2 anatase and rutile growth mechanism on the ATO nanobelt by CBD method

The function of acids

To investigate the function of acid, various acids, HNO₃, HCl, H₂SO₄, and HCOOH, were used for synthesis of TiO₂-ATO nanostructures, while keeping the concentration of the acids at 0.14 M. When HNO₃ was added, the products were rod-shaped after 3 h (as shown in Figure 4.2.13a), and the average size along the long- and short-axis was about 200 nm and 20 nm, respectively. For HCl, the morphology of the product was similar to with HNO₃ but its length was shorter. It was also confirmed by TEM images (Figure 4.2.14), indicating that length of TiO₂ NRs synthesized in HNO₃ (~180 nm) is longer than that in HCl (~140 nm). The Raman spectrum of HNO₃ and HCl in Figure 4.2.15 indicates that the products were pure rutile TiO₂. In addition, the peak intensity in HCl was lower than that in HNO₃ due to the shorter length of the TiO₂ rods in HCl as compared to the lengths in HNO₃. In the Raman spectrum of the rutile TiO₂, three fundamental Raman peaks at 608, 446, and 142 cm⁻¹ correspond to the A_{1g}, E_g, and B_{1g} vibration modes, respectively. The band near 240 cm⁻¹ is known as a second-order phonon [195]. For the H₂SO₄, TiO₂ nanorods rarely formed on the ATO nanobelt. This result was also confirmed by the Raman spectrum; only peaks related to Sb-doped SnO₂ appeared. The band near 636 cm⁻¹ is identified as the A_{1g} mode of the rutile SnO₂ [192], and the weak and broad bands near

452, 265, and 247 cm^{-1} appeared due to the doping of Sb or due to defects in the SnO_2 [193,194]. In the case of HCOOH, small TiO_2 nanorods were observed in the SEM image; accordingly the Raman spectra showed tiny rutile TiO_2 peaks.

It should be noted that the length of TiO_2 rods synthesized in the presence of different acids could be sequenced as $L_{\text{HNO}_3} > L_{\text{HCl}} > L_{\text{HCOOH}} \approx L_{\text{H}_2\text{SO}_4}$. Generally, a strong acid can accelerate the crystal growth, as it works as a chemical catalyst. Thus, it was clear that the addition of HCOOH had no effect on the formation of TiO_2 nanorods due to its weak acidity. In strong acids, the dependence of TiO_2 growth on the type of acid is attributed to the difference in the binding nature of anions to Ti^{4+} . It is well known that the affinity of anion ligands to coordinate follows the order of $\text{SO}_4^{2-} \gg \text{Cl}^- > \text{NO}_3^-$ [200]. In fact, in a high concentration of HNO_3 or HCl , insoluble TiO_2 species precipitated in the solution eventually as the stability of the solution decreased, consistent with a previous report [201]. Nitrate ions undergo much less complexing of Ti^{4+} compared to chloride, inducing low solubility of TiO_2 in a nitric medium [188]. In the classical theory of nucleation, the equation for the critical nucleation size for a solid–liquid system becomes [202]

$$r_{crit} = \frac{2\gamma_{sl}V_m}{\Delta\mu} \quad (1)$$

where γ_{sl} is the interfacial surface energy, V_m is the molecular volume, and $\Delta\mu$ is the chemical potential. As the solubility of TiO_2 decreases, the chemical potential of nucleation increases. Therefore, the critical nucleation size becomes smaller and the activation energy for nucleation is diminished, resulting in high nucleation rates. Therefore, both homo- and heterogeneous nucleation of TiO_2 in a solution and in ATO nanobelt, respectively, can easily occur in a nitric medium. Chloride can play the same role as nitrate ions, but its ability to facilitate the formation of TiO_2 nanorods is lower than that of nitrate ions, as the Cl^- ligand can participate in the titanium(IV) complex, $[Ti(OH)_nCl_m]^{2-}$ ($n + m = 6$), inducing relatively higher solubility in a chloride medium than in a nitric medium. Meanwhile, SO_4^{2-} exhibits higher affinity to Ti^{4+} than many other anions and the strongly chemically coordinated SO_4^{2-} inhibits the formation of the rutile phase [196,203]. Hence, when HNO_3 is added to a $TiCl_4$ solution, the nucleation and growth rate of rutile TiO_2 rods would be faster compared to when HCl , H_2SO_4 , or $HCOOH$ is used.

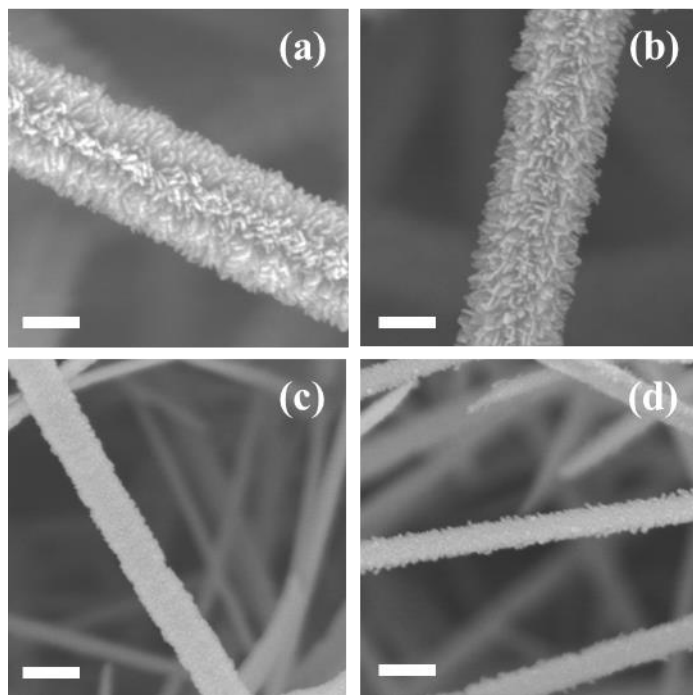


Figure 5.1.13. SEM images of nanobranches synthesized with the addition of different acids: (a) HNO₃, (b) HCl, (c) H₂SO₄, and (d) HCOOH. Scale bar, 300 nm.

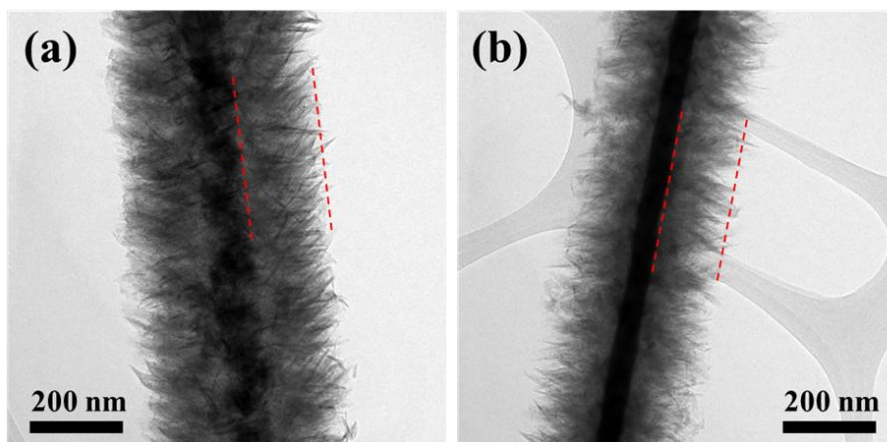


Figure 5.1.14. TEM images of TiO₂ nanobranched structures synthesized by CBD with the addition of (a) HNO₃ and (b) HCl.

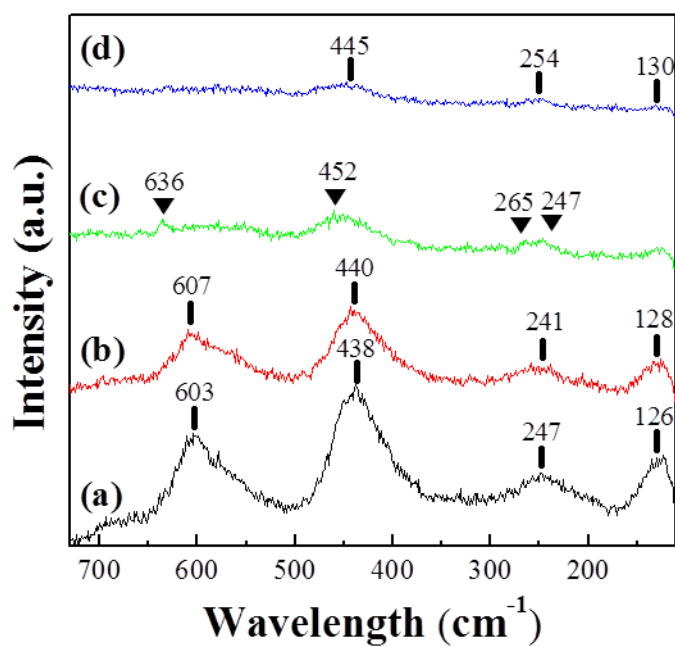


Figure 5.1.15. Raman spectra of nanobranched carbon nanotubes synthesized with the addition of different acids: (a) HNO₃, (b) HCl, (c) H₂SO₄, and (d) HCOOH.

The effect of concentration of HNO₃

Furthermore, a series of syntheses by altering the concentration of HNO₃ in a solution was performed, as summarized in Figure 4.2.16. Each synthesis lasted for 12 h for a sufficient reaction. As expected, synthesis at an extremely low concentration (0.02 M) of HNO₃ seldom produced TiO₂ nanorods on the ATO nanobelt surfaces. Under 0.3 M, as the concentration of HNO₃ in the solution increased, the length and density of the TiO₂ NRs also increased. This is yet more evidence that HNO₃ can promote the rate of nucleation and crystal growth in the current system. Meanwhile, a further increase in the concentration of HNO₃ to 0.6 M resulted in a decrease of the length of the TiO₂ nanorods, as shown in. The intensity of the TiO₂ (110) peaks in the XRD graphs also exhibited the same behavior (Figure 4.2.17). As discussed above, with 0.3M of HNO₃, the presence of H⁺ and NO₃⁻ can effectively facilitate the crystal growth and nucleation rate by working as a catalyst and lowering the solubility of TiO₂, respectively. However, when the concentration of HNO₃ is higher than 0.3 M, it was found there is another factor which affects the TiO₂ growth (to be discussed later). The dependence of the length and density of the TiO₂ nanorods on the concentration of the HNO₃ strongly suggests that HNO₃ plays a prominent

role in the synthesis of TiO₂ nanorod branching. Thus, their length and density can be controlled by HNO₃.

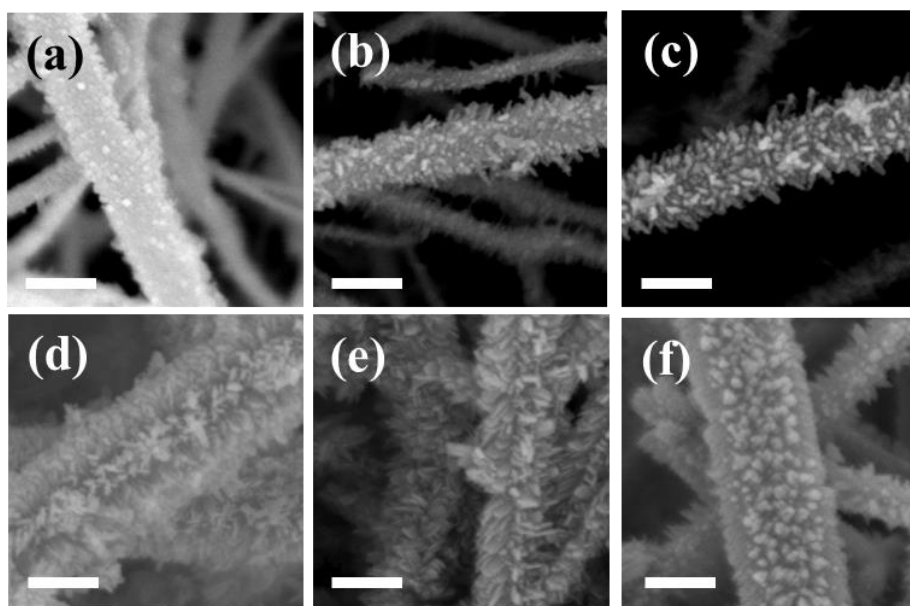


Figure 5.1.16. SEM images of nanobranched synthesized in the presence of HNO₃ at different concentrations: (a) 0.02 M, (b) 0.06 M, (c) 0.1 M, (d) 0.2 M, (e) 0.3 M, and (f) 0.6 M. Scale bar, 300 nm

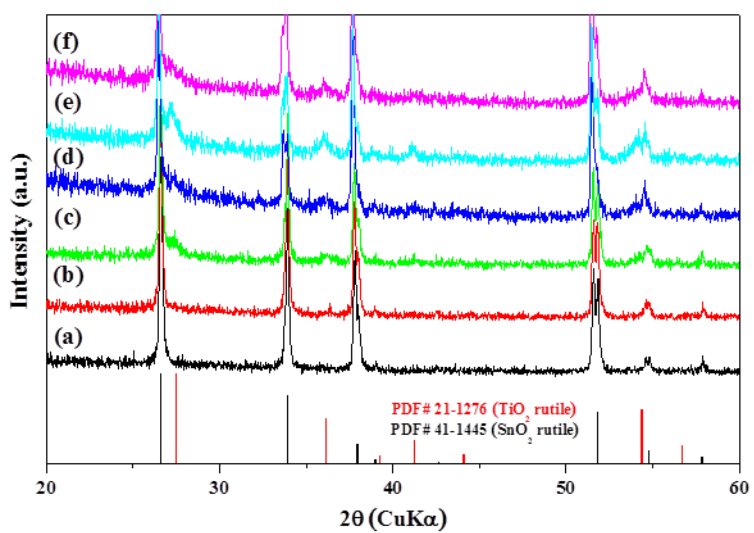


Figure 5.1.17. XRD graphs of nanobranches synthesized in the presence of HNO₃ at different concentrations: (a) 0.02 M, (b) 0.06 M, (c) 0.1 M, (d) 0.2 M, (e) 0.3 M, and (f) 0.6 M.

The effect of reaction time

To study the growth mechanism of TiO₂ nanorods on the ATO nanobelts, its formation process in TiCl₄ solution with varying reaction times was observed, as shown in Figure 4.2.18. The concentration of the HNO₃ in the solution was kept 0.2 M. It was noted that TiO₂ nanorods grew on the ATP nanobelts as reaction time increased. This was also confirmed by the increasing (110) peak intensity of the rutile TiO₂ in the XRD graphs (Figure 4.2.19). As for the ATO nanobelts deposited for 0.5 h, no TiO₂ nanorods were attached. TiO₂ particles were formed on the ATO nanobelt surfaces after 1 h and began to grow into nanorod shapes after 1.5 h. It is noteworthy that TiO₂ nanorods grew faster on the narrow side of the ATO nanobelt than on the broad side. After 2 h, TiO₂ nanorods formed on the narrow sides at an angle of 30° with vertical direction of sides. On the broad sides, however, TiO₂ nanorods formed vertically in the center and at a slope at the edge. After 2.5-3 h, TiO₂ nanorods rapidly grew, and the TiCl₄ solution became opaque. Above 3 h, growth rate of TiO₂ nanorods became low and their lengths were saturated at about 250 nm. This occurred because the TiCl₄ solution became cloudy after 2.5-3 h, suggesting that not only heterogeneous but also homogeneous nucleation reactions took place on the ATO nanobelts in the solution due to the excessive supply of Ti⁴⁺. Therefore, the

precipitated TiO₂ particles and TiO₂ nanorods on the ATO nanobelts grew competitively, inducing the depletion of the Ti⁴⁺ source in the solution. Essentially, it was observed that the TiO₂ particles or rods that precipitated in the solution were settled at the bottom and adhered to the ATO nanobelts at a time of more than 3 h. It is noteworthy that the length of the TiO₂ nanorods with a 20 nm diameter was adjustable minutely from 20 nm to 100 nm according to the reaction time when 0.2 M of HNO₃ was used. In the case of the heterostructures, the branching rods with a short length (< 100 nm) show higher activity than that with a long length (> 1 μm) [34,40,41]. Consequently, this fine tuning technique is beneficial for the synthesis of 3D hierarchical heterostructures. Moreover, because the growth rate is relatively slow during the low-temperature synthesis process, it is considered that control of the nanorod length is much easier in CBD as compared to a hydrothermal method.

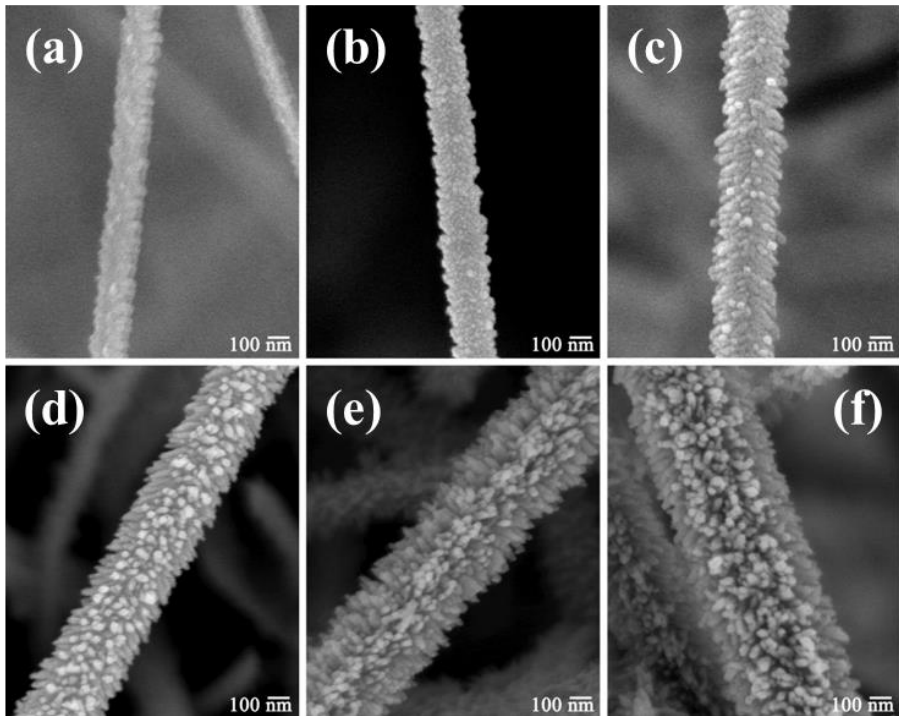


Figure 5.1.18. FESEM images of an ATO nanobelt covered with TiO_2 nanorod by TiCl_4 treatment for (a) 0.5 h, (b) 1 h, (c) 1.5 h, (d) 2 h, (e) 2.5 h, and (f) 3 h.

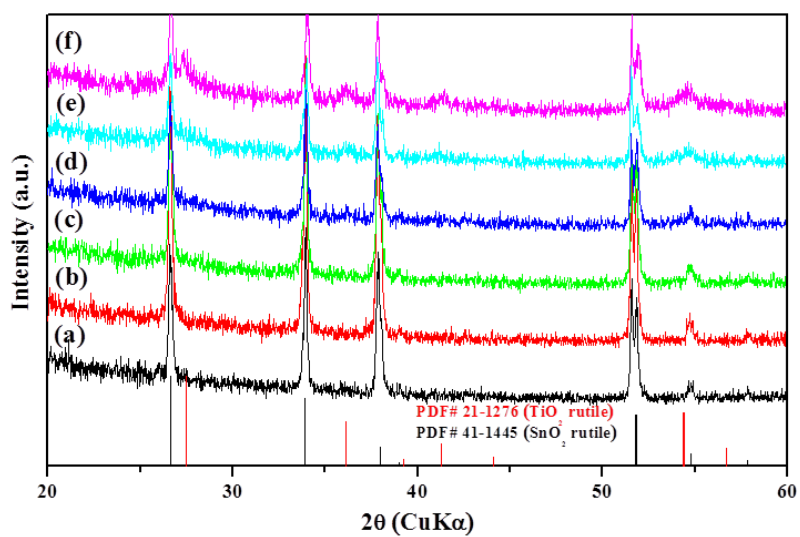


Figure 5.1.19. XRD graphs of nanobranches synthesized in the presence of 0.2 M HNO₃ along the reaction time: (a) 0.5 h, (b) 1 h, (c) 1.5 h, (d) 2 h, (e) 2.5 h, and (f) 3 h.

Length-controllable syntheses of TiO₂ nanobranched

At 0.2 M of HNO₃, TiO₂ nanorods scarcely grew longer regardless of how long they were reacted as the TiCl₄ solution became opaque after 2.5 h. This is because both the TiO₂ nanorods attached onto the ATO nanobelt and those precipitated in the solution grew simultaneously. Therefore, an alternative approach is required for synthesizing TiO₂ nanorods with a length longer than 200 nm. As mentioned above, TiO₂ nanorods were shorter with 0.6 M of HNO₃ compared to when 0.2 M was used. Additionally, it was found that the TiCl₄ solution with 0.6 M remained transparent for more than 12 h, indicating that the precipitation of TiO₂ nanorod from the solution was impeded by the concentrated HNO₃. Hence, it was expected that the TiO₂ nanorods could grow longer than 200 nm at 0.6 M with a relatively long reaction time. Figure 4.2.20 compares the morphology and shape of the TiO₂ nanorods on the ATO nanobelt formed at different HNO₃ concentration (0 to 5 M) and reaction stages (3 to 336 h), clearly showing that the growth process of TiO₂ nanorods differed above and below 0.2 M of HNO₃. It was found that as the concentration of HNO₃ in the solution increased, the nucleation rate of the TiO₂ nanorods became slow; nucleation occurred after 3 days with 2 M and did not occur even after 14 days with 5 M. Although the detailed mechanism is still under investigation, we speculate that NO₃⁻,

having a poor affinity with Ti^{4+} , could hinder and delay nucleation above 0.5 M because most acids may act as a hydrolysis inhibitor under high concentration [204]. Moreover, it was noteworthy that, above 0.5 M, the TiO_2 nanorods immediately grew to be longer than 200 nm after nucleation, whereas below 0.2 M, the length of TiO_2 nanorods became saturated after 12 h and particles that precipitated from the solution began to attach to the ATO nanobelts. This clearly demonstrates that longer growth above 0.5 M is attributed to the fact that particle precipitation from the solution was inhibited and heterogeneous growth mainly occurred. This phenomenon is well consistent with report by Zhou et al [205]. Based on these results, we believe that the length of rutile TiO_2 nanorods on the ATO nanobelts can be tuned from 20 m to 700 nm with the addition of HNO_3 at different concentrations, and this technique can be used as an alternative synthesis method for TiO_2 branching.

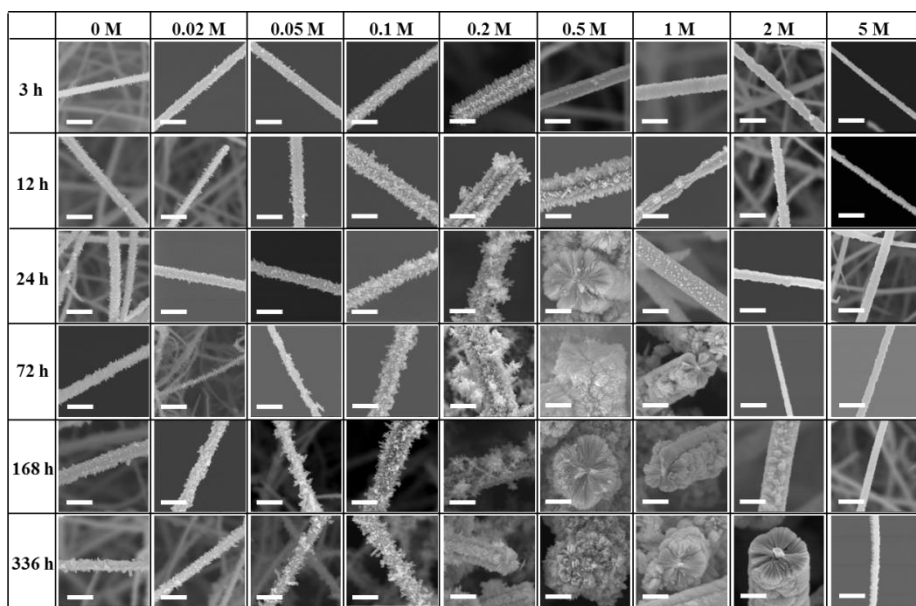


Figure 5.1.20. SEM images of nanobranched structures synthesized in the presence of HNO_3 with different concentrations and reaction time. Scale bar, 500 nm.

Formation mechanism

To investigate the effect of the HNO₃ concentration and the reaction duration on the formation of TiO₂ nanorods further, the average length of TiO₂ nanorods on ATO nanobelts in the form of the growth index was plotted against the concentration and time (Figure 4.2.21). It also confirms that growth mechanism differed above and below 0.2 M of HNO₃. It was found that the graphs for the rod length as a function of the reaction time under 0.2 M of HNO₃ (Figure 4.2.21b) were analogous to those of a diffusion-controlled growth model reported by Hyeon et al [206,207]. In their model, all of the nucleated clusters grow almost uniformly according to the rate of solute diffusion due to sufficiently high supersaturation level. Meanwhile, when the supersaturation level was low, small particles dissolved and are redeposited on larger particle by means of Ostwald ripening. Here, the low solubility of TiO₂ due to the NO₃⁻ can increase the supersaturation level and retard the dissolution of the particles. Considering that width of the TiO₂ nanorods had a fixed size of about 20 to 30 nm and that the TiO₂ nanorods mostly grew along the [001] direction, the growth rate equation of TiO₂ nanorods in the length direction can be derived as follows: [207]

$$\frac{dL}{dt} = \frac{S_r D}{L} (C_b - C_s) \quad (2)$$

Here, S_r is the surface area of the rod, D is the diffusion constant, C_b is the bulk concentration of the solution, and C_s is the concentration at the rod surface. Taking into account that the bulk concentration decreases as growth occurs, the graph for the length over time follows a sigmoidal curve [206,207], consistent with the tendency of the graphs shown in Figure 4.2.21b. Generally, when the ratio (K) between the diffusion rate (D) and the precipitation reaction rate (K_p) is much smaller than 1, the overall growth kinetics is controlled by the diffusion process [207]. Below 0.2 M of HNO_3 , the precipitation rate increases as NO_3^- ions diminish the solubility of TiO_2 , which is confirmed in that the solution became cloudy after 3 h. Consequently, the finding that TiO_2 nanorods grew short and uniform with less than 0.2 M of HNO_3 is attributed to the fact that homo- and hetero nucleation processes were generated by the high precipitation rate and that both of them grew by a diffusion-controlled growth mechanism.

Meanwhile, the precipitation rate above 0.2 M of HNO_3 decreased appreciably, which is confirmed in that the solution remained transparent even after 1 day. Because the ratio K is higher than 1 and supersaturation is low above 0.2 M of HNO_3 , the growth kinetics is controlled by the reaction rate in what is known as reaction-controlled growth [207]. This occurs because the acid with high concentration acts as a hydrolysis inhibitor,

retarding the formation of clusters for nucleation. According to thermodynamics, the correlation of the Gibbs free energy of heterogeneous nucleation with that of homogeneous nucleation is as follows:

$$\Delta G_r^{het} = \Delta G_r^{hom} S(\theta) \quad (3)$$

Because $S(\theta)$ is always lower than 1, heterogeneous nucleation should occur mainly above 0.2 M of HNO_3 . Accordingly, most formed monomers are consumed by the growth of heterogeneous nucleation rather than by the formation of homogeneous nucleation, inducing the abnormal growth of TiO_2 nanorods on the ATO nanobelt. Therefore, TiO_2 nanorods grow to about 700 nm in length, which is saturated when all of the monomer sources are depleted (Figure 4.2.21c).

On the basis of the series of above results, a possible mechanism based on nucleation and growth can be assumed for the formation of TiO_2 nanorods on ATO NB at different HNO_3 concentrations, as illustrated in Figure 4.2.22. In a TiCl_4 solution with strongly acidic media, it was reported that the Ti(IV) complex ion has the formula of $[\text{Ti}(\text{OH})_a\text{Cl}_b(\text{OH}_2)_c]^{(6-2)+}$, where $a + b + c = 6$, and a , b , and c are related to the acidity and concentration of the Cl^- ion; e.g., $[\text{Ti}(\text{OH})_2\text{Cl}(\text{OH}_2)_3]^+$ ($\beta_1=3.55$), $[\text{Ti}(\text{OH})_2\text{Cl}_2(\text{OH}_2)_2]^0$ ($\beta_2=0.4$), $[\text{Ti}(\text{OH})_2\text{Cl}_3(\text{OH}_2)]^-$ ($\beta_3=0.094$), and $[\text{Ti}(\text{OH})_2\text{Cl}_4]^{2-}$ ($\beta_4=0.083$) are sequentially formed as the concentration of Cl^- increases [195,208,209]. It

was noted that $[\text{Ti}(\text{OH})_2\text{Cl}(\text{OH}_2)_3]^+$ is dominant in highly acidic media. Therefore, it is reasonable to assume that $[\text{Ti}(\text{OH})_2\text{Cl}_4]^{2-}$, $[\text{Ti}(\text{OH})_2\text{Cl}_2(\text{OH}_2)_2]^0$, and $[\text{Ti}(\text{OH})_2\text{Cl}(\text{OH}_2)_3]^+$ predominate in a TiCl_4 solution when $\text{HNO}_3 < 5 \text{ mM}$, $5 \text{ mM} < \text{HNO}_3 < 0.2 \text{ M}$ and $\text{HNO}_3 > 0.2 \text{ M}$, respectively. When $\text{HNO}_3 < 5 \text{ mM}$, both nucleation and growth as a result of an oxolation reaction upon the elimination of HCl are slow because the Cl^- is more strongly bound than the aqua-ligands [208]. Thus, both homo- and heterogeneous nucleation occur slowly, indicating that the TiO_2 nanorods are short and barely attached to the ATO nanobelt. In the $5 \text{ mM} < \text{HNO}_3 < 0.2 \text{ M}$ case, nucleation and growth rate become fast due to the low solubility of the TiO_2 in the solution caused by HNO_3 and the oxolation reaction with the elimination of aqua-ligands. Furthermore, it was noted that the rapid precipitation of TiO_2 is facilitated by a non-electrically charged complex, $[\text{Ti}(\text{OH})_2\text{Cl}_2(\text{OH}_2)_2]^0$. Thus, both homo- and heterogeneous nucleation occur rapidly and the growth mechanism follows a diffusional-controlled growth model, inducing the uniformly short TiO_2 nanorod-branched ATO nanobelt. In the $\text{HNO}_3 > 0.2 \text{ M}$ case, the nucleation rate becomes slow because the acid with high concentration acts as a hydrolysis inhibitor and the precipitation rate becomes slow again due to the positively charged complex. As a result, heterogeneous nucleation mainly occurs and the growth

mechanism follows a reaction-controlled growth model, inducing the abnormal long TiO₂ nanorod-branched ATO nanobelt.

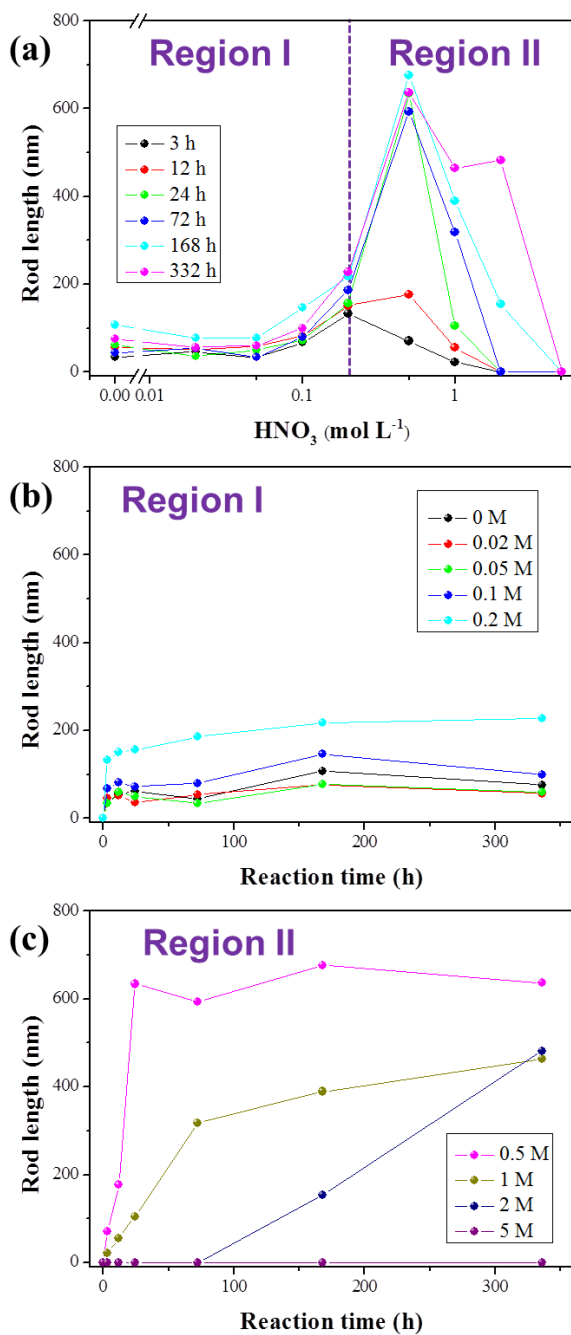


Figure 5.1.21. The dependence of average length of TiO_2 nanorods on (a) HNO_3 concentration and (b, c) reaction time.

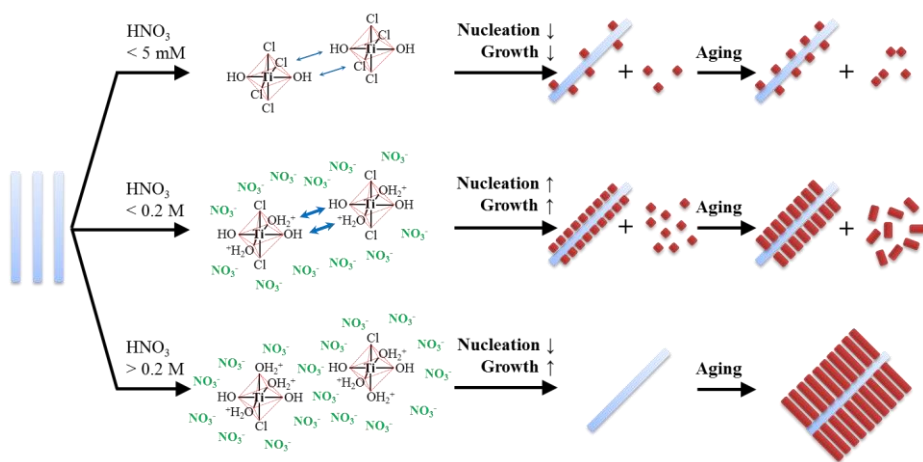


Figure 5.1.22. Schematic representations of the growth mechanism of TiO_2 nanorods on an ATO nanobelt at different HNO_3 concentrations.

5.1.3 Epitaxial relationship

To investigate the interface between TiO_2 nanorods and ATO nanobelt, the cross-sectional TEM specimen fabricated by focused ion beam (FIB) milling was observed (Figure 4.2.23). The specimen was coated with Au to protect it from the ion beam. The mass difference between the Ti, Sn and Au shows a contrast between TiO_2 (light), SnO_2 (dark) and Au (deep dark). The cross section of the ATO nanobelt had a rectangular shape with a width of 190 nm and length of 50 nm. TiO_2 nanorods with average length of about 130 nm were attached to each side of the ATO nanobelts like the spokes of a wheel. The SAED pattern of the ATO nanobelt region with [101] zone axis shows that broad and narrow sides of the ATO nanobelt belong to the {010} and {101} facets, respectively. Perpendicular to its cross section is [101], indicating that ATO nanobelt grew along the [101] direction. Figure 4.2.23c shows the SAED pattern of the TiO_2 nanorod region, of which 1st, 2nd, 3rd and 4th ring patterns have d-spacing with 0.32, 0.25, 0.23 and 0.16 nm, correspond to the (110), (101), (200) and (220) of rutile TiO_2 , respectively. It is interesting to note that the spots related to the (101) plane were strongly presented. This is attributed to two TiO_2 nanorods growing along the [001] direction. Two TiO_2 nanorods tilted to 30° from the vertical direction of the ATO (010) plane intersected in the marked region, leading to the intense

spots of (110) and (200) ring patterns. Hence, it is found that the length direction of the two TiO₂ NRs relates to [002], because [002] and [200] are perpendicular to each other in a tetragonal structure. Both (101) planes calculated from [200] and [002] of the two TiO₂ nanorods are parallel to the ATO (101) plane, causing the intense spots of (101) ring pattern.

Figure 4.2.23d-f show magnified HRTEM images of interfaces between the ATO nanobelt and TiO₂ nanorods. The lattice fringes are continuous across the interfaces between ATO and TiO₂ with good atomic registry, demonstrating the heteroepitaxial growth of rutile TiO₂ on rutile SnO₂. Figure 4d shows that the epitaxial relationship for the TiO₂ nanorods and the ATO nanobelts is TiO₂(101)||ATO(020) and TiO₂[010]||ATO[$\bar{1}$ 01]. The TiO₂ NR is found to be tilted with respect to the ATO (020) plane at an angle of about 30°, because the angle between the growth direction [001] and the normal of TiO₂ (101) is 32.8°. This result could also be interpreted in terms of the minimization of lattice mismatches [31]. Perpendicular growth of TiO₂ along [001] on the ATO (020) planes would result in a large lattice mismatch of -12.9% $\{(2.30-2.64 \text{ \AA})/2.64 \text{ \AA}\}$ between the TiO₂ (200) and ATO (101) planes. In contrast, when the TiO₂ NR grows at an angle of 30° to the normal of the ATO (020) plane, the interfacial lattice mismatch can be diminished to -0.8% $\{(2.66-2.64 \text{ \AA})/2.64 \text{ \AA}\}$, implying that the TiO₂ NR growing along the

[001] on the ATO (020) plane is inclined because of a thermodynamically stable epitaxial growth.

Figure 4.2.23e shows the interface between the TiO_2 nanorod and ATO (101) plane. The rutile (101) plane (d-spacing 0.25 nm) in the TiO_2 nanorod is found to be parallel with the (101) plane of the ATO NB (d-spacing 0.26 nm). Thus, the epitaxial relationship is $\text{TiO}_2(101)\parallel\text{ATO}(101)$ and $\text{TiO}_2[\bar{1}01]\parallel\text{ATO}[\bar{1}01]$. Interfacial lattice mismatch between the TiO_2 (200) plane and ATO (200) plane is found to be -3.0% $\{(2.30\text{-}2.37 \text{ \AA})/2.37 \text{ \AA}\}$, which is small enough to induce the epitaxial growth. Figure 4.2.23f shows another TiO_2 lattice arrangement on the ATO (020) plane and confirms the epitaxial relationship to be $\text{TiO}_2(020)\parallel\text{ATO}(020):\text{TiO}_2[\bar{1}01]\parallel\text{ATO}[\bar{1}01]$. The interfacial lattice mismatch between the TiO_2 (101) plane and ATO (101) plane is found to be -5.7% $\{(2.49\text{-}2.64 \text{ \AA})/2.64 \text{ \AA}\}$, which is 1.9 times that between the TiO_2 (200) plane and ATO (200) plane.

To understand the crystallographic epitaxial growth mechanism, a schematic representation is proposed in Figure 4.2.24. TiO_2 nanorods on the $\{\bar{1}01\}$ facets of ATO nanobelts grew at an angle of 30° with the normal of $\{\bar{1}01\}$ facets, which could be explained in the terms of tetragonal rutile structure and surface energy. A tetragonal unit cell of an ATO nanobelt was illustrated based on [101], $[\bar{1}01]$, and [010] of the ATO nanobelt in Figure

4.2.23b-A. A TiO_2 nanorod also has tetragonal structure when it grows on the $(\bar{1}01)$ plane of the ATO nanobelt, illustrated based on $[101]$ and $[010]$ on the $(\bar{1}01)$ plane of ATO nanobelt in Figure 4.2.23b-B. It is clearly observed that $[001]$ of the TiO_2 unit cell is tilted at an angle of approximately 30° to the normal of ATO $(\bar{1}01)$. The angle between $[101]$ and $[001]$ is calculated to be 32.8° from rutile TiO_2 in the literature. It is well known that most rutile TiO_2 nanorods grow along the $[001]$, because the $[001]$ nanorod has $\{110\}$ sides, which has the lowest surface energy among the rutile TiO_2 planes.

It was found that the TiO_2 nanorod grew at an angle of 30° with the normal of SnO_2 (020) plane. This result can be explained by the minimization of surface energy and lattice mismatches. Above mentioned, it was reported that TiO_2 nanorods grow along the $[001]$ direction to reduce the surface energy [188]. However, as illustrated in Figure 4.2.23c, the vertical growth of TiO_2 along $[001]$ on the SnO_2 (020) planes results in a large lattice mismatch of -12.9%. In contrast, TiO_2 NR inclined at an angle of 30° to the normal of the SnO_2 (020) plane reduces the interfacial lattice mismatch to be -0.8%.

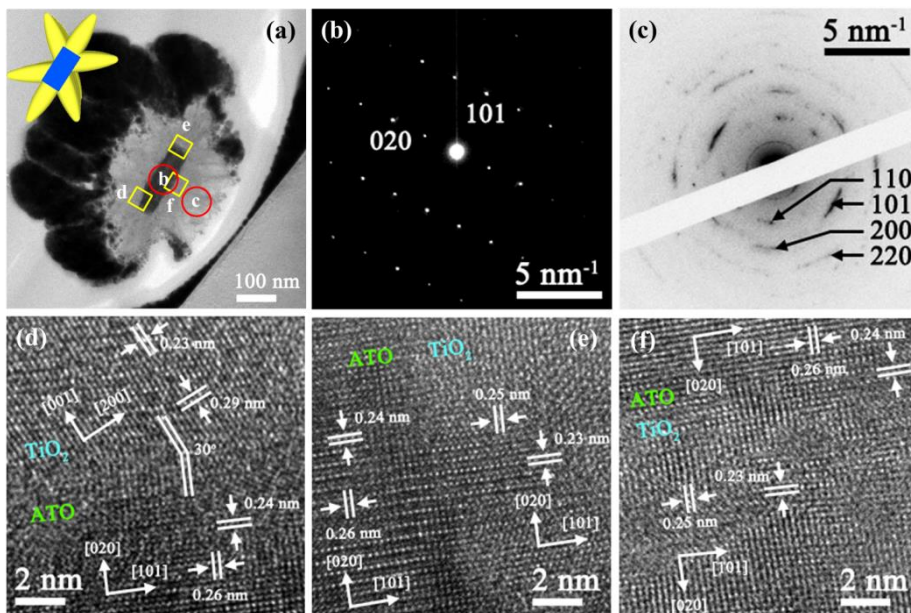


Figure 5.1.23. (a) A cross-sectional TEM image of a TiO₂-ATO. SAED patterns of (b) the ATO nanobelt region and (c) the TiO₂ nanorods region. (d-f) HRTEM images of interface between an ATO nanobelt and TiO₂ nanorods.

5.2 Dendritic growth II: Fe₂O₃–ATO

5.2.1 Morphology and structure

XRD graphs in Figure 4.3.1 reveal the crystal structure and phase purity of the three samples, which is α -Fe₂O₃ nanorods fabricated on ATO nanobelt arrays by a CBD method for 2 h, 4 h, and 12 h. All samples were further heat treated for phase-transition from FeOOH to α -Fe₂O₃. As the CBD reaction time increased, the diffraction peaks corresponding to α -Fe₂O₃ increased while that of SnO₂ decreased. Thus, it implies that the Fe₂O₃ nanorods grew on the ATO nanobelt trunk. All peaks for the three samples match well with the reference XRD patterns of the rutile SnO₂ and rhombohedral α -Fe₂O₃. No secondary peaks were detected in the XRD patterns of three products, which imply there was a successful conversion of FeOOH to α -Fe₂O₃ by the heat treatment.

Figure 4.3.2 shows the typical SEM images of Fe₂O₃–ATO nanostructures as clearly demonstrating the hierarchically branched α -Fe₂O₃ with a symmetric growth. The length of nanorods can be adjusted by varying the reaction time. The average length of the nanorods is estimated to be about 70 nm, 130 nm, and 160 nm for 2 h, 4 h, and 12 h, respectively. The diameter of the nanorods is found to be 40, 50, and 60 nm for 2 h, 4 h, and 12 h,

respectively. Also, length and density of ATO nanobelts seem to decrease as CBD reaction time increase. It is noteworthy that the Fe_2O_3 -ATO array is almost vertical even if the reaction time is over 12 h, which is beneficial to light scattering and trapping [34,40].

The crystallographic orientation of the α - Fe_2O_3 branch was investigated in detail by TEM analysis as shown in Figure 4.3.3. Figure 4.3.3a presents a TEM image of a branched Fe_2O_3 -ATO nanostructure. ATO nanobelts were tightly enclosed by α - Fe_2O_3 nanorods, which formed at an angle of approximately $40^\circ \sim 60^\circ$ to the normal of the NB sides. The SAED pattern of Fe_2O_3 -ATO shows the discontinuous ring patterns composed of spot patterns, which accurately correspond to the diffraction patterns of rhombohedral α - Fe_2O_3 single crystal (JCPDF #73-2234) at the $[\bar{1}\bar{1}1]$ zone axis. (Figure 4.3.3b) Thus, each α - Fe_2O_3 nanorod is single crystalline and well-aligned on the nanobelt surface. The magnification and high resolution (HR) image in Figure 4.3.3c&d also indicate a well-assembled α - Fe_2O_3 nanorod and its single-crystalline nature, respectively. The lattice fringes in the HR image show the 0.37 nm spacing of the (110) planes, indicating that α - Fe_2O_3 nanorods grew along the [110] direction.

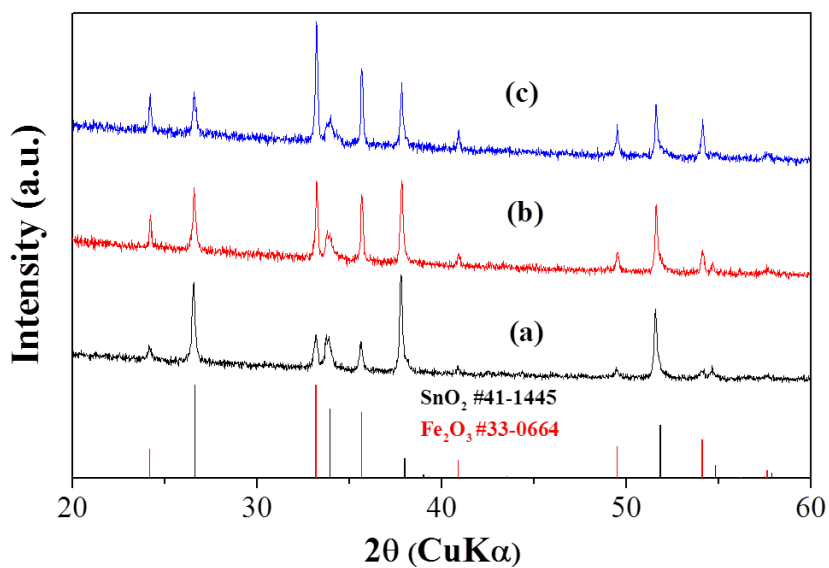


Figure 5.2.1. XRD patterns of (a-c) Fe₂O₃-ATO arrays synthesized by chemical bath deposition at different times: (a) 2 h, (b) 4 h, and (c) 12 h. The vertical lines denote the reference XRD patterns of the rutile SnO₂ (JCPDF #1-1445) and rhombohedral α -Fe₂O₃ (JCPDF #33-0664).

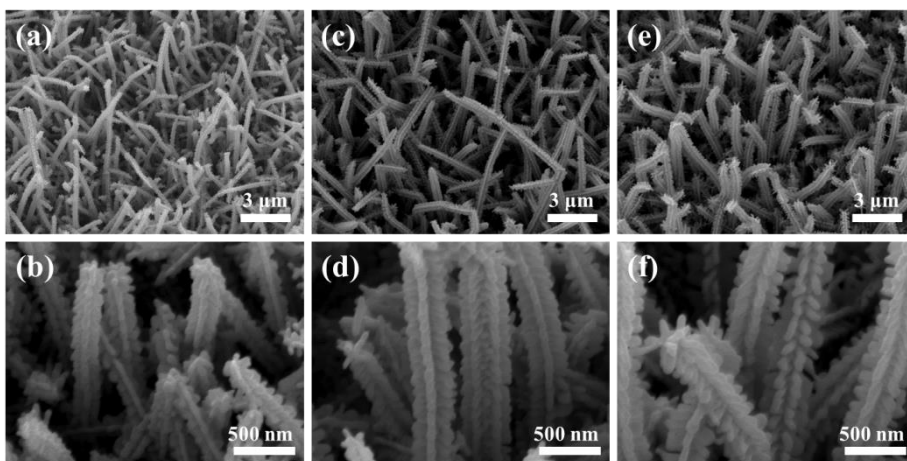


Figure 5.2.2. Low and high magnification FESEM images of Fe₂O₃-ATO arrays synthesized by chemical bath deposition at different times: (a-b) 2 h, (c-d) 4 h, and (e-f) 12 h.

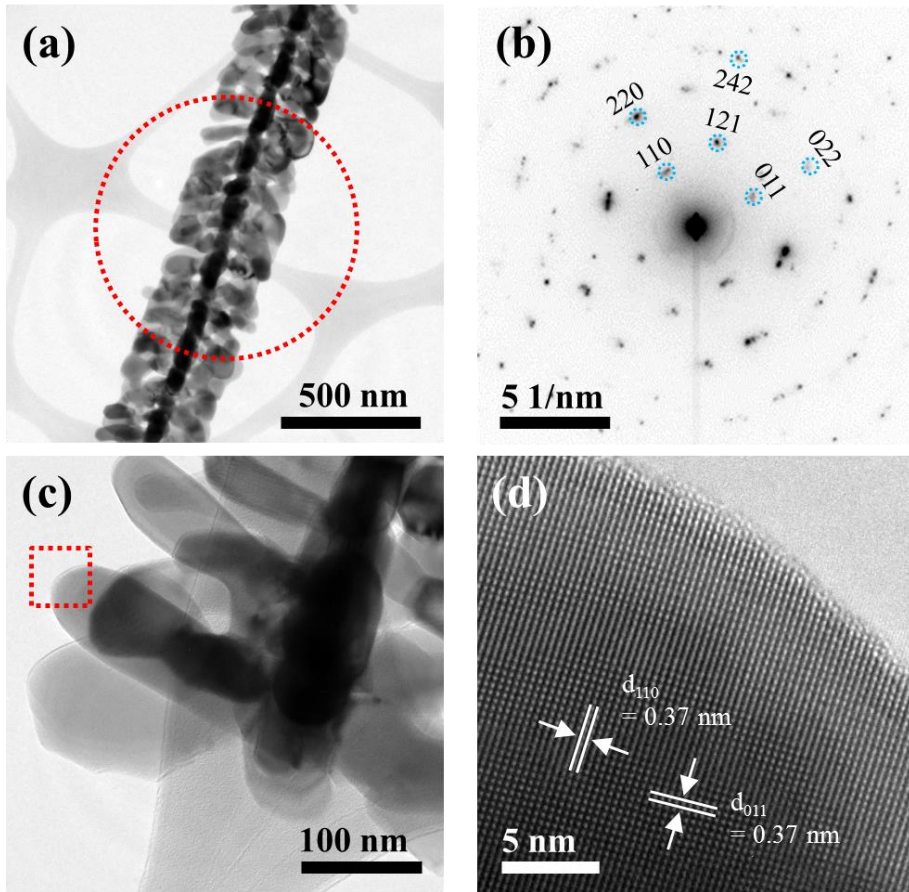


Figure 5.2.3. (a) TEM image of a Fe_2O_3 -ATO for 12 h, (b) the SAED pattern of the marked region in (a), (c) magnification of (a), and (d) the HRTEM image of the marked region in (c).

5.2.2 Epitaxial relationship

The tilted alignment of FeOOH and α -Fe₂O₃ nanorods on the ATO nanobelt can be interpreted as minimizing lattice mismatch, too. To investigate the interface between FeOOH nanorods and ATO nanobelt, the cross-sectional TEM specimen was observed (Figure 4.3.4). The specimen was coated with Au to protect it from the ion beam. The mass difference between the Fe, Sn and Au shows a contrast between FeOOH (light), SnO₂ (dark) and Au (deep dark). The cross section of the ATO nanobelt had a rectangular shape with a width of 100 nm and length of 50 nm. FeOOH nanorods with average length of about 200 nm were uniformly aligned to each side of the ATO nanobelts. Figure 4.3.4b show magnified HRTEM images of interfaces between the ATO nanobelt and FeOOH nanorods. The lattice fringes are continuous across the interfaces between ATO and FeOOH with good atomic registry, demonstrating the heteroepitaxial growth of FeOOH on rutile SnO₂. Figure 4.3.4b shows that the epitaxial relationship for the FeOOH nanorods and the ATO nanobelts is FeOOH(3 $\bar{3}$ 0)||ATO(020) and TiO₂[330]||ATO[101]. The FeOOH nanorod is found to be tilted with respect to the ATO (020) plane at an angle of about 25°, because the angle between the growth direction [1 $\bar{2}$ 0] and the normal of ATO (020) is 25°. This result could also be interpreted in terms of the minimization of lattice mismatches. Perpendicular growth of

FeOOH along $[1\bar{2}0]$ on the ATO (020) planes would result in a large lattice mismatch of -10.6% $\{(2.36-2.64 \text{ \AA})/2.64 \text{ \AA}\}$ between the FeOOH (420) and ATO (101) planes. In contrast, when the FeOOH nanorod grows at an angle of 25° to the normal of the ATO (101) plane, the interfacial lattice mismatch can be diminished to -1.5% $\{(2.60-2.64 \text{ \AA})/2.64 \text{ \AA}\}$, implying that the FeOOH nanorod on the ATO (020) plane is inclined because of a thermodynamically stable epitaxial growth.

After post annealing, similar tendency was observed in Fe_2O_3 -ATO. Figure 4.3.5 shows the cross-sectional TEM analysis of Fe_2O_3 -ATO. Because α - Fe_2O_3 nanorods and the ATO nanobelt have an interface epitaxial relationship of $(121)_{\alpha\text{-Fe}_2\text{O}_3} // (020)_{\text{SnO}_2}$, a perpendicular growth on the $\pm(020)_{\text{SnO}_2}$ planes would result in a large lattice mismatch of 12.2% $\{(2.70-2.37 \text{ \AA})/2.70 \text{ \AA}\}$ between the α - Fe_2O_3 (121) and SnO_2 (020) planes. Instead, when the α - Fe_2O_3 nanorods grow at an angle of 30° to the normal of the SnO_2 (020) plane, the lattice mismatch can be reduced to -1.1% $\{(2.70-2.73 \text{ \AA})/2.70 \text{ \AA}\}$. Therefore, α - Fe_2O_3 nanorods have to grow slantwise on the ATO nanobelt to satisfy the crystallographic criteria and thermodynamically stable epitaxial growth, inducing a self-assembled Fe_2O_3 -ATO nanostructure.

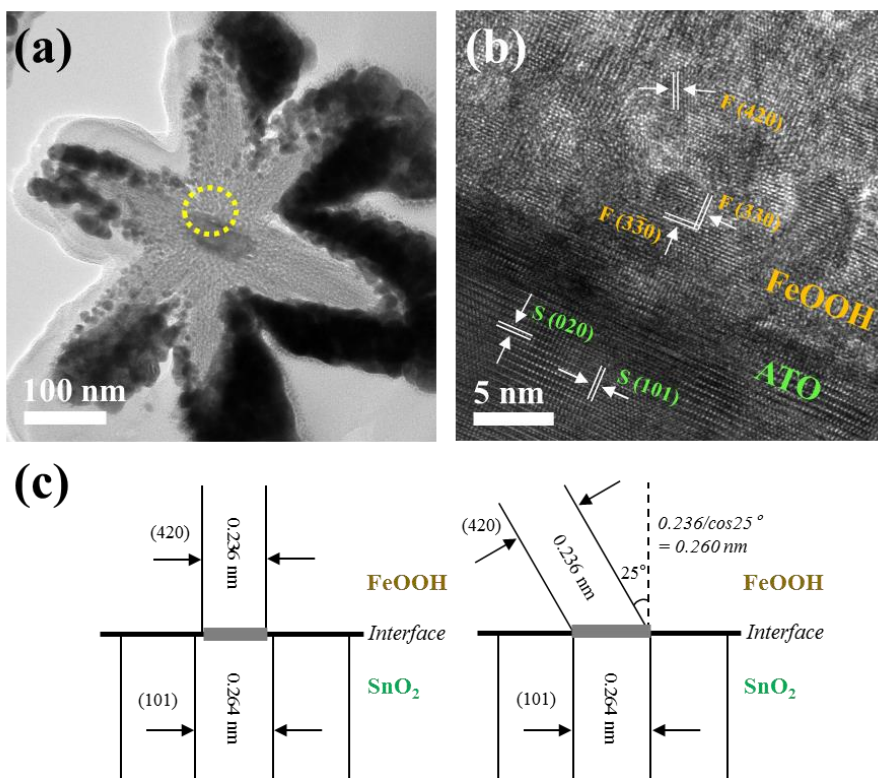


Figure 5.2.4. (a) A cross-sectional TEM image of a FeOOH–ATO; (b) HRTEM image of the marked region in (a); (c) Schematic of the interface of the (101)_{SnO₂} plane of a ATO nanobelt and the (420)_{FeOOH} plane of FeOOH nanorods, revealing the lower interfacial lattice mismatch of inclined growth compared to that of perpendicular growth.

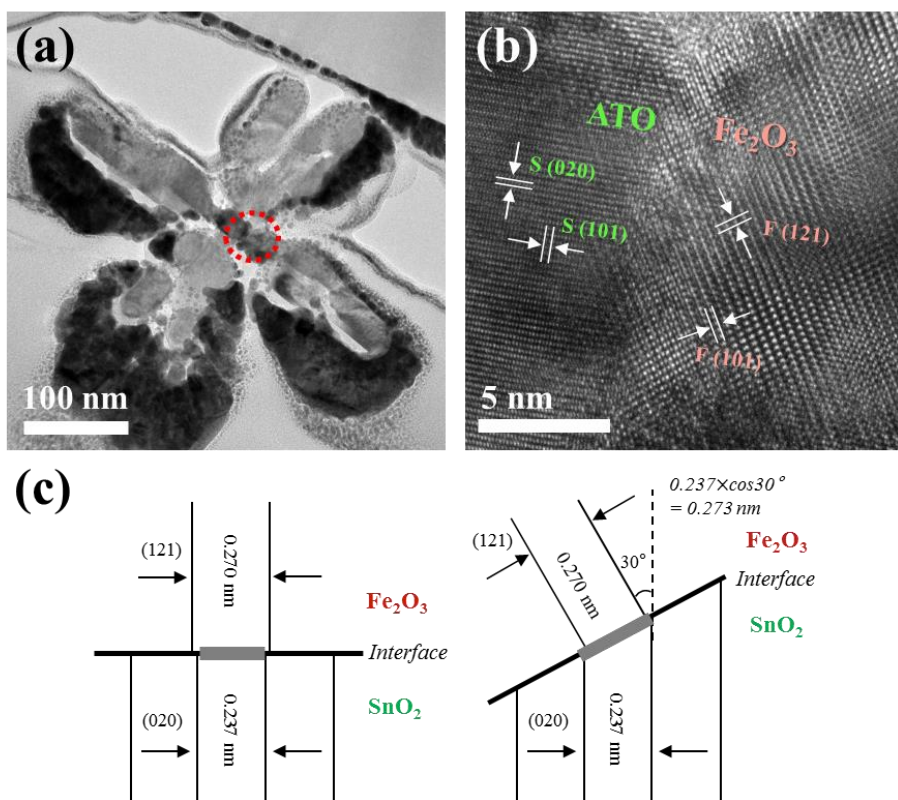


Figure 5.2.5. (a) A cross-sectional TEM image of a Fe_2O_3 -ATO; (b) HRTEM image of the marked region in (a); (c) Schematic of the interface of the $(020)_{\text{SnO}_2}$ plane of a ATO nanobelt and the $(121)_{\text{Fe}_2\text{O}_3}$ plane of Fe_2O_3 nanorods, revealing the lower interfacial lattice mismatch of inclined growth compared to that of perpendicular growth.

5.3 Linear growth: VO₂-ATO

5.3.1 Morphology and structure

Morphology and crystal structure of fabricated VO₂-ATO heterostructure arrays were analyzed. Morphology of VO₂-ATO was observed by SEM microscope, in which samples were prepared by hydrothermal reaction for 3 h (Figure 5.3.1). Low-magnification SEM image exhibits that VO₂-ATO are well-aligned in micro-scale range, indicating that vertical array of ATO nanobelts was maintained during nanobranched synthesis by solution route. Interestingly, nanobranched synthesis followed linear growth mode, in which VO₂ did not grow on broad surface of ATO nanobelt but only on narrow surface of the nanobelt with two quasi-symmetrical branches. An individual VO₂-ATO heterostructure was analyzed by TEM as shown in Figure 5.3.2, indicating that each VO₂ nanorod was tilted with respect to the nanobelt side at an angle of about 30°. SAED patterns were measured from the regions including single side of nanobelt and VO₂ nanorods grown on that, and it was found that VO₂ nanorods grew epitaxially on the nanobelt surface with [001] growth direction (c-axis in tetragonal rutile). EDS elemental mapping in Figure 5.3.3 shows that Sn and V atoms were located on the nanobelt and the branches, respectively, implying that there was no diffusion of Sn atoms into

the VO₂ nanobranched during synthesis. Although rutile VO₂ exists as monoclinic-type rather than tetragonal-type at room temperature, in this case, the lattice planes of VO₂ were simply marked on the basis of tetragonal rutile unit cell in order to emphasize the epitaxial relationship between VO₂ and SnO₂. Details were discussed in epitaxial relationship part. Based on information about morphology and crystallography obtained from TEM and SAED, atomic model along [010]_{SnO₂} projection was described at the interface between nanobelts and nanorods of a VO₂-ATO heterostructure (Figure 5.3.4). It thus can be deduced that VO₂ nanobranched may be constructed epitaxially on (101) surface of ATO nanobelt with one crystallographic orientation via same rutile crystal structures, regardless of phase transition between tetragonal-type and monoclinic-type. Also, according to this atomic description, the angle between (101) and (002) planes of VO₂ (R) is calculated to be 32.1°, which induces that nanobranched were formed slopingly on the nanobelts. Therefore, 3-D heteroepitaxial nanostructures of perfect two-fold-symmetry were formed with VO₂ nanobranched grown along [001] direction.

To further study the growth mechanism of VO₂-ATO, samples were collected at different reaction stages. The products prepared from various growth time from 2 h to 12 h were observed by SEM images as shown in

Figure 5.3.5, indicating the structural and morphological transformation from ATO nanobelts to VO₂-ATO heterostructures. After the initial 2 h reaction, thorn-like nanorods with a length of 10 nm were nucleated on the surfaces of the nanobelts (Figure 5.3.5a), and begun to grow in nanorod shape after another 30 min growth (Figure 5.3.5b). At the stage of 3 h reaction, branches exhibited the symmetrical feature and it was observed that two branches were formed on each narrow side of nanobelt (Figure 5.3.5c). By increasing the reaction time to 6 h, branched nanostructures of two-fold-symmetry were formed with increase of length of branches (Figure 5.3.5d). When the reaction time was further continued to 12 h, the lengths and thickness of branches increased and each branches started to hold together. Also, the unique morphology of VO₂-ATO – two-fold-symmetry and inclined growth – was revealed more clearly. This tendency was also confirmed by the XRD graphs: VO₂ related peaks increased as reaction time increased (Figure 5.3.6). Also, there were no secondary phases or other polymorphs of VO₂ in the whole range of reaction time, indicating that pure VO₂-ATO heterostructures could be formed. Interestingly, in contrast with bulk VO₂, the intensity of (101) peak is relatively higher than that of others for VO₂, which exhibits a strong (101) preferred orientation. It is due to linear growth of VO₂ on {101} surfaces of nanobelt, consistent with results

of SEM and TEM analysis. Interestingly, when the hydrothermal reaction was performed without ATO nanobelt substrate, microspheres composed of aggregation of nanoplates were obtained with VO₂ (B) phase (Figure 5.3.7). This result also supports the fact that rutile type VO₂ nanobranches could be fabricated by heteroepitaxial nucleation and growth mechanism on the surface of rutile SnO₂ nanobelts.

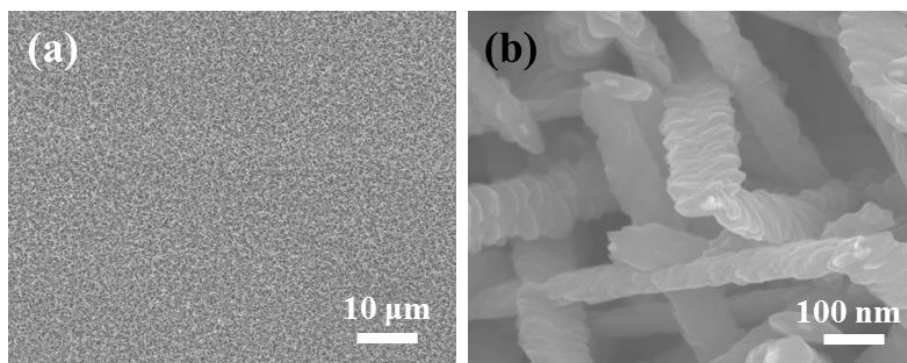


Figure 5.3.1 (a) A typical SEM image of VO₂-ATO arrays, in which VO₂ nanobranches were synthesized for 3 h by hydrothermal method, and (b) a magnification image of (a).

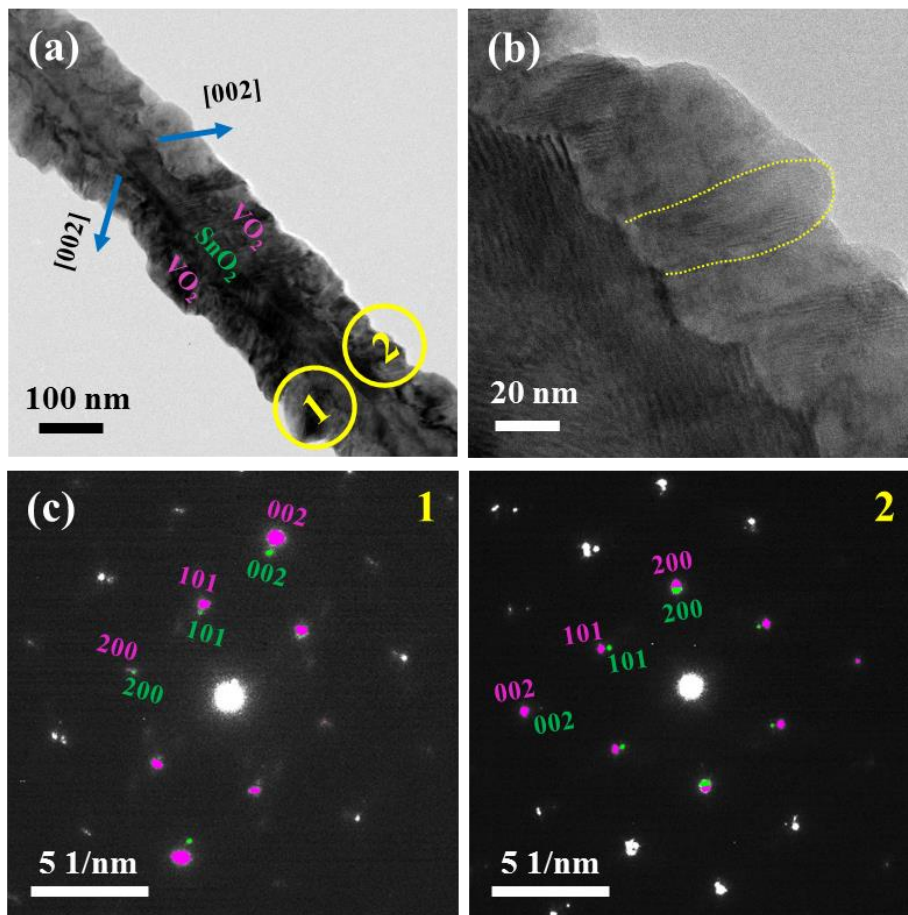


Figure 5.3.2 TEM analysis of a VO_2 -ATO heterostructure: (a) a low-mag TEM image, (b) a magnification image of (a), (c) a SAED pattern observed from region 1 of (a) and (d) a SAED pattern observed from region 2. SAED analysis indicates that VO_2 nanorods grew epitaxially on ATO nanobelt and their growth direction was $[001]$.

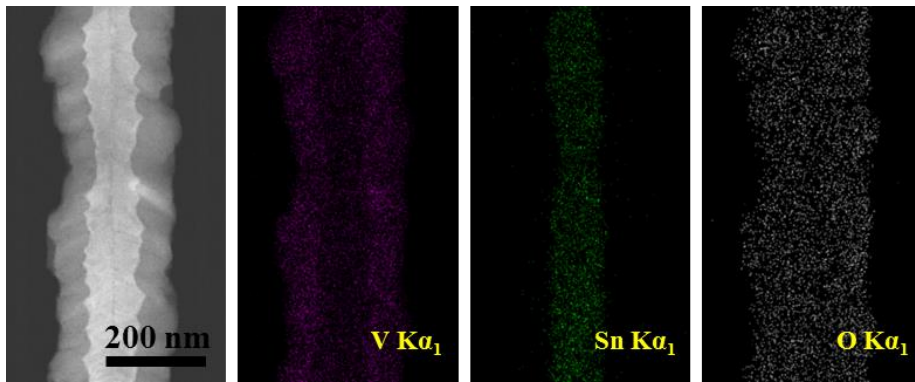


Figure 5.3.3 EDS elemental mapping of a VO₂-ATO heterostructure.

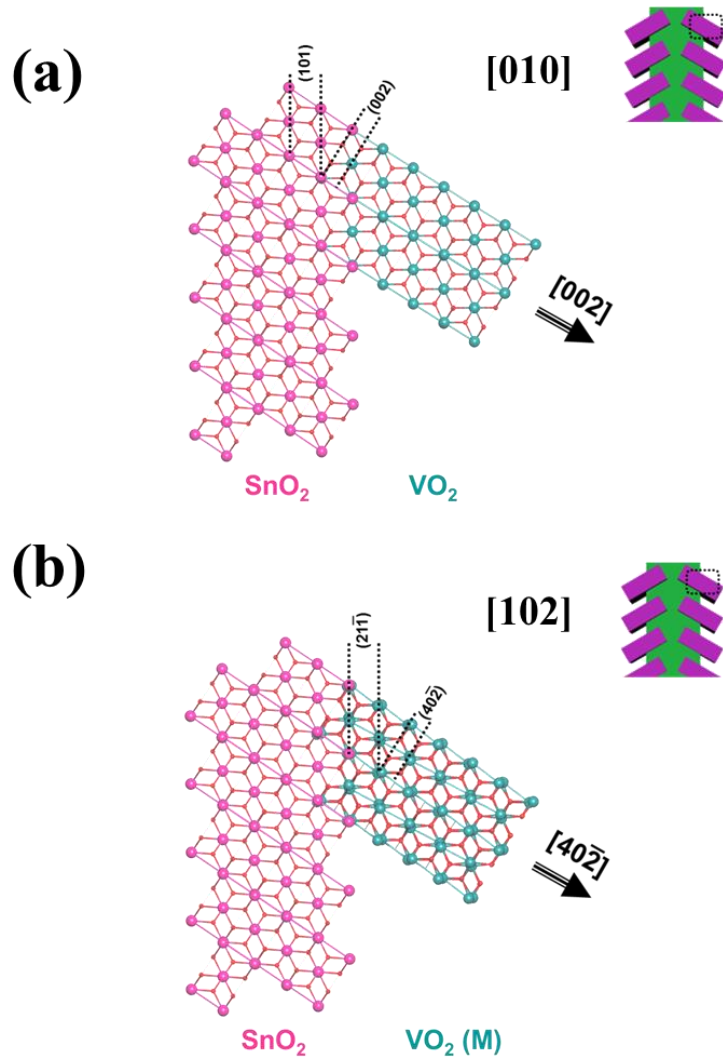


Figure 5.3.4 The illustrations of atomic arrangements at the interface between (a) SnO_2 and VO_2 (R) and (b) SnO_2 and VO_2 (M), which are projected along $[010]$ direction of SnO_2 .

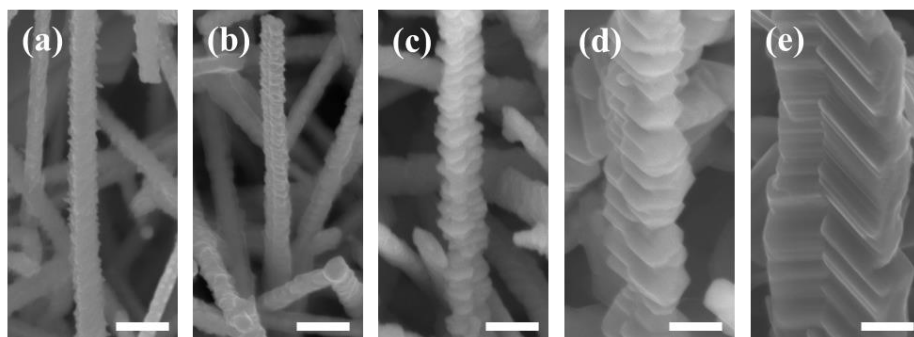


Figure 5.3.5 SEM images of the VO₂-ATO heterostructure at various reaction stages by setting the reaction time: (a) 2 h, (b) 2.5 h, (c) 3 h, (d) 6 h and (e) 12 h. Scale bar: 200 nm

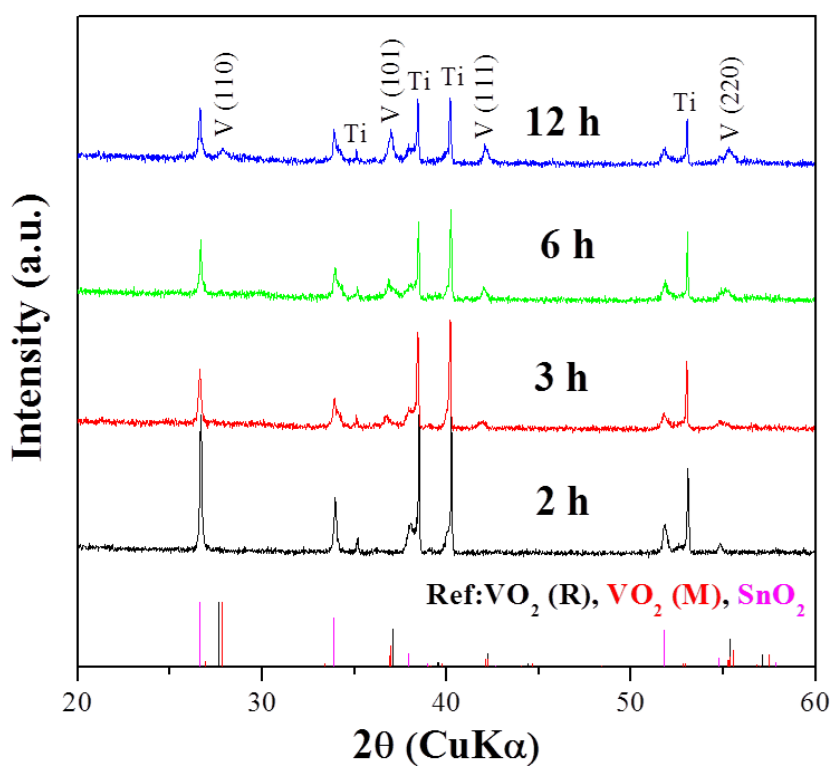


Figure 5.3.6 XRD graphs of VO₂-ATO heterostructure at various reaction stages by setting the reaction time.

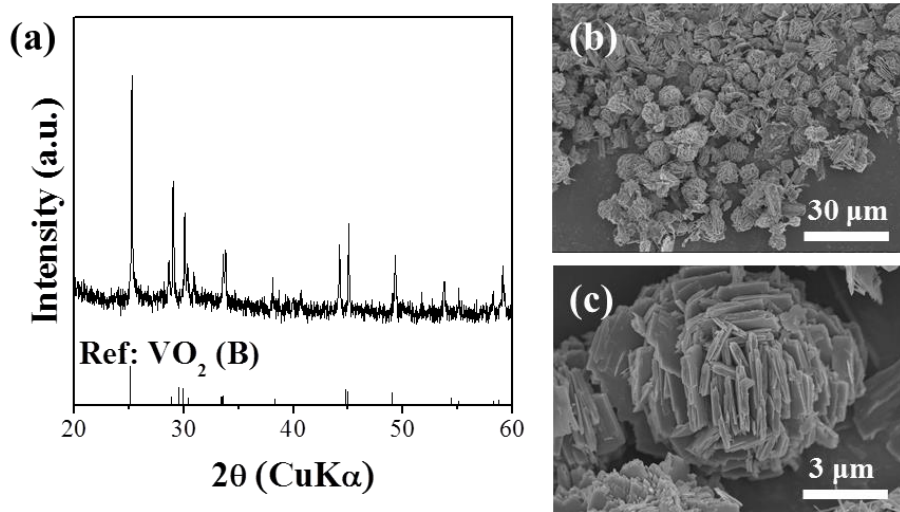


Figure 5.3.7 (a) XRD graphs and (b-c) SEM images of VO₂ (B) particles precipitated by hydrothermal method without insertion of ATO nanobelt substrate.

5.3.2 Epitaxial relationship

To further investigate the epitaxial relationship of VO₂–ATO hetero-structures, the cross-sectional specimen was fabricated by focus ion beam (FIB) milling, and then observed by TEM as shown in Figure 5.3.8. Because specimen was coated with Au before milling for protecting from the Ga ion beam, the mass difference among V, Sn and Au gives a contrast among VO₂ (light), SnO₂ (dark) and Au (deep dark), consistent with EDS elemental mapping (Figure 5.3.9). Cross section of the ATO nanobelt had of rectangular shape with width 100 nm and thickness 30 nm; whereas that of VO₂ nanobranches had average size of length 100 nm and thickness 25 nm. The nanobelt was covered with total four nanobranches, where each branch was attached to each edge of nanobelt. HRTEM images were observed from marked regions in Figure 5.3.8a. Figure 5.3.8b1 and 2 show that the lattice fringes are continuous across the interfaces between the nanobranch and the narrow side of nanobelt with good atomic registry. Because (21 $\bar{1}$) plane in the VO₂ (M) is found to be parallel with the (101) plane of the SnO₂, epitaxial relationship is VO₂(21 $\bar{1}$)||SnO₂(101) and VO₂[1 $\bar{2}$ 0]||SnO₂[$\bar{1}$ 01]. Theoretical lattice mismatch between a (002)_{VO₂(M)} plane and a (020)_{SnO₂} plane is calculated to be -4.2% $\{(2.27-2.37 \text{ \AA})/2.37 \text{ \AA}\}$, which is small enough to induce the epitaxial growth. This result was also confirmed by

SAED pattern (Figure 5.3.8c). Moreover, from the HR image and the SAED pattern, it was found that the d -spacing of $(002)_{\text{VO}_2(\text{M})}$ plane was slightly increased from 2.27 nm to 2.30 nm at the interface, implying that $(002)_{\text{VO}_2(\text{M})}$ plane was strained along tetragonal b -axis. It is well-known that epitaxial strain is induced in order to maintain the coherent interface in which all atom positions are in exact register with zero or small misfit [68]. Thus, strained $(002)_{\text{VO}_2(\text{M})}$ plane with reduced misfit from -4.2% to -3.0% may contribute to coherent interface between $(21\bar{1})_{\text{VO}_2(\text{M})}$ plane and a $(101)_{\text{SnO}_2}$ plane. On the other hands, at the interface between the nanobranche and the broad side of nanobelt, $(002)_{\text{VO}_2(\text{M})}$ plane and $(020)_{\text{SnO}_2}$ plane, semi-coherent with several point defects was observed (Figure 5.3.8b3). This result was also confirmed by the fast-Fourier transformation (FFT) patterns (Figure 5.3.8d). While the FFT pattern of the nanobelt region corresponded to the diffraction pattern of SnO_2 with zone axis of $[\bar{1}01]$, the FFT pattern of the nanobranche region had irregular diffraction pattern which differs from that of VO_2 (M) with zone axis of $[1\bar{2}0]$. It is mainly attributed to large lattice mismatch between a $(21\bar{1})_{\text{VO}_2(\text{M})}$ plane and a $(101)_{\text{SnO}_2}$ plane, which is calculated to be -8.1% $\{(2.42-2.64 \text{ \AA})/2.64 \text{ \AA}\}$. Phase transition from VO_2 (R) to VO_2 (M) may also contribute to coherence collapse. VO_2 (M) phase has a distorted structure of VO_2 (R) phase along the tetragonal c -axis (Figure 5.3.10). Thus, atoms

composing the $(101)_{\text{VO}_2(\text{R})}$ plane is shifted to the lattice positions of $(210)_{\text{VO}_2(\text{M})}$ plane, inducing the great change of atomic arrangement on $(020)_{\text{SnO}_2}$ surface and decrease of d -spacing. Actually, in HR image (Figure 5.3.8b3) and FFT pattern (Figure 5.3.8d), the lattice fringe of $(210)_{\text{VO}_2(\text{M})}$ plane is more clearly observed than that of $(21\bar{1})_{\text{VO}_2(\text{M})}$ plane, indicating that $(210)_{\text{VO}_2(\text{M})}$ plane originated from $(101)_{\text{VO}_2(\text{R})}$ plane. As listed in Table 5.3.1, d -spacing of lattice planes related to tetragonal c -axis is diminished significantly while that of lattice planes related only to tetragonal a or b -axis is almost same after phase transition to VO_2 (M). This is also why heteroepitaxy of VO_2 nanobranh on the (101) plane of the SnO_2 could be maintained after phase transition to VO_2 (M). Overall epitaxial behaviors of VO_2 -ATO heterostructures are presented based on crystallographic description as shown in Figure 5.3.11. Small misfit and similar lattice arrangement of VO_2 nanobranh on the $(101)_{\text{SnO}_2}$ surface provide coherent interface with tensile strained $(020)_{\text{VO}_2}$ plane, whereas large misfit and distorted lattice of VO_2 nanobranh on the $(020)_{\text{SnO}_2}$ surface induce the semi-coherent interface accommodating the lattice-mismatch with defects.

Table 5.3.1. Lattice planes (hkl) and their d -spacings of tetragonal rutile VO₂ (R) and monoclinic VO₂ (M).

VO ₂ (R)		VO ₂ (M)	
hkl	d (Å)	hkl	d (Å)
200	2.276	020	2.265
020	2.276	002	2.265
002	1.428	400	1.239
101	2.420	210	2.174

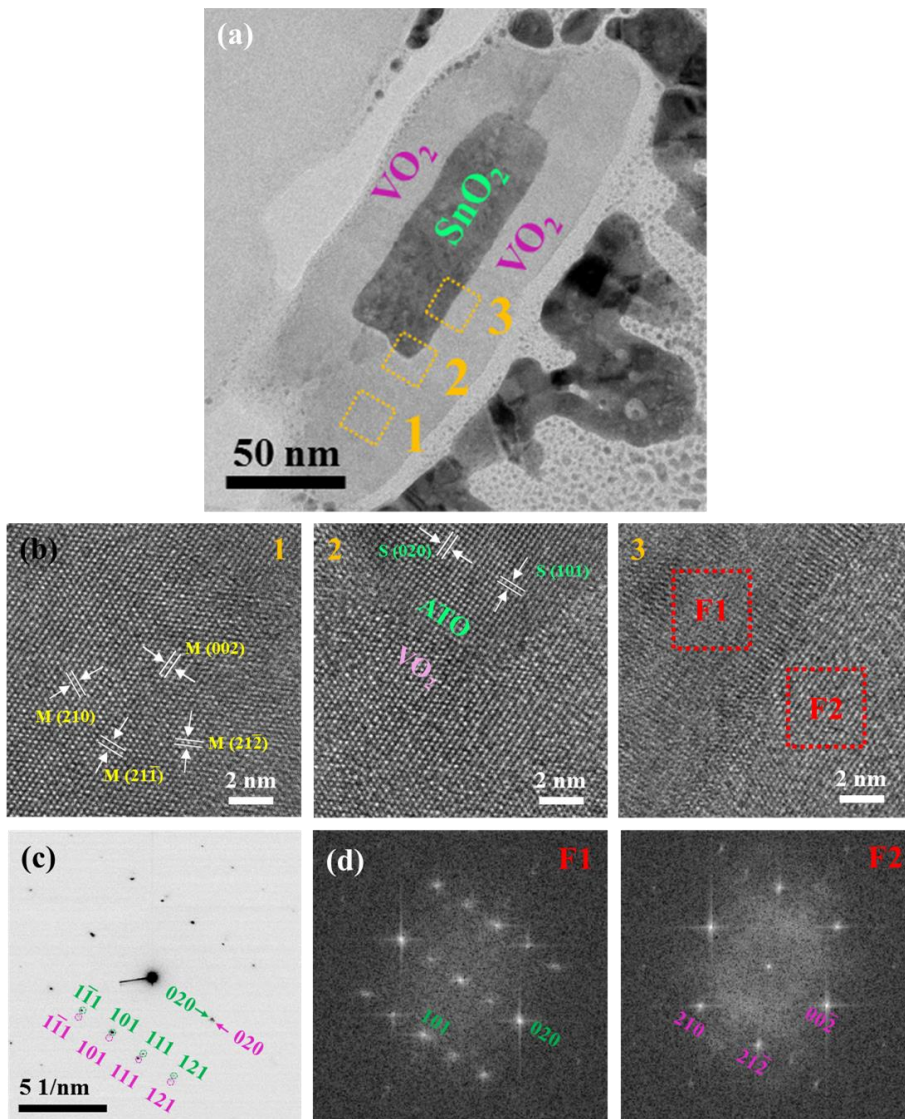


Figure 5.3.8 (a) A TEM image of cross-section of a VO₂-ATO fabricated by focused ion beam method. (b) HRTEM images obtained from marked regions in (a), (c) SAED pattern of (a) and (d) the fast-Fourier transformation (FFT) patterns of the backbone and branch of (b-3).

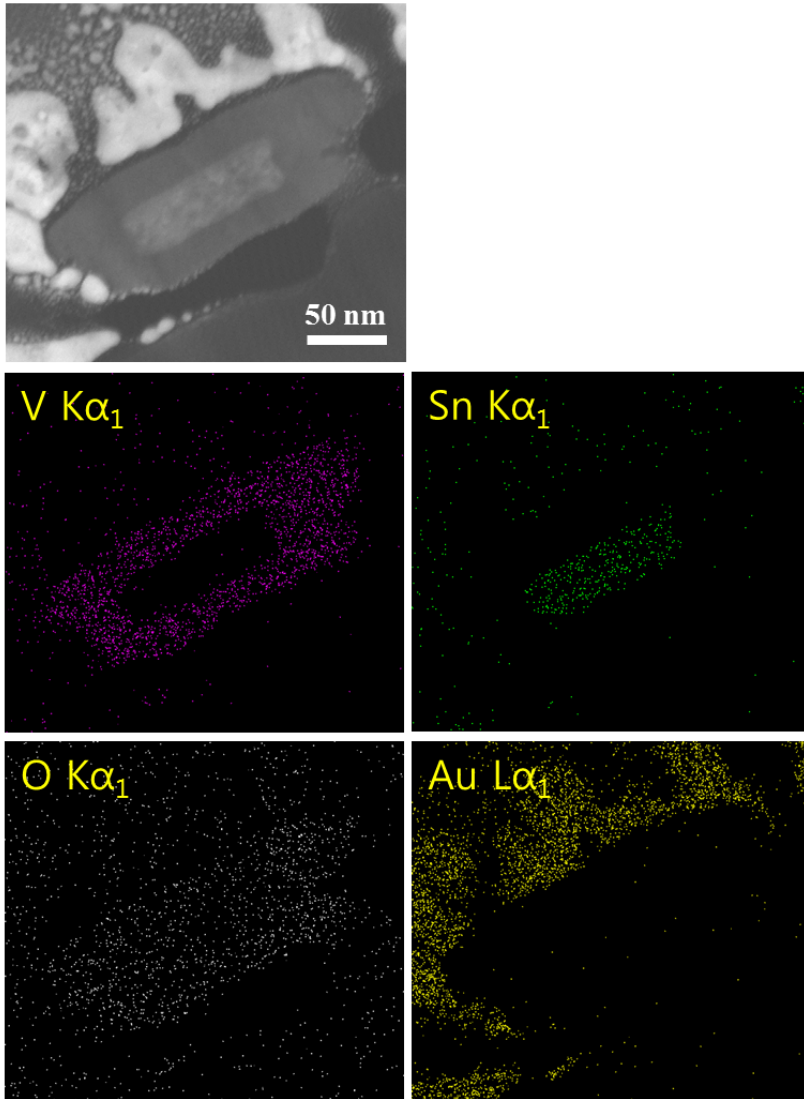


Figure 5.3.9 EDS elemental mapping of cross-section of a VO₂-ATO showing V, Sn, O and Au atomic profiles.

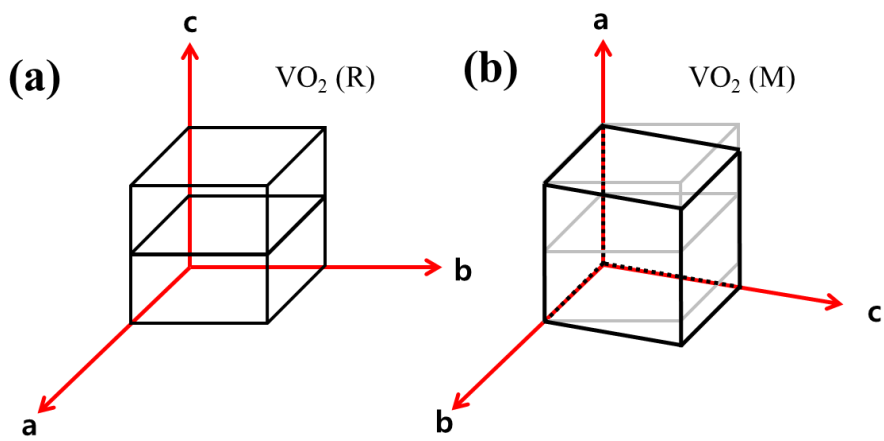


Figure 5.3.10 Schematic description of lattice deformation from (a) tetragonal rutile VO₂ (R) to (b) monoclinic VO₂ (M) with a small distortion along the tetragonal c-axis ($\beta=122.6^\circ$).

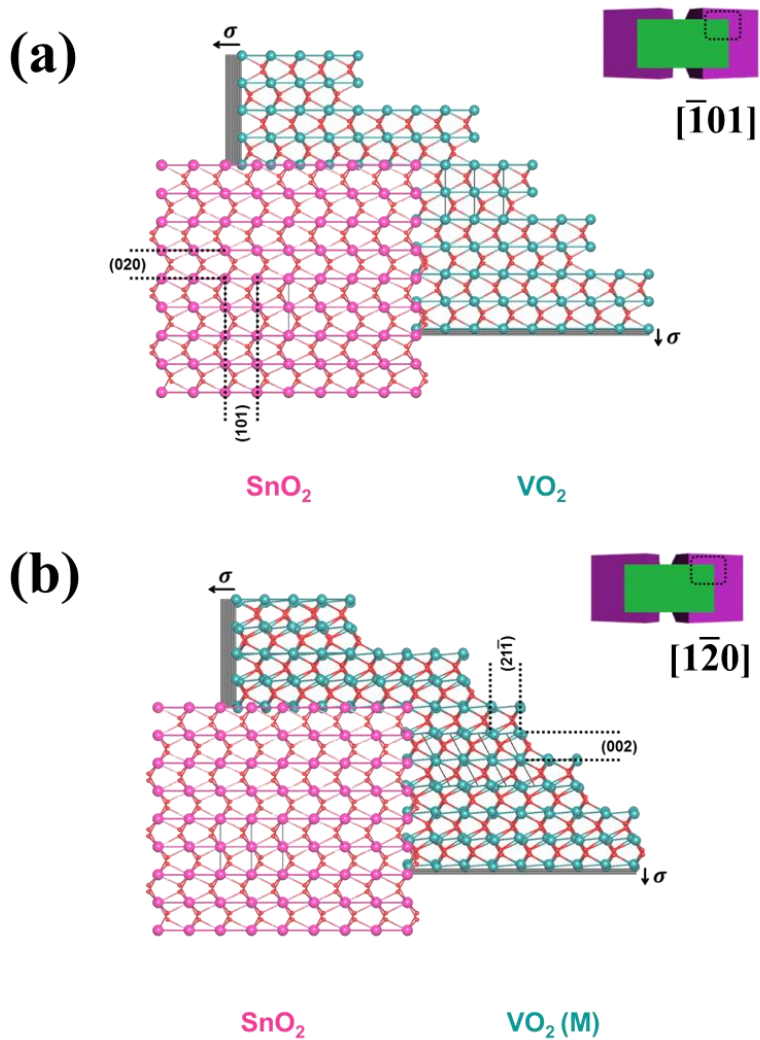


Figure 5.3.11 The descriptions of atomic arrangements at the interface between (a) SnO_2 and VO_2 (R) and (b) SnO_2 and VO_2 (M), which are projected along $[\bar{1}01]$ direction of SnO_2 . The b-axis length of VO_2 bulk (4.554 \AA) is shorter than that of SnO_2 (4.738 \AA) with the lattice mismatch of 4%, resulting in a tensile strain along the b axis for VO_2 nanorods.

5.3.3 Epitaxial strain effect

To elucidate the effect of such epitaxial strain on the formation of VO₂ nanobranched and their structural and physical properties, in-depth research was conducted based on crystal structure analysis and interpretation. The presence of the tensile-strain along tetragonal b-axis (monoclinic c-axis) was directly confirmed in VO₂-ATO heteroepitaxial system by XRD analysis (Figure 5.3.12), where the *c* lattice constant of the VO₂ (3 h) nanobranched is found to be increased to 5.420 Å, cf., 5.382 Å for bulk VO₂ (M). Also, the strain was relaxed relatively gradually in the longer (thicker) VO₂ nanobranched as shown in diffraction peaks measured from VO₂ (6 h) and VO₂ (12 h) samples. Strained lattice constants of VO₂ nanobranched were calculated from the Rietveld refinement of XRD patterns (Table 5.3.2), indicating the tensile strain along the tetragonal a, b-axis directions and the compressive strain along tetragonal c-axis. It is noted that while tensile-strain (a, b-axis) is released gradually, compressive strain (c-axis) remains constant as length of VO₂ nanobranched increases. It implies that strain of a, b-axis is caused by coherence between the {020} facets crossing the (101) interface, in which length of VO₂ nanobranched increases dramatically from 45 nm at 3 h sample (refer to cross sectional TEM image of Figure 5.3.8a) to 110 nm at 12 h sample (not shown here), whereas strain of c-axis is induced

by semi-coherence between the $\{101\}$ facets crossing the (020) interface, where thickness of VO_2 nanobranches only increases slightly from 25 nm to 35 nm.

As mentioned above, linear growth is observed for VO_2 during branching synthesis, which may be attributed to epitaxial strain accommodated during the initial formation of VO_2 epilayer on the surface of SnO_2 nanobelt. According to Stranski-Krastanow growth mode, the transition of 2D to 3D growth is induced by strain originated from different lateral lattice constant between 2D layer and substrate. As thickness of epilayer increases, strain accumulates and may be relaxed elastically below critical thickness in which misfit dislocations occurs by reorganization of flat surface, e.g. the formation of 3D surface structures [77], in order to minimize the strain and surface energy [98]. In the VO_2 -ATO heteroepitaxial branched structure, the decrease of misfit by strain occurred dominantly at the lattice plane containing tetragonal b-axis due to coherent interface on $(101)_{\text{SnO}_2}$ plane (Table 5.3.3), suggesting that strain could be more accumulated on $(101)_{\text{SnO}_2}$ plane rather than $(020)_{\text{SnO}_2}$ plane at the initial formation stage for VO_2 epilayer. Thus, 3D growth could be induced by strain on $(101)_{\text{SnO}_2}$ plane at the initial stage as shown in Figure 5.3.5a, and such 3D island structure could provide a preferred growth site and accounts for unidirectional growth.

Furthermore, such epitaxial strain had influence on the decrease of metal-insulator transition (MIT) temperature in VO₂ nanobranches. The temperature-dependent *in situ* XRD clearly confirmed the structural phase transition from monoclinic rutile VO₂ (M) to tetragonal rutile VO₂ (R) in a VO₂-ATO heterostructure (Figure 5.3.13). The broad peak in $27.5^\circ \leq 2\theta \leq 28.5^\circ$ was shifted from VO₂ (M) (011) to VO₂ (R) (110) during the heat process and thus could be readily indexed into VO₂ (M) at temperature under 55 °C and VO₂ (R) at temperature above 60 °C. It is also consistent with the results obtained from temperature-dependent Raman analysis (Figure 5.3.14). All peaks in Raman spectra measured at room temperature are indexed as the VO₂ (M) phase which is characterized by Raman-active modes of 9A_g + 9B_g [210,211]. On heating, all Raman peaks suddenly disappeared at 55 ~ 60 °C, implying that the transition to a metallic VO₂ (R) occurred. It is well-known that compressive strain lowers the MIT temperature of VO₂ [212,213]. In VO₂-ATO system, VO₂ is strained along the c-axis by -0.2% and has a T_{MIT} of ~55 °C, and such tendency is consistent with previously reported value (T_{MIT} of 27 °C by -1.2% strain along c-axis). T_{MIT} and transition behavior in 3 h sample was also similar to those in 12 h sample, attributed to same compressive strain value. Therefore, for the first time, it was demonstrated that epitaxial strain can affect the growth behavior and physical properties of

nanobranch in 3-D heteroepitaxial nanoarchitectures.

Table 5.3.2. Lattice parameter and strain of VO₂ nanorods epitaxially grown on ATO nanobelt by hydrothermal reaction for 3, 6 h and 12 h. Lattice parameters (*a*, *b* and *c*) were calculate from Rietveld refinement of XRD pattern. Strain at each axis was evaluated by difference of lattice parameters between unstrained VO₂ (M) phase and strained VO₂ nanorods.

Samples	a-axis		b-axis		c-axis	
	<i>a</i> (Å)	Strain (%)	<i>b</i> (Å)	Strain (%)	<i>c</i> (Å)	Strain (%)
VO ₂ (M) bulk	5.752	0	4.526	0	5.382	0
VO ₂ branch (3 h)	5.740	-0.20	4.555	0.64	5.420	0.70
VO ₂ branch (6 h)	5.740	-0.20	4.553	0.60	5.413	0.57
VO ₂ branch (12 h)	5.740	-0.20	4.532	0.13	5.392	0.19

Table 5.3.3. Lattice plane (*hkl*), *d*-spacings, lattice misfit and strain of VO₂ nanorods epitaxially grown on ATO nanobelt by hydrothermal reaction for 3 h, 6 h and 12 h. *d*-spacings of nanorods were calculate from Rietveld refinement of XRD pattern. Lattice misfit at each plane was derived by difference of *d*-spacing between SnO₂ backbone and VO₂ nanorods.

SnO ₂ (R)		VO ₂ (M)		VO ₂ (3 h)		VO ₂ (6 h)		VO ₂ (12 h)	
<i>hkl</i>	<i>d</i> (Å)	<i>hkl</i>	<i>d</i> (Å)	<i>d</i> (Å)	Misfit (%)	<i>d</i> (Å)	Misfit (%)	<i>d</i> (Å)	Misfit (%)
011	2.643	20 $\bar{2}$	2.433	2.442	-7.6	2.440	-7.7	2.433	-7.9
101	2.643	21 $\bar{1}$	2.428	2.428	-8.1	2.428	-8.1	2.428	-8.1
020	2.369	002	2.265	2.283	-3.6	2.280	-3.8	2.271	-4.1
1 $\bar{1}$ 1	2.309	21 $\bar{2}$	2.144	2.154	-6.7	2.150	-6.9	2.145	-7.1
1 $\bar{2}$ 1	1.764	21 $\bar{3}$	1.66	1.667	-5.5	1.665	-5.6	1.662	-5.8

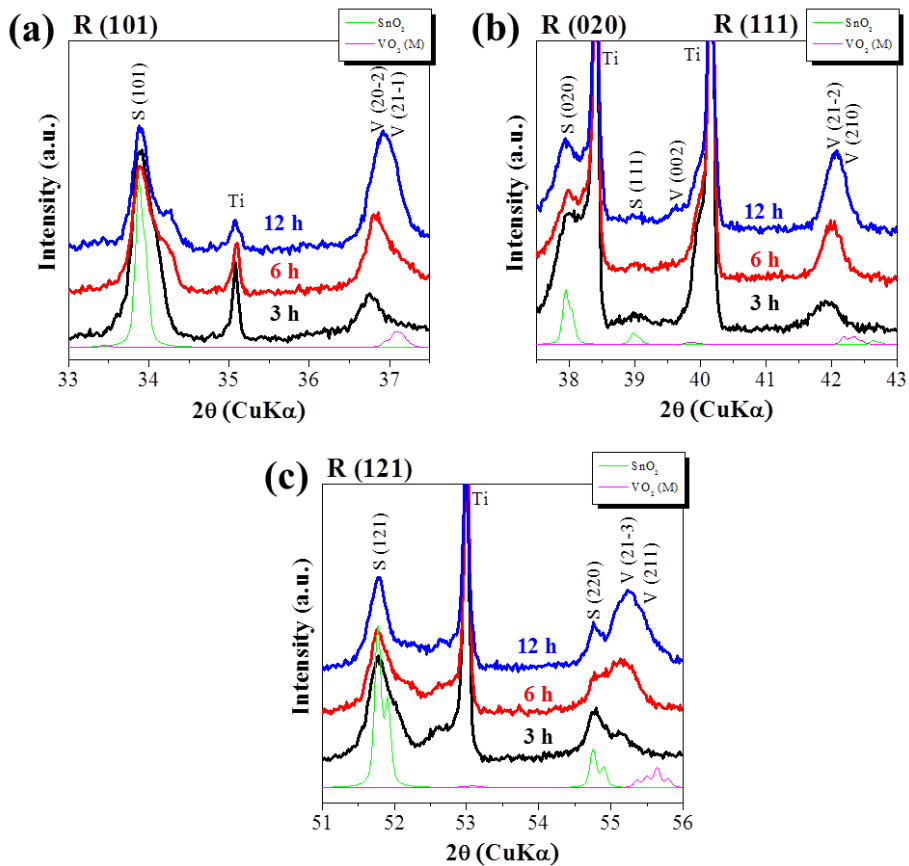


Figure 5.3.12 XRD graphs measured at a scan rate of 0.3 degrees per min (2θ) for VO₂-ATO heterostructure samples in which VO₂ nanobranched were synthesized for 3 h, 6 h and 12 h by hydrothermal method. Each 2θ region is related to (a) rutile (101), (b) rutile (020) and (111), and (c) rutile (121). Bold lines indicate XRD pattern measured from VO₂-ATO heterostructure. Sharp pink and green lines are simulated XRD patterns from crystallographic information file (CIF) of VO₂ (M) and SnO₂, respectively.

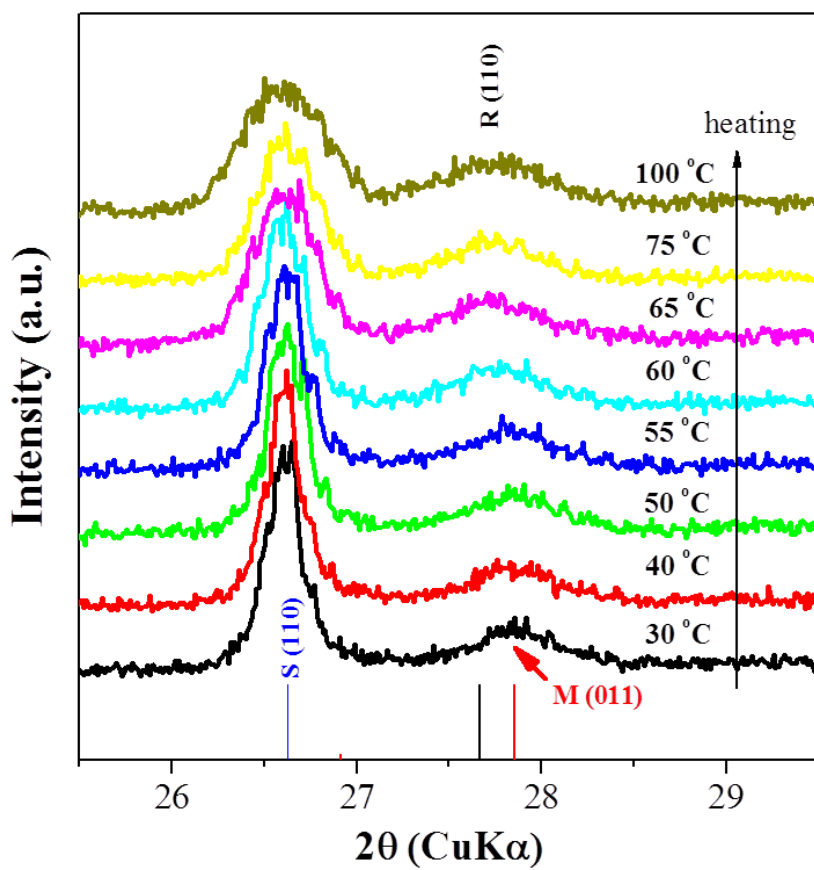


Figure 5.3.13 Temperature dependence of XRD data of VO₂-ATO arrays synthesized for 12 h, indicating the phase transition of VO₂ from monoclinic rutile (M) to tetragonal rutile (R) at about 55 ~ 60 °C.

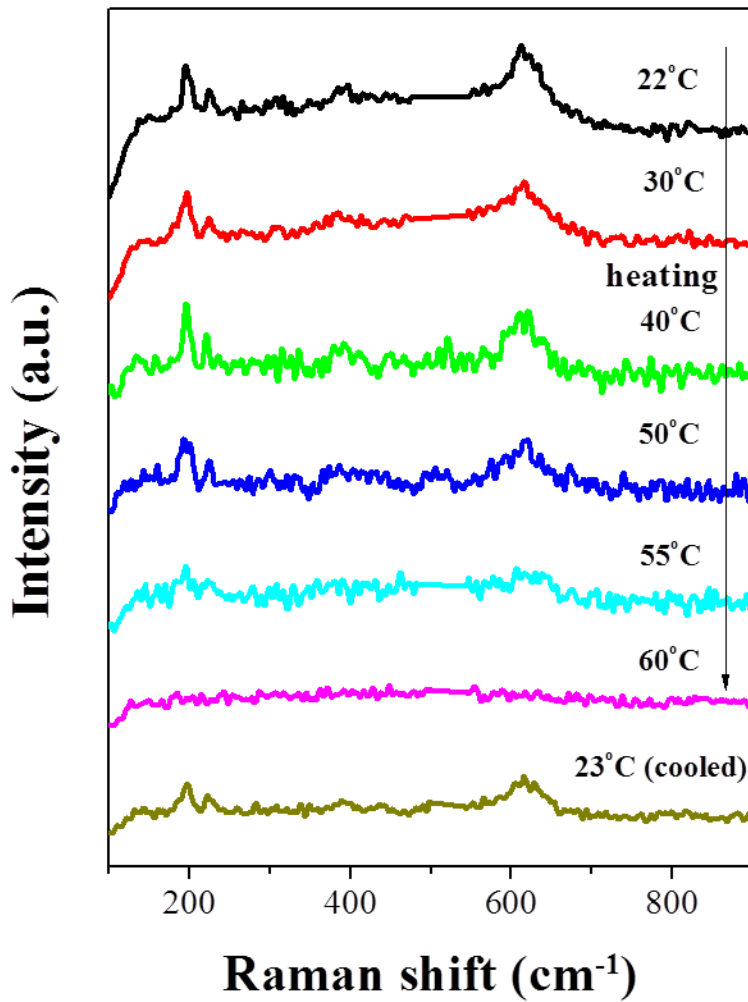


Figure 5.3.14 Temperature dependence of Raman spectra of individual VO₂-ATO heterostructure synthesized for 12 h, presenting the phase transition from insulating VO₂ (M) to metallic VO₂ (R) at about 55 ~ 60 °C during the temperature cycling..

Chapter 6. Electrochemical applications

6.1 Photoelectrochemical cell

6.1.1 TiO₂-ATO photoanode for water splitting

Linear sweep voltammograms were collected for the optimized 3D anatase sphere TiO₂-ATO (AS-ATO) and 3D rutile rod TiO₂-ATO (RR-ATO) samples in a three-electrode PEC device. Both the AS-ATO and RR-ATO electrodes showed increased photocurrent densities than conventional TiO₂ thin-film electrodes [40,45] (Figure 5.1.1), indicating that using 3D structures improves PEC performance. The RR-ATO electrode achieves a photocurrent density of $\sim 1.13 \text{ mA/cm}^2$ at 1.0 V vs. RHE, which is twofold the value achieved using AS-ATO ($\sim 0.58 \text{ mA/cm}^2$ at 1.0 V vs. RHE). Meanwhile, the AS-ATO electrode exhibits a lower open circuit potential than the RR-ATO electrode, showing that anatase TiO₂ has a higher Fermi energy level ($\sim 0.2 \text{ eV}$) than rutile TiO₂. The lower fill factor of AS-ATO as opposed to that of RR-ATO is attributed to the electrolyte permeation through the pores on the shell layer. Figure 5.1.2 shows the *I-t* curve of the AS-ATO and RR-ATO electrodes at 1.0 V vs. RHE. The photocurrent goes down to zero immediately as the light is shut off and returns to the original value again as the light is

illuminated, implying that the charge transport properties of both the AS-ATO and RR-ATO are very fast. Assuming that all of the photocurrent flowing through the circuit coincides with the evolution of hydrogen, the overall STH conversion efficiency for the PEC can be calculated from the J - V curves using the following equation: [214]

$$\eta (\%) = \frac{[J_p \times (1.23 - E_b)]}{P_t} \quad (4)$$

In this equation, J_p is the photocurrent density, P_t is the incident light intensity (100 mW/cm^2), and E_b is the bias voltage calculated as $E_b = E_{mea} - E_{aoc}$, where E_{mea} is the corresponding potential of the photocurrent and E_{aoc} is the potential under open-circuit conditions. As shown in Figure 5.1.3, the maximum STH efficiency for ASOP and RROP is 0.41% (at 0.61 V vs. RHE) and 0.93% (at 0.68 V vs. RHE) respectively. The semicircle in the frequency range of $1\text{-}10^3$ Hz on the Nyquist plot reflects the charge transfer property at the TiO_2 /electrolyte interface [189]. The AS-ATO semicircle is much larger than the RR-ATO semicircle, indicating that the charge transfer resistance of RR-ATO is lower than that of AS-ATO [215] (Figure 5.1.4). The high surface roughness of RR may be responsible for the low-charge transfer resistance. 3D RR-ATO showed better PEC performance than the 3D structure of TiO_2 nanorod- TiO_2 nanowire [40], but lower than that of TiO_2 nanorod-Si nanowire (2.1%) [34]. However, it should be noted that Si absorbs the entire

visible wavelength of light whereas TiO_2 only absorbs light in the UV region. Considering that TiO_2 can be sensitized greatly by combining it with a visible-light absorbing material, such as inorganic quantum dots and dye molecules, 3D RR-ATO has the potential to achieve highly efficient PEC energy conversion.

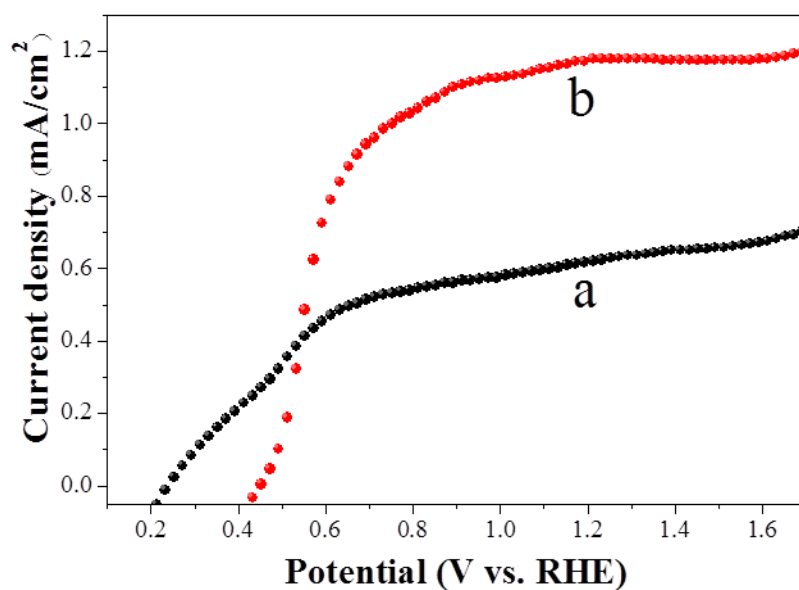


Figure 6.1.1. *J-V* curves of (a) anatase sphere TiO_2 -ATO and (b) rutile rod TiO_2 -ATO with ATO length of 10 μm and TiO_2 thickness of 130 nm.

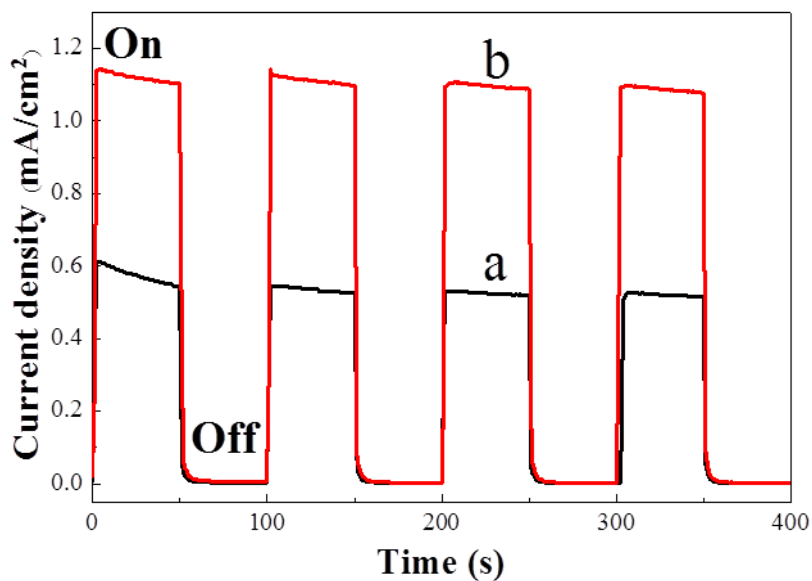


Figure 6.1.2. Amperometric $J-t$ curves of (a) anatase sphere $\text{TiO}_2\text{-ATO}$ and (b) rutile rod $\text{TiO}_2\text{-ATO}$ at an applied potential of 1.0 V vs. RHE.

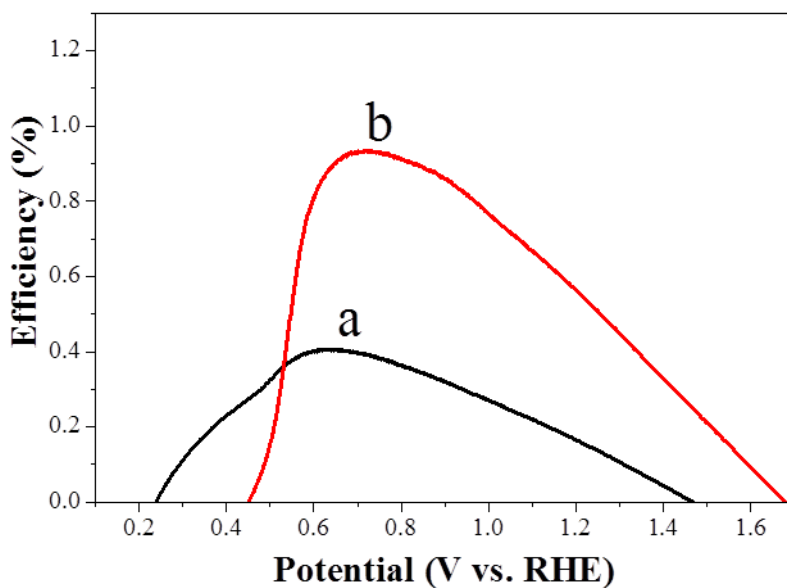


Figure 6.1.3. Photoconversion efficiency of (a) anatase sphere $\text{TiO}_2\text{-ATO}$ and (b) rutile rod $\text{TiO}_2\text{-ATO}$ calculated from $J-V$ data.

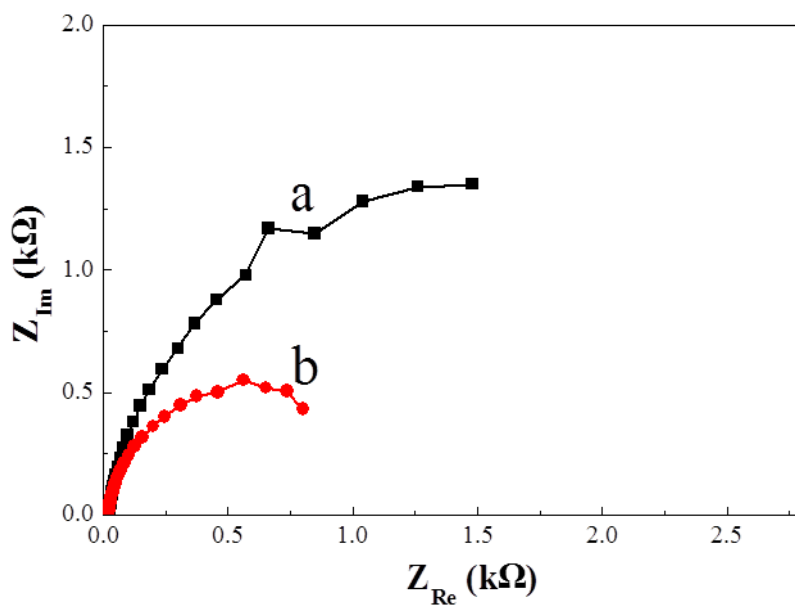


Figure 6.1.4. Nyquist plots of (a) anatase sphere TiO_2 -ATO and (b) rutile rod TiO_2 -ATO.

6.1.2 Quantum-dot-sensitized TiO₂-ATO

In this chapter, quantum dot (QD) sensitized TiO₂-ATO heterostructures were proposed as a conceptual model that satisfies every structural factor – high conductivity by a transparent conducting oxide (TCO) backbone, a high surface area by branching and low interfacial resistance via an epitaxial relationship. Moreover, in this structure, the light harvesting, charge collection and charge transport properties are mainly related to the absorber (CdS QD), branch (TiO₂) and backbone (ATO), respectively, implying that the effect of each property on the overall PEC performance can be determined and that the overall efficiency can be optimized by controlling each step.

Synthesis of QD sensitized heterostructures

The scheme in Figure 5.1.5 describes the experimental procedure used here for the fabrication of the CdS QD-sensitized TiO₂-ATO heterostructure. The procedure consists of three steps: (i) the deposition of single-crystalline one-dimensional (1D) ATO nanobelt arrays onto a FTO (F:SnO₂) glass substrate by thermal evaporation, (ii) the growth of single-crystalline TiO₂ nanorods on the ATO nanobelt by chemical bath deposition (CBD), and (iii) sensitization of the TiO₂-ATO heterostructure with CdS QDs by means of

electrodeposition (ED). Typical transmission electron microscopy (TEM) images and a detailed TEM analysis at each step are presented, clearly demonstrating the single-crystalline nature of the ATO nanobelts, TiO₂ nanorods and CdS QDs. The ATO nanobelts have a diameter of 50 to 100 nm and the SnO₂ rutile structure. The TiO₂ nanorods have a diameter of 20 nm, a length of 100 to 150 nm, and a rutile structure. Because both ATO and TiO₂ have the same rutile structure, TiO₂ nanorods were grown epitaxially on the ATO nanobelt. The size of the CdS QDs was determined to be 7.5 ± 0.8 nm from TEM images, and the crystal structure of the QDs was found to be greenockite according to the lattice fringes.

Shape tuning of TiO₂ branch

The PEC performance of the CdS-sensitized TiO₂-ATO heterostructure can be controlled by modulating each step, e.g., the length of the ATO nanobelts, the shape of the TiO₂ nanorods, and the loading amount of the CdS QDs. Hence, various shapes of TiO₂ were developed in an attempt to verify the correlation between the TiO₂ morphology and the PEC properties. The SEM images in Figure 5.1.6 show that dot, rod, and lamella-shaped TiO₂ were deposited on the ATO nanobelts. With the extension of the acid concentration and duration time, dot, rod, and lamella-shaped TiO₂ were

obtained in sequence. Dot, rod, and lamella-shaped TiO_2 were uniformly attached on the ATO nanobelt thoroughly. As shown in the TEM image in Figure 5.1.6, dot TiO_2 with lengths of 10 to 20 nm, rod TiO_2 with lengths of 100 to 150 nm, and lamella TiO_2 with lengths of 600 to 700 nm.

Distribution of CdS QDs

To evaluate the PEC performance of the TiO_2 -ATO heterostructures with a different TiO_2 morphology, the same amount of CdS was loaded by electrodeposition. To investigate the morphology of CdS QDs deposited heterostructures more details, the elemental distributions of three samples were measured by energy dispersion spectroscopy (EDS). Figure 5.1.7 shows EDS elemental mappings of CdS-sensitized dot, rod, and lamella TiO_2 -ATO samples. As a result of the quantitative analysis of the surface region, the atomic ratio of Ti: Cd was estimated to be about 0.74, 18.97, and 4.4 for the dot, rod, and lamella samples, respectively. This demonstrates that while CdS QDs were deposited more at the edges for the dot and lamella types, they were evenly distributed across the surface of the rod samples. This is attributed to the higher surface area of the rods compared to that of the dot and lamella samples.

Light absorption

The light absorption properties of CdS sensitized dot, rod and lamella TiO₂-ATO heterostructures were measured and compared at a wavelength range from 300 to 800 nm. Figure 5.1.8 shows the absorption with scattering ($A + S = 100 - R - T$) spectra calculated by transmittance and reflectance of CdS sensitized dot, rod and lamella TiO₂-ATO on FTO substrates. All three samples exhibited similar light absorption properties above 520 nm, corresponding to absorption edge of CdS (2.4 eV), due to almost same CdS loading amounts. Nonzero baseline was observed over 520 nm, revealing that scattering phenomenon appears [40]. It is noteworthy that broad shoulder peaks at a wavelength range from 500 to 700 nm were observed at dot, rod and CdS coated rod TiO₂-ATO heterostructures, which can be interpreted as antireflection characteristics of well-aligned 1-D subwavelength structures (SWSs) [216]. These scattering and antireflective effects of rod TiO₂-ATO heterostructure are expected to be beneficial to effective light absorption.

Photoelectrochemical properties

Figure 5.1.9 depicts a set of sweep-current-density versus potential (J - V) curves from CdS-sensitized dot, rod, and lamella TiO₂-ATO photoelectrodes

using chopped solar simulator illumination of 1SUN (AM 1.5G). The photocurrent densities of the dot, rod, and lamella samples are 2.81, 6.31, and 5.15 mA/cm², respectively, at 0.4 V vs. RHE. As the potential was swept anodically, the photocurrents of the rod and lamella samples increased sharply and became saturated close to 0.4 V, suggesting much more efficient charge collection and transport than in the dot [40]. Photoresponse of pure dot, rod, and lamella TiO₂-ATO were also measured in same condition of CdS coated one. (Figure 5.1.9b) The photocurrents of bare dot, rod, and lamella TiO₂-ATO were found to be 0.13, 0.80 and 0.36 mA/cm², respectively, at 0.4 V vs. RHE. Assuming that photocurrents by only CdS layer could be calculated by subtracting that of pure TiO₂ from that of CdS sensitized TiO₂, photocurrents by only CdS layer were estimated to be 2.68, 5.51 and 4.54 mA/cm² for dot, rod and lamella TiO₂-ATO, respectively. It indicates that rod and lamella samples can accept and transfer photogenerated electron in CdS QDs more effectively than dot one.

While the *J-V* curves show the overall PEC performance, the wavelength-dependent PEC properties can be obtained by incident-photon-to-current-conversion efficiency (IPCE) measurements. The IPCE profiles of dot, rod, and lamella photoelectrodes measured at 1 V vs. RHE are shown in Figure 5.1.10. For the rod TiO₂ photoelectrodes, a strong and almost constant

photoresponse is observed within the range of 350 to 500 nm. The IPCE values for the rod lie between 60 – 70 % with a nearly flat curve and are larger than those of the dot and lamella, resulting in a higher photocurrent. The IPCE profile of dot, rod, and lamella photoelectrodes were consistent with the tendency of the photoconversion efficiency.

The electrochemical impedance spectra (EIS) of the dot, rod and lamella photoelectrodes under solar simulator irradiation at 0 V vs. RHE (1.0 V vs. Ag/AgCl) were measured to verify the charge transfer. The Nyquist plots shown in Figure 5.1.11 indicate that the semicircles become smaller in the order of dot, lamella and rod. Inset of Figure 5.1.11 represents the equivalent circuit where R_s is a series resistance of TCO (FTO substrate and ATO NBs), R_{tr} is the electron transport resistance in the TiO_2 , R_{ct} is a charge-transfer resistance at the CdS/electrolyte interface, Z_d is the diffusion impedance in the electrolyte and RCE is the charge transfer resistance at the counter electrode/electrolyte interface. C_{μ} and C_{CE} is the chemical and interfacial capacitance, respectively. Semicircles in the frequency range of 1 to 10^3 Hz correspond to the charge transfer at the TiO_2 /CdS/electrolyte interface [189]. Thus, the charge-transfer resistance of the rod photoelectrode is lower than that of the dot and lamella photoelectrodes, implying that charge carriers in the rod photoelectrode are collected more efficiently [215].

To investigate the electron transport kinetics, open circuit voltage (V_{oc}) decay and electron lifetime as a function of V_{oc} were measured. V_{oc} decay rate decreased as TiO_2 layer became thicker, revealing that TiO_2 rod and lamella structures efficiently enhance charge transport and reduce electron recombination. (Figure 5.1.12) The electron life time (τ_n) corresponding to V_{oc} (calculated by voltage-recombination life time model [217]) is plotted in Figure 5.1.12. At comparable V_{oc} , rod and lamella structure exhibits a higher in electron life time than dot structure.

For a better explanation of the trend observed in the electron dynamics, a band diagram based on the relevant electronic states of the components is considered. (Figure 5.1.13) The Fermi level that shifted to the conduction band edge (CBE) by Sb doping in ATO [218] is nearly equal to that in TiO_2 , reducing the Schottky barrier and promoting electron transport. Moreover, The CBE of TiO_2 is lower than that of CdS but higher than that of ATO. Thus, TiO_2 nanorods can function not only to transfer photoexcited electrons from CdS to ATO but also to block the recombination of photoinjected electrons with electrolyte [219], allowing the following tendency in the electron lifetime: dot < rod ~ lamella.

Optimization

In comparison to dot and lamella TiO_2 , the rod TiO_2 -ATO photoelectrode is capable of efficient photo-conversion property, as confirmed by photocurrent and IPCE. The surface area of the rod TiO_2 -ATO is larger than that of the dot and lamella TiO_2 -ATO, consistent with the EDS mapping analysis. Generally, an increased surface area provides many more chemically reactive sites and facilitates the charge carrier transfer reaction in the catalyst [34,40,45,162,189,220]. Moreover, enhanced light scattering property of rod TiO_2 -ATO enables the effective light absorption [216]. To obtain high PEC efficiency, an electrode film must be sufficiently thick to absorb more light, and simultaneously the photogenerated carriers within film must be able to reach the surface, at which they can be collected [12]. As TiO_2 -ATO heterostructures were used for a branched backbone, the relatively large surface area of the rod TiO_2 can provide efficient collection and reactive sites. This was confirmed by the low charge transfer resistance of the rod TiO_2 photoelectrode, which was ascribed to the thin and well-distributed CdS QDs on the TiO_2 surface. Furthermore, as mentioned above, TiO_2 can serve as a charge-transfer bridge between CdS and ATO. Therefore, the better performance of the rod TiO_2 compared to the other types is attributed to the high surface area, effective light absorption path and the efficient charge collection property.

To increase the PEC performance further, the loading amount of CdS onto the rod TiO₂-ATO heterostructure was optimized. In general, successive ionic layer adsorption and reaction (SILAR) method were more effective than ED method because CdS layer was attached uniformly by SILAR while CdS QDs was grown up by ED. Figure 5.1.14a shows TEM image of rod TiO₂-ATO heterostructure covered with CdS using a SILAR method for 7 times. Although the CdS material was thickly attached, a well-ordered branched structure was preserved. The thickness of the CdS layer is around 20 nm (Inset of Figure 5.1.14a). As shown in Figure 5.1.14b, the photocurrent density was 7.75 mA/cm² at 0.4 V vs. RHE, which is an increase of more than 23 % from that of the CdS-rod TiO₂-ATO with a thickness of 7 nm. It is relatively high as compared to other CdS-sensitized structures with photocurrent levels [161,189,217,219-225]. This is attributed to the fact that the photocurrent of the TiO₂-ATO heterostructures was saturated rapidly at a very low applied bias compared to other structures. This result demonstrates that the epitaxial TiO₂-ATO heterostructure is an efficient backbone for the collection and transport of charge carriers generated from a sensitizer, also demonstrating that the strategy of modulating each PEC factor separately is an effective approach for the optimization of the PEC performance.

Furthermore, good stability and efficient hydrogen generation [226,227] was demonstrated with a CdS-rod TiO₂-ATO electrode. As shown in Figure 5.1.15, CdS layer in TiO₂-ATO heterostructure have good stability for a long-time PEC performance. Hydrogen evolution rate of CdS-TiO₂-ATO electrode in PEC device at 1st, 2nd and 3rd cycle was 95 $\mu\text{mol}/\text{cm}^2\cdot\text{h}$, 90 $\mu\text{mol}/\text{cm}^2\cdot\text{h}$ and 86 $\mu\text{mol}/\text{cm}^2\cdot\text{h}$, respectively. The ability of hydrogen evolution at 3rd cycle was still over 90 % of that at 1st cycle. It indicates that CdS-TiO₂-ATO heterostructure have good stability. The good stability of CdS sensitized rod TiO₂-ATO heterostructure is attributed to their geometric structure and morphology. In rod TiO₂-ATO heterostructure, the excited electrons and holes can be efficiently transferred to the Pt and electrolyte, respectively, due to high surface area and thin CdS layer. It prevents the photocorrosion of electrode. Contrastingly, it have been reported that, for the quantum dot sensitized electrodes (e.g. TiO₂-ATO or CdSe-TiO₂-ATO) without passivation layer (e.g. ZnS), the hydrogen evolution rate steadily decreases with the operation time, which is ascribed to the photocorrosion of these electrodes [227]. Passivation layer also acts as a role of preventing the recombination of excited electrons to the oxidized species in the electrolyte. In the rod TiO₂-ATO heterostructure, beneficial geometrical and structural effects can replace the role of passivation layer. Therefore, the good stability

of CdS sensitized rod TiO_2 -ATO heterostructure without passivation layer is attributed to their efficient structure and morphology.

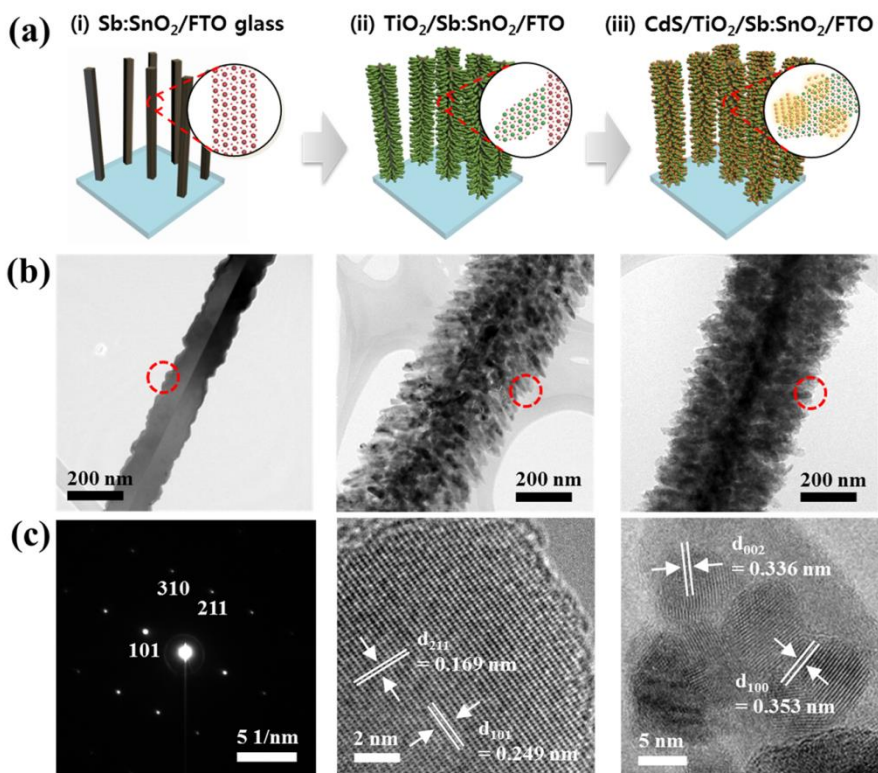


Figure 6.1.5. (a) Schematic description of the fabrication procedure : i) ATO nanobelt, ii) TiO_2 -ATO nanostructure and iii) CdS sensitized TiO_2 -ATO heterostructure; (b) TEM images at each fabrication procedure stage; (c) SAED and HRTEM images at each stage were also measured.

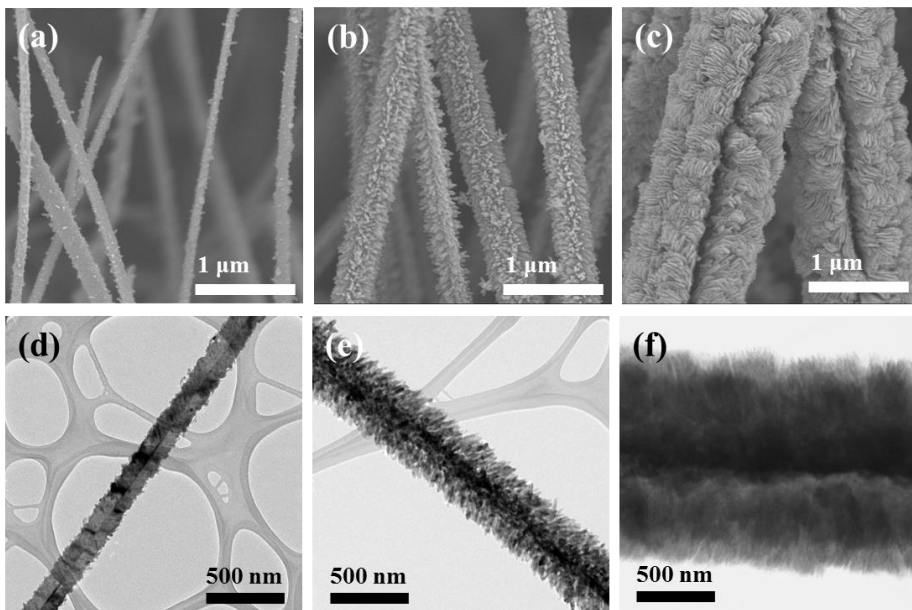


Figure 6.1.6. (a-c) Cross-sectional SEM images and (d-f) TEM images of TiO_2 -ATO heterostructures: (a, d) dot TiO_2 -ATO, (b, e) rod TiO_2 -ATO and (c, f) lamella TiO_2 -ATO.

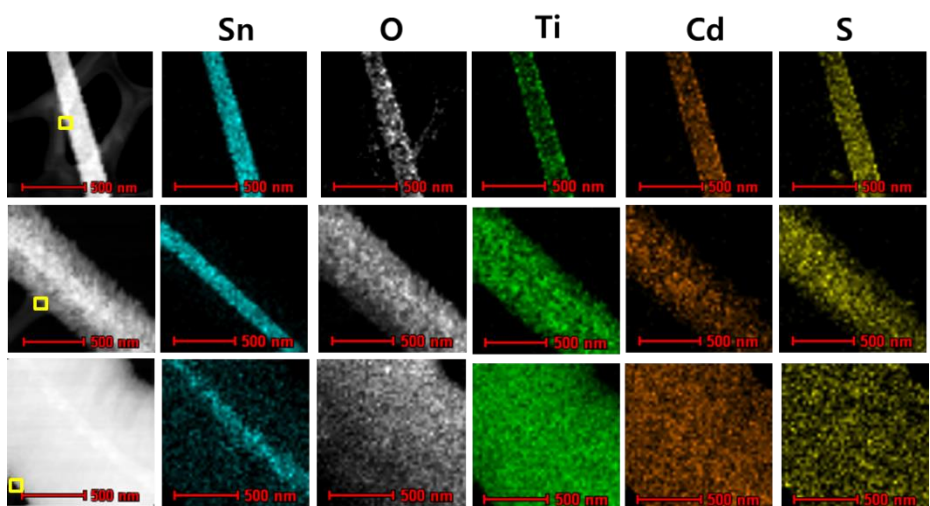


Figure 6.1.7. EDS mapping of the CdS-sensitized TiO₂-ATO heterostructure with (a) dot, (b) rod and (c) lamella shaped TiO₂. The Ti/Cd ratio was obtained by means of a quantitative analysis of the marked region.

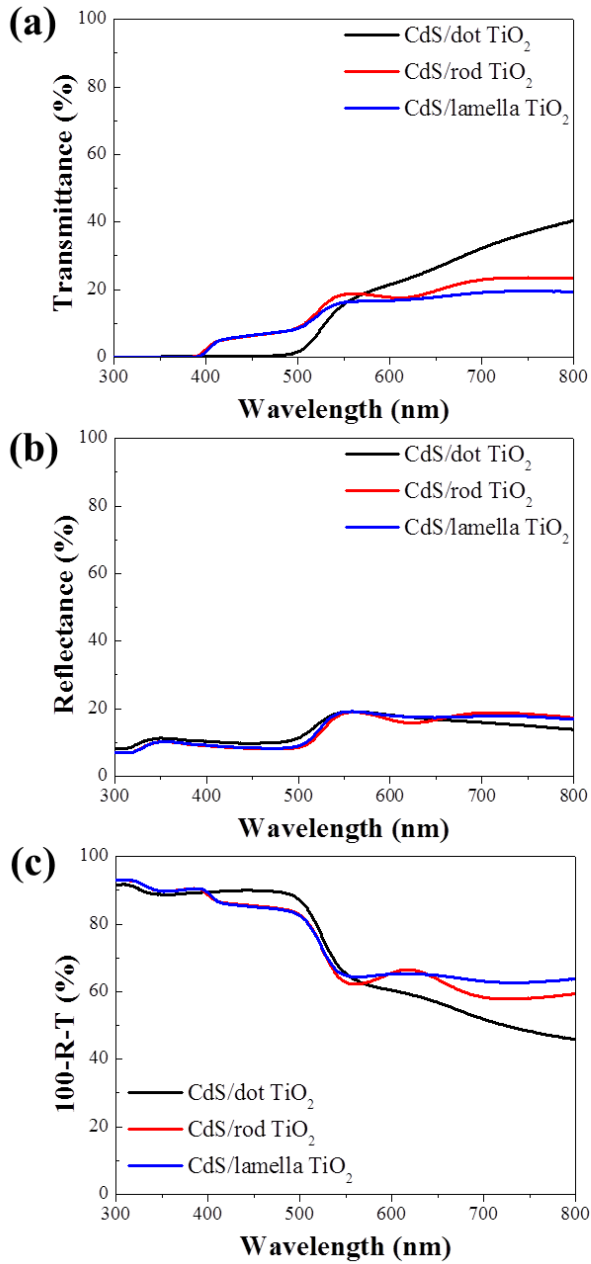


Figure 6.1.8. Optical characterization of CdS sensitized TiO₂-ATO heterostructures: (a) transmittance, (b) reflectance and (c) absorption plus scattering ($A + S = 100 - R - T$) properties.

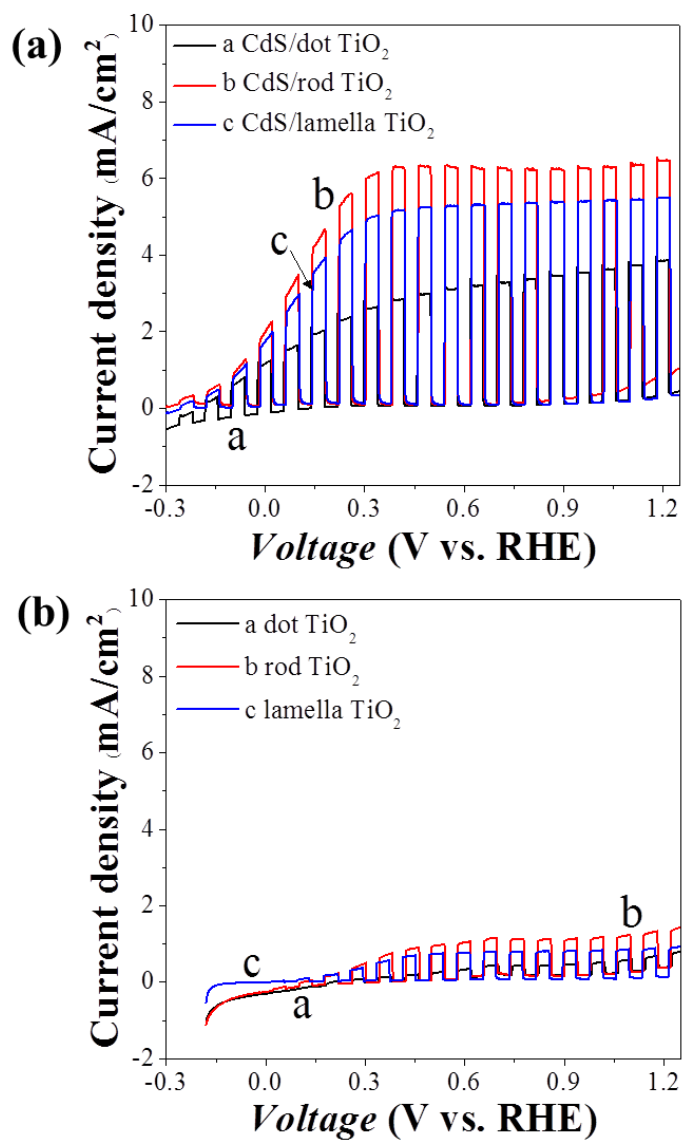


Figure 6.1.9. Chopped J - V curves under illumination by a solar simulation (AM 1.5G, 1SUN) (scan rate of 20 mV/s): (a) CdS sensitized dot, rod and lamella shaped TiO₂-ATO heterostructures and (b) bare dot, rod and lamella shaped TiO₂-ATO.

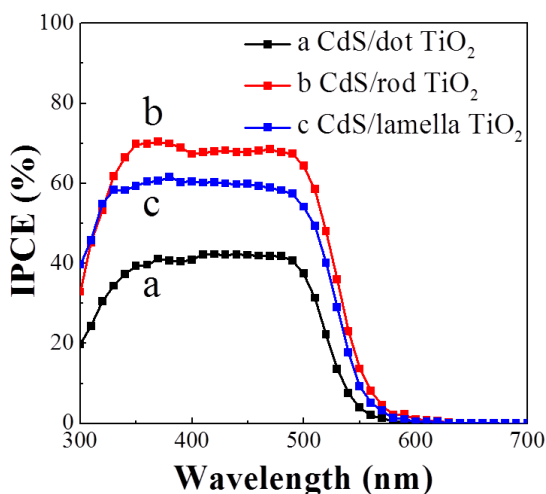


Figure 6.1.10. Measurements of the incident photon-to-electron conversion efficiency (IPCE) under 1 V vs. RHE for CdS sensitized dot, rod and lamella shaped TiO_2 -ATO heterostructures.

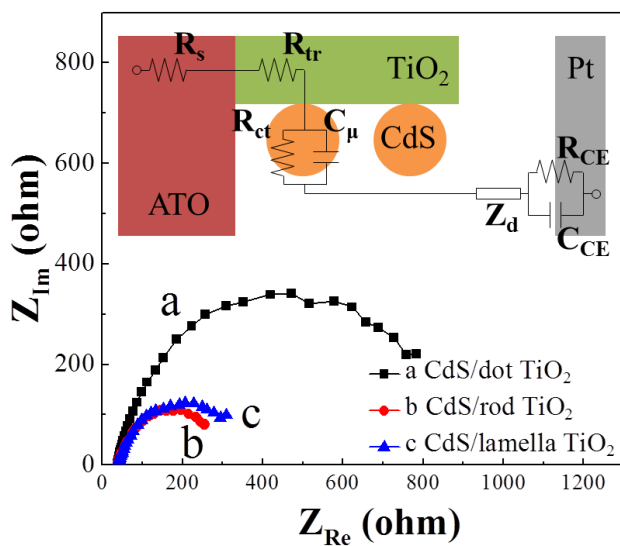


Figure 6.1.11. Nyquist plots for CdS sensitized dot, rod and lamella shaped TiO_2 -ATO heterostructures measured at 0 V vs. RHE (1 V vs. Ag/AgCl) under illumination. The inset of d shows an analogous equivalent circuit for the PEC device.

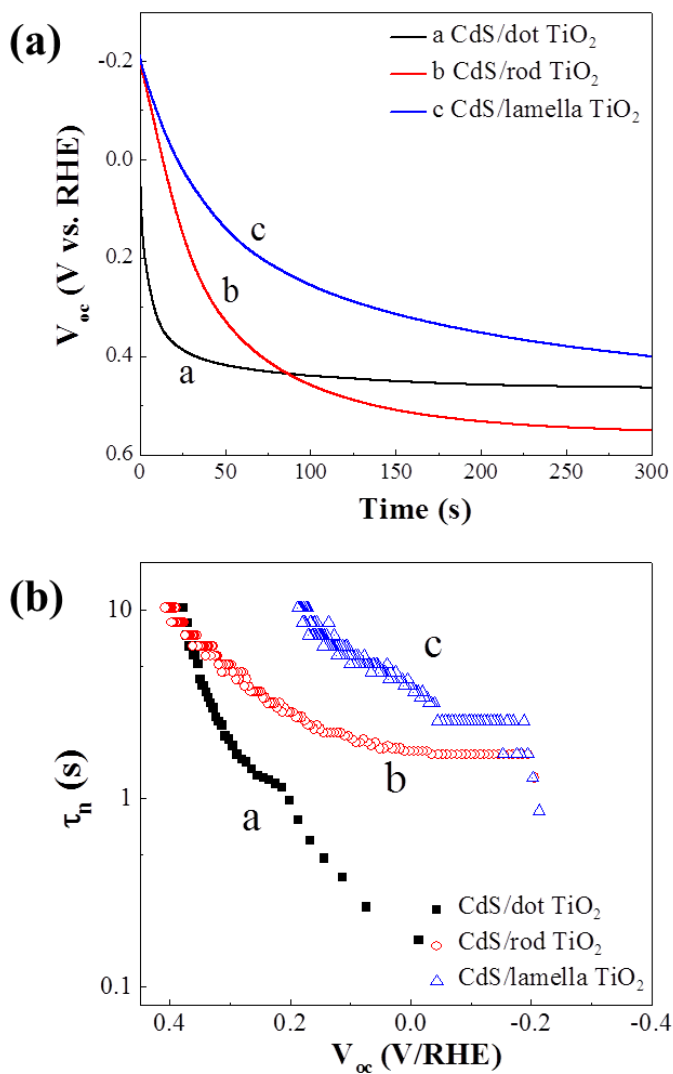


Figure 6.1.12. (a) Open circuit voltage decay spectra of the CdS sensitized TiO_2 -ATO heterostructure with dot, rod and lamella shaped TiO_2 and (b) electron lifetime as a function of open circuit voltage (V_{oc}) derived from the V_{oc} decay rates.

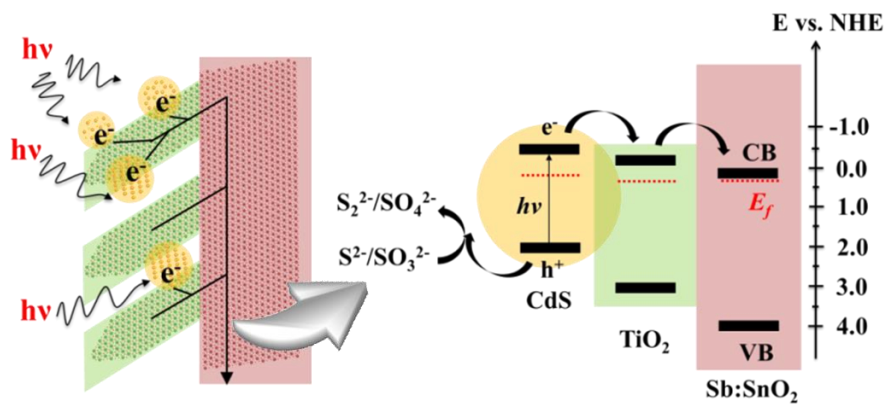


Figure 6.1.13. Diagram of relative energy levels of QD, TiO₂ and ATO at pH 0 and possible charge carrier pathway

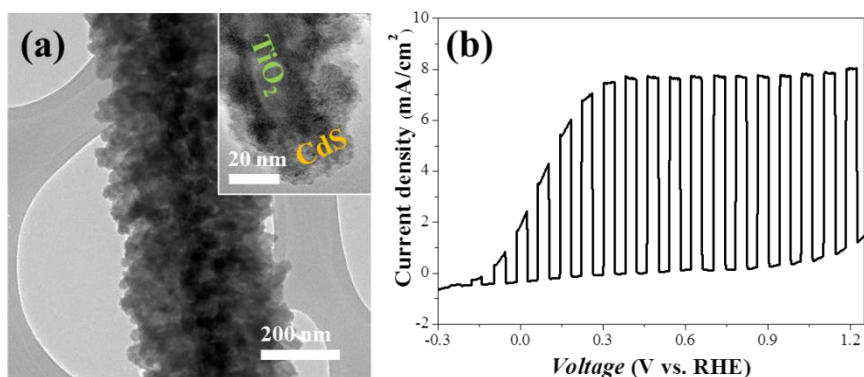


Figure 6.1.14. (a) TEM images of CdS sensitized-rod TiO₂-ATO fabricated by SILAR method (Inset shows magnification of a) and (b) Chopped *J-V* curves under Solar simulator illumination. (scan rate of 20 mV/s)

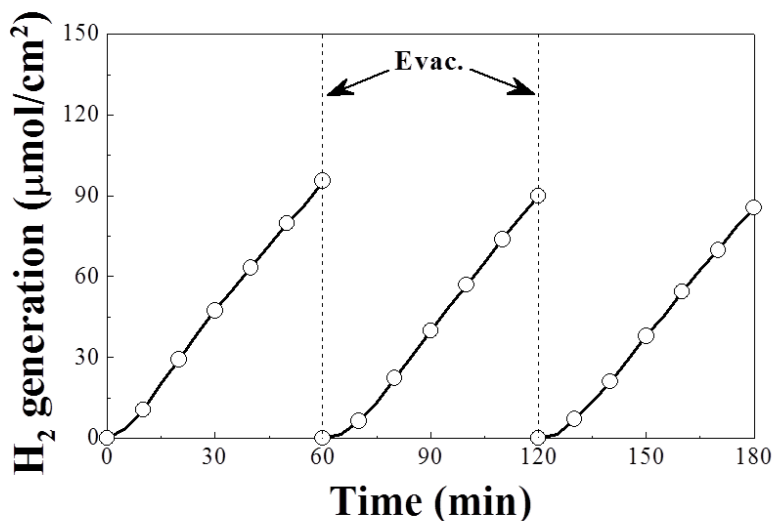


Figure 6.1.15. Time course of H₂ evolution for photoelectrochemical device equipped with CdS sensitized rod TiO₂-ATO electrode as working electrode. The applied potential was fixed to 0.6 V vs. RHE. The gas phase was evacuated at every 1 h after startup.

6.1.3 Fe₂O₃–ATO photoanode for solar water oxidation

A hematite (α -Fe₂O₃) has the short hole diffusion length (2-20 nm) and poor carrier mobility, which limits its charge separation and collection efficiency as a PEC anode[228]. Therefore, the combination of the doping and nanoarchitecturing methods has been regarded as a promising approach to improve the PEC performance of the α -Fe₂O₃ photoanode [215,229-233]. However, it is still difficult to control both the morphology and doping-level simultaneously in a wet chemical route that is simple, inexpensive, and scalable for industrial production [234,235]. It is due to critical morphology changes, such as an agglomeration by a dopant source [232]. In this chapter, a Sn self-doped, three dimensional (3D) α -Fe₂O₃ nanorod nanostructure was proposed by using a conductive ATO nanobelt array as a dopant source and a backbone. Sn atoms were successfully diffused from ATO nanobelts to Fe₂O₃ nanorods by post annealing at relatively low temperatures (650 °C). The Sn doped and hierarchical α -Fe₂O₃ nanostructure yields a superior PEC performance than the doped or branched α -Fe₂O₃ electrodes.

Doping effect

In order to incorporate the Sn from the ATO nanobelts into the α -Fe₂O₃ nanorods, as-prepared Fe₂O₃–ATO nanostructures were post-annealed at 650 °C for 24 h. Figure 5.1.16 shows the EDS mapping of as-prepared and post-

annealed Fe₂O₃-ATO, clearly demonstrating that Sn elements were successfully implanted into the α -Fe₂O₃ nanorods in the post-annealing process. Quantitative EDS point analysis indicates that the atomic ratio of Sn incorporated into Fe sites is found to be about 0.2% in the α -Fe₂O₃ nanorods after post annealing. However, no Sn signal was detected in the α -Fe₂O₃ nanorods from the as-prepared sample. EDS line-scan across the Fe₂O₃ nanorod was also conducted to confirm the distribution of Sn dopant in Fe₂O₃ matrix. Figure 5.1.17 show the EDS line-scan on the Fe₂O₃-ATO post-annealed at 650 °C for 24 h. As shown in Figure 5.1.17b, Fe element is located at the branch while Sn element is placed at the nanobelt. Interestingly, Sn element also existed in Fe₂O₃ nanorod region and amount of Sn dopant in Fe₂O₃ nanorod steadily decreased from root to edge (Figure 5.1.17c). It clearly demonstrates that Sn atoms were diffused from SnO₂ nanobelt to Fe₂O₃ nanorods through post-annealing.

The effect of Sn doping on the electronic property of α -Fe₂O₃ nanorods was investigated by Mott-Schottky analysis in the dark. The flatband potential (E_{fb}) of a semiconductor can be estimated from the intercept of the Mott-Schottky plot as in the following equation:

$$\frac{1}{C^2} = \frac{2}{q\epsilon\epsilon_0 N_D} \left(E - E_{fb} - \frac{kT}{q} \right) \quad (5)$$

where C is the specific capacitance (F/cm²), q is the electron charge, ϵ is the

dielectric constant of the material, ϵ_0 is the permittivity of the vacuum, N_D is the carrier density, E is the applied potential, k is the Boltzmann's constant, and T is the temperature (K). Figure 5.1.18 shows the Mott-Schottky plot for Fe_2O_3 -ATO nanostructures before and after post annealing at 650 °C (denoted as FS-BP and FS-AP, respectively). For comparison, α - Fe_2O_3 nanorods deposited on the FTO glass substrate before and after post annealing at 650 °C (denoted as FF-BP and FF-AP, respectively) were also observed. While the E_{fb} for Fe_2O_3 -FTO remains constant (0.6 V/RHE) consistent with literature value [236], that for Fe_2O_3 -ATO increases from 0.6 V to 0.46 V due to post annealing. This can reveal that Sn elements are effectively doped into α - Fe_2O_3 lattice at Fe_2O_3 -ATO nanostructures. Moreover, the negative shift of E_{fb} in FS-AP indicates that α - Fe_2O_3 was doped n-type, suggesting that the Sn^{4+} dopants are incorporated at the Fe^{3+} sites [237].

The apparent carrier densities of Fe_2O_3 -ATO nanostructures were also evaluated by the Mott-Schottky analysis (summarized in Table 5.1.1). The carrier density (N_D) of a semiconductor is inversely proportional to the slope of the Mott-Schottky plot as known in equation (1). Assuming that the dielectric constant of α - Fe_2O_3 is 80 in all samples, the N_D for FF-BP and FF-AP is calculated to be $5.7 \times 10^{18} \text{ cm}^{-3}$ and $8.1 \times 10^{18} \text{ cm}^{-3}$, respectively, which are comparable to the reported value for undoped hematite [238,239]. In the

case of $\alpha\text{-Fe}_2\text{O}_3/\text{SnO}_2$, the carrier density dramatically increases from $1.7 \times 10^{21} \text{ cm}^{-3}$ to $4.7 \times 10^{21} \text{ cm}^{-3}$ after post annealing, implying that Sn^{4+} dopants were effectively doped into the Fe^{3+} lattice and served as an electron donor. The FS-BP also has a much larger carrier density than the $\text{Fe}_2\text{O}_3\text{-FTO}$, which is attributed to the high carrier concentration ($>10^{20} \text{ cm}^{-3}$) of the ATO nanobelt [53]. An increased flatband potential and carrier concentration in FS-AP reveals that the development of Sn self-doped, nanobranched $\alpha\text{-Fe}_2\text{O}_3$ 3D structure was achieved.

It is interesting that the Sn elements were well doped into $\alpha\text{-Fe}_2\text{O}_3$ nanorods under the relatively low temperature of $650 \text{ }^\circ\text{C}$. According to previous reports where conventional $\alpha\text{-Fe}_2\text{O}_3$ films were deposited on the FTO glass substrate, high temperature annealing above $800 \text{ }^\circ\text{C}$ is required for the sufficient diffusion of Sn from the FTO glass substrate to the Fe_2O_3 compound [240], leading to severe glass distortion [241]. Sn elements in the FTO start to diffuse in small amount at $650 \text{ }^\circ\text{C}$, inducing the little increase of photocurrent [232]. Therefore, $650 \text{ }^\circ\text{C}$ is expected to be an optimized doping temperature to minimize glass distortion. As discussed previously the doping amount at $650 \text{ }^\circ\text{C}$ was too small to increase the electronic property of $\text{Fe}_2\text{O}_3\text{-FTO}$. In contrast doped Sn sufficiently affected the electronic property and increased the flat band potential and carrier concentration of $\text{Fe}_2\text{O}_3\text{-ATO}$ at $650 \text{ }^\circ\text{C}$. The ATO

nanobelts function as an abundant dopant source as well as the conductive backbone.

Optical property

The optical characteristics of Fe_2O_3 -FTO and Fe_2O_3 -ATO after post annealing were measured at a wavelength range from 300 to 800 nm. The CBD reaction was fixed to 4 h for both samples. Figure 5.1.19 shows the transmittance, reflectance, and absorption with scattering (A+S) spectra of FF-AP and FS-AP. Both samples have similar reflectance properties above the bandgap of $\alpha\text{-Fe}_2\text{O}_3$ ($\lambda < 620$ nm), but different transmission and absorption spectra. FS-AP exhibits less transmittance and high absorption properties than FF-AP. The light absorption with scattering over a wavelength range from 300 nm to 620 nm is 82 and 91 % for FF-AP and FS-AP, respectively. Furthermore, a nonzero baseline was observed for both samples over 620 nm, which is due to the scattering events in the $\alpha\text{-Fe}_2\text{O}_3$ nanorods [242]. This significant light scattering in the FS-AP increases the light absorption path length. Consequently, this induces the higher absorption property in comparison with FF-AP. Therefore, the 3D branched $\alpha\text{-Fe}_2\text{O}_3$ nanostructure is beneficial to light absorption, which is attributed to an increase of light-scattering by the introduction of hierarchically structures.

Photoelectrochemical performance

Linear sweep voltammograms were collected for Fe₂O₃-ATO and Fe₂O₃-FTO samples in a three-electrode PEC device. Figure 5.1.20 depicts a set of photocurrent-potential (*J-V*) curves from FS-BP and FS-AP photoanodes fabricated for 2 h, 4 h, and 12 h in CBD method. For as-prepared (FS-BP) samples, the photocurrent increases as the reaction time increases. After post annealing, all three samples achieved significantly enhanced photocurrent density: 0.66, 0.88 and 0.82 mA/cm² at 1.23 V vs. RHE for 2h, 4h, and 12 h, respectively. PEC behavior through post-annealing condition (different annealing time and temperature) was also investigated using α -Fe₂O₃/SnO₂ prepared for 4 h in CBD method (Figure 5.1.21). As shown in Figure 5.1.21a, the photocurrent level increased as annealing time increased. As annealing temperature increased, the photocurrent level also increased and saturated at 700 °C. Because glass distortion occurred at 700 °C, it was concluded that optimum post-annealing temperature and time is 650 °C and 24 h, respectively. The photoresponse of Fe₂O₃-FTO samples were measured in the same conditions for Fe₂O₃-ATO, as shown in Figure 5.1.20b. Although the values were still low, the photocurrents in as-prepared (FF-BP) samples increased by post annealing. The photocurrents of FF-AP for 2h, 4h, and 12 h

are 0.19, 0.28, and 0.12 mA/cm² at 1.23 V vs. RHE, respectively. These results suggest that the great increase of the PEC performance in FF-AP can be attributed to the highly increased Sn doping ratio. Moreover, the best photocurrent value in FS-AP (0.88 mA/cm² for 4 h) is 3 times higher than that in FF-AP (0.28 mA/cm² for 4 h). It is noteworthy that these photocurrent levels could be achieved by low temperature (650 °C) annealing. As comparison with other hematite electrodes post-annealed at same condition (650 °C), this value (0.88 mA/cm²) is relatively high [215,232,240,241]. It indicates that doped and branched structures effectively improve PEC performance.

The PEC performance improvements in Fe₂O₃-ATO photoanodes can be described in terms of three main factors: structural, optical, and electronic property. Fe₂O₃-ATO has a well-assembled and branched nanostructure, which can enlarge the surface contact area with an electrolyte. Additionally, a vertically aligned backbone and dense arranged branch lead to the significant light scattering that increases the light absorption property. Furthermore, the conductive ATO backbone can assist the transport of electrons from each α -Fe₂O₃ nanorods to the counter electrode. Because ATO nanobelts are also an abundant dopant source, the beneficial electronic property of α -Fe₂O₃ nanorods can be obtained by self-doped Sn after annealing at a relatively low

temperature (650 °C).

To understand the electron dynamics in Fe₂O₃-ATO, electrochemical impedance spectra (EIS) analysis was conducted under solar illumination. Figure 5.1.22 shows the Nyquist plots for FF-BP, FF-AP, FS-BP and FS-AP at 1.23 V/RHE. It is well known that semicircles in the frequency range of 1 to 1000 Hz conform to the charge transfer resistance at the semiconductor/electrolyte interface. For both FF and FS samples, post-annealed electrode gave smaller semicircles than the as-prepared, indicating that self-doped Sn has substantially lower charge transfer resistance. In addition, FS-AP has the lowest charge transfer resistance, which means that the photogenerated holes in FS-AP could easily transfer to an electrolyte, which is explained by two aspects: band bending and electrical conductivity. Given that hematite has a small hole diffusion length (~2 nm) [243] and short excited state lifetime (~1 ps) [244], most of the photo-induced electron-hole pairs recombine very quickly. Thus, significant anodic bias is required to effectively move the electrons and holes within the space charge layer [245]. Because Sn doped α -Fe₂O₃ has a higher flat band potential than the undoped, valence band bending on the surface of doped α -Fe₂O₃ is much steeper than the undoped at the same voltage. Therefore, the voltage drop for the hole transfer becomes larger in Sn doped α -Fe₂O₃ than undoped, inducing low hole

transfer resistance. The carrier generation from Sn dopant improves the electrical conductivity of α -Fe₂O₃, promoting the electron transport in Sn doped α -Fe₂O₃. Thus, residual holes that avoid recombination with electrons can accumulate at the α -Fe₂O₃ surface and drive water oxidation. Consequently, the low hole transfer resistance of post annealed Fe₂O₃-ATO is attributed to the enhanced flat band potential and carrier density in α -Fe₂O₃ nanorods by self-doped Sn from SnO₂ nanobelt.

In terms of structural, optical, and electronic property, the result that the 4 h sample exhibit the best PEC performance compared to the other samples (2 h and 12 h) could be interpreted. In viewpoint of structural property, as CBD reaction time increased, thickness and length of Fe₂O₃ increased, but length and density of ATO nanobelt decreased (Figure 4.3.2). Thus, surface areas of Fe₂O₃-ATO were almost saturated at 4 h and 12 h samples. In addition, absorption properties were also saturated at 4 h and 12 h samples. Doping level from EDS spectra was calculated to be 0.2 at% in both 4 h and 12 h samples. So, 4 h and 12 h samples exhibit higher PEC performance than 2 h sample. As mentioned above, Fe₂O₃ nanorod of 4 h sample is slightly thinner than that of 12 h sample. Therefore, slightly higher value (0.88 mA/cm²) of 4 h sample than that (0.82 mA/cm²) of 12 h sample is attributed that 4 h sample has relatively short hole diffusion path from Fe₂O₃ nanorod to electrolyte.

Although Sn-doped hematite nanobranched electrodes in this study possess the enhanced structural, optical, and electrical properties compared to those from other studies, the products in this study show a lower photocurrent density than the previous research for several reasons [230,232,238,241,246-248]. First of all, doping concentration is lower than previous value. The samples in current study were doped by only low temperature annealing, whereas chemical and physical doping processes were used in early reports. Also, as discussed above, there is a trade-off between morphological merits (surface area and absorption property) and demerit (hole diffusion path from Fe_2O_3 nanorod to electrolyte) in this branched structure. Further study is needed to determine the optimum Fe_2O_3 nanorod length for achieving superior PEC performance.

Table 6.1.1. The electrical properties of Fe₂O₃-FTO at 4 h before and after post annealing at 650 °C and Fe₂O₃-ATO for 4 h before and after post annealing at 650 °C. (ϵ : dielectric permittivity, E_{fb} : flat band potential, N_D : carrier concentration)

	ϵ	E_{fb} (V / RHE)	N_D (cm ⁻³)
Fe ₂ O ₃ -FTO BP	80	0.6	5.7×10 ¹⁸
Fe ₂ O ₃ -FTO AP	80	0.6	8.1×10 ¹⁸
Fe ₂ O ₃ -ATO BP	80	0.6	1.7×10 ²¹
Fe ₂ O ₃ -ATO AP	80	0.46	4.7×10 ²¹

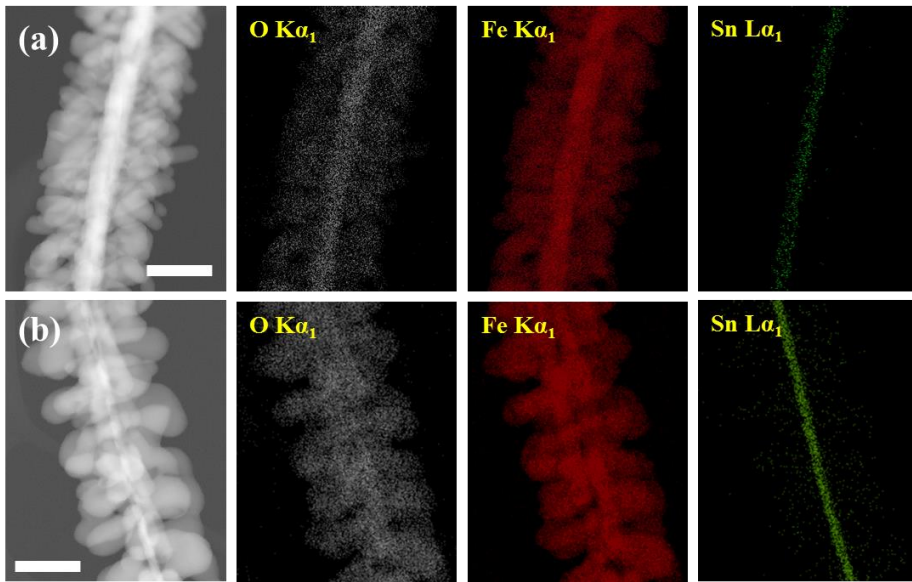


Figure 6.1.16. EDS elemental Mapping of a Fe_2O_3 -ATO at 12 h (a) before and (b) after post annealing at 650 °C during the 24 h. Scale bar : 200 nm

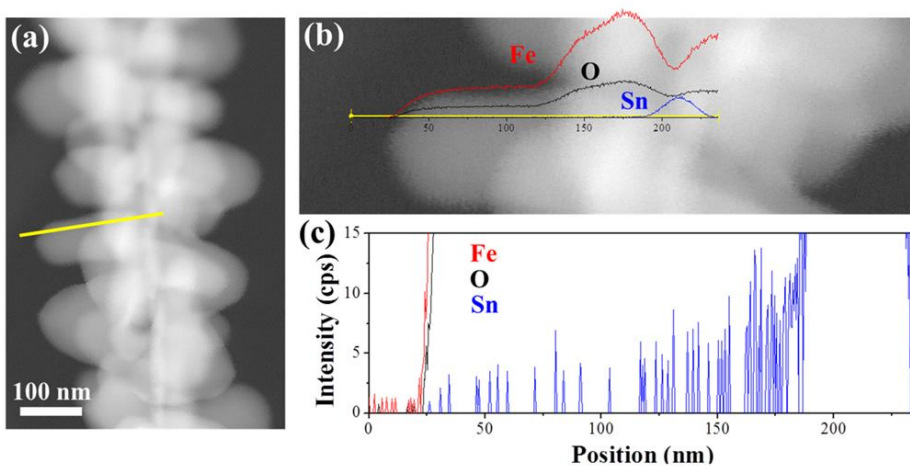


Figure 6.1.17. (a) A Dark field STEM image of Fe₂O₃-ATO for 12 h, (b) the EDS line-scan across the Fe₂O₃ branch revealing the concentration and distribution of Fe, Sn, and O, and (c) magnified EDS line-scan indicating the Sn distribution in the Fe₂O₃ nanorod.

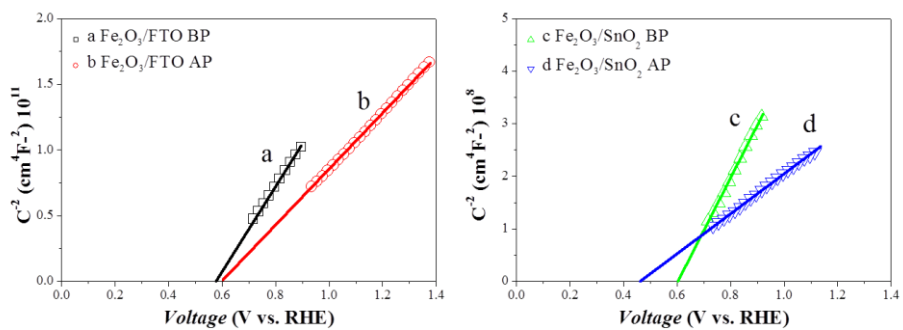


Figure 6.1.18. (a) Mott-Schottky analysis of Fe_2O_3 -FTO at 4 h (a) before and (b) after post annealing at 650°C and Fe_2O_3 -ATO for 4 h (c) before and (d) after post annealing at 650°C under frequency of 500 Hz.

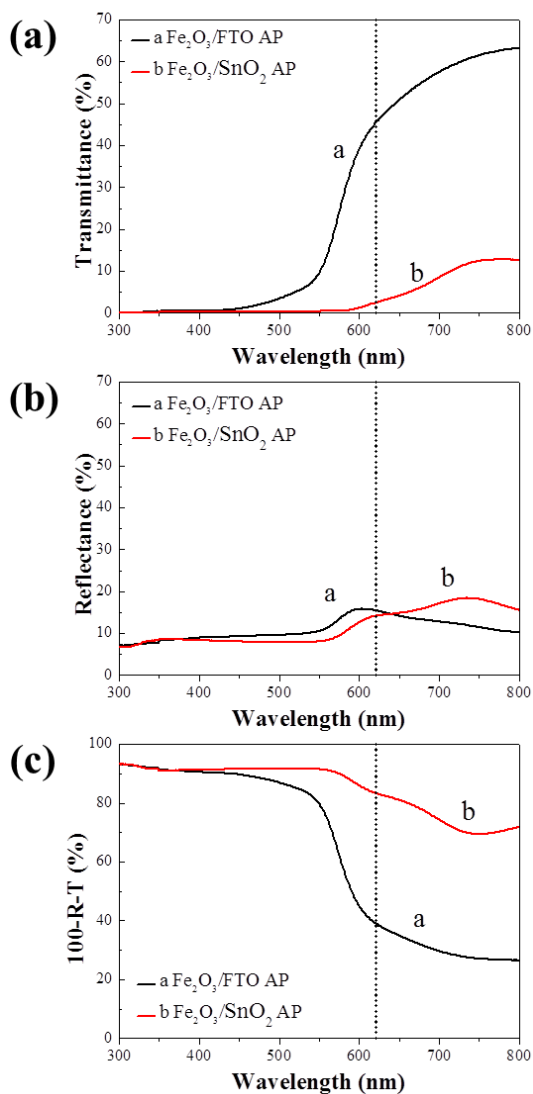


Figure 6.1.19. Optical characterization of a Fe₂O₃-FTO and Fe₂O₃-ATO at 4 h after post annealing at 650 °C during the 24 h : (a) Transmittance (T), (b) reflectance (R) and (c) absorbance plus scattering ($A + S = 100 - R - T$) properties. A vertical line presents the 620 nm wavelength conforming to the bandgap of α -Fe₂O₃.

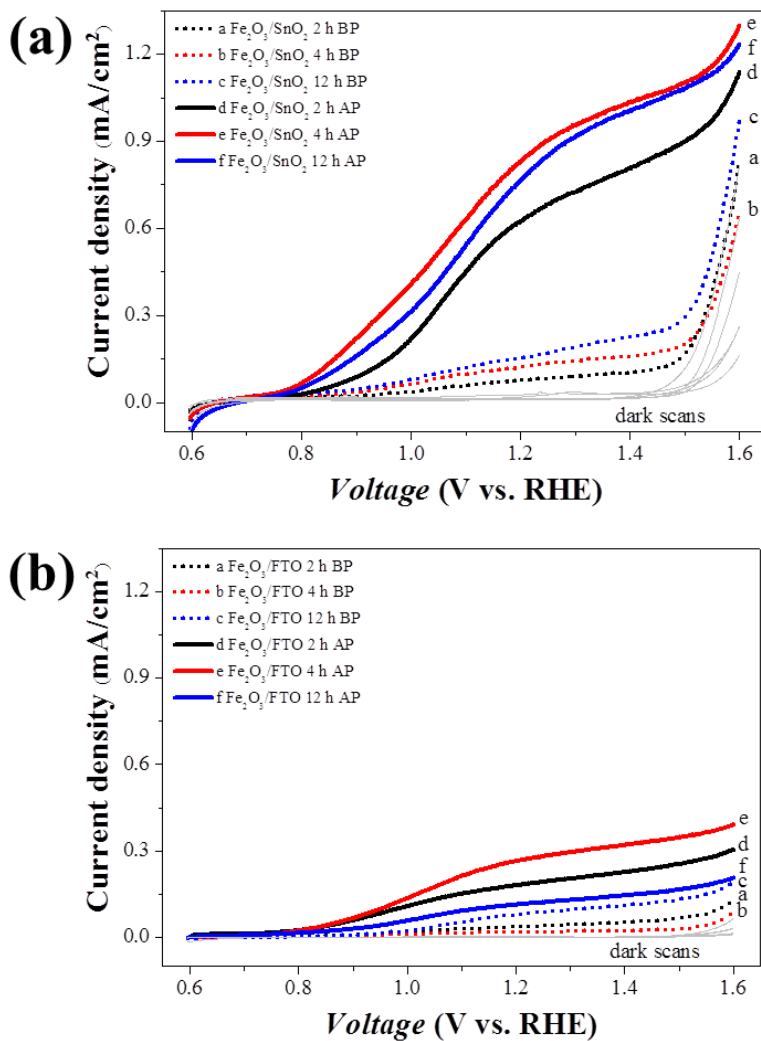


Figure 6.1.20. (a) *J-V* curves collected for Fe₂O₃-ATO photoanodes prepared for a different reaction time before and after post annealing (650 °C and 24 h), with a scan rate of 10 mV/s, 1 M NaOH electrolyte (pH 13.6) and AM 1.5G simulated solar light at 72 mW/cm². (b) *J-V* curves of α-Fe₂O₃ nanorods on the FTO substrate at different times before and after post annealing (650 °C and 24 h) under same conditions.

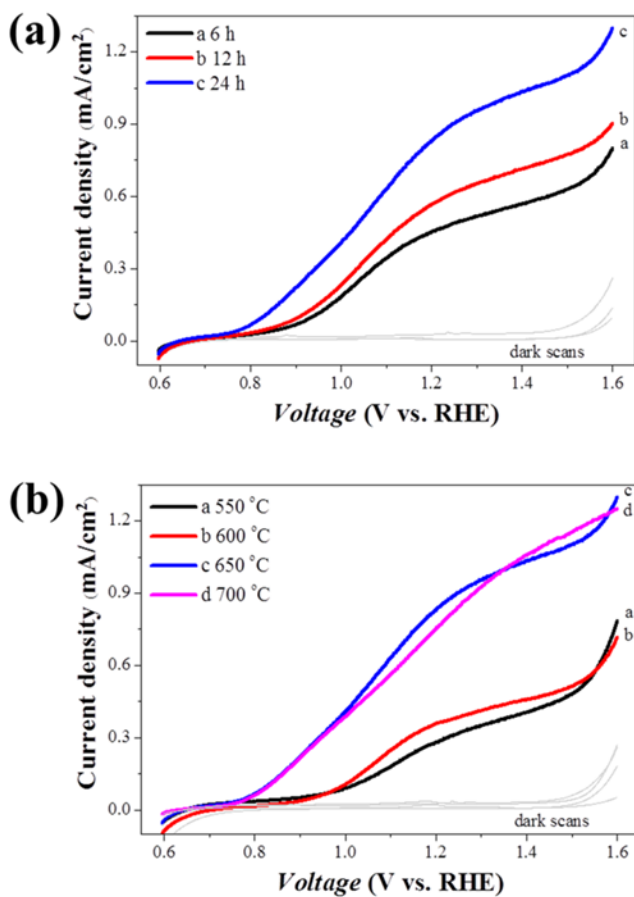


Figure 6.1.21. (a) *J-V* curves collected for Fe₂O₃-ATO photoanodes prepared at 100 °C for 4 h, with a scan rate of 10 mV/s, 1 M NaOH electrolyte (pH 13.6) and AM 1.5G simulated solar light at 72 mW/cm². Each sample was post-annealed at 650 °C for different reaction time (6 h, 12 h and 24 h). (b) *J-V* curves of Fe₂O₃-ATO photoanodes prepared at 100 °C for 4 h. Each sample was post-annealed for 24 h at different temperature (550 °C, 600 °C, 650 °C and 700 °C).

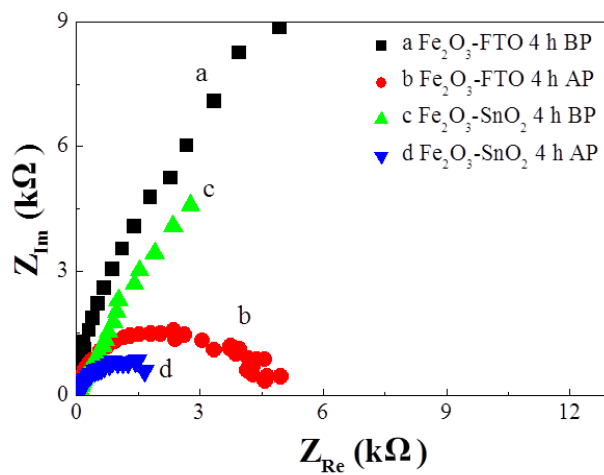


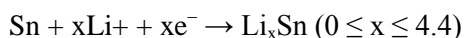
Figure 6.1.22. Nyquist plots of a Fe₂O₃-FTO at 4 h (a) before and (b) after post annealing at 650 °C and a Fe₂O₃-ATO at 4 h (c) before and (d) after post annealing at 650 °C under 1.23 V/RHE.

6.2 Li ion battery

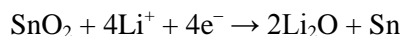
6.2.1 TiO₂-ATO anode for Li ion battery

Electrochemical performance of both TiO₂ and SnO₂

The TiO₂-ATO nanostructure samples with the 130-nm-length TiO₂ nanorod branches were subjected to electrochemical evaluation. The Li electroactivities of the pure ATO nanobelts and TiO₂-ATO nanostructured electrodes were confirmed by cyclic voltammograms (CVs) shown in Figure 5.2.1. CVs were performed over the voltage window of 2.5–0.0 V versus Li/Li⁺. The appearance of CV profiles obtained at two electrodes was similar to that given in other reports on the SnO₂ films and nanostructured electrodes [41, 42]. A large irreversible reduction peak observed near 0.53V during the first cathodic process may be ascribed to the formation of solid electrolyte interface (SEI) layer and/or partial decomposition of active material structures. In subsequent cycles, two pairs of peaks corresponding to c/c' (0.55 V/0.7 V) and d/d' (0.16 V/0.55 V) were obviously observed in the CV profile (Figure 5.2.1a and b). These are related to the formation of Li_xSn according to the following process: [249,250]



Other pairs of peaks marked by a/a' (1.26 V/1.94 V) and b/b' (0.87 V/1.34 V) were derived from Li₂O formed through the following reaction: [250,251]



It should be noted that second reaction is generally considered to be an irreversible reaction. However, some researchers reported recently that the reaction was reversible to some extent [251,252]. As observed after the first cycle, the redox peaks of the pure ATO nanobelt electrode (Figure 5.2.1a) decreased faster compared to those of the TiO₂-ATO nanostructured electrode (Figure 5.2.1b), while the current density of the former was higher than that of the latter. Based on these results, it is found that TiO₂ nanorod branches can bring about an improvement of the cyclability of the ATO nanobelt electrode.

To evaluate the electrochemical performance of the pure ATO nanobelt and TiO₂-ATO nanostructured electrodes, typical voltage-specific capacity curves were recorded at a current rate of C/5 (Figure 5.2.2). The metallic Sb reacts with Li by an alloying mechanism [253,254]. However, in this work, the contribution of Sn dopant to the electrochemical performance of the TiO₂-ATO nanostructured electrodes was not considered because its atomic concentration was very low (below 1 at%). In the case of the pure ATO nanobelt electrode, the first specific discharge capacity reached ~1138 mA h g⁻¹. Such abnormally high discharge capacity was attributed to the irreversible decomposition of SnO₂ into active Sn nanodomains and inactive

Li₂O matrix, as evidenced by the voltage plateau observed near 0.75 V (Figure 5.2.2a), and the irreversible formation of a SEI layer [255,256]. Although discharge-charge properties of the pure ATO nanobelt electrode were stabilized after a large irreversible reaction in the first cycle, the specific capacity decreased gradually upon prolonged cycling (Figure 5.2.2a). In the case of the TiO₂-ATO nanostructured electrode, the appearance and tendency of the voltage-specific capacity profile were similar to that of the ATO nanobelt electrode (Figure 5.2.2b), indicating both electrodes reacted with Li by the same mechanism. However, in the initial cycles, the TiO₂-ATO nanostructured electrode delivered lower specific capacity compared to the pure ATO nanobelt electrode because of the capacity contribution of TiO₂ nanorods with low theoretical capacity. It is noteworthy that the theoretical capacity of the TiO₂-ATO nanostructured electrode calculated on the basis of ATO and TiO₂ mass was 528 mA h g⁻¹.

Figure 5.2.3 shows the variation of the discharge-charge specific capacity versus the cycle number at a rate of C/5, based on the theoretical capacity of each electrode, for the pure ATO nanobelt and TiO₂-ATO nanostructured electrodes. In region I shown in Figure 8, the specific capacity of the pure ATO nanobelt electrode (592 mA h g⁻¹ in the 40th cycle), which surpassed the values that have been reported on ATO-based electrodes [150,152]. It

was higher than that (432 mA h g^{-1} in the same cycle) of the $\text{TiO}_2\text{-ATO}$ nanostructured electrode because of higher theoretical capacity. However, its reversible capacity faded slightly faster compared to that of the $\text{TiO}_2\text{-ATO}$ nanostructured electrode. This is ascribed to the volume expansion of ATO nanobelts occurring during Li insertion/extraction. Subsequently, in region II, the specific capacity of the ATO nanobelt electrode faded drastically from 592 mA h g^{-1} (40th cycle) to 92 mA h g^{-1} (70th cycle) because of the pulverization of the ATO nanobelts induced by the limits of alleviating volume change. In contrast to the ATO nanobelt electrode, the $\text{TiO}_2\text{-ATO}$ nanostructured electrode exhibited superior cycle retention in regions I and II. In particular, it was confirmed that the specific capacity between two electrodes was reversed in the 54th cycle, indicating longer cycle life of the $\text{TiO}_2\text{-ATO}$ nanostructured electrode, as seen in Figure 8. The inset of Figure 8 shows cycling performance measured by considering the area (0.785 cm^2) of the $\text{TiO}_2\text{-ATO}$ nanostructured electrode at a current density of 135 mA cm^{-2} during 50 cycles. The $\text{TiO}_2\text{-ATO}$ nanostructured electrode exhibited superior cycle stability and a high reversible capacity of 318 mA h cm^{-2} after 50 cycles, which were better than $\text{SnO}_2/\text{TiO}_2$ -based electrodes with various morphologies reported previously [65-67].

Additionally, the $\text{TiO}_2\text{-ATO}$ nanostructured electrode demonstrated

outstanding rate capabilities, as depicted in Figure 5.2.4. The electrode delivered high reversible discharge capacities of 740 mA h g⁻¹ at 0.1 C, 635 mA h g⁻¹ at 0.2 C, 545 mA h g⁻¹ at 0.5 C, 460 mA h g⁻¹ at 1 C, and 340 mA h g⁻¹ at 3 C, which surpassed the values reported on SnO₂/TiO₂ nanotube electrodes [65,66] and were comparable to pure ATO nanopowder electrodes reported previously [151]. Moreover, the TiO₂-ATO nanostructured electrode cycled with a high Coulombic efficiency of ~95% at 0.1 C, ~96% at 0.2 C, ~95% at 0.5 C, ~94% at 1 C, and ~90% even at 3 C. Furthermore, the capacity of the TiO₂-ATO electrode was higher compared with that of the pure ATO electrode under high rate above 1 C (Figure 5.2.5), indicating that the rate performance can be enhanced by nanosized rutile TiO₂ decoration.

The aforementioned superior electrochemical performance of the TiO₂-ATO nanostructured electrodes can be explained by a variety of beneficial factors: (i) the TiO₂ nanorods could efficiently mitigate the severe volume expansion of the ATO nanobelts occurring during the Li-alloying/de-alloying process. (ii) The epitaxial relationship between ATO nanobelts and TiO₂ nanorods facilitates the formation of structures without defects such as dislocations in the interface, resulting in the minimization of electron loss, thereby enhancing Li storage. (iii) As is known, the Sb incorporation into

SnO₂ nanobelts produced advantageous effects such as the inducement of high electronic conductivity and enhanced formation, restrained crystallite growth, and efficient dispersion into amorphous Li₂O matrix of metallic Sn nanoparticles formed during cycling [150-153].

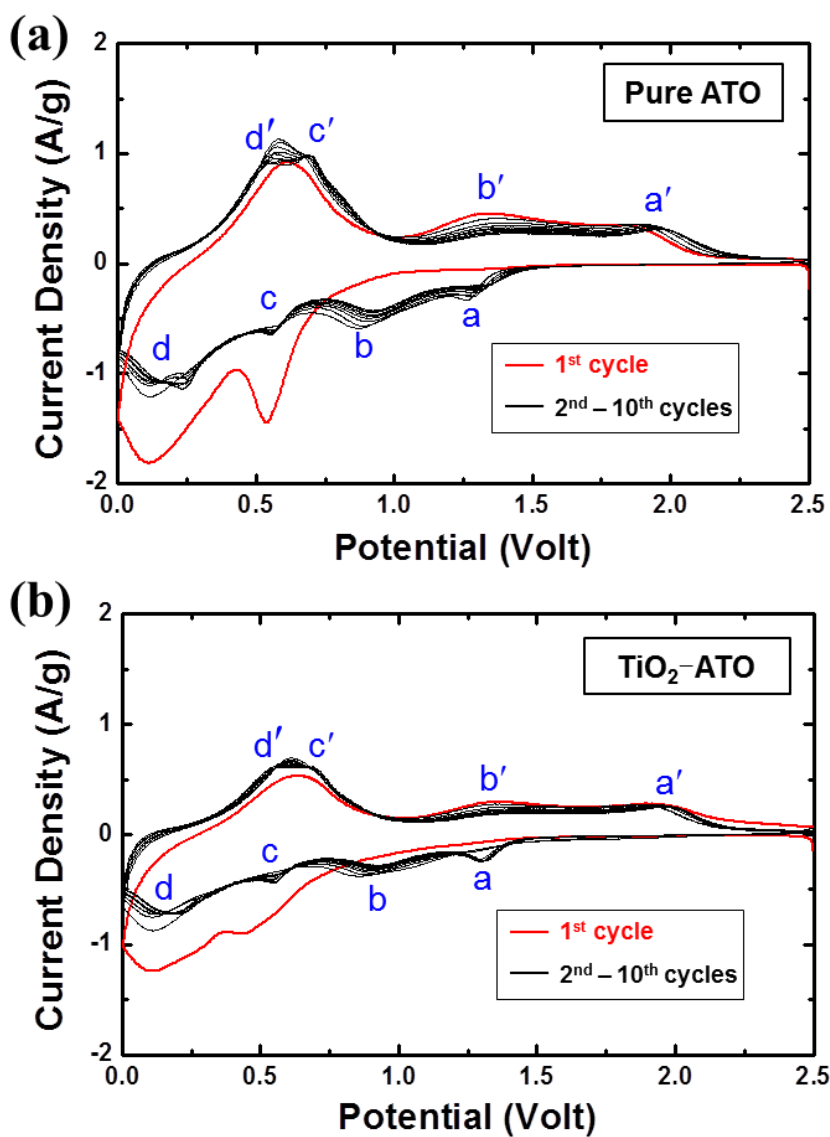


Figure 6.2.1. Cyclic voltammograms of the (a) pure ATO nanobelt and (b) TiO₂-ATO nanostructured electrodes at scanning rate of 0.3 mV s⁻¹ in the first ten cycles.

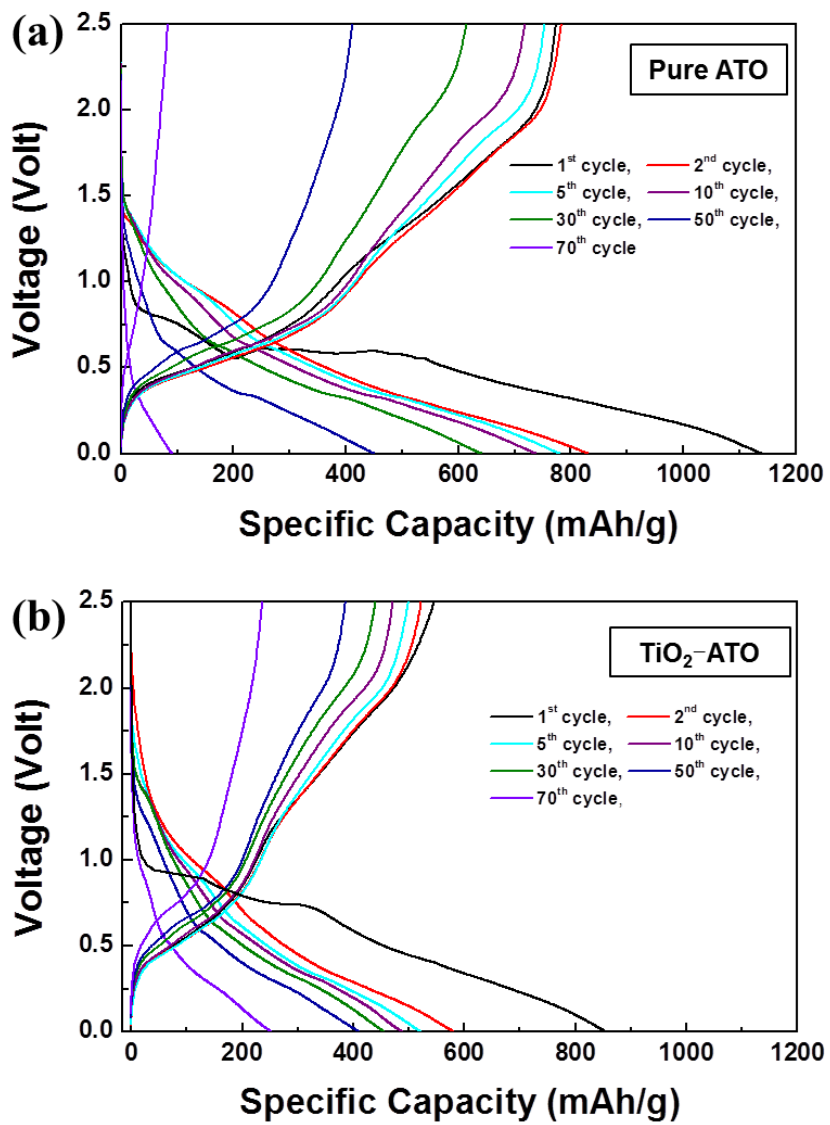


Figure 6.2.2. Charging-discharging curves of the (a) pure ATO nanobelt and (b) TiO₂-ATO nanostructured electrodes at a rate of C/5.

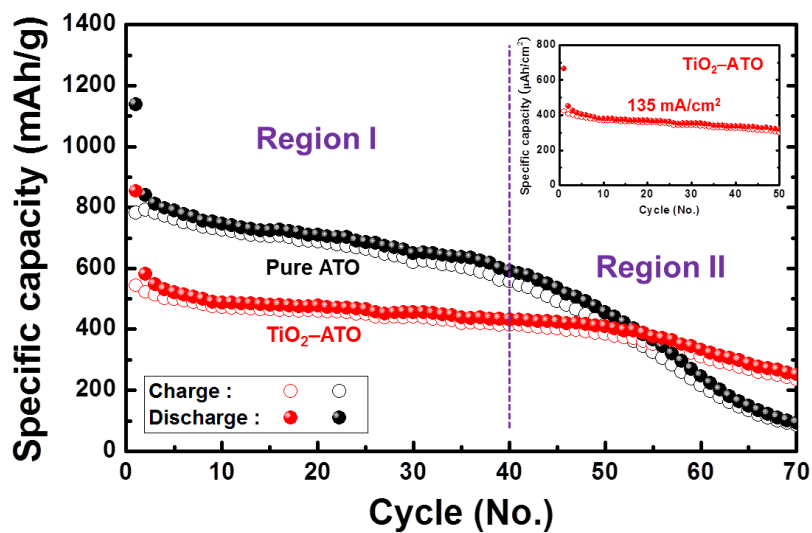


Figure 6.2.3. Variation of the discharge-charge specific capacity versus the cycle number at a rate of C/5 for the pure ATO nanobelt and TiO_2 -ATO nanostructured electrodes. Inset shows cycling performance of the TiO_2 -ATO nanostructured electrode measured by considering area of the electrode at a current density of 135 mA cm^{-2} .

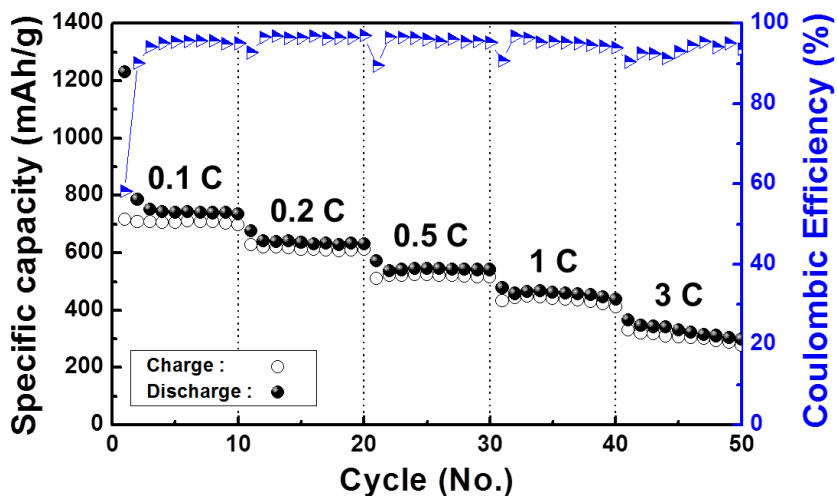


Figure 6.2.4. Specific capacity versus cycle number of the $\text{TiO}_2\text{-ATO}$ nanostructured electrode cycled ten times at every C-rate (0.1 C, 0.2 C, 0.5 C, 1 C, and 3 C) and its corresponding Coulombic efficiency.

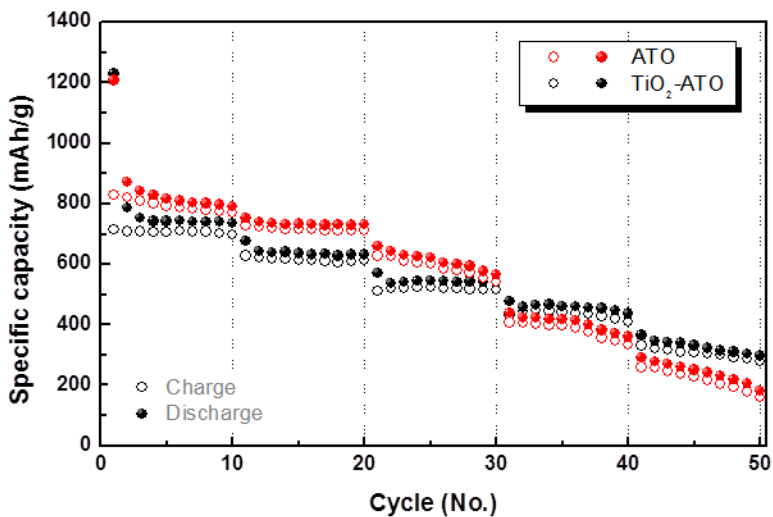


Figure 6.2.5. Specific capacity versus cycle number of ATO nanobelts and $\text{TiO}_2\text{-ATO}$ electrodes cycled ten times at every C-rate (0.1 C, 0.2 C, 0.5 C, 1 C, and 3 C).

Electrochemical performance of only TiO₂

To investigate the electrochemical performance of only TiO₂ nanorods in TiO₂-ATO nanostructured electrode, the voltage-specific capacity curves over the voltage window of 2.5–1.0 V versus Li/Li⁺ was recorded (Figure 5.2.6). The cell was galvanostatically cycled at various C rates which was increased sequentially from 0.1 C to 2 C (1 C = 168 mA g⁻¹ based on the reaction, TiO₂ + 0.5Li = Li_{0.5}TiO₂) [26]. High discharge capacities of 267 and 214 were obtained at the rate of 0.1 and 0.2, indicating that 0.79 (Li_{0.79}TiO₂) and 0.64 (Li_{0.64}TiO₂), respectively, of Li ions were inserted into the TiO₂. Moreover, there was no clear plateau, which is frequently generated due to a two phase intercalation process in TiO₂ [164]. These unusual high-capacity and sloped charge-discharge potential curves could be attributed to solid solution behavior of the nanosized TiO₂ particles [26,165,166] and different thermodynamics of insertion reaction from bulk TiO₂ [167,168]. The theoretical capacity of SnO₂ is 782 mAh g⁻¹ but the lithium electroactivity of the sole ATO nanobelts was negligible in the voltage range from 2.5 to 1.0 V (Figure 5.2.7), which means that ATO nanobelts in these TiO₂-ATO nanostructured electrodes just act as a conducting paths [26]. Thus, the specific capacities in Figure 5.2.6 were mainly originated from TiO₂ nanorods in this voltage range. Therefore, the present TiO₂ nanorods with

about 20 nm diameter and 130 nm lengths in the TiO₂-ATO nanostructures can be expected to achieve high-capacity delivery.

Furthermore, the high capacity retention and rate capability of the TiO₂-ATO nanostructures were clearly demonstrated as shown in Figure 5.2.8. They exhibited large reversible capacity of 175 mAh g⁻¹ at a c-rate of 0.5 C, which is higher than the theoretical specific capacity (168 mAh g⁻¹). Also, high cycling stability was verified by extremely low average capacity fading, ~0.1% per cycle under every 10 cycle at all different rates of 0.1, 0.2, 0.5, 1, and 2 C. In addition, specific capacity of the electrode was maintained even after 150 cycles. (Figure 5.2.9) It is proposed that the excellent cycling stability and rate capabilities of TiO₂-ATO nanostructures may be attributed to superior charge collection properties due to the highly conductive 1-D Sb doped SnO₂ nanobelts and low TiO₂/SnO₂ interface resistance due to their epitaxial relationship as well as large surface area of TiO₂ branches.

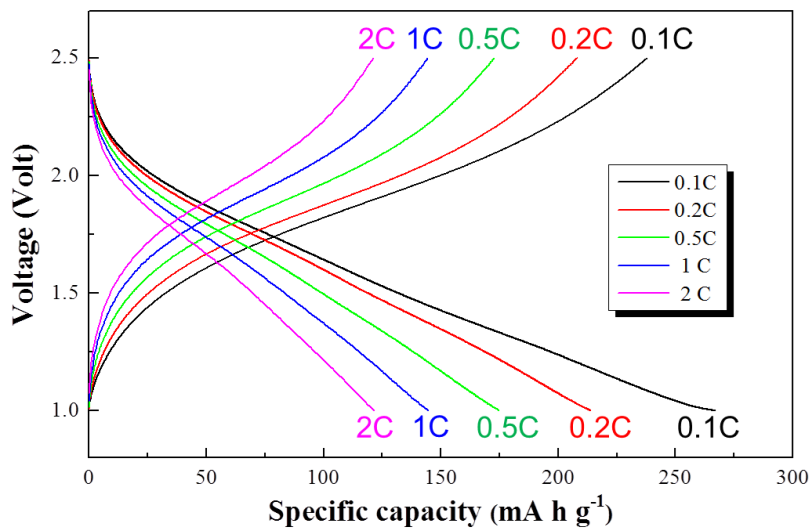


Figure 6.2.6. Charging-discharging curves of the $\text{TiO}_2\text{-ATO}$ at various C-rate (0.1 C, 0.2 C, 0.5 C, 1 C, and 2 C).

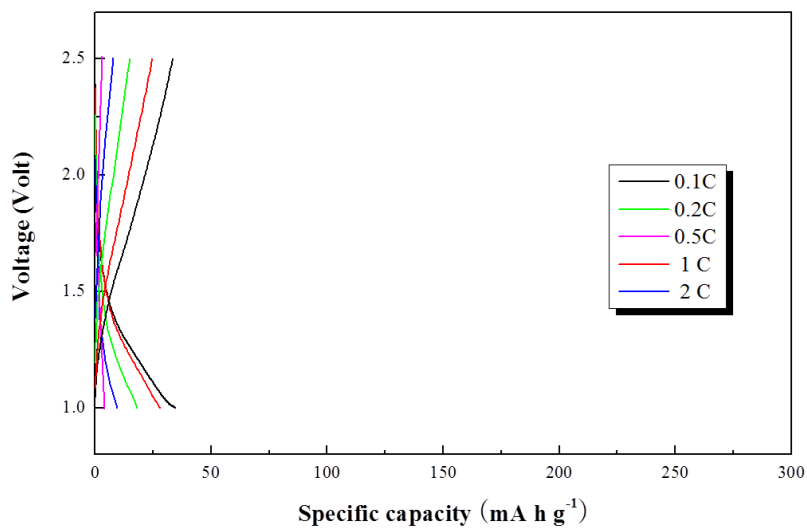


Figure 6.2.7. Charging-discharging curves of the ATO nanobelts electrode over 1.0 – 2.5 V.

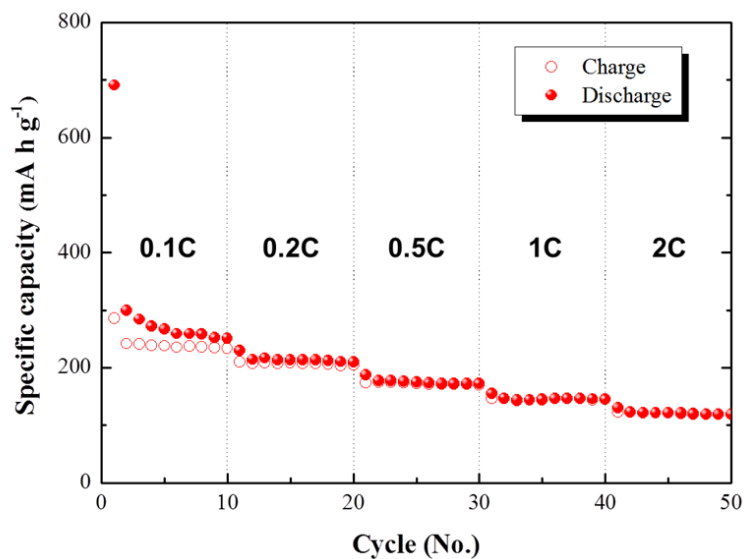


Figure 6.2.8. Specific capacity versus cycle number of the TiO₂-ATO electrode cycled ten times at every C-rate (0.1 C, 0.2 C, 0.5 C, 1 C, and 2 C).

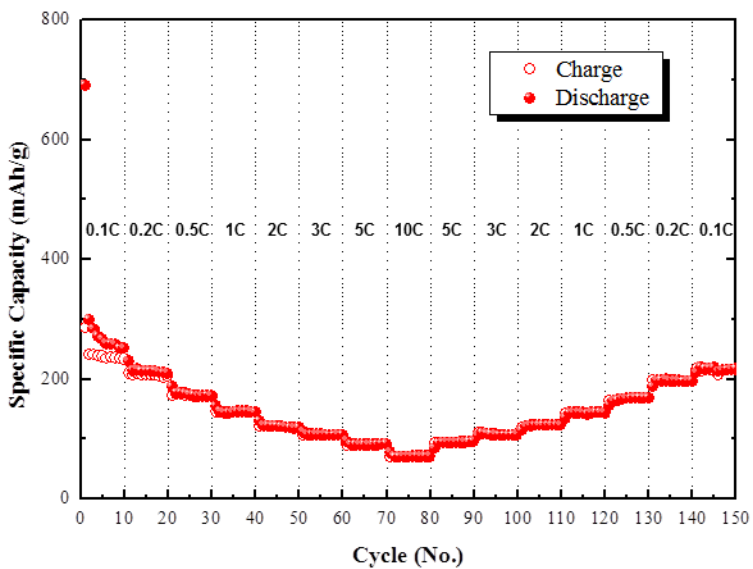


Figure 6.2.9. Specific capacity versus cycle number of the TiO₂-ATO electrode cycled ten times at every C-rate (0.1 C, 0.2 C, 0.5 C, 1 C, 2 C, 3 C, 6 C, and 10 C) over 1.0–2.5 V.

6.2.2 VO₂-ATO cathode for Li ion battery

Electrochemical properties of the VO₂-ATO nanostructured electrodes were evaluated as a cathode for Li ion battery within the voltage range of 1.5 – 3.5 V. Figure 6.2.10 shows the discharge-charge specific capacity versus the cycle number at a rate of 100 mA g⁻¹ for the VO₂-ATO electrodes. A very high and stable reversible capacity of about 350 mAh g⁻¹, even higher than the theoretical value (320 mAh g⁻¹ for Li_{1.0}VO₂), is achieved at initial cycles and stabilized at about 300 mAh g⁻¹ even after 80 cycles, delivering 86% capacity retention. This superior performance of VO₂-ATO is not only higher than the value measured from VO₂ (M) bulk powder electrode, but also surpassed the all values that have been reported on VO₂ (M)-based electrodes [186,257]. More remarkably, the VO₂-ATO demonstrates fast discharging and charging capability (Figure 6.2.11), where the electrode delivered reversible discharge capacities of 230 mA h g⁻¹ at 500 mA g⁻¹ and 196 mA h g⁻¹ at 2000 mA g⁻¹. It is one of the most outstanding performances in VO₂ nanostructures even containing different polymorphs such as VO₂ (B) or VO₂ (A) (Table 6.2.1).

The excellent electrochemical performance of VO₂-ATO heterostructured electrodes is attributed to geometrical and structural benefits. Cyclic voltammograms (CVs) confirmed that Li insertion/extraction reactions occur

during charging-discharging process in VO₂-ATO (Figure 6.2.12), where the cathodic peak at around 2.4V and anodic peak at around 2.7V indicate the insertion and desertion of Li⁺ ions, respectively [258-260]. It is well known that rutile structures show only a low amount of volume change, e.g. 4% in rutile TiO₂, during Li insertion/extraction, which could mitigate a structure collapse and improve the cycle retention [26]. Similarly, in VO₂-ATO system, it was obviously observed that morphology and structure of VO₂ nanobranched could be maintained after charging-discharging process (Figure 6.2.13), which is due to rutile crystal structure of VO₂. Figure 6.2.14 compares the voltage-specific capacity curves of VO₂-ATO and VO₂ (M) bulk powder in the range from 1st to 80th cycle. Flat plateaus are observed in all charge/discharge curves of both heterostructure and bulk materials, corresponding to lithium insertion and extraction reactions of Li_xVO₂ [260-262]. The VO₂-ATO has a more sloped profile relative to the bulk powders, which could be explained in terms of the pseudocapacitive Li⁺ insertion behavior that is often observed for nanostructured materials [262]. In this mechanism, the surface of nanostructure acts as a solid solution host to Li⁺ insertion, which is dominated by the fast charge-transfer processes rather than slow diffusion-controlled Faradaic insertion processes; it may attribute the high rate capabilities of VO₂-ATO. Pseudocapacitive charging also

contributes the increase of the overall capacity of the nano-sized material [183,262], and the higher discharge capacity of VO₂-ATO rather than theoretical value at initial few cycles could be interpreted in this manner. Because Li diffusion behavior in rutile is highly anisotropic, e.g. diffusion coefficient of Li ion in rutile TiO₂ is 10⁻⁶ cm² s⁻¹ along the *c*-direction while it is only 10⁻¹⁵ cm² s⁻¹ in the *ab*-plane [261], Li diffusion proceeds dominantly through the *c* channels in rutile structure [263]. As shown in Figure 6.2.14c, VO₂ nanobranched were grown along tetragonal [001] direction in VO₂-ATO rutile heterostructure, providing the effective Li channels along *c*-axis. Therefore, the high reversible capacities, cycle stability and rate capabilities of VO₂-ATO are attributed to several factors based on structural and geometrical benefits of 3-D heteroepitaxial nanostructure as follow. (i) All regions of VO₂ branches could be reacted with Li ions by the nanometric scale morphology and effective Li diffusion channels provided by linear growth along *c*-axis, inducing the high capacity. (ii) Heteroepitaxial structure could be maintained during Li insertion/extraction by well-aligned array of nanobranched and low volume expansion of rutile VO₂, enhancing the cycle retention. (iii) Electron transport and transfer could be promoted by high conductive 1-D pathway of ATO nanobelt and large contact area with electrolyte of nanobranched, respectively, improving the rate capabilities.

Table 6.2.1. Comparison of the electrochemical performance with various reported VO₂-based cathode materials for Li-ion batteries.

Materials	Structures	Voltage	Cycles	Current density	Capacity	Ref.
		V		mA g ⁻¹	mAh g ⁻¹	
VO ₂ (B)	Hollow microsphere	4.5 - 1.5	50	50	220	[264]
VO ₂ (B)	Powder	3.5 - 1.0	20	1 mA cm ⁻²	300	[180]
VO ₂ (B)	Powder-Carbon belt	4.0 - 1.5	100	50	153	[260]
VO ₂ (B)	Powder-CNT	3.25 - 1.0	100	323	170	[258]
VO ₂ (B)	Powder-Graphene	3.5 - 1.5	1000	37200	200	[179]
VO ₂ (B)	Powder-LNCMO	3.5 - 2.0	25	12.5	200	[265]
VO ₂ (B)	Powder-R-Graphene	3.5 - 2.0	200	160	133	[266]
VO ₂ (B)	Nanoparticles	4.0 - 1.5	20	0.5 mA cm ⁻²	260	[267]
VO ₂ (B)	Nanorod	3.5 - 1.5	17	-	75	[182]
VO ₂ (B)	Nanorod	4.0 - 1.5	47	0.1	108	[268]
VO ₂ (B)	Nanorods	3.5 - 1.5	30	150	100	[269]
VO ₂ (B)	Nanowire	3.5 - 2.0	50	50	180	[183]

VO ₂ (B)	Nanowire	3.0 - 2.0	600	500	104	[270]
VO ₂ (B)	Nanowire- CNT	3.5 - 1.5	100	323	150	[177]
VO ₂ (B)	Nanobelt	4.0 - 1.5	50	50	107	[271]
VO ₂ (B)	Nanobelt	3.25 - 1.5	60	200	125	[272]
VO ₂ (B)	Nanobelt	4.0 - 2.0	50	100	116	[273]
VO ₂ (B)	Nanofibers	4.0 - 1.5	1	C/55	334	[274]
VO ₂ (B)	Nanoribbon- Graphene	3.0 - 0.0	50	0.1	380	[259]
VO ₂ (B)	Nanotube- Graphene	4.0 - 1.5	20	40	350	[275]
VO ₂ (B)	Nanosheet	4.0 - 1.5	50	20	200	[276]
VO ₂ (B)	Nanosheet- CNT	4.0 - 1.5	50	50	151	[277]
VO ₂ (B)	Nanosheet- N-Graphene	3.5 - 1.5	50	50	251	[278]
VO ₂ (A)	Nanowire	4.0 - 1.5	50	90	116	[185]
VO ₂ (M)	Nanoparticle	4.0 - 1.5	15	C/11	230	[186]
VO ₂ (M)	Nanobelt- Carbon	4.0 - 1.5	50	50	60	[257]
VO ₂ (M)	Heteroepitaxial 3-D branch	3.5 - 1.5	60	2000	196	This work

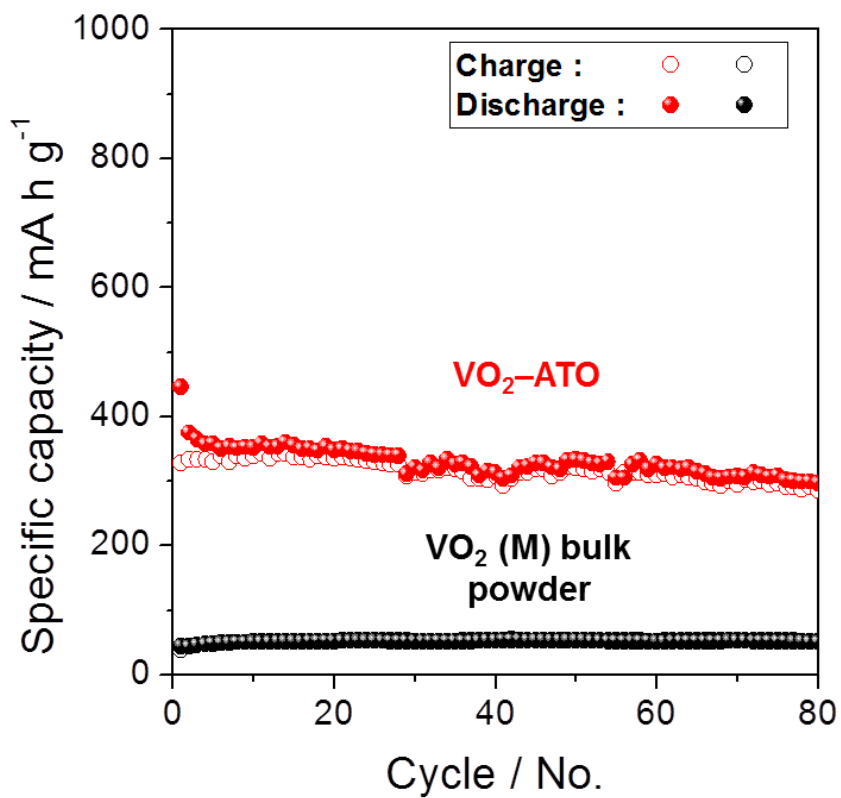


Figure 6.2.10 The discharge–charge specific capacity versus the cycle number for VO₂–ATO heterostructure and VO₂ (M) bulk powder, which was operated at a rate of 100 mA g⁻¹ over a voltage window between 3.5 and 1.5 V. VO₂–ATO heterostructure prepared for 3 h was used as cathode.

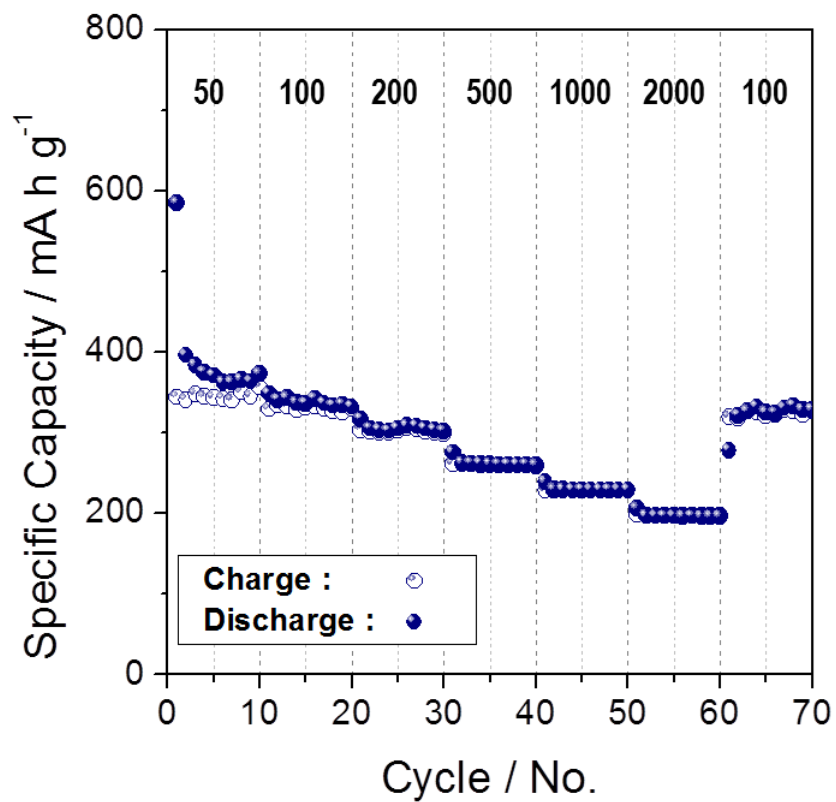


Figure 6.2.11 Specific capacity versus the cycle number for VO₂-ATO cathode cycled 10 times at different current density (50, 100, 200, 500, 1000 and 2000 mA g⁻¹) over a voltage window between 3.5 and 1.5 V.

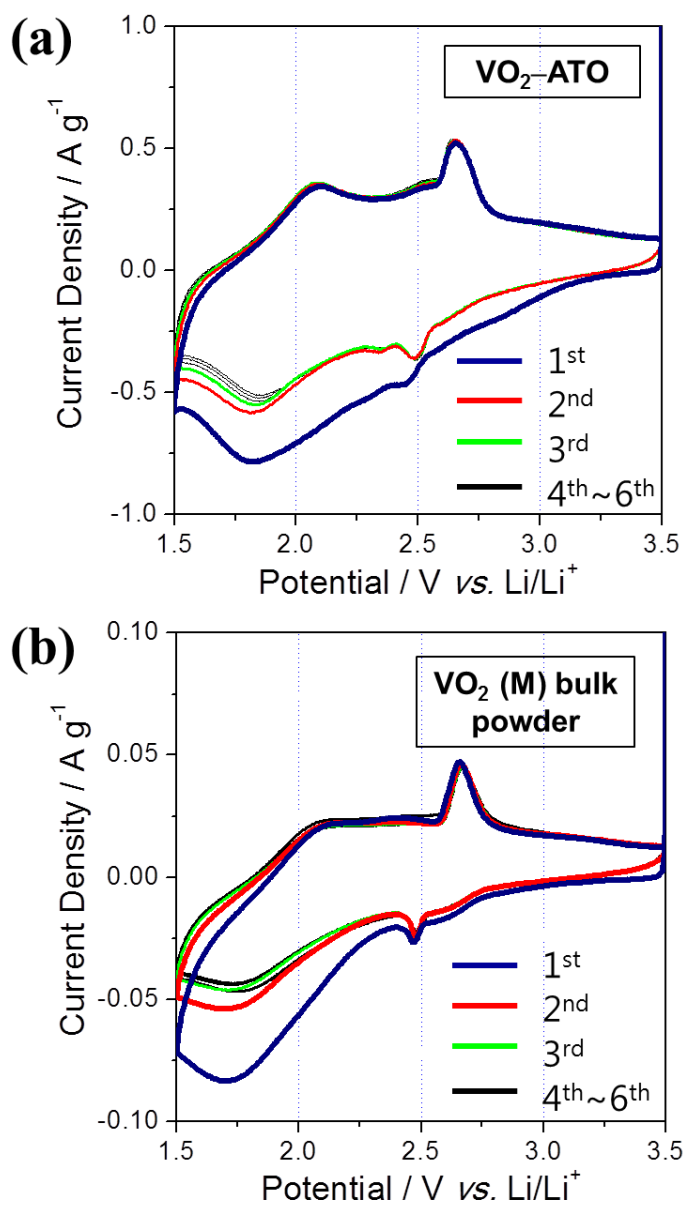


Figure 6.2.12 Cyclic voltammograms of electrodes for (a) VO₂-ATO and (b) VO₂ (M) bulk powder at a scanning rate of 0.3 mV s⁻¹ in the first 6 cycles.

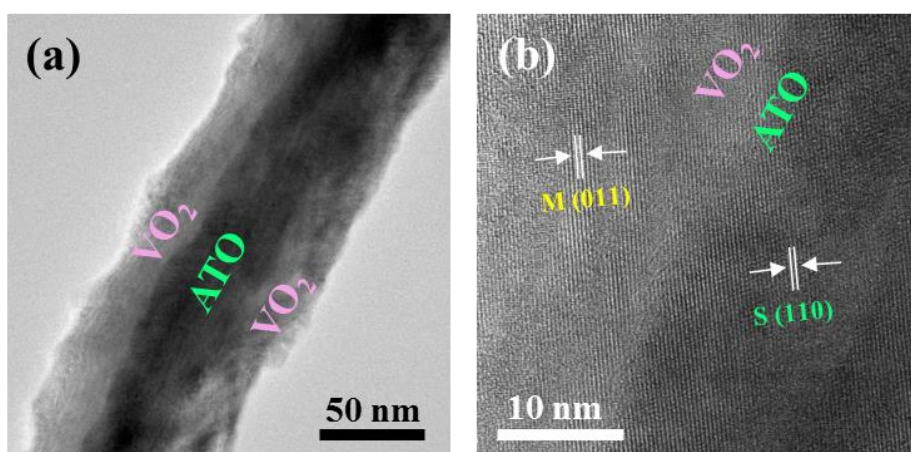


Figure 6.2.13 (a) Typical TEM image of the discharged VO₂-ATO heterostructured electrodes after 55 cycles. (b) Magnified HRTEM image of a VO₂-ATO at the discharged state (extraction of Li⁺) after 55 cycles.

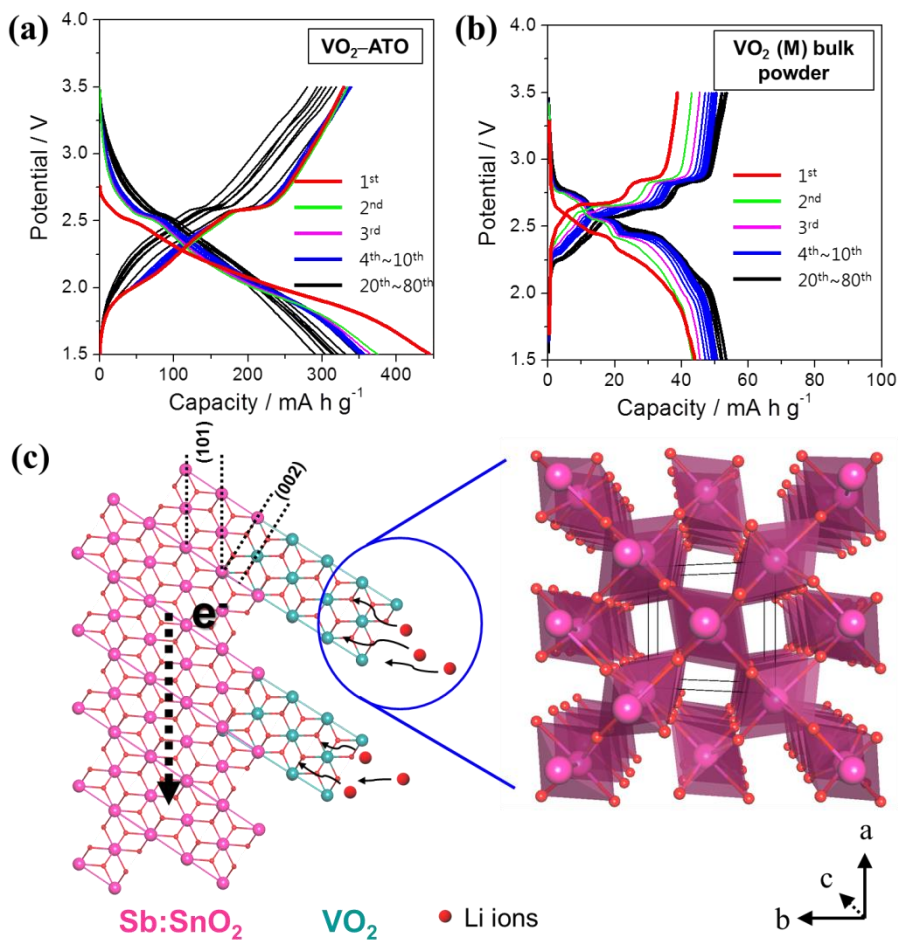


Figure 6.2.14 Charging–discharging curves of electrodes for (a) VO₂-ATO and (b) VO₂ (M) bulk powder at a rate of 100 mA g⁻¹. (c) Illustration of Li ion diffusion and electron transport in VO₂-ATO heterostructures based on rutile crystal structure. Crystallography of rutile type VO₂ projected along c-axis was also presented, in which the tunnel can function as pathway for the diffusion of Li⁺ ions during Li insertion/extraction.

Chapter 7. Conclusion

Three dimensional (3-D) heteroepitaxial nanoarchitectures composed of transparent conducting oxide (TCO) backbones and metal oxide branches were fabricated, and their electrochemical properties in energy conversion and storage devices such as photoelectrochemical (PEC) cells and Li-ion batteries were explored to create a fundamental understanding of optimization and design in metal oxide based electrodes for enhancing their energy conversion efficiency and long-term stability.

The rutile based heteroepitaxial structure was selected as a conceptual model to fully and systematically understand the epitaxial growth mechanism in a 3-D heterostructure. In order to develop thermally and chemically stable 1-D backbone that can withstand harsh solution synthesis conditions, rutile SnO₂ was selected as the 1-D TCO material. Vertical aligned and conductive 3.2% Sb-doped SnO₂ (ATO) nanobelts were fabricated on both the FTO glass and Ti substrate by the vapor-liquid-solid mechanism. The ATO nanobelt arrays were well connected with the substrate and have low resistivity of approximately $9.7 \times 10^{-2} \Omega \text{ cm}$. Sb doping played a significant role in imposing both verticality and conductivity on SnO₂ nanobelts. To clear the effect of the epitaxial relationship between the backbone and branch on 3-D growth mode, TiO₂,

Fe_2O_3 , and VO_2 were deposited on ATO nanobelts by surfactant-free wet-chemical routes. Dendritic growth occurred in TiO_2 and Fe_2O_3 , which induced hierarchically branched TiO_2 -ATO and Fe_2O_3 -ATO heterostructures. TEM analysis indicated that both TiO_2 and Fe_2O_3 nanorods were epitaxially grown on all four ATO nanobelt sides like wheel spokes. From crystallographic and interfacial analysis, the tilted and self-aligned TiO_2 and Fe_2O_3 nanobranches were found to minimize surface energy and lattice mismatch. Detailed nanobranch growth mechanism was also investigated in TiO_2 -ATO as a representative structure. A high-density, uniform, and epitaxial TiO_2 nanobranch can be grown on ATO nanobelts by a facile chemical bath deposition (CBD) method at low temperatures (25 ~ 50 °C); this is partially attributed to the epitaxial relationship between rutile TiO_2 and rutile SnO_2 . The addition of an acid like HNO_3 acts as a novel morphology control agent and offsets the disadvantages of the CBD method (i.e., the slow reaction time and non-uniform particle formation). The specific concentration of HNO_3 in the solution induced low TiO_2 solubility in the solution due to poor ligand affinity of the NO_3^- and non-electrically charged H^+ complex, leading to a high precipitation rate and diffusional-controlled growth. Therefore, uniform and short TiO_2 NRs with approximately 20 nm diameter and an

average 100 nm length became attached to the ATO nanobelt. The high HNO_3 concentration induced a slow precipitation rate due to the low hydrolysis rate caused by NO_3^- and positively charged complex caused by H^+ , which retarded the homogenous nucleation and promoted abnormal hetero growth. Thus, long TiO_2 NRs with average 700 nm length became attached to the ATO nanobelt. The length of the TiO_2 NRs was easily adjustable from 20 nm to 700 nm via the reaction time. For VO_2 , linear growth occurred that induced the two-fold branched VO_2 -ATO heterostructure. XRD and TEM analysis revealed that VO_2 nanorods with (101) preferred orientation grew on the {101} sides of the ATO nanobelts. Additionally, VO_2 nanorods were tensile-strained along the tetragonal b-axis due to lattice-mismatch of ~3% between SnO_2 (020) and VO_2 (020) *d*-spacing that induced well-matched atomic arrangement at the interface between VO_2 (101) and SnO_2 (101). On the other hand, the atomic arrangement remained unmatched at the interface between VO_2 (010) and SnO_2 (010) due to a relatively large lattice-mismatch of ~8%. As VO_2 nanorod length increased, the VO_2 epitaxial strain was released. Consequently, epitaxial strain affects the preferred orientation of VO_2 nanorod on ATO nanobelts. Furthermore, the epitaxial strain effect also reduced the MIT temperature of VO_2 nanorods from 68 °C to 55 °C due to

compressive strain along the c-axis ($\sim 0.2\%$). For the first time, the epitaxial strain effect on the 3-D nanobranched growth was revealed through linear growth of VO_2 -ATO heteroepitaxial nanostructures.

In addition, the 3-D heteroepitaxial nanoarchitecturing of metal oxide was proposed for efficient charge transfer and transport of PEC cells and Li-ion batteries. Vertical and defect-free single crystal ATO nanobelt arrays with 100 nm diameter and 25 μm length were selected with two types of TiO_2 -ATO nanostructures (core-shell structures and heteroepitaxially branched structures) applied to PEC cells. Both core-shell and branch structures showed efficient charge transport properties by 1-D TCO. The solar to hydrogen efficiency of branch structures is 0.93% (at 0.68 V vs. RHE), which is twice that of core-shell structures (0.41 % at 0.61 V vs. RHE). This difference was attributed to efficient charge transfer properties of the direct rod pathway. The epitaxially branched TiO_2 -ATO heterostructures were sensitized by CdS quantum dots as the visible-light absorber and each CdS- TiO_2 -ATO synthesis step was modulated (i.e., ATO, TiO_2 , and CdS dimensions) to optimize every conversion efficiency – light harvesting, charge collection, and charge transport efficiency that were mainly related to the absorber (CdS), branch (TiO_2), and backbone (ATO), respectively. Among the various TiO_2 morphologies, the rod TiO_2 -ATO heterostructure

showed better PEC performance than the dot and lamella TiO_2 types at the same CdS QDs loading, which are mainly attributed to high surface areas and efficient pathways. Photoelectrodes made using optimized CdS– TiO_2 –ATO had a saturated photocurrent density of 7.75 mA/cm^2 at 0.4 V vs. RHE under simulated solar light illumination, which surpasses all previously reported values for PEC performance based on CdS-sensitized nanostructures. A Fe_2O_3 –ATO was also applied to PEC cells. Surprisingly, Sn^{4+} was considerably diffused and self-doped into the $\alpha\text{-Fe}_2\text{O}_3$ lattice at low annealing temperatures ($650 \text{ }^\circ\text{C}$) so that each $\alpha\text{-Fe}_2\text{O}_3$ nanorod was directly junctioned with SnO_2 nanobelts. An increase in the flat band potential (from 0.6 V to 0.46 V/RHE) and carrier density (from 1.7×10^{21} to 4.7×10^{21}) was achieved by incorporating Sn^{4+} into $\alpha\text{-Fe}_2\text{O}_3$ nanorods. In optimum conditions, the Sn doped $\alpha\text{-Fe}_2\text{O}_3/\text{SnO}_2$ nanostructure achieved a photocurrent density of 0.88 mA/cm^2 at 1.23 V vs. RHE under simulated solar light illuminations, which is 3 times higher than that for $\alpha\text{-Fe}_2\text{O}_3$ nanorods on a FTO glass substrate. The improved PEC performance is attributed to enhanced structural, optical, electrical, and doping effects such as larger surface area, more effective light absorption, higher conductive one dimensional pathway, and higher flat band potential & donor density.

In addition to PEC application, TiO₂-ATO and VO₂-ATO heteroepitaxial structures were proposed to apply to anode and cathode Li-ion batteries, respectively. ATO nanobelt arrays with 10 μm length were selected and TiO₂-ATO with short TiO₂ nanorods (100 nm length) was applied to the Li-ion battery anode. When assembled cells were galvanostatically cycled between 2.5 – 0.01V, both SnO₂ and TiO₂ took part in Li insertion/extraction and the synergetic effect was observed between SnO₂ and TiO₂. While the sole ATO nanobelt electrode's specific capacity faded drastically from 592 mA h g⁻¹ in the 40th cycle to 92 mA h g⁻¹ in the 70th cycle, the TiO₂-ATO electrode exhibited superior cycle retention (432 mAh g⁻¹ in the 40th cycle and 251 mAh g⁻¹ in the 70th cycle). In addition, the TiO₂-ATO electrode delivered high reversible discharge capacities of 340 mA h g⁻¹ at 3 C, which surpassed the values reported on TiO₂- SnO₂ heterostructured electrodes. Furthermore, the TiO₂-ATO electrode cycled with a high Coulombic efficiency of ~95% under all applied current densities. This synergistic performance originated from advantageous geometric and structural features involving the mitigation of huge volume change and heteroepitaxial growth as well as doping effects deriving high electronic conductivity of the backbone and efficient dispersion of Sn nanodomains formed during cycling. When the cells operated between 2.5

to 1.0 V, the specific capacities originating only from TiO₂ nanorods could be obtained. Consequently, the TiO₂-ATO electrode exhibited large reversible capacity of 175 mAh g⁻¹ at 0.5 C, which is higher than the theoretical specific capacity of rutile TiO₂ (168 mAh g⁻¹). A high cycling stability was also verified by extremely low average capacity fading of ~0.1% per cycle every 10 cycles at all different rates of 0.1, 0.2, 0.5, 1, and 2 C. In addition, the specific capacity of the electrode was maintained even after 150 cycles. The excellent cycling stability and rate capabilities of TiO₂-ATO heterostructures was attributed to superior charge collection properties by the highly conductive 1-D pathway and low TiO₂/SnO₂ interface resistance by their epitaxial relationship as well as large surface area of TiO₂ branches. A VO₂-ATO was also applied to Li-ion batteries as the cathode. Interestingly, the outstanding specific capacity and cycling stability of 307 mA h g⁻¹ after the 70th cycle were evaluated at a rate of 100 mA g⁻¹, which is near the theoretical specific capacity of VO₂ (320 mAh g⁻¹). The superior rate capabilities of 196 mA h g⁻¹ at 2000 mA g⁻¹ was observed, in which extremely low average capacity fading was evaluated. These excellent electrochemical properties surpassed the reported values on vanadium based electrodes and VO₂ (M) based electrodes, which are attributed to a higher active area due to well-aligned nanobranches ,

effective Li diffusion by 1-D channel along the [001] direction and superior charge collection properties by the conductive 1-D backbone.

Design and development of 3-D heteroepitaxial nanoarchitectures can lead to a structural-factor-optimizable nanostructure with high conductive channel, large surface area, and low interfacial resistance. Additionally, the synthetic strategy suggested in this thesis will improve the electrochemical performance, which can be extended to other TCO, metal oxide, and multi-junction nanostructures. Therefore, these findings will significantly contribute to the development of advanced electrodes and create breakthroughs in energy conversion and storage devices.

Bibliography

- [1] Lewis, N. S.; Crabtree, G. *Basic Research Needs for Solar Energy Utilization: report of the Basic Energy Sciences Workshop on Solar Energy Utilization, April 18-21, 2005*, US Department of Energy, Office of Basic Energy Science, Washington, DC., **2005**.
- [2] Smalley, R. E. *Mrs Bull.* **2005**, *30*, 412.
- [3] Xing, J.; Fang, W. Q.; Zhao, H. J.; Yang, H. G. *Chem.-Asian J.* **2012**, *7*, 642.
- [4] Ni, M.; Leung, M. K. H.; Leung, D. Y. C.; Sumathy, K. *Renew. Sust. Energ. Rev.* **2007**, *11*, 401.
- [5] Turner, J.; Sverdrup, G.; Mann, M. K.; Maness, P. C.; Kroposki, B.; Ghirardi, M.; Evans, R. J.; Blake, D. *Int. J. Energ. Res.* **2008**, *32*, 379.
- [6] Aydil, E. S. *Nanotech. L. & Bus.* **2007**, *4*, 275.
- [7] Scaife, D. *Sol. Energy* **1980**, *25*, 41.
- [8] Bard, A. J.; Fox, M. A. *Accounts Chem. Res.* **1995**, *28*, 141.
- [9] Bak, T.; Nowotny, J.; Rekas, M.; Sorrell, C. *Int. J Hydrogen Energ.* **2002**, *27*, 991.
- [10] Kitano, M.; Hara, M. *J. Mater. Chem.* **2010**, *20*, 627.
- [11] Walter, M. G.; Warren, E. L.; McKone, J. R.; Boettcher, S. W.; Mi, Q.; Santori, E. A.; Lewis, N. S. *Chem. Rev.* **2010**, *110*, 6446.

- [12] Li, Z.; Luo, W.; Zhang, M.; Feng, J.; Zou, Z. *Energ. Environ. Sci.* **2013**, *6*, 347.
- [13] Scrosati, B. *Electrochim. Acta* **2000**, *45*, 2461.
- [14] Tarascon, J.-M.; Armand, M. *Nature* **2001**, *414*, 359.
- [15] Ortiz, G. F.; Hanzu, I.; Djenizian, T.; Lavela, P.; Tirado, J. L.; Knauth, P. *Chem. Mater.* **2008**, *21*, 63.
- [16] Etacheri, V.; Marom, R.; Elazari, R.; Salitra, G.; Aurbach, D. *Energ. Environ. Sci.* **2011**, *4*, 3243.
- [17] Zhang, W.-J. *J. Power Sources* **2011**, *196*, 13.
- [18] Alkire, R. C.; Gogotsi, Y.; Simon, P.; Eftekhari, A. *Nanostructured materials in electrochemistry*, John Wiley & Sons, **2008**.
- [19] Leite, E. R. *Nanostructured materials for electrochemical energy production and storage*, Vol. 4, Springer, **2009**.
- [20] Abu-Lebdeh, Y.; Davidson, I. *Nanotechnology for Lithium-Ion Batteries*, Springer, **2012**.
- [21] Yi, G.-C. *Semiconductor Nanostructures for Optoelectronic Devices: Processing, Characterization and Applications Series*, Springer, **2012**.
- [22] Cao, G. *Synthesis, properties and applications*, World Scientific, **2004**.
- [23] Nam, S.; Jiang, X.; Xiong, Q.; Ham, D.; Lieber, C. M. *Proc. Natl. Acad. Sci. USA* **2009**, *106*, 21035.

- [24] Javey, A.; Nam, S. W.; Friedman, R. S.; Yan, H.; Lieber, C. M. *Nano Lett.* **2007**, *7*, 773.
- [25] Ahn, J. H.; Kim, H. S.; Lee, K. J.; Jeon, S.; Kang, S. J.; Sun, Y.; Nuzzo, R. G.; Rogers, J. A. *Science* **2006**, *314*, 1754.
- [26] Park, K. S.; Kang, J. G.; Choi, Y. J.; Lee, S.; Kim, D. W.; Park, J. G. *Energ Environ. Sci.* **2011**, *4*, 1796.
- [27] Noh, J. H.; Han, H. S.; Lee, S.; Kim, J. Y.; Hong, K. S.; Han, G. S.; Shin, H.; Jung, H. S. *Adv. Energ. Mater.* **2011**.
- [28] Kang, J.-G.; Lee, G.-H.; Park, K.-S.; Kim, S.-O.; Lee, S.; Kim, D.-W.; Park, J.-G. *J. Mater. Chem.* **2012**, *22*, 9330.
- [29] Fan, Z.; Ruebusch, D. J.; Rathore, A. A.; Kapadia, R.; Ergen, O.; Leu, P. W.; Javey, A. *Nano Res.* **2009**, *2*, 829.
- [30] Fan, Z.; Razavi, H.; Do, J.; Moriwaki, A.; Ergen, O.; Chueh, Y. L.; Leu, P. W.; Ho, J. C.; Takahashi, T.; Reichertz, L. A. *Nat. Mater.* **2009**, *8*, 648.
- [31] Zhou, W.; Cheng, C.; Liu, J.; Tay, Y. Y.; Jiang, J.; Jia, X.; Zhang, J.; Gong, H.; Hng, H. H.; Yu, T. *Adv. Func. Mater.* **2011**, *21*, 2439.
- [32] Zhou, J.; Ding, Y.; Deng, S. Z.; Gong, L.; Xu, N. S.; Wang, Z. L. *Adv. Mater.* **2005**, *17*, 2107.
- [33] Shi, J.; Sun, C.; Starr, M. B.; Wang, X. *Nano Lett.* **2011**, *11*, 624.
- [34] Shi, J.; Hara, Y.; Sun, C.; Anderson, M. A.; Wang, X. *Nano Lett.* **2011**,

11, 3413.

[35] Shang, M.; Wang, W.; Yin, W.; Ren, J.; Sun, S.; Zhang, L. *Chem.-Eur. J.* **2010**, *16*, 11412.

[36] Gu, Z.; Liu, F.; Howe, J. Y.; Paranthaman, M. P.; Pan, Z. *Cryst. Growth Des.* **2008**, *9*, 35.

[37] Gautam, U. K.; Fang, X.; Bando, Y.; Zhan, J.; Golberg, D. *ACS Nano* **2008**, *2*, 1015.

[38] Gao, P. X.; Lao, C. S.; Hughes, W. L.; Wang, Z. L. *Chem. Phys. Lett.* **2005**, *408*, 174.

[39] Dick, K. A.; Deppert, K.; Larsson, M. W.; Martensson, T.; Seifert, W.; Wallenberg, L. R.; Samuelson, L. *Nat. Mater.* **2004**, *3*, 380.

[40] Cho, I. S.; Chen, Z.; Forman, A. J.; Kim, D. R.; Rao, P. M.; Jaramillo, T. F.; Zheng, X. *Nano Lett.* **2011**, *11*, 4978.

[41] Cheng, C.; Tay, Y. Y.; Hng, H. H.; Fan, H. J. *J. Mater. Res.* **2011**, *26*, 2254.

[42] Chen, Y.; Zhu, C.; Shi, X.; Cao, M.; Jin, H. *Nanotechnology* **2008**, *19*, 205603.

[43] Bierman, M. J.; Jin, S. *Energ. Environ. Sci.* **2009**, *2*, 1050.

[44] Park, H. G.; Holt, J. K. *Energ. Environ. Sci.* **2010**, *3*, 1028.

[45] Wang, G.; Wang, H.; Ling, Y.; Tang, Y.; Yang, X.; Fitzmorris, R. C.;

- Wang, C.; Zhang, J. Z.; Li, Y. *Nano Lett.* **2011**, *11*, 3026.
- [46] Aricò, A. S.; Bruce, P.; Scrosati, B.; Tarascon, J. M.; Van Schalkwijk, W. *Nat. Mater.* **2005**, *4*, 366.
- [47] Bruce, P. G.; Scrosati, B.; Tarascon, J. M. *Angew. Chem. Int. Ed.* **2008**, *47*, 2930.
- [48] Deng, D.; Kim, M. G.; Lee, J. Y.; Cho, J. *Energ. Environ. Sci.* **2009**, *2*, 818.
- [49] Liu, R.; Duay, J.; Lee, S. B. *Chem. Commun.* **2011**, *47*, 1384.
- [50] Wang, D.; Luo, H.; Kou, R.; Gil, M. P.; Xiao, S.; Golub, V. O.; Yang, Z.; Brinker, C. J.; Lu, Y. *Angew. Chem. Int. Ed.* **2004**, *43*, 6169.
- [51] Yuan, G. D.; Zhang, W. J.; Jie, J. S.; Fan, X.; Tang, J. X.; Shafiq, I.; Ye, Z. Z.; Lee, C. S.; Lee, S. T. *Adv. Mater.* **2008**, *20*, 168.
- [52] Wan, Q.; Wei, M.; Zhi, D.; MacManus-Driscoll, J. L.; Blamire, M. G. *Adv. Mater.* **2006**, *18*, 234.
- [53] Wan, Q.; Dattoli, E. N.; Lu, W. *Appl. Phys. Lett.* **2007**, *90*, 222107.
- [54] Xiang, D. G.; Su, J.; Zhang, A. Q.; Gao, Y. H.; Han, X. Y.; Sun, M.; Zhang, X. H.; Shen, G. Z.; Chen, D.; Jin, L.; Wang, J. B. *J. Nanosci. Nanotech.* **2010**, *10*, 6629.
- [55] Sathe, B. R.; Patil, M.; Walke, P. S.; Vivek, J. P.; Lele, A.; Pillai, V. K.; Mulla, I. S. *Sci. Adv. Mater.* **2009**, *1*, 38.

- [56] Noh, J. H.; Ding, B.; Han, H. S.; Kim, J. S.; Park, J. H.; Park, S. B.; Jung, H. S.; Lee, J. K.; Hong, K. S. *Appl. Phys. Lett.* **2012**, *100*, 084104.
- [57] Kormos, F.; Rotariua, I.; Tolaib, G.; Pávai, M.; Romanc, C.; Kálmánb, E. *Dig. J. Nanomater. Bios.* **2006**, *1*, 107.
- [58] Lei, Y.; Chim, W.-K. *J. Am. Chem. Soc.* **2005**, *127*, 1487.
- [59] Lauhon, L. J.; Gudiksen, M. S.; Wang, D.; Lieber, C. M. *Nature* **2002**, *420*, 57.
- [60] Kim, D.-W.; Hwang, I.-S.; Kwon, S. J.; Kang, H.-Y.; Park, K.-S.; Choi, Y.-J.; Choi, K.-J.; Park, J.-G. *Nano lett.* **2007**, *7*, 3041.
- [61] Fu, L.; Liu, H.; Zhang, H.; Li, C.; Zhang, T.; Wu, Y.; Holze, R.; Wu, H. *Electrochem. Comm.* **2006**, *8*, 1.
- [62] Zhang, D.-F.; Sun, L.-D.; Jia, C.-J.; Yan, Z.-G.; You, L.-P.; Yan, C.-H. *J. Am. Chem. Soc.* **2005**, *127*, 13492.
- [63] Jung, Y.; Ko, D.-K.; Agarwal, R. *Nano Lett.* **2007**, *7*, 264.
- [64] Yang, Z.; Du, G.; Meng, Q.; Guo, Z.; Yu, X.; Chen, Z.; Guo, T.; Zeng, R. *RSC Adv.* **2011**, *1*, 1834.
- [65] Wu, X.; Zhang, S.; Wang, L.; Du, Z.; Fang, H.; Ling, Y.; Huang, Z. *J. Mater. Chem.* **2012**, *22*, 11151.
- [66] Du, G.; Guo, Z.; Zhang, P.; Li, Y.; Chen, M.; Wexler, D.; Liu, H. *J. Mater. Chem.* **2010**, *20*, 5689.

- [67] Chen, J. S.; Luan, D.; Li, C. M.; Boey, F. Y. C.; Qiao, S.; Lou, X. W. *Chem. Comm.* **2010**, 46, 8252.
- [68] Wolf, D.; Yip, S. *Materials interfaces: atomic-level structure and properties*, Springer, **1992**.
- [69] Stringfellow, G. *Rep. Prog. Phys.* **1982**, 45, 469.
- [70] Royer, L. *Recherches expérimentales sur l'épitaxie ou orientation mutuelle des cristaux d'espèces différentes*, Société Générale d'Imprimerie et d'Édition, **1928**.
- [71] Herman, M. A.; Richter, W.; Sitter, H. *Epitaxy: physical principles and technical implementation*, Vol. 62, Springer, **2004**.
- [72] Hartman, P.; Hartman, P. *Crystal growth: an introduction*, North-Holland Publishing Company, **1973**.
- [73] Van Der Merwe, J. H. *Crc. Cr. Rev. Sol. State.* **1978**, 7, 209.
- [74] Wood, D.; Zunger, A. *Phys. Rev. B* **1989**, 40, 4062.
- [75] Ismail, K.; Meyerson, B. *J. Mater. Sci.-Mater. El.* **1995**, 6, 306.
- [76] Van de Walle, C. G.; Martin, R. M. *Phys. Rev. B* **1986**, 34, 5621.
- [77] Pohl, U. W. *Epitaxy of Semiconductors: Introduction to Physical Principles*, Springer, **2013**.
- [78] Kimerling, L.; Cahn, R. W.; Mahajan, S. *Concise encyclopedia of semiconducting materials & related technologies*, Pergamon, **1992**.

- [79] Sakaki, H.; Noge, H. *Nanostructures and quantum effects: proceedings of the JRDC international symposium, Tsukuba, Japan, November 17-18, 1993*, Vol. 31, Springer Verlag, **1994**.
- [80] Cho, A. *J. Cryst. Growth* **1991**, *111*, 1.
- [81] Bimberg, D.; Grundmann, M.; Ledentsov, N. N. *Quantum dot heterostructures*, John Wiley Chichester, **1999**.
- [82] Jones, A. C.; O'Brien, P. *CVD of Compound Semiconductors: Precursor Synthesis, Developmeny and Applications*, John Wiley & Sons, **2008**.
- [83] Tung, R. T.; Poate, J.; Bean, J.; Gibson, J.; Jacobson, D. *Thin Solid Films* **1982**, *93*, 77.
- [84] Bauer, S.; Rosenauer, A.; Skorsetz, J.; Kuhn, W.; Wagner, H.; Zweck, J.; Gebhardt, W. *J. Cryst. Growth* **1992**, *117*, 297.
- [85] Ghozlene, H. B.; Beaufrère, P.; Authier, A. *J. Appl. Phys.* **2008**, *49*, 3998.
- [86] Stangl, J.; Holý, V.; Bauer, G. *Rev. Mod. Phys.* **2004**, *76*, 725.
- [87] Teichert, C. *Phys. Rep.* **2002**, *365*, 335.
- [88] Park, B.; Peterson, E.; Jia, Q.; Lee, J.; Zeng, X.; Si, W.; Xi, X. *Appl. Phys. Lett.* **2001**, *78*, 533.
- [89] Welp, U.; Vlasko-Vlasov, V.; Liu, X.; Furdyna, J.; Wojtowicz, T. *Phys. Rev. Lett.* **2003**, *90*, 167206.

- [90] Jeong, J.; Aetukuri, N.; Graf, T.; Schladt, T. D.; Samant, M. G.; Parkin, S. S. *Science* **2013**, 339, 1402.
- [91] Hurler, D. T. *Handbook of crystal growth*, Elsevier, **1994**.
- [92] Eizenberg, M.; Segmüller, A.; Heiblum, M.; Smith, D. *J. Appl. Phys.* **1987**, 62, 466.
- [93] Frank, F.; van der Merwe, J. H. *Proceedings of the Royal Society of London. Series A. Mathematical and Physical Sciences* **1949**, 198, 205.
- [94] Volmer, M.; Weber, A. *Z. Phys. Chem* **1926**, 119, 277.
- [95] Stranski, I. N.; Von Krastanow, L. *Akademie der Wissenschaften und der Literatur in Mainz* **1939**, 146, 797.
- [96] Hansson, P.; Albrecht, M.; Strunk, H.; Bauser, E.; Werner, J. *Thin Solid Films* **1992**, 216, 199.
- [97] Markov, I. V. *Crystal growth for beginners*, World Scientific, **1995**.
- [98] Shchukin, V.; Ledentsov, N.; Kop'Ev, P.; Bimberg, D. *Phys. Rev. Lett.* **1995**, 75, 2968.
- [99] Wang, L.; Kratzer, P.; Scheffler, M.; Moll, N. *Phys. Rev. Lett.* **1999**, 82, 4042.
- [100] Mane, R.; Lokhande, C. *Mater. Chem. Phys.* **2000**, 65, 1.
- [101] Nair, P.; Nair, M.; Garcia, V.; Arenas, O.; Peña, A. C.; Ayala, I.; Gomezdaza, O.; Sanchez, A.; Campos, J.; Hu, H. *Sol. Energ. Mat. Sol. C.*

1998, 52, 313.

[102] O'Regan, B. C.; Durrant, J. R.; Sommeling, P. M.; Bakker, N. J. *J. Phys. Chem. C* **2007**, 111, 14001.

[103] Sommeling, P.; O'regan, B.; Haswell, R.; Smit, H.; Bakker, N.; Smits, J.; Kroon, J.; Van Roosmalen, J. *J. Phys. Chem. B* **2006**, 110, 19191.

[104] More, A. M.; Gujar, T. P.; Gunjekar, J. L.; Lokhande, C. D.; Joo, O.-S. *Appl. Surf. Sci.* **2008**, 255, 2682.

[105] Vayssieres, L.; Keis, K.; Lindquist, S. E.; Hagfeldt, A. *J. Phys. Chem. B* **2001**, 105, 3350.

[106] Yang, L. L.; Zhao, Q. X.; Willander, M. *J. Alloy. Compd.* **2009**, 469, 623.

[107] Wang, W.; Gu, B.; Liang, L.; Hamilton, W. A.; Wesolowski, D. J. *J. Phys. Chem. B* **2004**, 108, 14789.

[108] Wu, Y.; Yan, H.; Huang, M.; Messer, B.; Song, J. H.; Yang, P. *Chem.-Eur. J.* **2002**, 8, 1260.

[109] Cheng, C.; Fan, H. *J. Nano Today* **2012**, 7, 327.

[110] Gu, F.; Gai, L.; Shao, W.; Li, C.; Schmidt-Mende, L. *Chem. Comm.* **2011**, 47, 8400.

[111] Guo, Z.; Chen, X.; Li, J.; Liu, J. H.; Huang, X. *J. Langmuir* **2011**, 27, 6193.

- [112] Yang, Y.; Zhang, Z. C.; Wang, P. P.; Zhang, J. C.; Nosheen, F.; Zhuang, J.; Wang, X. *Inorg. Chem.* **2013**, *52*, 9449.
- [113] Mi, Y.; Cao, Y. H.; Liu, X. L.; Yi, J. B.; Tan, H. R.; Ma, P.; Hao, H.; Zhang, X.; Fan, H. M. *Mater. Chem. Phys.* **2013**, *143*, 311.
- [114] Kargar, A.; Jing, Y.; Kim, S. J.; Riley, C. T.; Pan, X.; Wang, D. *ACS Nano* **2013**, *7*, 11112.
- [115] Yang, C.; Li, M.; Zhang, W.-H.; Li, C. *Sol. Energ. Mat. Sol. C.* **2013**, *115*, 100.
- [116] Kim, D. H.; Seong, W. M.; Park, I. J.; Yoo, E. S.; Shin, S. S.; Kim, J. S.; Jung, H. S.; Lee, S.; Hong, K. S. *Nanoscale* **2013**, *5*, 11725.
- [117] Gu, X.; Chen, L.; Ju, Z.; Xu, H.; Yang, J.; Qian, Y. *Adv. Func. Mater.* **2013**, *23*, 4049.
- [118] Wu, H.; Xu, M.; Wang, Y.; Zheng, G. *Nano Res.* **2013**, *1*.
- [119] Sun, P.; Cai, Y.; Du, S.; Xu, X.; You, L.; Ma, J.; Liu, F.; Liang, X.; Sun, Y.; Lu, G. *Sensor Actuat. B-Chem.* **2013**, *182*, 336.
- [120] Wang, B. B.; Fu, X. X.; Liu, F.; Shi, S. L.; Cheng, J. P.; Zhang, X. B. *J. Alloy. Compd.* **2014**, *587*, 82.
- [121] Prudnikau, A.; Chuvilin, A.; Artemyev, M. *J. Am. Chem. Soc.* **2013**, *135*, 14476.
- [122] Suteewong, T.; Sai, H.; Hovden, R.; Muller, D.; Bradbury, M. S.;

- Gruner, S. M.; Wiesner, U. *Science* **2013**, *340*, 337.
- [123] Wu, Z.; Wu, Y.; Pei, T.; Wang, H.; Geng, B. *Nanoscale* **2013**.
- [124] Forticaux, A.; Hacialioglu, S.; DeGrave, J. P.; Dziedzic, R.; Jin, S. *ACS Nano* **2013**, *7*, 8224.
- [125] Pan, K.; Dong, Y.; Zhou, W.; Pan, Q.; Xie, Y.; Xie, T.; Tian, G.; Wang, G. *ACS Appl. Mater. Interfaces* **2013**, *5*, 8314.
- [126] Dong, A.; Tang, R.; Buhro, W. E. *J. Am. Chem. Soc.* **2007**, *129*, 12254.
- [127] Sayed, S. Y.; Wang, F.; Malac, M.; Meldrum, A.; Egerton, R. F.; Buriak, J. M. *ACS Nano* **2009**, *3*, 2809.
- [128] Devika, M.; Reddy, N. K.; Pevzner, A.; Patolsky, F. *Chemphyschem* **2010**, *11*, 809.
- [129] Lugstein, A.; Andrews, A. M.; Steinmair, M.; Hyun, Y.-J.; Bertagnolli, E.; Weil, M.; Pongratz, P.; Schramböck, M.; Roch, T.; Strasser, G. *Nanotechnology* **2007**, *18*, 355306.
- [130] Liu, X.; Song, M.; Wang, S.; He, Y. *Physica E* **2013**, *53*, 260.
- [131] Devika, M.; Koteeswara Reddy, N.; Kang, J. W.; Park, S. J.; Tu, C. W. *ECS Solid State Lett.* **2013**, *2*, P101.
- [132] Li, C.; Yu, Y.; Chi, M.; Cao, L. *Nano Lett.* **2013**, *13*, 948.
- [133] Yan, C.; Li, X.; Zhou, K.; Pan, A.; Werner, P.; Mensah, S. L.; Vogel, A. T.; Schmidt, V. *Nano Lett.* **2012**, *12*, 1799.

- [134] Bolzan, A. A.; Fong, C.; Kennedy, B.; Howard, C. J. *Acta. Crystall. B-Stru.* **1997**, *53*, 373.
- [135] Wells, A. F. *Structural inorganic chemistry*, Oxford University Press, **2012**.
- [136] Gervais, F.; Kress, W. *Phys. Rev. B* **1985**, *31*, 4809.
- [137] Jarzebski, Z.; Marton, J. J. *Electrochem. Soc.* **1976**, *123*, 199C.
- [138] Kay, A.; Grätzel, M. *Chem. Mater.* **2002**, *14*, 2930.
- [139] Gubbala, S.; Chakrapani, V.; Kumar, V.; Sunkara, M. K. *Adv. Func. Mater.* **2008**, *18*, 2411.
- [140] Choi, Y. J.; Hwang, I. S.; Park, J. G.; Choi, K. J.; Park, J. H.; Lee, J. H. *Nanotechnology* **2008**, *19*, 095508.
- [141] He, J. H.; Wu, T. H.; Hsin, C. L.; Li, K. M.; Chen, L. J.; Chueh, Y. L.; Chou, L. J.; Wang, Z. L. *Small* **2006**, *2*, 116.
- [142] Hammad, T. M.; Hejazy, N. K. *Int. Nano Lett.* **2012**, *2*, 1.
- [143] He, Y.-S.; Campbell, J. C.; Murphy, R. C.; Arendt, M.; Swinnea, J. S. *J. Mater. Res.* **1993**, *8*, 3131.
- [144] Wan, Q.; Dattoli, E.; Lu, W. *Small* **2008**, *4*, 451.
- [145] Wu, J.-M. *Thin Solid Films* **2008**, *517*, 1289.
- [146] Park, M. S.; Wang, G. X.; Kang, Y. M.; Wexler, D.; Dou, S. X.; Liu, H. K. *Angew. Chem. Int. Ed.* **2007**, *119*, 764.

- [147] Ko, Y. D.; Kang, J. G.; Park, J. G.; Lee, S.; Kim, D. W. *Nanotechnology* **2009**, *20*, 455701.
- [148] Yao, J.; Shen, X.; Wang, B.; Liu, H.; Wang, G. *Electrochem. Comm.* **2009**, *11*, 1849.
- [149] Wang, Y.; Zeng, H. C.; Lee, J. Y. *Adv. Mater.* **2006**, *18*, 645.
- [150] Wang, Y.; Chen, T. *Electrochim. Acta* **2009**, *54*, 3510.
- [151] Wang, Y.; Djerdj, I.; Smarsly, B.; Antonietti, M. *Chem. Mater.* **2009**, *21*, 3202.
- [152] Santos-Pena, J.; Brousse, T.; Sanchez, L.; Morales, J.; Schleich, D. J. *Power sources* **2001**, *97*, 232.
- [153] Morales, J.; Sanchez, L. *J. Electrochem. Soc.* **1999**, *146*, 1640.
- [154] Chen, X.; Mao, S. S. *Chem. Rev.* **2007**, *107*, 2891.
- [155] Asahi, R.; Taga, Y.; Mannstadt, W.; Freeman, A. *Phys. Rev. B* **2000**, *61*, 7459.
- [156] Sorantin, P. I.; Schwarz, K. *Inorg. Chem.* **1992**, *31*, 567.
- [157] Wu, Z.; Ouvrard, G.; Gressier, P.; Natoli, C. *Phys. Rev. B* **1997**, *55*, 10382.
- [158] Szczepankiewicz, S. H.; Colussi, A.; Hoffmann, M. R. *J. Phys. Chem. B* **2000**, *104*, 9842.
- [159] Howe, R. F.; Gratzel, M. *J. Phys. Chem.* **1985**, *89*, 4495.

- [160] Fujishima, A.; Honda, K. *Nature* **1972**, *238*, 37.
- [161] Sun, W.-T.; Yu, Y.; Pan, H.-Y.; Gao, X.-F.; Chen, Q.; Peng, L.-M. *J. Am. Chem. Soc.* **2008**, *130*, 1124.
- [162] Hwang, Y. J.; Boukai, A.; Yang, P. *Nano Lett.* **2009**, *9*, 410.
- [163] Hwang, Y. J.; Hahn, C.; Liu, B.; Yang, P. *ACS Nano* **2012**, *6*, 5060.
- [164] Ren, Y.; Hardwick, L. J.; Bruce, P. G. *Angew. Chem. Int. Ed.* **2010**, *49*, 2570.
- [165] Cao, F. F.; Xin, S.; Guo, Y. G.; Wan, L. J. *Phys. Chem. Chem. Phys.* **2011**, *13*, 2014.
- [166] Park, K.-S.; Min, K.-M.; Jin, Y.-H.; Seo, S.-D.; Lee, G.-H.; Shim, H.-W.; Kim, D.-W. *J. Mater. Chem.* **2012**, *22*, 15981.
- [167] Borghols, W. J. H.; Wagemaker, M.; Lafont, U.; Kelder, E. M.; Mulder, F. M. *Chem. Mater.* **2008**, *20*, 2949.
- [168] Wagemaker, M.; Borghols, W. J. H.; Mulder, F. M. *J. Am. Chem. Soc.* **2007**, *129*, 4323.
- [169] Yang, T.-H.; Mal, S.; Jin, C.; Narayan, R. J.; Narayan, J. *Appl. Phys. Lett.* **2011**, *98*, 022105.
- [170] Guiton, B. S.; Gu, Q.; Prieto, A. L.; Gudixsen, M. S.; Park, H. *J. Am. Chem. Soc.* **2005**, *127*, 498.
- [171] Pergament, A. *J. Phys.-Condens. Mat.* **2003**, *15*, 3217.

- [172] Booth, J. M.; Casey, P. S. *Phys. Rev. Lett.* **2009**, *103*, 086402.
- [173] Hiroi, Z.; Yamauchi, T.; Muraoka, Y.; Muramatsu, T.; Yamaura, J.-I. *J. Phys. Soc. Jpn.* **2003**, *72*, 3049.
- [174] Zhou, H.; Chisholm, M. F.; Yang, T.-H.; Pennycook, S. J.; Narayan, J. *J. Appl. Phys.* **2011**, *110*, 073515.
- [175] Cao, A. M.; Hu, J. S.; Liang, H. P.; Wan, L. J. *Angew. Chem. Int. Ed.* **2005**, *44*, 4391.
- [176] Li, B.; Ni, X.; Zhou, F.; Cheng, J.; Zheng, H.; Ji, M. *Solid State Sci.* **2006**, *8*, 1168.
- [177] Yan, C.; Chen, Z.; Peng, Y.; Guo, L.; Lu, Y. *Nanotechnology* **2012**, *23*, 475701.
- [178] Ren, Y.; Liu, Z.; Pourpoint, F.; Armstrong, A. R.; Grey, C. P.; Bruce, P. *G. Angew. Chem. Int. Ed.* **2012**, *124*, 2206.
- [179] Yang, S.; Gong, Y.; Liu, Z.; Zhan, L.; Hashim, D. P.; Ma, L.; Vajtai, R.; Ajayan, P. M. *Nano Lett.* **2013**, *13*, 1596.
- [180] Kannan, A. *Solid State Ionics* **2003**, *159*, 265.
- [181] Pan, A.; Wu, H. B.; Yu, L.; Lou, X. W. D. *Angew. Chem. Int. Ed.* **2013**, *125*, 2282.
- [182] Subba Reddy, C. V.; Walker, E. H.; Wicker, S. A.; Williams, Q. L.; Kalluru, R. R. *Curr. Appl. Phys.* **2009**, *9*, 1195.

- [183] Armstrong, G.; Canales, J.; Armstrong, A. R.; Bruce, P. G. *J. Power Sources* **2008**, *178*, 723.
- [184] Ji, S.; Zhang, F.; Jin, P. *Sol. Energ. Mater. Sol. C.* **2011**, *95*, 3520.
- [185] Dai, L.; Gao, Y.; Cao, C.; Chen, Z.; Luo, H.; Kanehira, M.; Jin, J.; Liu, Y. *RSC Adv.* **2012**, *2*, 5265.
- [186] Munozrojas, D.; Baudrin, E. *Solid State Ionics* **2007**, *178*, 1268.
- [187] Zhang, Q. H.; Gao, L.; Guo, J. K. *Nanostruct. Mater.* **1999**, *11*, 1293.
- [188] Cassaignon, S.; Koelsch, M.; Jolivet, J.-P. *J. Mater. Sci.* **2007**, *42*, 6689.
- [189] Cheng, C.; Karuturi, S. K.; Liu, L.; Liu, J.; Li, H.; Su, L. T.; Tok, A. I.; Fan, H. J. *Small* **2012**, *8*, 37.
- [190] Leonardy, A.; Hung, W.-Z.; Tsai, D.-S.; Chou, C.-C.; Huang, Y.-S. *Cryst. Growth Des.* **2009**, *9*, 3958.
- [191] Montilla, F.; Morallón, E.; De Battisti, A.; Barison, S.; Daolio, S.; Vázquez, J. *J. Phys. Chem. B* **2004**, *108*, 15976.
- [192] Sun, S. H.; Meng, G. W.; Zhang, G. X.; Gao, T.; Geng, B. Y.; Zhang, L. D.; Zuo, J. *Chem. Phys. Lett.* **2003**, *376*, 103.
- [193] Ono, T.; Yamanaka, T.; Kubokawa, Y.; Komiyama, M. *J. Catal.* **1988**, *109*, 423.
- [194] Rumyantseva, M. N.; Gaskov, A. M.; Rosman, N.; Pagnier, T.; Morante, J. R. *Chem. Mater.* **2005**, *17*, 893.

- [195] Cheng, H.; Ma, J.; Zhao, Z.; Qi, L. *Chem. Mater.* **1995**, *7*, 663.
- [196] Li, J. G.; Ishigaki, T.; Sun, X. *J. Phys. Chem. C* **2007**, *111*, 4969.
- [197] Matero, R.; Rahtu, A.; Ritala, M. *Chem. Mater.* **2001**, *13*, 4506.
- [198] Yamabi, S.; Imai, H. *Chem. Mater.* **2002**, *14*, 609.
- [199] Chen, C. A.; Chen, Y. M.; Korotcov, A.; Huang, Y. S.; Tsai, D. S.; Tiong, K. K. *Nanotechnology* **2008**, *19*, 075611.
- [200] Neuhoff, J. *Speciation of Cr(II) and Cr(III) complexes by IC-ICP-OES and HPLC*, Ph.D. Thesis, University of Johannesburg, **2008**.
- [201] Yoldas, B. E. *J. Mater. Sci.* **1986**, *21*, 1087.
- [202] Granberg, R. A.; Ducreux, C.; Gracin, S.; Rasmuson, Å. C. *Chem. Eng. Sci.* **2001**, *56*, 2305.
- [203] Yang, S.; Liu, Y.; Guo, Y.; Zhao, J.; Xu, H.; Wang, Z. *Mater. Chem. Phys.* **2003**, *77*, 501.
- [204] Wu, M.; Long, J.; Huang, A.; Luo, Y.; Feng, S.; Xu, R. *Langmuir* **1999**, *15*, 8822.
- [205] Zhou, W.; Liu, X.; Cui, J.; Liu, D.; Li, J.; Jiang, H.; Wang, J.; Liu, H. *CrystEngComm* **2011**, *13*, 4557.
- [206] Kwon, S. G.; Piao, Y.; Park, J.; Angappane, S.; Jo, Y.; Hwang, N. M.; Park, J. G.; Hyeon, T. *J. Am. Chem. Soc.* **2007**, *129*, 12571.
- [207] Park, J.; Joo, J.; Kwon, S. G.; Jang, Y.; Hyeon, T. *Angew. Chem. Int.*

Ed. **2007**, *46*, 4630.

[208] Pottier, A.; Chanéac, C.; Tronc, E.; Mazerolles, L.; Jolivet, J. P. *J. Mater. Chem.* **2001**, *11*, 1116.

[209] Zheng, W.; Liu, X.; Yan, Z.; Zhu, L. *ACS Nano* **2008**, *3*, 115.

[210] Schilbe, P. *Physica B* **2002**, *316*, 600.

[211] Srivastava, R.; Chase, L. *Phys. Rev. Lett.* **1971**, *27*, 727.

[212] Nag, J.; Payzant, E. A.; More, K. L.; Haglund, R. F. *Appl. Phys. Lett.* **2011**, *98*, 251916.

[213] Narayan, J.; Bhosle, V. M. *J. Appl. Phys.* **2006**, *100*, 103524.

[214] Shin, K.; Seok, S. I.; Im, S. H.; Park, J. H. *Chem. Comm.* **2010**, *46*, 2385.

[215] Qin, D.-D.; Tao, C.-L.; In, S.-i.; Yang, Z.-Y.; Mallouk, T. E.; Bao, N.; Grimes, C. A. *Energ. Fuel.* **2011**, *25*, 5257.

[216] Diedenhofen, S. L.; Vecchi, G.; Algra, R. E.; Hartsuiker, A.; Muskens, O. L.; Immink, G.; Bakkers, E. P. A. M.; Vos, W. L.; Rivas, J. G. *Adv. Mater.* **2009**, *21*, 973.

[217] Kim, H.; Seol, M.; Lee, J.; Yong, K. *J. Phys. Chem. C* **2011**, *115*, 25429.

[218] Song, N.; Zhu, H.; Liu, Z.; Huang, Z.; Wu, D.; Lian, T. *ACS Nano* **2013**, *7*, 1599.

- [219] Chen, C.; Xie, Y.; Ali, G.; Yoo, S. H.; Cho, S. O. *Nanotechnology* **2011**, *22*, 015202.
- [220] Wang, G.; Yang, X.; Qian, F.; Zhang, J. Z.; Li, Y. *Nano. Lett.* **2010**, *10*, 1088.
- [221] Banerjee, S.; Mohapatra, S. K.; Das, P. P.; Misra, M. *Chem. Mater.* **2008**, *20*, 6784.
- [222] Li, J.; Hoffmann, M. W. G.; Shen, H.; Fabrega, C.; Prades, J. D.; Andreu, T.; Hernandez-Ramirez, F.; Mathur, S. *J. Mater. Chem.* **2012**, *22*, 20472.
- [223] Luo, J.; Ma, L.; He, T.; Ng, C. F.; Wang, S.; Sun, H.; Fan, H. J. *J. Phys. Chem. C* **2012**, *116*, 11956.
- [224] Qi, X.; She, G.; Liu, Y.; Mu, L.; Shi, W. *Chem. Comm.* **2012**, *48*, 242.
- [225] Sang, L.; Tan, H.; Zhang, X.; Wu, Y.; Ma, C.; Burda, C. *J. Phys. Chem. C* **2012**, *116*, 18633.
- [226] Chi, C.-F.; Lee, Y.-L.; Weng, H.-S. *Nanotechnology* **2008**, *19*, 125704.
- [227] Lee, Y.-L.; Chi, C.-F.; Liao, S.-Y. *Chem. Mater.* **2010**, *22*, 922.
- [228] Osterloh, F. E. *Chem. Soc. Rev.* **2013**, *42*, 2294.
- [229] Hahn, N. T.; Mullins, C. B. *Chem. Mater.* **2010**, *22*, 6474.
- [230] Kay, A.; Cesar, I.; Grätzel, M. *J. Am. Chem. Soc.* **2006**, *128*, 15714.
- [231] Lee, M. H.; Park, J. H.; Han, H. S.; Song, H. J.; Cho, I. S.; Noh, J. H.;

- Hong, K. S. *Int. J. Hydrogen Energ.* **2013**.
- [232] Ling, Y.; Wang, G.; Wheeler, D. A.; Zhang, J. Z.; Li, Y. *Nano. Lett.* **2011**, *11*, 2119.
- [233] Yang, T.-Y.; Kang, H.-Y.; Jin, K.; Park, S.; Lee, J.-H.; Sim, U.; Jeong, H.-Y.; Joo, Y.-C.; Nam, K. T. *J. Mater. Chem. A* **2014**, *2*, 2297.
- [234] Dong, L.; Chu, Y.; Zhang, Y. *Mater. Lett.* **2007**, *61*, 4651.
- [235] Thong, L. V.; Loan, L. T. N.; Van Hieu, N. *Sensor. Actuat. B-Chem.* **2010**, *150*, 112.
- [236] Qi, X.; She, G.; Wang, M.; Mu, L.; Shi, W. *Chem. Comm.* **2013**, *49*, 5742.
- [237] Jang, J. S.; Lee, J.; Ye, H.; Fan, F.-R. F.; Bard, A. J. *J. Phys. Chem. C* **2009**, *113*, 6719.
- [238] Cao, D.; Luo, W.; Li, M.; Feng, J.; Li, Z.; Zou, Z. *CrystEngComm* **2013**, *15*, 2386.
- [239] Cesar, I.; Sivula, K.; Kay, A.; Zboril, R.; Grätzel, M. *J. Phys. Chem. C* **2008**, *113*, 772.
- [240] Sivula, K.; Zboril, R.; Le Formal, F.; Robert, R.; Weidenkaff, A.; Tucek, J.; Frydrych, J.; Gratzel, M. *J. Am. Chem. So.* **2010**, *132*, 7436.
- [241] Wang, G.; Ling, Y.; Wheeler, D. A.; George, K. E.; Horsley, K.; Heske, C.; Zhang, J. Z.; Li, Y. *Nano. Lett.* **2011**, *11*, 3503.

- [242] Chao, Y.-C.; Chen, C.-Y.; Lin, C.-A.; He, J.-H. *Energ. Environ. Sci.* **2011**, *4*, 3436.
- [243] Kennedy, J. H.; Frese, K. W. *J. Electrochem. Soc.* **1978**, *125*, 709.
- [244] Joly, A. G.; Williams, J. R.; Chambers, S. A.; Xiong, G.; Hess, W. P.; Laman, D. M. *J. Appl. Phys.* **2006**, *99*, 053521.
- [245] Barroso, M.; Pendlebury, S. R.; Cowan, A. J.; Durrant, J. R. *Chem. Sci.* **2013**, *4*, 2724.
- [246] Wheeler, D. A.; Wang, G.; Ling, Y.; Li, Y.; Zhang, J. Z. *Energ. Environ. Sci.* **2012**, *5*, 6682.
- [247] Cesar, I.; Kay, A.; Gonzalez Martinez, J. A.; Grätzel, M. *J. Am. Chem. Soc.* **2006**, *128*, 4582.
- [248] Lin, Y.; Zhou, S.; Sheehan, S. W.; Wang, D. *J. Am. Chem. Soc.* **2011**, *133*, 2398.
- [249] Park, M. S.; Kang, Y. M.; Wang, G. X.; Dou, S. X.; Liu, H. K. *Adv. Func. Mater.* **2008**, *18*, 455.
- [250] Wang, D.; Kou, R.; Choi, D.; Yang, Z.; Nie, Z.; Li, J.; Saraf, L. V.; Hu, D.; Zhang, J.; Graff, G. L. *ACS Nano* **2010**, *4*, 1587.
- [251] Mohamedi, M.; Lee, S. J.; Takahashi, D.; Nishizawa, M.; Itoh, T.; Uchida, I. *Electrochim. Acta* **2001**, *46*, 1161.
- [252] Brousse, T.; Retoux, R.; Herterich, U.; Schleich, D. *J. Electrochem.*

Soc. **1998**, *145*, 1.

[253] Aldon, L.; Garcia, A.; Olivier-Fourcade, J.; Jumas, J. C.; Fernández-Madrigal, F. J.; Lavela, P.; Vicente, C. P.; Tirado, J. L. *J. Power sources* **2003**, *119*, 585.

[254] Simonin, L.; Lafont, U.; Tabrizi, N.; Schmidt-Ott, A.; Kelder, E. *J. Power Sources* **2007**, *174*, 805.

[255] Courtney, I. A.; Dahn, J. *J. Electrochem. Soc* **1997**, *144*, 2045.

[256] Jin, Y. H.; Min, K. M.; Seo, S. D.; Shim, H. W.; Kim, D. W. *The J. Phys. Chem. C* **2011**, *115*, 22062.

[257] Zhang, Y.; Chen, C.; Zhang, J.; Hu, L.; Wu, W.; Zhong, Y.; Cao, Y.; Liu, X.; Huang, C. *Curr. Appl. Phys.* **2013**, *13*, 47.

[258] Rahman, M. M.; Wang, J.-Z.; Idris, N. H.; Chen, Z.; Liu, H. *Electrochim. Acta* **2010**, *56*, 693.

[259] Shi, Y.; Chou, S.-L.; Wang, J.-Z.; Li, H.-J.; Liu, H.-K.; Wu, Y.-P. *J. Power Sources* **2013**, *244*, 684.

[260] Zhao, Q.; Jiao, L.; Peng, W.; Gao, H.; Yang, J.; Wang, Q.; Du, H.; Li, L.; Qi, Z.; Si, Y.; Wang, Y.; Yuan, H. *J. Power Sources* **2012**, *199*, 350.

[261] Hu, Y. S.; Kienle, L.; Guo, Y. G.; Maier, J. *Adv. Mater.* **2006**, *18*, 1421.

[262] Dylla, A. G.; Henkelman, G.; Stevenson, K. J. *Accounts Chem. Res.* **2013**, *46*, 1104.

- [263] Jiang, C.; Honma, I.; Kudo, T.; Zhou, H. *Electrochem. Solid St.* **2007**, *10*, A127.
- [264] Liu, H.; Wang, Y.; Wang, K.; Hosono, E.; Zhou, H. *J. Mater. Chem.* **2009**, *19*, 2835.
- [265] Lee, E. S.; Manthiram, A. *J. Electrochem. Soc.* **2011**, *158*, A47.
- [266] Sun, Y.; Yang, S.-B.; Lv, L.-P.; Lieberwirth, I.; Zhang, L.-C.; Ding, C.-X.; Chen, C.-H. *J. Power Sources* **2013**, *241*, 168.
- [267] Tsang, C.; Manthiram, A. *J. Electrochem. Soc.* **1997**, *144*, 520.
- [268] Ganganagappa, N.; Siddaramanna, A. *Mater. Charact.* **2012**, *68*, 58.
- [269] Liu, Y.; Uchaker, E.; Zhou, N.; Li, J.; Zhang, Q.; Cao, G. *J. Mater. Chem.* **2012**, *22*, 24439.
- [270] Mai, L.; Wei, Q.; An, Q.; Tian, X.; Zhao, Y.; Xu, X.; Xu, L.; Chang, L.; Zhang, Q. *Adv Mater* **2013**.
- [271] Huang, J.; Wang, X.; Liu, J.; Sun, X.; Wang, L.; He, X. *Int J Electrochem. Sci.* **2011**, *6*, 1709.
- [272] Li, N.; Huang, W.; Shi, Q.; Zhang, Y.; Song, L. *Ceram. Int.* **2013**, *39*, 6199.
- [273] Rui, X.; Sim, D.; Xu, C.; Liu, W.; Tan, H.; Wong, K.; Hng, H. H.; Lim, T. M.; Yan, Q. *RSC Adv.* **2012**, *2*, 1174.
- [274] Li, H.; He, P.; Wang, Y.; Hosono, E.; Zhou, H. *J. Mater. Chem.* **2011**,

21, 10999.

[275] Nethravathi, C.; Viswanath, B.; Michael, J.; Rajamath, M. *Carbon* **2012**, *50*, 4839.

[276] Wang, W.; Jiang, B.; Hu, L.; Lin, Z.; Hou, J.; Jiao, S. *J. Power Sources* **2014**, *250*, 181.

[277] Zhou, X.; Wu, G.; Gao, G.; Cui, C.; Yang, H.; Shen, J.; Zhou, B.; Zhang, Z. *Electrochim. Acta* **2012**, *74*, 32.

[278] Nethravathi, C.; Rajamathi, C. R.; Rajamathi, M.; Gautam, U. K.; Wang, X.; Golberg, D.; Bando, Y. *ACS Appl. Mater. Interfaces* **2013**, *5*, 2708.

초 록

본 연구에서는 에너지 변환 및 저장 디바이스에서의 전기화학적 특성을 향상시키기 위하여 투명 전극 줄기와 금속 산화물 가지로 구성된 삼차원 이중 적층 나노구조체를 설계하고 합성하였다. 합성된 이중 적층 나노구조 전극의 전기화학적 특성을 평가하였고, 이들의 공간적, 구조적 요소와 전기화학적 특성과의 상관관계를 심도 있게 다루었다. 구체적으로, 재생가능한 태양에너지로부터 생산된 수소 에너지 시스템에서 대표적인 에너지 변환 및 저장 디바이스인 광전기화학 셀(photoelectrochemical cells) 및 리튬 이차전지(Li-ion batteries)에 관하여 연구하였다. 이러한 광전기화학 셀 및 리튬 이차전지가 실제 활용 되기 위해서는 현재 그들의 낮은 효율과 낮은 장기간 안정성 문제를 극복해야만 한다. 두 디바이스에서 금속 산화물 전극 재료는 전하 전달 및 이동을 위한 핵심 구성 요소이며, 그들의 구조 제어 및 효율적 디자인으로 효율 및 안정성 개선을 이룰 수 있을 것으로 예상된다. 나노구조체, 특별히 3 차원 나노구조체는 높은 전하 전달 및 이동 특성을 갖는 것으로 알려져 있지만 현재 금속 산화물의 나노구조화는 제작 방법이나 구조 개선 모두의 측면에서 한계에 도달한 것으로 판단되며 높은 전하 전달 및 이동 효율을 위해서는 새로운 접근 방식이 필요하다. 본 연구에서는 이러한 점에 착안하여 높은 전하 전달 및 이동 효율을 위해 두 가지 전략을 제시하였다. 첫째로, 일차원 투명전극 줄기를 적용하여 금속 산화물로부터의 효과적인 전하 추출 및 이동 효율을 갖게 하는 것이다. 둘째로, 결함 없는 계면과 자가 조립된 배열을 갖는 삼차원 이중 적층 나노구조체를 제작하여 전기화학 디바이스의 특성을 향상시키는 것이다.

먼저 삼차원 나노구조화에서의 적층 성장에 대한 체계적인 연구를 위해 루타일(rutile) 결정구조를 기반으로 하는 이중적층 구조를 선택하고 분석하였다. 열적 및 화학적으로 안정한 루타일 SnO_2 에 Sb 를 도핑함으로써 일차원 투명전극 줄기를 제작하였다. 이러한 Sb-doped SnO_2 (ATO) 나노벨트는 FTO 유리 및 Ti 기판에 수직으로

성장하였고 금속 수준의 전도도를 가졌는데 이는 독특한 Sb 도핑 거동에 기인하는 것으로 밝혀졌다. 이종적층 성장이 나노줄기의 합성에 미치는 영향을 근본적으로 이해하기 위해 다양한 금속 산화물 - TiO_2 , Fe_2O_3 , VO_2 -을 ATO 나노벨트 위에 용액 공정으로 합성하였다. TiO_2 및 Fe_2O_3 나노막대는 ATO 나노벨트의 모든 면에 방사형으로 성장한 반면, VO_2 나노막대는 ATO 나노벨트의 옆면에서만 선형으로 성장하였다. 구조분석을 통하여 이러한 방사형 및 선형 성장은 모두 계면에서의 격자 불일치에 기인함을 밝혔다. TiO_2 및 Fe_2O_3 의 경우 줄기와 가지 사이의 격자 불일치가 기울어 성장한 나노가지에 의해 최소화 되었고, 이는 방사형 성장을 유도하였다. VO_2 의 경우 격자 불일치는 변형된 나노줄기에 의해 최소화 되었고, 이는 선형 성장을 유도하였다. 나노막대의 에피택셜 변형은 VO_2 의 금속-절연체 전이 온도를 낮추었고, 이는 c 축으로의 압축변형 (~0.3%)에 기인하였다.

둘째로, 광전기화학 셀 및 리튬 이차전지에서 이종적층 나노 구조화가 금속 산화물 전극의 전하 전달 및 이동 특성에 미치는 효과를 연구하였다. TiO_2 -ATO Core-shell 구조와 이종 적층 가지화된 구조의 비교연구를 통해 가지화된 구조가 잘 배열된 나노막대에 의해 향상된 전하 전달 특성을 가짐을 확인하였고, 이로 인해 가지화된 구조는 Core-shell 구조보다 두 배 높은 효율을 나타내었다. 추가적으로, 구조적 요소가 최적화된 나노구조체를 실현하기 위하여 CdS- TiO_2 -ATO 다중접합 나노 구조체를 개발하였고, 태양광에서 7.75 mA/cm^2 의 포화 광전류를 얻을 수 있었다. Fe_2O_3 나노막대의 형상 및 전자 특성을 동시에 제어하기 위해 Fe_2O_3 -ATO의 후열처리 연구를 진행한 결과, SnO_2 나노벨트로부터 Fe_2O_3 로 확산된 Sn^{4+} 이온에 의해 Fe_2O_3 의 플랫폼 전위와 전하농도가 효율적으로 증가하였으며, 이로 인해 전하 전달 특성이 향상됨을 알아내었다.

또한 TiO_2 -ATO와 VO_2 -ATO 이종적층 구조체를 리튬 이차전지에서의 장기 안정성 향상을 위한 구조로 제안하였다. ATO 나노벨트와 둘러싸여진 TiO_2 나노막대의 조합으로 인해 음극에서의 싸이클 유지특성과 방전용량비를 향상되는 시너지 효과가 발생하였고, 이는

공간적 구조적 유리함에 기인하였다. 흥미롭게도 TiO_2 나노막대에서만 생성된 비용량은 거의 TiO_2 의 이론용량에 근접했으며 150 사이클 이후에도 유지되었다. 같은 방식으로, 두드러진 방전용량비와 사이클 안정성이 VO_2 -ATO 양극에서 관찰되었다. TiO_2 -ATO 와 VO_2 -ATO 에서 향상된 전기화학적 특성은 일차원 전도성 줄기에 의한 우수한 전하수집 특성과 나노막대 안에 [001] 방향으로 형성된 1 차원 확산 채널에 의한 효과적인 Li 이동에 기인하였다.

현재까지 서술한 바와 같이 본 연구는 광전기화학 셀 및 리튬 이차전지에서 전하 전달 및 이동 특성 개선을 위해 일차원 투명전극 줄기 위에 이중적층으로 형성된 금속산화물 가지의 합성 및 제어에 초점을 맞췄으며 현재 직면해 있는 에너지 변환 및 저장 디바이스의 문제점을 해결하고 돌파구를 마련할 수 있는 가능성을 제시 하고자 하였다.

주요어: 나노 구조, 이중 구조, 에피택셜, 삼차원, VLS 메커니즘, 화학적 용액성장, 주석산화물, 투명 전도성 산화물, 이산화 타이타늄, 산화철, 이산화 바나듐, 광전기화학, 리튬 이온 배터리, 사이클 특성.
학 번: 2007-22950

Research Achievements

1) Refereed papers

22. **S. Park**, S.-D. Seo, H. J. Kim, C. W. Lee, H. J. Song, S. S. Shin, H. K. Park, K. S. Hong*, D.-W. Kim*, “Three-dimensional hierarchical $\text{Li}_4\text{Ti}_5\text{O}_{12}$ nanoarchitecture by a sacrificial template route”, *J. Nanosci. Nanotechnol.* (Accepted).
21. **S. Park**, S. Kim, H. J. Kim, C. W. Lee, H. J. Song, S. W. Seo, H. K. Park, D.-W. Kim*, K. S. Hong*, “Hierarchical assembly of TiO_2 - SrTiO_3 heterostructures on conductive SnO_2 backbone nanobelts for enhanced photoelectrochemical and photocatalytic performance”, *J. Hazard. Mater.*, DOI: 10.1016/j.jhazmat.2014.04.019 (Accepted).
20. S. Lee, **S. Park**, G.-S. Han, D. H. Kim, J. H. Noh, I. S. Cho, H. S. Jung, K. S. Hong, “Transparent-Conducting-Oxide Nanowire Arrays for Efficient Photoelectrochemical Energy Conversion”, *Nanoscale*, DOI: 10.1039/C4NR02298J (In press).
19. K. Jin, J Park, J Lee, K. D. Yang,, G. K. Pradhan, U. Sim, D. Jeong, H. L. Jang, **S. Park**, D. Kim, N. Sung, S. H. Kim, S. Han, K. T. Nam, “Hydrated Manganese (II) Phosphate ($\text{Mn}_3(\text{PO}_4)_2 \cdot 3\text{H}_2\text{O}$) as a Water Oxidation Catalyst”, *J. Am. Chem. Soc.*, DOI: 10.1021/ja5026529 (In press).
18. **S. Park**, C. W. Lee, M. G. Kang, S. Kim, H. J. Kim, J. E. Kwon, S. Y. Park, J. Y. Kang, K. S. Hong*, K. T. Nam*, “Ferroelectric photocatalyst for enhancing hydrogen evolution: Polarized particulate suspension”, *Phys. Chem. Chem. Phys.*, DOI: 10.1039/c4cp01267d (In press).
17. **S. Park**, H. J. Kim, C. W. Lee, H. J. Song, S. S. Shin, S. W. Seo, H. K. Park, S. Lee, D.-W. Kim*, K. S. Hong*, “Sn self-doped α - Fe_2O_3 nanobranch arrays supported on a transparent, conductive SnO_2 trunk to

- improve photoelectrochemical water oxidation”, *Int J Hydrogen Energ*, DOI:10.1016/j.ijhydene.2014.02. 165 (In press).
16. **S. Park**, C. W. Lee, I. S. Cho, S. H. Kim, J. H. Park, H. J. Kim, D.-W. Kim, S. Lee*, K. S. Hong*, “Growth of anatase and rutile TiO₂@Sb:SnO₂ heterostructures and their application in photoelectrochemical water splitting”, *Int. J. Hydrogen. Energ.*, DOI: 10.1016/j.ijhydene.2013.10.030 (In press).
 15. S. W. Seo, T. H. Noh, **S. Park**, C. W. Lee, S. H. Kim, H. J. Kim, H. K. Park, K. S. Hong*, “Solvothermal synthesis of SnNb₂O₆ nanoplates and enhanced photocatalytic H₂ evolution under visible light”, *Int. J. Hydrogen. Energ.*, DOI: 10.1016/j.ijhydene.2013.09.032 (In press).
 14. T.-Y. Yang, H.-Y. Kang, K. Jin, **S. Park**, J.-H. Lee, U. Sim, H.-Y. Jeong, Y.-C. Joo*, K. T. Nam*, “An iron oxide photoanode with hierarchical nanostructure for efficient water oxidation”, *J. Mater. Chem. A*, **2014**, 2, 2297.
 13. **S. Park**, D. Kim, C. W. Lee, S.-D. Seo, S. W. Seo, S. H. Kim, H. S. Han, K. S. Hong*, D.-W. Kim*, “Surface-area-tuned, quantum-dot-sensitized heterostructured nanoarchitectures for highly efficient photoelectrodes” *Nano Res.*, **2014**, 7, 144.
 12. **S. Park**, S. Lee, S. W. Seo, S.-D. Seo, C. W. Lee, D. Kim, D.-W. Kim*, K. S. Hong*, “Tailoring nanobranches in three-dimensional hierarchical rutile heterostructures: a case study of TiO₂-SnO₂”, *CrystEngComm*, **2013**, 15, 2939.
 11. C. W. Lee, S.-D. Seo, D. W. Kim, **S. Park**, K. Jin, D.-W. Kim*, K. S. Hong*, “Heteroepitaxial Growth of ZnO Nanosheet Bands on ZnCo₂O₄ Submicron Rods toward High-Performance Li Ion Battery Electrodes”, *Nano Res.*, **2013**, 6, 348.
 10. **S. Park**, S. D. Seo, S. Lee, S. W. Seo, K. S. Park, C. W. Lee, D. W. Kim*, K. S. Hong*, “Sb:SnO₂@TiO₂ Heteroepitaxial Branched Nanoarchitectures for Li ion battery electrodes” *J. Phys. Chem. C*, **2012**, 116, 21717.

9. **S. Park**⁺, S. W. Seo⁺, H. Y. Jeong, S. H. Kim, U. Sim, C. W. Lee, K. T. Nam^{*}, K. S. Hong^{*}, "Enhanced performance of NaTaO₃ using molecular co-catalyst [Mo₃S₄]⁴⁺ for water splitting into H₂ and O₂" *Chem. Commun.*, **2012**, 48, 10452. ⁺ (Equally contributed)
8. **S. Park**, S. Lee, D. H. Kim, C. W. Lee, I. -S, Cho^{*}, K. S. Hong^{*}, "Fabrication of TiO₂/Tin-Doped Indium Oxide-Based Photoelectrode Coated with Overlayer Materials and Its Photoelectrochemical Behavior", *J. Nanosci. Nanotechno.*, **2012**, 12, 1390.
7. T. H. Noh, I. -S. Cho, S Lee, D. W. Kim, **S. Park**, S. W. Seo, C. W. Lee, K. S. Hong^{*}, "Photophysical and photocatalytic properties of Zn₃M₂O₈ (M = Nb, Ta)", *J. Am. Ceram. Soc.*, **2012**, 95, 443.
6. J. H. Noh, B. Ding, H. S. Han, J. S. Kim, J. H. Park, **S. Park**, H. S. Jung, J. -K Lee, K. S. Hong^{*}, "Tin doped indium oxide core—TiO₂ shell nanowires on stainless steel mesh for flexible photoelectrochemical cells", *Appl. Phys. Lett.*, **2012**, 100, 084104.
5. C. W. Lee, D.W. Kim, I. S. Cho, **S. Park**, S. S. Shin, S. W. Seo, K. S. Hong^{*}, "Simple synthesis and characterization of SrSnO₃ nanoparticles with enhanced photocatalytic activity" *Int. J. Hydrogen. Energ.*, **2012**, 37, 10557.
4. S. H Kim, **S. Park**, C. W. Lee, B. S. Han, S. W. Seo, J. S. Kim, I. S. Cho^{*}, K. S. Hong^{*}, "Photophysical and photocatalytic water splitting performance of stibiotantalite type-structure compounds, SbMO₄ (M = Nb, Ta), *Int. J. Hydrogen. Energ.*, **2012**, 37, 16895.
3. J. Y. Kim, J. H. Noh, K. Zhu, Adam F. Halverson, Nathan R. Neale, **S. Park**, K. S. Hong, Arthur J. Fran^{*}, "General Strategy for Fabricating Transparent TiO₂ Nanotube Arrays for Dye-Sensitized Photoelectrodes: Illumination Geometry and Transport Properties", *ACS Nano*, **2011**, 5, 2647.
2. S. Lee, I.-S. Cho, D. K. Lee, D. W. Kim, T. H. Noh, C. H. Kwak, **S. Park**, K. S. Hong, J.-K. Lee^{*}, H. S. Jung^{*}, "Influence of nitrogen

chemical states on photocatalytic activities of nitrogen-doped TiO₂ nanoparticles under visible light", *J Photoch Photobio A*, **2010**, *213*, 129.

1. J. H. Noh, H. S. Han, S. Lee, D. H. Kim, J. H. Park, **S. Park**, J. Y. Kim, H. S. Jung*, K. S. Hong*, "A Newly Designed Nb-Doped TiO₂/Al-Doped ZnO Transparent Conducting Oxide Multilayer for Electrochemical Photoenergy Conversion Devices", *J. Phys. Chem. C*, **2010**, *114*, 13867.

2) Patents

9. K. S. Hong, **S. Park**, K. T. Nam, J. Y. Kang, "Polarized photocatalyst powder and manufacturing method thereof", Korean Patent 10-2013-0153802 (2013).
8. K. S. Hong, J. H. Suk, **S. Park**, J. H. Park, I. S. Cho, D. W. Kim, "Method of preparing Sn-based oxide semiconductor nanopowder and method of manufacturing photoelectric electrode using Sn-based oxide semiconductor nanopowder", U. S. Patent 13/546,833 (2012).
7. K. S. Hong, S. S. Shin, J. H. Suk, **S. Park**, J. H. Park, I. S. Cho, D. W. Kim, "Manufacturing Method of Sn based Oxide Semiconductor Nano Powder And Manufacturing Method of Opto-electronic Electrode Using Sn based Oxide Semiconductor Nano Powder", Korean Patent 10-2012-0075415 (2012).
6. T. H. Noh, I. S. Cho, S. Lee, D. W. Kim, D. K. Lim, H. S. Noh, **S. Park**, S. W. Seo, C. W. Lee, K. S. Hong, "Photocatalysts for water splitting and synthesis methods thereof", Korean Patent 10-12298240000 (2012).
5. S. T. Bae, **S. Park**, C. H. Kwak, I. S. Cho, J. H. Noh, J. S. Ahn, T. H. Noh, H. S. Jung, H. H. Shin, K. S. Hong, "Manufacturing Method of Operation Electrode for Photoelectrochemical cell, Electrode Structure therefrom and Apparatus Comprising the Same", Korean Patent 10-10519460000 (2011).
4. J. H. Noh, **S. Park**, H. S. Han, J. H. Park, J. M. Cho, S. T. Bae, I. S. Cho,

- S. Lee, D. K. Lee, K. S. Hong, "Substrate having an Antistatic Function and Method for manufacturing the Same", Korean Patent 10-10738780000 (2011).
3. H. S. Jung, G. S. Han, S. Lee, J. H. Noh, H. S. Han, **S. Park**, K. S. Hong, S. H. Han, "Method of fabricating device comprising film structure of various dimension and shape", Korean Patent 10-10751850000 (2011).
 2. **S. Park**, S. Lee, H. S. Jung, I. S. Cho, J. H. Noh, D. W. Kim, D. Kim, J. H. Park, K. S. Hong, "Flexible transparent electrode with good conductivity and transparency and manufacturing method thereof", Korean Patent 10-10946350000 (2011).
 1. S. T. Bae, **S. Park**, I. S. Cho, S. Lee, C. M. Cho, D. W. Kim, H. S. Noh, H. S. Jung, H. H. Shin, K. S. Hong, "Working electrode for opto-electrochemical cell and apparatus using the same", Korean Patent 10-2008-0067918 (2008).

3) Presentations at Technical and Professional Meetings

23. **S. Park**, K. S. Hong, S.-D. Seo, H. J. Kim, C. W. Lee, H. J. Song, S. S. Shin, H. K. Park, "Three-dimensional hierarchical $\text{Li}_4\text{Ti}_5\text{O}_{12}$ architecture by a sacrificial template route" *Internatinoal conference on surface engineering (ICSE 2013)*, Nov 18-21, 2013, Busan, Korea
22. **S. Park**, H. J. Kim, C. W. Lee, H. J. Song, S. H. Kim, S. S. Shin, D.-W. Kim, K. S. Hong, "Three-dimensional hierarchical hematite architecture with self-doped Sn^{4+} for photoelectrochemical water splitting", *The 2nd International conference on advanced electromaterials (ICAE 2013)*, Nov 12-15, 2013, Jeju, Korea.
21. C. W. Lee, S. D. Seo, D. W. Kim, **S. Park**, K. Jin, D. W. Kim, K. S. Hong, "Heteroepitaxial Growth of ZnO Nanosheet Bands on ZnCo_2O_4 Submicron rods Toward High-Performance Li Ion battery electrodes", *3rd European Energy Conference (E2C)*, Oct 27-30, 2013, Budapest,

Hungary.

20. H. J. Song, K.-M. Min, H.-S. Roh, C. W. Lee, **S. Park**, D.-W. Kim, K. S. Hong, "Synthesis of Size-Tunable and Nitrogen-Doped Anatase TiO₂ as An Anode for Lithium-Ion Batteries", *International Congress on Materials and Renewable Energy (MRE 2013)*, July 1-3, 2013, Athens, Greece.
19. **S. Park**, S. H. Kim, C. W. Lee, H. J. Song, S. W. Seo, H. J. Kim, D.-W. Kim, K. S. Hong, "Two-step hydrothermal method-based SrTiO₃@TiO₂ heterostructures with uniform morphology for efficient photoelectrochemical devices", *International Congress on Materials and Renewable Energy (MRE 2013)*, July 1-3, 2013, Athens, Greece.
18. S. W. Seo, T. H. Noh, **S. Park**, C. W. Lee, S. H. Kim, K. S. Hong, "Solvothermal synthesis of SnNb₂O₆ and their photocatalytic H₂ evolution under visible light", *Nanosmat-asia*, March 13-15, 2013, Wuhan, China.
17. **S. Park**, S. Lee, C. W. Lee, S. W. Seo, S.-D. Seo, D. Kim, S. H. Kim, D.-W. Kim, K. S. Hong, "Growth of anatase nanoshells and rutile nanorods on 1D TCO nanowire via surfactant-free wet chemical route", *Nanosmat-asia*, March 13-15, 2013, Wuhan, China.
16. **S. Park**, S. W. Seo, C. W. Lee, S. H. Kim, S. Lee, D.-W. Kim, K. S. Hong, "Heteroepitaxial Branched TiO₂ Nanorods on Sb:SnO₂ Nanobelt backbones for Photoelectrochemical Hydrogen Production", *37th international conference and exposition on advanced ceramics and composites (ICACC 37th)*, January 27-February 1, 2013, Florida, USA
15. S. Kim, **S. Park**, C. W. Lee, S. W. Seo, J. Kim, K. S. Hong, "Photophysical and photocatalytic water splitting performance of stibiotantalite type-structure compounds, SbMO₄ (M=Nb, Ta)", *Electronic Materials and application*, January 23-25, 2013, Florida, USA
14. S. W. Seo, T. H. Noh, **S. Park**, C. W. Lee, S. H. Park, K. S. Hong, "Solvothermal synthesis and photocatalytic property of SnNb₂O₆", *E-*

MRS 2012 spring meeting, 2012, Strasbourg, France.

13. I. J. Park, S. Lee, **S. Park**, K. S. Hong. "Photocatalytic Degradation of Phenol with Preferred-oriented TiO₂ Nanotube Arrays", *Internatinoal conference on surface engineering (ICSE 2011)*, November 7-10, 2011, Jeju, Korea
12. **S. Park**, D. Kim, C. Lee, S. Lee, H. Jung and K. Hong. "Synthesis of Sb Doped SnO₂ Nanowire for Application to Dye-sensitized Solar Cells (DSSCs)", *ECS 219th Meeting*, May 1-6, 2011, Montreal, Canada.
11. S. Lee, **S. Park**, G. S. Han, J. H. Noh, H. S. Han, H. S. Jung, K. S. Hong, "Indium-Tin-Oxide Nanowire-based Photoelectrodes for Photoelectrochemical System", *2011 MRS Spring Meeting and Exhibit*, April 25-29, 2011, San Francisco, USA.
10. J. H. Noh, H. S. Han, S. Lee, D. Kim, J. H. Park, **S. Park**, K. S. Hong, "Dye Sensitized Solar Cells Employing Nb doped TiO₂/Al-doped ZnO Transparent Conducting Multilayer Films", *35th international conference and exposition on advanced ceramics and composites (ICACC 35th)*, Jan 23-28, 2011, Florida, USA.
9. T. H. Noh, H. S. Roh, S. W. Seo, **S. Park**, C. W. Lee, K. S. Hong, "Electronic structure and optical absorption of band gap tailored SrBi₂Nb_{2-x}V_xO₉ solid solutions", *Electronic Materials and Applications 2011 (EMA 2011)*, Jan 19-21, 2011, Florida, USA.
8. S. Lee, **S. Park**, K. S. Hong, D.-W. Kim, "Facile synthesis and photocatalytic properties of pure brookite-type TiO₂ nanoparticles", *5th International Conference on Surfaces, Coatings and Nanostructured Materials (Nanosmat-5)*, October 18-21, 2010, Reims, France.
7. J. H. Noh, H. S. Han, S. Lee, **S. Park**, J. S. Kim, H. S. Jung, K. S. Hong, "Synthesis of indium tin oxide nanowire array on glass substrate", *IUMRS-ICEM 2010*, August 22-27, 2010, KINTEX, Korea.
6. J. H. Noh, H. S. Han, S. Lee, **S. Park**, J. S. Kim, H. S. Jung, K. S. Hong, "Synthesis of Indium Tin Oxide, Hwire Array on Glass Substrate",

IUMRS-ICEM 2010, August 22-27, 2010, KINTEX, Korea.

5. **S. Park**, S. Lee, D. Kim, I.-S. Cho, C. W. Lee, K. S. Hong, “Fabrication of TiO₂/ITO-based photoelectrode coated with overlayer materials and its photoelectrochemical behavior”, *IUMRS-ICEM 2010*, August 22-27, 2010, KINTEX, Korea.
4. **S. Park**, S. Lee, J. H. Noh, H. S. Han, C. W. Lee, H. S. Jung, K. S. Hong, “Tin-doped indium nanowires for photoelectrochemical water splitting”, *E-MRS 2010 Spring Meeting*, June 07-11, 2010, Strasbourg, France.
3. T. H. Noh, I. S. Cho, H.-S. Roh, **S. Park**, K. S. Hong, “Photophysical and Photocatalytic activity of Zn₃M₂O₈ (M=Nb, Ta)”, *Proceeding of the 6th european meeting on solar chemistry&photocatalysis: Environmental Applications (ICAE6)*, June 13-16, 2010, Prague, Czech Republic.
2. **S. Park**, J. H. Noh, K. S. Hong, “Structure and optical properties of Cu-Al-O thin film by RF magnetron sputtering”, *Joint Symposium of International Workshop on Piezoelectric Materials and Applications in Actuators (IWPMA 2009) & International Symposium on Electroceramics (ISE 2009)*, Nov 8-11, 2009 Jeju, Korea.
1. **S. Park**, S. Lee, D. Kim, I.-S. Cho, K. S. Hong, “Effect of overlayer materials on photoelectrochemical characteristics of TiO₂/ITO-based photoelectrode and their application to water splitting”, *The 10th Asian Hydrogen Energy Conference (AHEC)*, April 8-10, 2009, Pohang, Korea.